Flow and Heat Transfer in a Radially Spreading Liquid Metal Jet Related to Casting of Ferroalloys

Dr. ing. thesis by

Harald T. Haaland

Department of Materials Technology and Electrochemistry
Norwegian University of Science and Technology
IME rapport 2000:20

This thesis has been submitted to the Norwegian University of Science and Technology (NTNU) in partial fulfilment of the doctoral degree Doktor Ingeniør.

URN:NBN:no-6407

Acknowledgement

This work has been carried out at the Department of Materials Technology and Electrochemistry at the Norwegian University of Science and Technology (NTNU), Trondheim, Norway between September 1993 and July 2000. My supervisor during this period was Professor Jon Arne Bakken, whom I am much grateful to for his continued patience, support and wit. I highly value his solid tutoring and relaxed manner.

The study was initiated by Thor Mühlbradt in Elkem Technology Services as part of an EXPOMAT project. I am grateful to Elkem for their financial support through the major part of this study.

I am also very grateful for having met and worked with the staff at the Department of Process Metallurgy and Ceramics, SINTEF. I highly value the relationships that were built and the help received.

Invaluable help has been received from the various highly skilled workshops at NTNU.

Special thanks are due to "the dwellers in the Shed" - for their practical help and the stimulating and extremely friendly atmosphere there.

Parts of this thesis have been presented at the Electric Furnace Conference in 1996 (recipient of Charles W. Briggs award for best paper) and 1997, at Norsk Metallurgisk Selkaps summer meeting in 1998 and in the journal ”Iron and Steelmaker”, October 1997.

Trondheim 2000, Harald T. Haaland

ABSTRACT

In the past more and more advanced and fine-tuned processes for steel production have resulted in increased demands for new and more cost-effective ferroalloys used as constituents in the processes. Casting techniques and equipment are continually studied for potential improvements. In order to ensure a high and consistent quality in the alloys and the casting equipment, the heat transfer from the alloy to the mould during casting must be understood. Research on free metal flows is scarce and to remedy this a doctoral study at the Norwegian University of Science and Technology was initiated.

The study was limited to the region around the impingement point of the metal jet, because this is the critical area for both heat and mass transfer. The flow develops radially, first as a thin film spreading evenly over the surface. At a certain point the thickness of the film increases suddenly - known as a hydraulic jump. Only steady-state conditions on a flat plate (without accumulation of fluid) are studied. The jump develops before the flow reaches the edge of the plate and maintains this position until steady-state conditions are obtained. This system is believed to be a good approximation for the initial conditions during the filling of an open mould. This is also the period when the thermal load on the mould is greatest.

Numerous practical and mathematical simulations have been carried out and a relatively simple analytical model depicting the surface profile of the liquid metal including heat transfer to the surroundings has been developed. The computational fluid dynamics code FLUENT was also used to compute the surface profile with the Volume-Of-Fluid technique, but with little success. The code was instead used to determine the flow and temperature fields inside the already established surface profile. Various laminar and turbulent flow models (variations of the k - ε model) were tried and compared. Experiments with water were carried out for studying the flow field. Tin was used for heat transfer studies. Finally, these simulations were compared with results from the practical experiments.

Introductory experiments were carried out with ferrosilicon with the intent to perform complete experiments with this metal.

URN:NBN:no-6407

Measured heat flow usually exceeded predicted values, particularly in the stagnation region. Good agreement is shown between the results from the FLUENT simulations and the new analytic model, which shows good promise of acting as a useful alternative to the much more demanding numerical simulations.

URN:NBN:no-6407

Table of Contents

1. Introduction and Background

In the last century production of ferroalloys has been one of Norway's major industries, especially when measured in export value. Research within the field has mainly been aimed towards the production process, while the products themselves have not received as much attention. For many years, demands regarding product quality have been uncomplicated. The products are after all only used as raw materials for other industries, for example steel processing.

Lately, however, the growing number of advanced and fine-tuned processes for steel production has resulted in demands for new and more effective ferroalloys used as constituents in the processes. These requirements apply to the shape, strength and chemical composition of the alloys. To meet these demands better, more cost-effective technology must be put to use, so as to deliver products of a higher value and quality to the customers. This contributes to stronger focus on casting, crushing and screening at the different plants and production centres.

The ferroalloys produced in Norway include various grades of chromium, manganese and silicon. It is customary to divide them into grades depending on the content of one or more elements, for example FeSi75. This is an iron-silicon alloy with 75 weight % silicon.

The manganese bearing alloys are ferromanganese and siliconmanganese of various grades. In 1999 the global production totalled around 7 070 000 metric tons with Norway's share about 7% of this. Practically all of this goes to the steel industry as alloying elements for steel production.

The silicon products are pure silicon and ferrosilicon of different compositions. The global production in 1999 was 950 000 and 3 250 000 metric tons for the two groups respectively - Norway accounting for about 13% of both. Their main applications are:

- deoxidation and alloying of steel and cast iron (primarily ferrosilicon)
- alloying of other metals, principally aluminium (primarily silicon metal)

- raw materials for the chemical industry (primarily silicon metal, some high-silicon ferrosilicon)
- raw materials for the semiconductor industry (primarily silicon metal, some high-silicon ferrosilicon)
    - electronic devices (silicon with impurities in the ppb range)
    - photovoltaic cells (silicon with impurities in the ppm range)

In 1999 the global production of ferrochromium was in the region of 3 500 000 metric tons. About 7% of this was produced in Norway and it is mostly used as alloying elements in steel processing.

The ferroalloys mentioned here are all produced in electric smelting furnaces - so-called submerged electric arc furnaces.

The contents of the furnaces are tapped into ladles (where refinement can take place) and cast in various methods. The most traditional are casting into *beds of sand* or *metal fines* and casting into *iron moulds* of different sizes. The metal can be cast in layers or all in one batch. After solidification the metal is transported to a crushing station where it is broken down into pieces of a size acceptable to customers. The primary disadvantage of crushing is the inherent production of fines. This undersized material is unwanted by the customers and can subsequently only to a very limited extent be sold. Most of it is remelted.

A more advanced method used for silicon and ferrosilicon is *water granulation*, where the metal, under strict conditions, is poured into water. This produces small, quickly-solidified metal pellets and subsequent downsizing is superfluous.

Extensive research has been directed towards alternative casting techniques. In 1991, Elkem ASA Technology Services began a five-year development program called Post Taphole 1995. The goal of the program was to create a new process for casting ferroalloys and silicon metal. Two of the requirements that had to be met were minimal handling of the metal after casting and reduction of the off-grade production (i.e. fines, sculls and metal loss). One solution that can satisfy these and other requirements is a *continuous cast-to-shape* (*CTS*) process. Elkem has worked on such projects a number of times during the past few decades, but they have all

been rejected for technical, market, cost and financial reasons. With the Post Taphole program, the idea resurfaced.

Without going into detail, a bar casting technique seemed the most promising choice. The bars are cast directly to their final size in two dimensions and need only to be cut in the longitudinal direction to meet customer specifications. In this way the fines generation is reduced by 2/3. Numerous mathematical and practical simulations of flow and heat transfer in open channels were performed and a pilot plant was built. The system worked as planned, but thermocouples in the mould registered temperatures that were somewhat higher than calculated, especially beneath the impingement point of the metal jet. This is a critical area for both heat and mass transfer. A decision was made to investigate more closely the heat transfer and metal flow around such an impingement point. This doctoral study was initiated as a result.

The flow analyzed is a vertical jet impinging on a horizontal flat plate. In order to simplify matters as best as possible, the fluid is left to flow over the edge of the plate. In this way there is no filling of a receptacle as in traditional casting, but the simplified flow is believed to reliably reflect the conditions during the initial stages of a casting process. This period, before the mould has started filling, is when the thermal loads are at their greatest. Moulds have then been known to crack.

The casting temperature of the alloys in question is in the range of 1400 to 1700 °C and it is obvious that the equipment involved is subject to high mechanical and thermal loads. Also, the strength and quality of metals in general are highly dependent on casting and cooling conditions. If a reliable tool for heat transfer calculations is obtained, casting techniques and equipment can hopefully be optimized - with increased product quality, increased lifetime of equipment and increased cost-efficiency as the result.

In addition to the casting process, heat transfer from liquid metals is important in the furnace itself (to the lining and taphole), in tundishes and runners, and in ladles.

Product quality and level of cost are two key factors for future competitiveness within the ferroalloy field. Increased quality will in many cases yield lower costs, for example by reduced offgrade production. Casting processes and equipment are continuously trying to be improved.

The impingement of liquid jets on barriers is widely used in metallurgical and chemical engineering processes. In such conditions *convective* heat and mass transfer is experienced. It is therefore a great advantage to have knowledge of the velocity and temperature distributions in the liquid films formed. This has indeed been studied for a long time, but some points still remain obscure.

Figure 1.1 Photograph taken during casting of ferrosilicon from ladle to open mould. Elkem Thamshavn, Norway, 2000.

2. Basic Flow and Heat Transfer Theory

2.1 Introduction

In order to simulate casting processes, it is vital to know the principles of heat transfer involved. This chapter describes the different modes of heat transfer and gives an overview of the equations that must be solved in flow and heat transfer problems. The theory is taken from various textbooks in the reference list.

2.2 Heat Transfer

2.2.1 Heat Transfer in Solids

Heat transport in solid bodies is restricted to one mechanism: *conduction*, also called *diffusion*, of heat. In a solid there is no *bulk motion* of the material and heat is transferred by random molecular motion. *Fourier's law* describes this. In a one-dimensional system with heat flow in the *x*-direction it takes the form

$$q_x = -k\frac{\partial T}{\partial x} \tag{2-1}$$

q_x is the *heat flux density* [W/m^2], k the *thermal conductivity* [W/mK] of the solid and $\frac{\partial T}{\partial x}$ the *temperature gradient* [K/m]. The minus sign appears because heat flow is defined as positive when occurring from a region of higher temperature to one of lower temperature. In a Cartesian three-dimensional system, we have

$$\vec{q} = -k\left(\vec{e}_x\frac{\partial T}{\partial x} + \vec{e}_y\frac{\partial T}{\partial y} + \vec{e}_z\frac{\partial T}{\partial z}\right) \tag{2-2}$$

$\vec{e}_x, \vec{e}_y$ and $\vec{e}_z$ are the unit vectors in the *x, y* and *z* directions.

2.2.2 Heat Transfer in Fluids

Conduction is also present in fluids, but here there is an additional heat transfer due to the bulk, or macroscopic, motion of the fluid, known as *convection*. Heat transfer between a solid body and a fluid is very complex to theoretically describe exactly. For practical calculations a *convective heat transfer coefficient*, h_c, is used. The heat flux density is then written as

$$q = -h_c (T_\infty - T_s) \tag{2-3}$$

T_s is the local surface temperature of the solid and T_∞ the temperature in the fluid "far from the surface" (i.e. outside the boundary layer), also called the *bulk temperature* of the fluid. The convective heat transfer coefficient is a complex and variable quantity, depending on the surface geometry, the characteristics of the flow and the physical properties of the fluid. It is not a material property like for example the thermal conductivity. Theoretical studies and practical experiments determine its value.

2.2.3 Radiation

All matter at temperatures above 0 K emits thermal energy by electromagnetic waves, known as *radiation*. This is a strongly temperature dependent mechanism as prescribed by the *Stefan-Boltzmann law*:

$$q_{rad} = \varepsilon \sigma T_s^{\,4} \quad [\mathrm{W/m^2}] \tag{2-4}$$

T_s is the surface temperature of the material and σ Stefan-Boltzmann's constant (=$5.67 \cdot 10^{-8}$ $\mathrm{W/m^2K^4}$). ε is the total *emissivity*, a radiative property of the surface with values in the range $0 \le \varepsilon \le 1$. It depends on the material

and surface finish. Often there is the problem of radiative exchange between two or more surfaces. A concave body, for example, can exchange radiation with itself. Such geometrical features are taken into account by use of *view factors* (also called *configuration* or *shape factors*). The computation of these can be quite complex.

When radiation and convection occur simultaneously at a surface, it can be convenient to express the radiation in terms of a *radiative* heat transfer coefficient. Ignoring possible view factors, this is described as

$$h_r = \varepsilon\sigma(T_1 + T_2)(T_1^2 + T_2^2) \tag{2-5}$$

2.2.4 Combined Modes of Heat Transfer

Let us consider two fluids at temperatures T_a and T_b separated by a composite wall. The system is in a steady state and the wall is exchanging heat by convection and radiation at both sides. If T_a is highest, we can formulate the heat flow as:

$$q = -U(T_a - T_b) \tag{2-6}$$

U is an *overall heat transfer coefficient* defined as

$$\frac{1}{U} = \frac{1}{h_{ca} + h_{ra}} + \frac{t_1}{k_1} + \frac{t_2}{k_2} + \frac{t_3}{k_3} + \frac{1}{h_{cb} + h_{rb}} \tag{2-7}$$

t_1 is the thickness of material 1 in the wall and k_1 its thermal conductivity, etc. See Figure 2.1.

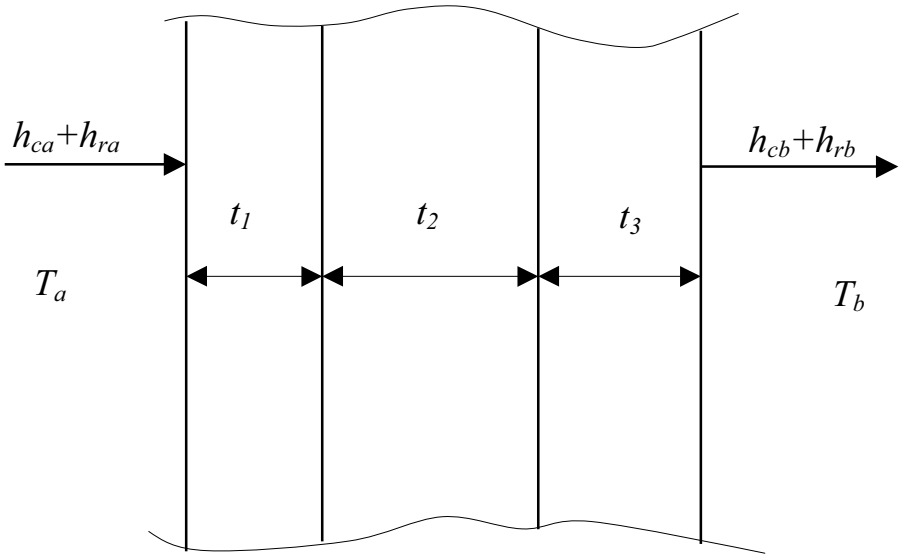

Figure 2.1 Heat exchange between two fluids at temperature T_a and T_b through a composite wall.

2.3 Governing Equations

Numerical solution of heat transfer, fluid flow and other related processes is based on solving certain *conservation equations*, which govern the processes. These equations for mass, momentum, energy and turbulent quantities are derived and explained in a variety of textbooks. In the following they are expressed in cylindrical coordinates (r, θ, z) with velocity components u, v and w. Our system is assumed *axisymmetric*, hence there are no variations or gradients in the azimuthal (θ) direction.

2.3.1 Conservation of Mass

$$\frac{\partial \rho}{\partial t} + \frac{\partial (\rho u)}{\partial z} + \frac{1}{r}\frac{\partial (r \rho w)}{\partial r} = 0 \qquad (2\text{-}8)$$

ρ is the density of the fluid.

2.3.2 Conservation of Momentum

r direction:

$$\frac{\partial}{\partial t}(\rho u)+\frac{\partial}{\partial z}(\rho uw)+\frac{1}{r}\frac{\partial}{\partial r}(r\rho uu)=-\frac{\partial P}{\partial r}+$$

$$\frac{\partial}{\partial z}\left[\mu_{eff}\left(\frac{\partial u}{\partial z}+\frac{\partial w}{\partial r}\right)\right]+\frac{1}{r}\frac{\partial}{\partial r}\left[2r\mu_{eff}\frac{\partial u}{\partial r}-\frac{2}{3}\mu_{eff}\left(\frac{\partial (ru)}{\partial r}+r\frac{\partial w}{\partial z}\right)\right] \tag{2-9}$$

z direction:

$$\frac{\partial}{\partial t}(\rho w)+\frac{\partial}{\partial z}(\rho ww)+\frac{1}{r}\frac{\partial}{\partial r}(r\rho uu)=-\frac{\partial P}{\partial z}+$$

$$\frac{1}{r}\frac{\partial}{\partial r}\left[r\mu_{eff}\left(\frac{\partial u}{\partial z}+\frac{\partial w}{\partial r}\right)\right]+\frac{\partial}{\partial z}\left[2\mu_{eff}\frac{\partial w}{\partial z}-\frac{2}{3}\mu_{eff}\left(\frac{1}{r}\frac{\partial (ru)}{\partial r}+\frac{\partial w}{\partial z}\right)\right] \tag{2-10}$$

P is the static pressure and μ_{eff} the *effective* dynamic viscosity of the fluid - composed of a molecular viscosity and a *turbulent* contribution if the flow is turbulent. Turbulence is addressed more closely in Chapters 3 and 5.

It is assumed that the flows considered in this work are *incompressible*, which implies that the pressure differences are relatively small and that pressure influence on density, enthalpy and the transport coefficients is negligible.

It is also assumed that the fluids are *newtonian*, i.e. the viscous shear stresses in the fluids are proportional to their velocity gradients, the proportionality factor being the viscosity $\left(\tau = \mu \frac{\partial u}{\partial y}\right)$.

2.3.3 Conservation of Energy

$$\frac{\partial}{\partial t}(\rho h) + \frac{\partial}{\partial z}(\rho w h) + \frac{1}{r}\frac{\partial}{\partial r}(r\rho u h) = \frac{\partial}{\partial z}\left(\frac{k_{eff}}{c_p}\frac{\partial h}{\partial z}\right) + \frac{1}{r}\frac{\partial}{\partial r}\left(r\frac{k_{eff}}{c_p}\frac{\partial h}{\partial r}\right) + S_h \tag{2-11}$$

h is the specific enthalpy of the fluid and k_{eff} its effective thermal conductivity, defined analogously to the viscosity. c_p is the specific heat capacity of the fluid and S_h a source term, which can contain heat transfer by radiation and heat generation due to viscous dissipation (internal friction in the fluid). This is not considered in this work. Using the relation $c_p = \frac{dh}{dT}$, the temperature can be found.

All these partial differential equations are similar in structure and can be arranged in a common form, with Φ as the unknown variable. The Cartesian notation is:

$$\frac{\partial}{\partial t}(\rho \bar{u}) + \frac{\partial(\rho u_i \Phi)}{\partial x_i} = \frac{\partial}{\partial x_i}\left(\tilde{u}_{\bar{u}}\frac{\partial \bar{u}}{\partial x_i}\right) + S_{\bar{u}} \tag{2-12}$$

The terms are from left to right the time-derivative, the convective, diffusive and source terms. Γ_Φ is the diffusion coefficient, e.g. $\frac{k_{eff}}{c_p}$ in equation (2-11).

2.4 Boundary Layers

2.4.1 General

When a viscous fluid in motion is in contact with a solid boundary (flow on a plate, inside a tube, etc.), the fluid near the boundary is slowed down by viscous forces. The velocity u varies from zero at the boundary to a finite value, U_∞, associated with the flow (generally the bulk velocity). This region of flow retardation is known as the *hydrodynamic*, or, *velocity boundary layer*. The thickness of this layer varies with the flow conditions. The region outside the boundary layer is called the *free stream* or *undisturbed* or *potential flow regime* and the effect of viscous forces here are often neglected. The quantity δ_v is termed the *velocity boundary layer thickness* and it is typically defined as the distance from the boundary to where $u = 0.99U_\infty$. Another much used definition is the so-called *equivalent film thickness* for momentum transfer.

If the boundary and bulk fluid temperatures differ, there will be a region through which the temperature varies from the boundary temperature to the bulk fluid temperature. This region, called the *thermal boundary layer*, may be smaller, larger or the same size as through which the velocity varies. The quantity δ_T is termed the *thermal boundary layer thickness*, defined similarly to the velocity boundary layer. In problems where mass is exchanged between the boundary and the fluid, a *concentration boundary layer* similarly exists. Situations can arise in which all three boundary layers are present. In such cases they rarely grow at the same rate and their values at a given location are not necessarily the same.

Since most of the resistance to momentum, heat and mass transfer resides in the boundary layers, special theories for these regions have been developed. In solving most convective heat and mass transfer problems, the corresponding fluid dynamic problem must first be solved, provided it is not completely *coupled* to the heat and mass transfer problems. To help us in such work three *dimensionless parameters* are defined. These have physical interpretations that relate to conditions in the flow.

The first of these is the *Reynolds number, Re*, which may be interpreted as the *ratio of inertia to viscous forces*;

$$Re = \frac{UL}{\nu}$$

where U is a velocity, ν the kinematic viscosity of the fluid [m^2/s^3] and L a characteristic length depending on the geometry of the flow.

Secondly there is the *Prandtl number*, *Pr*, which provides a *measure of the relative effectiveness of momentum and energy transport by diffusion in the velocity and thermal boundary layers,* respectively.

$$Pr = \frac{c_p \mu}{k} = \frac{\nu}{\alpha}$$

α is the thermal diffusivity of the fluid [m^2/s]. *Pr* may vary from 10^{-3} for liquid metals to 4000 for very viscous oils. The value of *Pr* strongly influences the relative growth of the velocity and thermal boundary layers. If $Pr << 1$ the energy diffusion rate greatly exceeds the momentum diffusion rate, i.e. the thermal boundary layer develops much faster than the velocity boundary layer. In such problems little error is introduced if the velocity everywhere in the thermal boundary layer is assumed to be the bulk velocity U_∞. On the other hand, when the Prandtl number is very high, the velocity boundary layer develops quickest and will be much thicker than its thermal counterpart. In such cases simple solutions can be obtained by assuming an approximately linear velocity profile inside the thermal boundary layer. For gases *Pr* is near unity, indicating that energy and momentum transfer by diffusion are of comparable proportions.

Finally there is the *Schmidt number, Sc*, which is *a measure of the relative effectiveness of momentum and mass transport by diffusion in the velocity and concentration boundary layers*, respectively. Mass or species transport is, however, not pertinent to this study.

In summary, the velocity boundary layer is characterised by the presence of *velocity gradients* and *shear stresses*. The thermal boundary layer is characterised by *temperature gradients* and *heat transfer* and the concentration boundary layer by *concentration gradients and mass transfer*. From a more practical point of view analyses of these regions can help us define three key boundary layer parameters, namely the *friction coefficient,* c_f, and the *heat* and *mass transfer coefficients,* h_c *and* h_m. Theoretical results are, however, obtained mostly for simple flow situations. More often it is necessary to calculate the parameters from practical experiments, resulting in so-called *empirical correlations*. The problem is far from simple, for in addition to depending on numerous fluid properties, the coefficients depend on surface geometry and flow conditions.

In this study liquid metals are of main concern. The Reynolds numbers for these and for water are roughly the same. This means that *water* can be used to in experiments to *simulate* the flow of *liquid metal*. This is a great practical benefit. Unfortunately the Prandtl number for liquid metals can be several orders of magnitude less than that of water. Because of this, the relative development of the velocity and thermal boundary layers in these liquids is vastly different and water can definitely *not* be used to simulate the thermal conditions in a liquid metal. Hence a liquid metal must be used in experiments involving heat transfer in liquid metals. As a result of its comfortably low melting point, *tin* has been used in many of the experiments described in this work.

In their separate conservation equations (converted to dimensionless form) the dimensionless variables often assume analogous roles. This implies that the boundary layers generally are of the same functional forms.

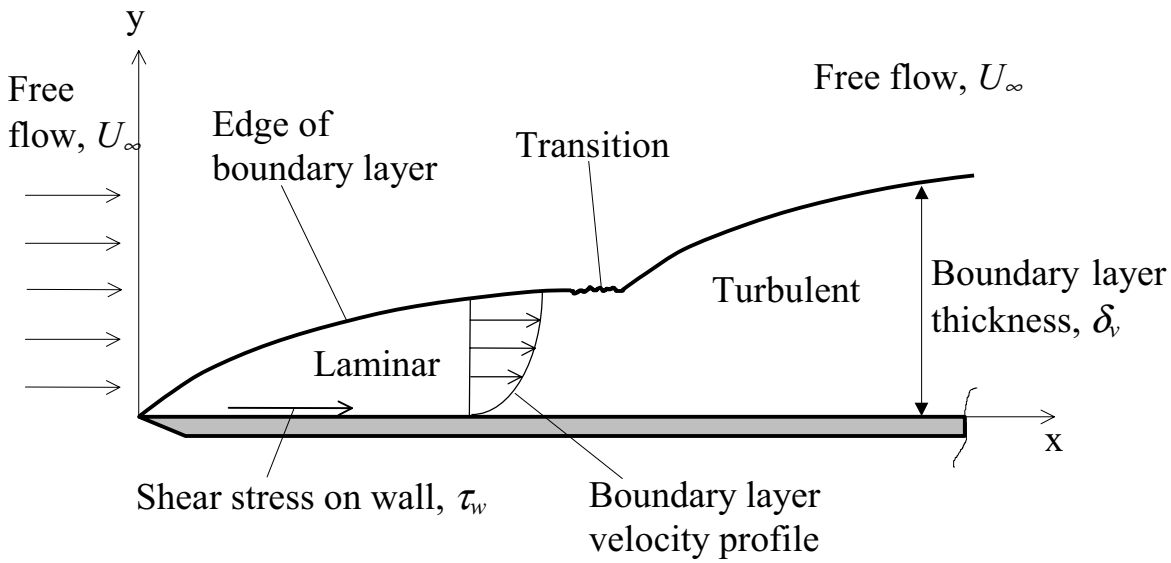

Figure 2.2 Details of velocity boundary layer for flow along a thin flat plate.

The conservation equations in boundary layers can be simplified when the boundary layer thickness is small compared to all other flow dimensions. In a two-dimensional system the following conditions then prevail within the layer:

$$\frac{\partial^2 \bar{u}}{\partial y^2} >> \frac{\partial^2 \bar{u}}{\partial x^2}$$

These are referred to as *boundary layer approximations* and result in the following conservation equations for a steady-state incompressible problem:

Momentum, *r*-direction:

$$u\frac{\partial u}{\partial r} + w\frac{\partial u}{\partial z} = -\frac{1}{\rho}\frac{\partial p}{\partial r} + \nu\frac{\partial^2 u}{\partial z^2} \qquad (2\text{-}13)$$

Energy, *r*-direction:

$$u\frac{\partial T}{\partial r}+w\frac{\partial T}{\partial z}=\alpha\frac{\partial^2 T}{\partial z^2} \tag{2-14}$$

2.4.2 Turbulent flow

In all convection problems it is essential to determine whether the boundary layer is turbulent or laminar. Surface friction and convection transfer rates depend strongly on which of these conditions exists. In laminar situations the flow is highly ordered and it is possible to identify streamlines along which the fluid particles move. A turbulent flow is highly irregular and characterised by velocity fluctuations and intermingling of fluid particles, which enhance the transfer of momentum, energy and species. Boundary layer thicknesses are larger, and velocity, temperature and concentration profiles flatter than in a laminar flow. Near the wall turbulent boundary layers have a thin laminar or *viscous sublayer*.

Figure 2.3 shows the velocity boundary layer development on a flat plate. Initially it is laminar, but at some distance from the leading edge fluid fluctuations become noticeable (*transition region* from laminar to turbulent) and eventually the flow becomes turbulent. The location of the transition is described by the Reynolds number and depends on the type of flow (such as flow over a flat plate or in a closed channel). The expected development of the convective heat transfer coefficient is also shown. It is generally higher for turbulent than laminar flows.

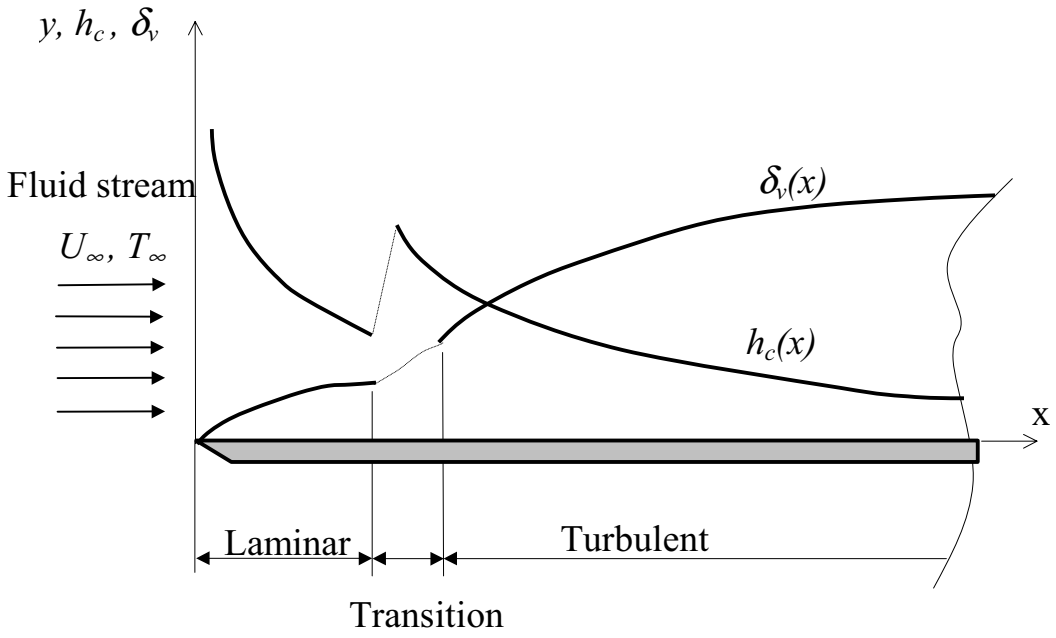

Figure 2.3 Presumed variation of velocity boundary layer thickness δ_v and heat transfer coefficient h_c for flow over an isothermal flat plate.

2.5 Flow Over a Flat Plate

Only *laminar* velocity boundary layers are considered in this section. An *x, y* coordinate system with *u* and *v* velocity components is used.

2.5.1 Similarity Solution

2.5.1.1 Velocity Boundary Layer

Even though the boundary layer equations result in considerable simplifications of the complete set of conservation equations, exact analytical solutions have unfortunately only been found for a few simple cases, and a great deal of work is often required to obtain them. One of these is flow over a flat plate with uniform free-stream velocity, which has been studied by Prandtl, Blasius and Pohlhausen.

Let us consider a steady, incompressible and two-dimensional laminar flow along a flat plate with constant free-stream velocity, U_∞, and free-stream temperature, T_∞. The plate is kept isothermal at a temperature T_w. Thermal energy generation due to viscous dissipation is considered negligible and will be neglected here. Properties are assumed to be constant.

A so-called *stream function, $\Psi(x, y)$* is introduced such that

$$u = \frac{\partial \psi}{\partial y} \text{ and } v = -\frac{\partial \psi}{\partial x}.$$

In this way the continuity equation is satisfied and the momentum equation "reduces" to

$$\frac{\partial \psi}{\partial y}\frac{\partial^2 \psi}{\partial x \partial y} - \frac{\partial \psi}{\partial x}\frac{\partial^2 \psi}{\partial y^2} = \nu \frac{\partial^3 \psi}{\partial y^3} \tag{2-15}$$

The stream function is simply a way of replacing the u and v (or x and y) components of a velocity with one single function.
Blasius introduced the similarity variable

$$\eta = y\sqrt{\frac{U_\infty}{\nu x}}$$

and showed that the solution to equation (2-15) is given by

$$\psi = g(\eta)\sqrt{U_\infty \nu x},$$

where $g(\eta)$ is a function to be determined. After skilful manipulation, equation (2-15) can be transformed to the more pleasant-looking

$$\frac{d^3 g}{d\eta^3} + \frac{1}{2} g \frac{d^2 g}{d\eta^2} = 0 \tag{2-16}$$

This is a non-linear dimensionless equation and can be solved generically once and for all. However, no analytical solution can be obtained, but the problem can be solved numerically on a computer or in the form of a power series expansion. Tables presenting values for η, g, g' and g'' can be found in most fluid flow textbooks. The velocities can now be expressed as

$$u = U_\infty g'(\eta)$$

$$v = \sqrt{\frac{U_\infty \nu}{4x}}[\eta\, g'(\eta) - g(\eta)]$$

The following three boundary conditions are utilised to determine the solution for $g(\eta)$:

1) $g'(\eta) = 0$ *at* $\eta = 0$ *(u = 0 at y = 0)*

2) $g(\eta) = 0$ *at* $\eta = 0$ *(v = 0 at y = 0)*

3) $g'(\eta) = 1$ *as* $\eta \to \infty$ *($u \to U_\infty$ far from the plate)*

If the velocity boundary layer thickness is said to be the distance from the plate at which u reaches 99% of the free stream velocity $\left(\frac{u}{U_\infty} = g'(\eta) = 0.99\right)$, it is found (knowing the solution for $g(\eta)$) that

$$\delta_v = 4.92\sqrt{\frac{\nu x}{U_\infty}} \qquad (2\text{-}17)$$

2.5.1.2 Thermal Boundary Layer

By inserting the velocity components found in the preceding section in the energy equation for the boundary layer, the temperature field here can be determined. The necessary boundary conditions are:

1) $T = T_w$ at $y = 0$
2) $T = T_\infty$ as $y \to \infty$
3) $T = T_\infty$ at $x = 0$

The heat flow is in this work defined to be *from* the fluid *to* the plate, i.e. $T_\infty > T_w$. This has no influence on the generality of the work, and is just a matter of convenience. If the dimensionless temperature, θ, defined as

$$\theta = \frac{T - T_w}{T_\infty - T_w}$$

is introduced, the energy equation may be written as

$$u\frac{\partial \theta}{\partial x} + v\frac{\partial \theta}{\partial y} = \alpha \frac{\partial^2 \theta}{\partial y^2}.$$

Once again a similarity solution is used with $\theta = \theta(\eta)$, η being the same as before. With the velocity components from the Blasius solution, the following ordinary non-linear differential equation is obtained

$$\frac{d^2\theta}{d\eta^2} + \frac{1}{2} Pr\, g(\eta)\frac{d\theta}{d\eta} = 0$$

In short, the solution for the dimensionless temperature distribution is

$$d(\eta, Pr) = \frac{\int_0^{\eta} (g'')^{Pr}\, d\eta}{\int_0^{\infty} (g'')^{Pr}\, d\eta}$$

The local heat flux from (or to) the plate is given by

$$q(x) = -k\left.\frac{\partial T}{\partial y}\right|_{y=0} = -k(T_\infty - T_w)\left.\frac{d\theta}{d\eta}\right|_{\eta=0} \frac{\partial \eta}{\partial y} = k(T_w - T_\infty)\sqrt{\frac{U_\infty}{3x}}\left.\frac{d\theta}{d\eta}\right|_{\eta=0}.$$

We have

$$\left.\frac{d\theta}{d\eta}\right|_{\eta=0} = \frac{(g''(0))^{Pr}}{\int_0^{\infty} (g'')^{Pr}\, d\eta}. \qquad (2\text{-}18)$$

Pohlhausen has evaluated this expression numerically for a range of Prandtl numbers. The results can be approximated by

$$\left.\frac{d\theta}{d\eta}\right|_{\eta=0} = \begin{cases} 0.564(Pr)^{\frac{1}{2}} & Pr \to 0 \\ 0.332(Pr)^{\frac{1}{3}} & 0.6 < Pr < 15 \\ 0.339(Pr)^{\frac{1}{3}} & Pr \to \infty \end{cases}$$

For *liquid metals* we consequently have

$$q(x) = 0.564k(T_w - T_\infty)\, Pr^{\frac{1}{2}} \sqrt{\frac{U_\infty}{\nu x}}\,. \tag{2-19}$$

It can be noted that the above expression results in an infinitely large heat flux at the leading edge of the plate *(x=0)*. The boundary layer equations are not valid here.

Furthermore we obtain the local heat transfer coefficient*,* h_c, and the local *Nusselt number*, Nu_x.

$$h_c = 0.564k\, Pr^{\frac{1}{2}} \sqrt{\frac{U_\infty}{\nu x}} \tag{2-20}$$

$$Nu_x = 0.564\, Re_x^{\frac{1}{2}}\, Pr^{\frac{1}{2}} \tag{2-21}$$

Re_x is the local Reynolds number:

$$Re_x = \frac{U_\infty x}{\nu}$$

The Nusselt number can be interpreted as a nondimensional version of the heat transfer coefficient:

$$Nu = \frac{h_c L}{k},$$

where L is a characteristic length in the system and k the fluid's heat conductivity.

The average heat transfer coefficient for a plate of length L is defined as

$$\overline{h_c} = \frac{1}{L}\int_0^L h_c(x)dx = 1.128k\,Pr^{\frac{1}{2}}\sqrt{\frac{U_\infty}{\nu L}} \tag{2-22}$$

and for the average Nusselt number, Nu, we have

$$Nu = \frac{\overline{h_c}L}{k} = 1.128\sqrt{Re_L\,Pr} \tag{2-23}$$

where $$Re_L = \frac{U_\infty L}{\nu}$$

In this analysis we assumed constant fluid properties, but since the fluid temperature varies between T_w and T_∞, some variations in properties can be expected. For small temperature differences the variations can be taken into account by evaluating the properties at the *film temperature*, T_f, defined as

$$T_f = \frac{T_w + T_\infty}{2}. \tag{2-24}$$

By means of classical boundary layer theory and Pohlhausen's evaluation of equation (2-18), it can be shown that the ratio between the thermal and velocity boundary layers for liquid metals ($Pr << 1$) is

$$\frac{\breve{u}_T}{\breve{u}_v} = \frac{0.589}{\sqrt{Pr}} \tag{2-25}$$

For fluids with $Pr = 1$ (in practice used for $0.6 < Pr < 15$), it can be shown that the same ratio is

$$\frac{\delta_T}{\delta_v} = Pr^{-\frac{1}{3}} \tag{2-26}$$

The boundary layer reviewed here is laminar. If it is allowed to develop along the plate, it eventually becomes unstable and turns turbulent. There is unfortunately no exact analytical solution of these boundary layer equations, even for a flat plate. However, there are many solutions based on semi-empirical models. These will not be considered here.

2.5.2 The Integral Method

The *integral method* is an *approximate* method for solving boundary-layer equations. The basic conservation equations are applied to a control volume, which extends through the whole boundary layer (and readily beyond it). The continuity, momentum and energy equations are required to be satisfied on an average inside the control volume, rather than at each point within it. Figure 2.4 shows an example of a control volume.

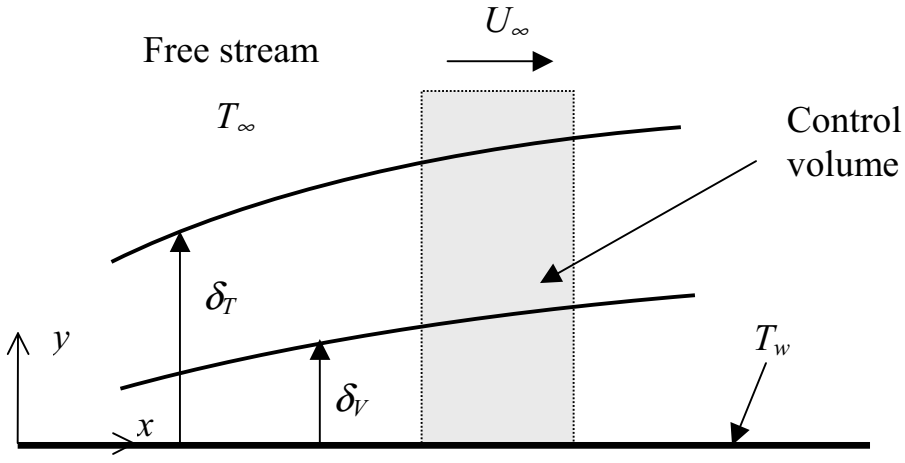

Figure 2.4 Control volume for the derivation of the energy integral equation.

The conservation equations can be solved by *assuming* suitable velocity and temperature profiles inside the boundary layers. These profiles must of course satisfy the appropriate boundary conditions. Many methods using profile assumptions have been presented. It is not the most accurate method, but produces differential equations that are relatively simple to solve. Another method is to employ *empirical correlations* among the integral parameters.

The integral form of the momentum equation for a two-dimensional laminar boundary layer across a flat plate with free-stream velocity U_∞ is

$$\frac{d}{dx}\int_0^{\delta_v}(U_\infty - u)u\,dy = \nu\left.\frac{\partial u}{\partial y}\right|_{y=0} \tag{2-27}$$

u is the radial velocity. Various functions can be chosen to approximate the velocity profile. For a *third degree polynomial*, the following boundary conditions must be satisfied:

1) $u = 0$ at $y = 0$
2) $u = 0$ at $y = \delta_v$
3) $\frac{\partial u}{\partial y} = 0$ at $y = \delta_v$
4) $\frac{\partial^2 u}{\partial y^2} = 0$ at $y = 0$ $(u = v = 0)$

This leads to

$$u = U_\infty\left[\frac{3}{2}\frac{y}{\delta_v} - \frac{1}{2}\left(\frac{y}{\delta_v}\right)^3\right] \tag{2-28}$$

Integrating equation (2-27) with this velocity and utilising the condition $\delta_v = 0$ at $x = 0$, yields

$$\delta_v = 4.64\sqrt{\frac{\nu x}{U_\infty}}$$

The third-degree polynomial for the velocity profile has resulted in an estimated velocity boundary layer thickness about 6% less than the exact result. An estimate of the wall shear stress is about 3% less than the exact value.

A temperature profile should satisfy the following three conditions:

1) $T = T_w$ at $y = 0$
2) $T = T_\infty$ at $y = \delta_T$
3) $\frac{\partial T}{\partial y} = 0$ at $y = \delta_T$

The energy equation yields a fourth condition:

4) $\frac{\partial^2 T}{\partial y^2} = 0$ at $y = 0$ $(u = v = 0)$

Assuming a third-degree polynomial for the temperature distribution too, we find in dimensionless form:

$$\frac{T - T_w}{T_\infty - T_w} = \frac{3}{2}\frac{y}{\delta_T} - \frac{1}{2}\left(\frac{y}{\delta_T}\right)^3 \tag{2-29}$$

For a steady, incompressible, two-dimensional laminar flow with constant thermophysical properties and isothermal free stream, it can be deduced that the conservation of energy is described by the following relationship:

$$\frac{d}{dx}\int_0^{\delta_T}(T_\infty - T)u\,dy = \alpha\left(\frac{\partial T}{\partial y}\right)_{y=0} \tag{2-30}$$

Viscous dissipation and lateral heat conduction are neglected.

When employing assumed velocity and temperature profiles, equation (2-30) is reduced to a first-order ordinary differential equation for the thermal boundary layer thickness, δ_T. For liquid metals $Pr << 1$ (in practice < 0.06), which implies that $\delta_T > \delta_v$. A reasonable assumption in our system is therefore to state that $u = U_\infty$ *(= constant)* throughout the thermal boundary layer in equation (2-30).

The local heat flux from the plate is

$$q(x) = -k\left.\frac{\partial T}{\partial y}\right|_{y=0} = h_c(T_\infty - T_w)$$

and h_c between the plate and the fluid can be calculated, resulting in:

$$h_c = \frac{k}{T_\infty - T_w}\left.\frac{\partial T}{\partial y}\right|_{y=0} = \frac{3}{2\sqrt{8}}\frac{k}{x}Re_x^{\frac{1}{2}}Pr^{\frac{1}{2}} \approx 0.53\frac{k}{x}\sqrt{Re_x\,Pr},$$

or, in terms of the local Nusselt number:

$$Nu_x \approx 0.53\sqrt{Re_x\,Pr}$$

The average Nusselt number for a plate of length L is

$$Nu = 1.06\sqrt{Re_L\,Pr}$$

where

$$Re_L = \frac{U_\infty L}{\nu}$$

For *liquid metals* it can be deducted that

$$\frac{\delta_T}{\delta_v} = \sqrt{\frac{13}{35}\frac{1}{Pr}} \approx \frac{0.61}{\sqrt{Pr}} \qquad (Pr << 1) \qquad (2\text{-}31)$$

The results obtained by integral estimates compare well with the "exact" results.

3. Theory on Numerical Simulations

3.1 Outline of FLUENT

3.1.1 General Description

At the beginning of this work it was expected that the finite difference computer program FLUENT could solve the flow and heat transfer problem of interest. This is a general program for numeric modelling of fluid flow and heat transfer. The code contains models for a wide range of physical phenomena/applications. The source code is written in FORTRAN 77 and comprises a number of files and subroutines linked together. The user can add new routines or modify existing ones.

The partial differential equations (conservation equations) are solved numerically by a *control volume* based *finite-difference* method following the ideas described by Patankar (1980). The equations are *discretized* over control volumes (or cells) defined by the computational grid determined by the user. There is one control volume surrounding each grid point, see Figure 3.1 A discretization equation is an algebraic relation connecting the values of an unknown quantity, for example called Φ, for a group of grid points. Such an equation is used to evaluate a differential equation and can be solved relatively easy with a wide variety of techniques. As the number of grid points becomes very large, the solution of the discretization equations is expected to approach the exact solution of the corresponding differential equations. Time and computer resources will be the natural limiting factor.

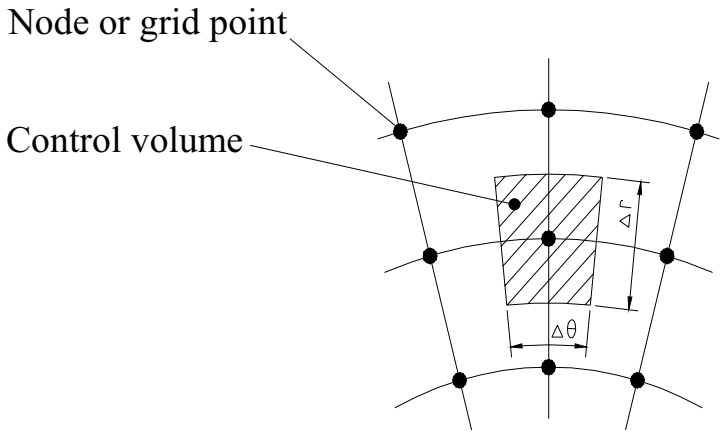

Figure 3.1 Example of grid and control volume in cylindrical coordinates.

With the exception of velocity, all variable values are calculated in the node or grid point of each cell. The velocities are evaluated on the cell boundaries. This approach is known as the *staggered grid method*. First order approximations are used for differentials and interpolation of values is by a first-order *Power Law* scheme. The system of linear equations is solved with an iterative line-by-line matrix solver. The pressure and velocity fields are solved by the SIMPLE (Semi-Implicit Method for Pressure-Linked Equations) algorithm based on using a relationship between velocity and pressure corrections in order to iteratively advance the solution of the governing equations for conservation of mass, momentum, energy, etc. The important operations, in order of their execution, are:

1. Guess the initial pressure field P^*.
2. Solve the momentum equations to obtain the velocity components.
3. Compute a corrected pressure field based on the continuity equations.
4. Apply a velocity correction formula to obtain improved velocity estimates.
5. Solve the conservation equations for other variables such as enthalpy and turbulence quantities.
6. Treat the corrected pressure as a new guessed pressure, return to step 2 and repeat the whole procedure until a converged solution is obtained.

The pressure and velocity correction formulae are presented by Patankar, pp. 123-126 (1980).

The convergence of the standard line solver can be accelerated by employing a *multigrid* scheme. Briefly described, the original finite-difference grid is rearranged into a number of successively coarser grid levels. The basic conservation equations are solved starting on the top (most coarse level) of this hierarchy, transferring corrections onto the finer levels in an effort to achieve global balances and reduce overall solution error. The multigrid corrections used in FLUENT are derived via the Additive Correction scheme as described in the FLUENT manual.

Our flow problem is highly transient from the fluid exits the nozzle and strikes the plate and until steady-state conditions are reached. Thus the solutions to the conservation equations vary with time. Progressing in time is by *time steps*. In a typical time step, Δt, the task is: given the grid point values of Φ at time t, find the values of Φ at time $t+\Delta t$. The discretization equation is derived by integrating over the control volume and time from t to $t+\Delta t$. FLUENT uses an *implicit* scheme which in essence assumes that the new value prevails throughout the time step. An *explicit* scheme assumes that the old value (at time t) prevails throughout the whole time step. Several other schemes also exist.

The flow of interest involves an axisymmetric, incompressible, two-phase, free-surface flow with water or liquid metal as one phase and air as the other. The fluids are assumed immiscible. For solving such problems FLUENT uses *the volume-of-fluid* (*VOF*) *algorithm*. This method, pioneered by Hirt and Nichols, is a powerful tool that enables a finite difference representation of free surfaces (i.e. the interface between a liquid and a gas or two liquids) that are arbitrarily oriented with respect to the computational grid without resorting to body fitted grids adapted to the free surface geometry.

The process of embedding a discontinuous surface, such as a free surface, on a matrix of computational cells involves three separate tasks. First, one

has to find a method for numerically describing the shape and location of the interface. Secondly, an algorithm for computing the interface's evolution in time must be found. Finally one has to correctly impose the desired free surface or interface conditions on the surrounding computational mesh. The VOF method (amongst others) can be employed for solving the first two problems.

3.1.2 VOF Method

In the VOF method a *volume fraction function, F*, is introduced and used for each cell in the mesh. Its value is unity for a cell fully occupied by liquid and zero for a cell containing no liquid (full of air). In each control volume all volume fractions add to unity. Cells with *F* values between zero and one are thus *partly filled* and therefore contain a *free surface* and provide interface information. As opposed to some other techniques, only one storage value for each cell is necessary.

The normal to the surface or interface points in the direction in which the value of *F* changes most rapidly. *F* is not a smooth function and its derivatives must therefore be computed in a special way. When this is done the derivatives can be used to determine the boundary normal. In FLUENT the interface normal is used in conjunction with surface forces. With more mathematical manipulation of the interface normal, the *F* value and the fluid fluxes in the cell, it is possible to construct a line (or a surface in 3-dimensional cases) that approximates the interface in the cell. This is a complicated and time-consuming task. In short, the free surface in FLUENT simulations is reconstructed as a set of not necessarily continuous horizontal or vertical lines in each surface cell, depending on its relation to neighbouring cells. When postprocessing, the *F* values in each cell are plotted, giving a representation of where the interface is.

In addition to the governing equations for the flow (Chapter 2), the following equation of continuity is used for computing the evolution of the *F* field:

$$\frac{\partial F}{\partial t} + u\frac{\partial F}{\partial x} + v\frac{\partial F}{\partial y} + w\frac{\partial F}{\partial z} = S \qquad (3\text{-}1)$$

Since $\Sigma F_n = 1$, the equation for the last phase need not be solved, i.e. it is generally solved for all phases but one. The source term on the right-hand side is normally zero, but can be used to simulate mass transfer between the phases. The method is conservative in use of stored information, which is highly advantageous.

Later versions of FLUENT allow the user to choose between solving the VOF equation for every iteration within a time step or just once per time step. The latter is the more stable of the two and requires the least computational effort per iteration, but the overall result can be less accurate in time. It can be beneficial when large time steps are being used in the hope of reaching a quick steady-state solution.

Once a computational mesh has been established, a suitable time step necessary for numerical stability must be chosen. There are two options available for choosing the time step in FLUENT - fixed or automatically refined. The latter is based on the user-input maximum *Courant number* allowed near the free surface. The Courant number is a dimensionless number that compares the time step, Δt, in a calculation, to the characteristic time a fluid uses to traverse a control volume or cell:

$$Courant\ number = \frac{\Delta t}{\Delta t_t}$$

In the region near the fluid interface, FLUENT divides the volume of each cell by the sum of the outgoing fluid fluxes. The result is the time it will take to empty the cell. The smallest such time in the domain is the characteristic "transit time", Δt_t, in the equation above. The maximum time step allowed in the calculations will be this transit time multiplied by the user-specified Courant number. As a rule, material cannot move through more than one cell in a time step because the difference equations assume

fluxes only between adjacent cells. The Courant number must therefore always be less than or equal to unity, typically 0.25 to 0.33. The user can also set time steps directly. This value will then be used if it is smaller than the computed time step based on the Courant number.

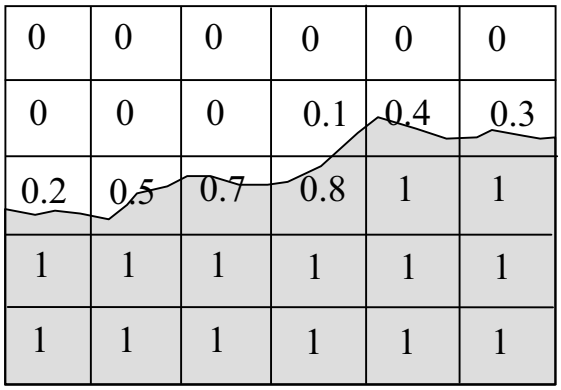

Figure 3.2 Example of volume fraction (F) field in a computational grid. A value of 1 can for example indicate a cell that is completely filled with liquid, while a value of 0 is for a cell containing only gas. Shaded region indicates liquid.

3.1.2.1 Properties

Based on the local F value, i.e. the relative amount of each phase in a cell, the appropriate properties and variables will be assigned to each control volume within the domain. In our system, with the phases represented by the subscripts 1 and 2, the density of each cell is given by

$$\rho = F_1\rho_1 + F_2\rho_2,$$

where $F_2 = 1\text{-}F_1$.

In general, for an n-phase system, the volume-fraction-averaged density in a cell has the form:

$$\rho = \sum_{1}^{n} F_i \rho_i$$

All other properties are computed in this manner (viscosity and thermal conductivity for example), with the exception of the specific heat/enthalpy, which is mass fraction averaged:

$$c_p = \frac{\sum_{1}^{n} F_i \rho_i c_{pi}}{\sum_{1}^{n} F_i \rho_i}$$

3.1.2.2 Momentum Equation

A single momentum equation in each direction is solved throughout the domain and the resulting velocity field is shared by the two phases, i.e. each cell has just *one velocity*. The F value influences the momentum equations through the properties μ and ρ. One limitation to the shared-velocity approximation is that the accuracy of the velocities computed near the interface can be adversely affected in cases where the phases exhibit large velocity differences.

3.1.2.3 Enthalpy Equation

The enthalpy equation is also *shared* between the phases, with a common density and thermal conductivity. Likewise, as in the velocity field, the accuracy of the enthalpy and consequently the temperature near the interface is limited in cases where large temperature differences exist between the phases. Such problems can also arise when large differences in properties between the phases exist, for example when liquid metal is in contact with air. The thermal conductivities of the materials can differ by as much as 4 orders of magnitude. This can lead to equation sets with

anisotropic coefficients, which in turn lead to *convergence and precision limitations*.

3.1.3 Turbulence

In turbulent flows a scalar quantity Φ (such as velocity, pressure, temperature) is assumed to consist of a steady component $\overline{\Phi}$ and a turbulent fluctuating component, Φ'. The steady quantity is assumed to be an averaged value over a time span larger than any significant period of the fluctuations in Φ. As an example the instantaneous velocity, u, can be expressed as:

$$u = \overline{u} + u' \tag{3-2}$$

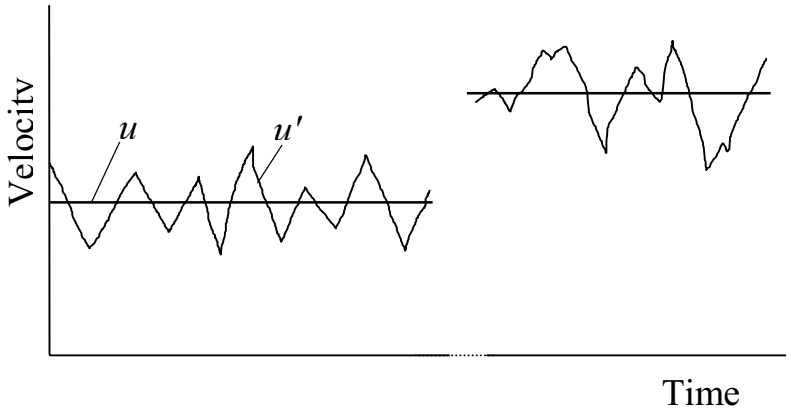

Figure 3.3 Illustration of turbulent velocities at two different times.

Equation (3-2) is referred to as *Reynolds decomposition*. The time-average of the fluctuating component is zero. The fluctuations are explained as the motion of swirls or *eddies*, i.e. small portions of fluid which move about for a short time before losing their identity. Because of this motion, the

transport of momentum, energy and species is greatly enhanced. Material properties can also fluctuate in response to the temperature and pressure fields. It is a time consuming task to numerically model turbulence in time and length scales accommodating the minute fluctuations. For this reason various turbulence models solving the statistically mean quantities have been developed. New conservation equations are derived by substituting the Reynolds decompositions into the original basic equations.

In this way the *instantaneous* conservation-of-mass equation becomes:

$$\frac{\partial \rho}{\partial t} + \frac{\partial}{\partial x}[\rho(\overline{u} + u')] + \frac{\partial}{\partial y}[\rho(\overline{v} + v')] + \frac{\partial}{\partial z}[\rho(\overline{w} + w')] = 0 \qquad (3\text{-}3)$$

In FLUENT density fluctuations are neglected, so that (also in compressible flows) $\rho = \overline{\rho}$. With further manipulation following *time-averaging rules*, the *Reynolds-averaged* equation becomes:

$$\frac{\partial \rho}{\partial t} + \rho \frac{\partial}{\partial x}(\overline{u}) + \rho \frac{\partial}{\partial y}(\overline{v}) + \rho \frac{\partial}{\partial z}(\overline{w}) = 0 \qquad (3\text{-}4)$$

Similarly, for the conservation-of-momentum equations, in tensor form:

$$\rho \frac{\partial}{\partial t}(\overline{u}_i) + \rho \frac{\partial}{\partial x_j}\left(\overline{u}_i \overline{u}_j + \overline{u'_i u'_j}\right) = \frac{\partial}{\partial x_j}\left[-\overline{p}\delta_{ij} + \mu\left(\frac{\partial \overline{u}_i}{\partial x_j} + \frac{\partial \overline{u}_j}{\partial x_i}\right)\right] + \rho g_i \qquad (3\text{-}5)$$

This equation would present no difficulties were it not for the new term $\rho\overline{u'_i u'_j}$. It is highly non-linear and reflects the time-dependent character of a turbulent flow. The term is known as the *Reynolds stress tensor*. Many models have been developed to solve the problem. A traditional

assumption is based on the Boussinesq hypothesis (1877) which makes this a gradient diffusion term, analogous to molecular shear:

$$\rho \overline{u'_i u'_j} = \frac{2}{3}\rho k \delta_{ij} - \mu_t \left(\frac{\partial \bar{u}_i}{\partial x_j} + \frac{\partial \bar{u}_j}{\partial x_i} \right) + \frac{2}{3}\mu_t \frac{\partial \bar{u}_k}{\partial x_k} \delta_{ij} \qquad (3\text{-}6)$$

δ_{ij} is the Kronecker delta defined as:

$$\delta_{ij} = \begin{cases} 1 & when\ i = j \\ 0 & otherwise \end{cases}$$

<u>*k*- ε Turbulence Model</u>

The last term in equation (3-6) contains the divergence of $\vec{v}$, $\nabla \cdot \vec{v}$, which is zero in incompressible flows. It is omitted in FLUENT also for compressible flows. μ_t is the *turbulent* or *eddy viscosity*, which has the same dimensions as μ but is not a fluid property. It varies instead with the flow conditions and geometry. In the *k*- ε *scheme* it is defined as:

$$\mu_t = \rho C_\mu \frac{k^2}{\varepsilon} \qquad (3\text{-}7)$$

k is the *specific kinetic energy of turbulence* [J/kg=m^2/s^2];

$$k = \frac{1}{2}\sum_i \overline{(u_i')^2} \qquad (3\text{-}8)$$

Applying these conventions, the momentum conservation equation can be written:

$$\rho \frac{D\overline{u}_i}{Dt} = -\frac{\partial \hat{p}}{\partial x_i} + \frac{\partial}{\partial x_j}\left[\mu_{eff}\left(\frac{\partial \overline{u}_i}{\partial x_j} + \frac{\partial \overline{u}_j}{\partial x_i}\right)\right] + \frac{\partial}{\partial x_j}\left(\frac{2}{3}\mu_t \frac{\partial \overline{u}_k}{\partial x_k}\delta_{ij}\right) \tag{3-9}$$

We have now introduced the *substantial derivative*, defined as

$$\frac{D}{Dt} = \frac{\partial}{\partial t} + \overline{u}\frac{\partial}{\partial x} + \overline{v}\frac{\partial}{\partial y} + \overline{w}\frac{\partial}{\partial z} \tag{3-10}$$

$\hat{p} = \overline{p} + \frac{2}{3}\rho k$ is an effective pressure obtained by inserting equation (3-6) into equation (3-5). The effective viscosity, μ_{eff}, is equal to $\mu+\mu_t$. In many fluids, but not liquid metals, μ can often be ignored, as μ_t may be several orders of magnitude larger. ε is the *specific dissipation rate* for turbulent energy [m^2/s^3]:

$$\varepsilon = \nu\overline{\frac{\partial u'_i}{\partial x_j}\frac{\partial u'_i}{\partial x_j}},$$

To solve the turbulence problem, conservation equations for k and ε are introduced.

- Turbulent kinetic energy:

$$\frac{Dk}{Dt} = \frac{1}{\rho}\frac{\partial}{\partial x_k}\left(\frac{\mu_t}{\sigma_k}\frac{\partial k}{\partial x_k}\right) + \frac{\mu_t}{\rho}\left(\frac{\partial \overline{u}_i}{\partial x_k} + \frac{\partial \overline{u}_k}{\partial x_i}\right)\frac{\partial \overline{u}_i}{\partial x_k} - \varepsilon \tag{3-11}$$

- Turbulent energy dissipation:

$$\frac{D\varepsilon}{Dt} = \frac{1}{\rho}\frac{\partial}{\partial x_k}\left(\frac{\mu_t}{\sigma_\varepsilon}\frac{\partial \varepsilon}{\partial x_k}\right) + \frac{C_1\mu_t}{\rho}\frac{\varepsilon}{k}\left(\frac{\partial \overline{u}_i}{\partial x_k} + \frac{\partial \overline{u}_k}{\partial x_i}\right)\frac{\partial \overline{u}_i}{\partial x_k} - C_2\frac{\varepsilon^2}{k} \tag{3-12}$$

C_1, C_2, C_μ, σ_ε and σ_k are empirically derived constants with values as in Table 3-1.

C_1	C_2	C_μ	σ_ε	σ_k
1.44	1.92	0.09	1.30	1.00

Table 3-1 Values for the constants in FLUENT's standard k-ε model.

The k-ε model thus involves simultaneous solution of the continuity, momentum, k and ε equations. These equations all have the same general structure. These two last quantities are also shared (locally, in a cell) by the phases throughout the flow field.

This so-called *standard* k-ε model is popular, robust, economical with respect to CPU time and reasonably accurate for a wide range of turbulent flows. It may be inaccurate when applied to complex flows where buoyancy, swirl, strong streamline curvature or density gradients are important phenomena.

The Renormalization Group (RNG) k-ε model

This model also follows the two-equation (k-ε) turbulence scheme outlined above, but uses in addition mathematical techniques called Renormalization Group (RNG) methods. This provides for a more general and fundamental "analytical" turbulence model as opposed to the semi-empirical standard k-ε model (where empiricism and phenomenological considerations are taken into account when deriving the model equations and constants). The extra terms and functions increase the CPU time with 10-15% compared to the standard k-ε model.

The RNG model is particularly beneficial in the following conditions:

- separated and recirculating flows (e.g. backward- or forward-facing steps, sudden expansions, diffusers

- flows in curved geometries and flows that are rapidly strained (e.g. curved ducts, highly accelerating/decelerating flows, stagnation flows)

- time-dependent flows with large-scale organised structures (e.g. vortex shedding, shear layer instability)

- low Reynolds-number or transitional flows (e.g. flows with both laminar and turbulent regions)

- swirling flows (e.g. swirl cumbustors, cyclones)

- flows with streamwise vortices and secondary flows (e.g. secondary flows in curved ducts and transition ducts, streamwise vortices behind aerodynamic/hydrodynamic bodies such as ground vehicles, under-water bodies, aeroplanes)

- heat transfer in low Prandtl number fluid flows (e.g. liquid metal flows)

Like the standard k-ε model, the RNG model is based on the isentropic eddy-viscosity concept. In flows dominated by anisotropic turbulence, this model may be inadequate. Examples are highly swirling flows, flows with strong streamline curvature, stress-driven secondary flows and evolution of streamwise vortices. In simulations where such features are prominent, the *Reynolds Stress Model* should be considered.

The momentum equations derived from the RNG theory are

$$\frac{\partial}{\partial t}(\rho u_i) + \frac{\partial}{\partial x_j}(\rho u_i u_j) = \frac{\partial}{\partial x_j}\left[\mu_{eff}\left(\frac{\partial u_i}{\partial x_j} + \frac{\partial u_j}{\partial x_i}\right)\right] - \frac{\partial p}{\partial x_i} \qquad (3\text{-}13)$$

μ_{eff} is calculated differently from the standard k-ε model, yielding more accurate calculations for low Reynolds-number flows, near-wall flows and vorticity/swirl.

The equations for k and ε are:

$$\frac{\partial}{\partial t}(\rho k)+\frac{\partial}{\partial x_i}(\rho u_i k)=\frac{\partial}{\partial x_i}\left(\alpha_k \mu_{eff}\frac{\partial k}{\partial x_i}\right)+\mu_t S^2-\rho\varepsilon \qquad (3\text{-}14)$$

and

$$\frac{\partial}{\partial t}(\rho\varepsilon)+\frac{\partial}{\partial x_i}(\rho u_i \varepsilon)=\frac{\partial}{\partial x_i}\left(\alpha_\varepsilon \mu_{eff}\frac{\partial \varepsilon}{\partial x_i}\right)+C_{1\varepsilon}\frac{\varepsilon}{k}\mu_t S^2-C_{2\varepsilon}\rho\frac{\varepsilon^2}{k}-R \qquad (3\text{-}15)$$

α_k and α_ε are the inverse effective "Prandtl" numbers for k and ε, respectively. They are calculated by a formula analytically derived by the RNG theory:

$$\left|\frac{\alpha-1.3929}{\alpha_0-1.3929}\right|^{0.6321}\left|\frac{\alpha+2.3929}{\alpha_0+2.3929}\right|^{0.3679}=\frac{\mu}{\mu_{eff}} \qquad (3\text{-}16)$$

where $\alpha_0 = 1$. S is the modulus of the mean rate-of-strain tensor, S_{ij}, defined as

$$S=\sqrt{2S_{ij}S_{ij}}$$

and

$$R=\frac{C_\mu \rho\eta^3(1-\frac{\eta}{\eta_0})}{1+\beta\eta^3}\frac{\varepsilon^2}{k} \qquad (3\text{-}17)$$

where $\eta = \frac{Sk}{\varepsilon}$, $\eta_0 \approx 4.38$, $\beta = 0.012$. $C_{1\varepsilon}$ and $C_{2\varepsilon}$ are derived analytically and are 1.42 and 1.68, respectively (compared to 1.44 and 1.92 in the standard k - ε model).

Equation (3-16) is stated in the FLUENT manual for finding both α_k and α_ε , which subsequently will be identical. It is, however, not declared explicitly that these two values are equal, except in the high Reynolds-number limit ($\mu/\mu_{eff} << 1$), where $\alpha_k = \alpha_\varepsilon \approx 1.3929$.

It can be noted that the RNG model has a new source term in its ε-equation compared to the standard k-ε model. The R term is one of the most important features of the RNG model that improves accuracy for a wide range of complex flows.

Reynolds Stress Model (RSM)

As mentioned in the preceding section, some flows are better simulated with the Reynolds Stress Model. This is the most elaborate turbulence model that FLUENT provides. It is, however, not regarded as being advantageous in the flows pertinent to this work and will only very briefly be described.

The Reynolds Stress Model involves calculation of the individual Reynolds stresses, $\overline{u'_i u'_j}$, by way of a special continuity equation. The effects encountered in highly swirling flows, flows with strong streamline curvature, stress-driven secondary flows and evolution of streamwise vortices are then automatically accounted for. These features are not considered dominant in the type of flow studied in this work.

Compared with the k - ε models, the RSM requires 15-20% more memory and 50-60% more CPU time per iteration. For more comprehensive information the reader is referred to the FLUENT manual.

3.1.4 Near-Wall Treatments in FLUENT

Turbulence in regions close to a wall is obviously affected by the wall's existence. Turbulence is damped very close to the wall and the mean velocity field is also influenced due to the no-slip condition at the wall. It is also in this region that the flow variables (e.g. velocity, temperature) often exhibit the largest gradients. The turbulence models mentioned earlier are not valid all the way to the wall, so the near-wall region must be modelled differently.

Studies have shown that the near-wall region can for the most part be subdivided into three layers. In the outer, *fully turbulent* layer, turbulence dominates, i.e. every particle is a part of fluid eddies that are turning over in various directions. This is where the turbulence models are valid. The thin innermost layer, the *viscous sublayer*, has many characteristics of a laminar boundary layer and molecular viscosity plays the important role in momentum, heat and mass transfer. The third layer - the *buffer layer* - connects the inner and outer layers, with molecular viscosity and turbulence playing equally important roles.

It is customary to use a set of nondimensional variables based on relevant quantities in the near-wall region, so-called *wall coordinates*. Only one of these units will be described here, namely y^+. This can be interpreted as a local thickness Reynolds number and is defined as:

$$y^+ = \frac{y u_\tau}{\nu}, \tag{3-18}$$

$$u_\tau = \sqrt{\frac{\tau_w}{\rho}} \tag{3-19}$$

τ_w is the wall shear stress and y the distance from the wall. The viscous sublayer extends up to $y^+ \approx 5$ and the fully turbulent region starts at $y^+ \approx 50$, with the buffer layer constituting the region in between.

FLUENT offers two ways of modelling the near-wall region. The first is called a *wall function* or *law of the wall* approach. Semi-empirical formulas (wall functions) are used from the fully turbulent region to the wall. The buffer layer is not modelled explicitly. Either the *standard* or the *nonequilibrium* wall function is available. The standard type assumes that the *production* and *dissipation* of turbulent kinetic energy are *equal* in the wall-adjacent cells. This is a local *equilibrium hypothesis*. The nonequilibrium wall function relaxes this equilibrium assumption (production = dissipation) and is more sensitive to pressure gradient effects. This is recommended in complex flows involving separation, reattachment and impingement. In such cases rapid changes can occur in the mean flow and in turbulent properties, in addition to severe pressure gradients.

For temperature, only the *standard law of the wall* is available. Coincident with velocity, there is a linear law in the viscous sublayer where conduction is important, and a logarithmic law where turbulence dominates. The RNG theory provides an analytical formula for turbulent Prandtl numbers, while these are *constant, user-specified* values in the standard k-ε theory. In the RNG model there is an extra option for temperature that allows the user to skip this method altogether. This can be useful when modelling fluids with high thermal conductivities such as liquid metals. Here the entire velocity boundary layer is inside the thermal conduction layer and a *laminar* temperature profile is used at the wall. The viscous heating terms in the energy equation are normally ignored by FLUENT, but can be activated by the user. This was considered unnecessary.

In the second near-wall region approach (often called the *two-layer model*), wall functions are not used at all. The whole domain is divided in a *viscosity-affected near-wall region* and a *fully turbulent region*. In the

latter, one of the (user chosen) turbulence models is employed. In the near-wall region, the so-called one-equation model of Wolfstein (1969) is used. The momentum and k equations are unaltered, but μ_t and ε are computed differently. The method requires a fine grid for the near-wall computations with y^+ at the wall-adjacent cell most ideally near the value of 1. However, a higher y^+ is acceptable as long as it is well inside the viscous sublayer ($y^+ < 5$). This procedure should be considered in cases with

- existence of low Reynolds numbers or near-wall effects (e.g. flows through a small gap, highly viscous, low velocity flow)
- massive transpiration through the wall (blowing/suction)
- severe pressure gradients leading to boundary layer separations
- strong body forces (e.g. flow near rotating disks, buoyancy-driven flows)
- high three-dimensionality in near-wall region (e.g. Ekman spiral flow, strongly skewed 3-D boundary layers)

It requires more computational resources than the wall function approach.

3.1.5 Surface Tension

Surface tension arises as a result of molecular forces between different materials. In regions where two fluids are separated, the surface tension acts to decrease the area of interface. The surface tension model in FLUENT is the Continuum Surface Force (CSF) proposed by Brackbill et al. (1992). The addition of this surface tension model to the VOF calculation results in a source term in the momentum equations. The model can be augmented by specifying a contact angle that one of the fluids makes with another material, for example a solid wall.

3.2 Numerical Solution of the Governing Equations

Initial FLUENT simulations seemed to produce reasonable results. When analysing these more closely however, it was found that conservation of mass in the domain was not at all maintained. In some simulations pockets of air appeared in the liquid and vice versa. After testing several numerical solution techniques it was attempted to modify the code itself. Stein Tore Johansen performed this work at the Norwegian University of Science and Technology.

In a numerical iterative code it is possible to attain F values greater than unity and less than zero, due to numerical inaccuracies inherent in such techniques. In FLUENT, values greater than one are simply set to one and negative values to zero. In this cut-off method it is evident that mass can *disappear* or be *created*. Johansen suggested to adjust the fluxes in cells with too large or too small volume fractions. With values greater than one, the outflux from the cell is increased. With values less than one, the flux of matter into the cell is increased. In this way all F values will remain between zero and one without losing or creating mass.

In addition, cut-off errors can influence equation (3-1) in such a way that (without a source term) the right hand side of the expression is not zero. This will also affect the mass balance in the flow problem. If the mass conservation equation is added to the volume fraction equation, the latter can be written in a non-conservative form, which can be beneficial for the solution:

$$\frac{\partial F}{\partial t} + \frac{\partial}{\partial x_k}(u_k F) = F\frac{\partial u_k}{\partial x_k} \tag{3-20}$$

The equation is valid for an incompressible flow with no source term.

These two alterations were implemented in version 3.03 of FLUENT. A slight improvement of the results was achieved, but all in all it was still not

satisfactory. It was found that the code must be *extensively modified*. This requires a considerable amount of additional work and is well beyond the scope of this study.

Later on, FLUENT versions 4.3, 4.4 and 4.5 were installed. Mass balance now seemed to be correct, but otherwise simulations with these gave similar problems as the earlier version. No version could correctly simulate a hydraulic jump. A possible way of solving the flow and heat transfer problem is to find some other method for depicting the surface profile of the flow, and then instruct our finite-difference code to perform a more exact calculation of velocities and heat transfer within this flow profile.

In the literature three different models describing the axisymmetric flow of a vertical liquid jet impinging on a flat horizontal plate have been elected. In addition, a simpler model, the so-called *Bernoulli model*, has been *developed* in the course of this study. *It was therefore decided that the calculated surface profile from one of these models should be used as input for FLUENT simulations.* First a detailed velocity distribution inside the profile is computed, followed by a thermal analysis.

3.3 Other Methods of Computing Interfaces

It is a complicated problem to numerically describe the evolution of free surfaces and interfaces between two or more liquids and a wide variety of methods exist. It is an area of active research and techniques are constantly being developed and enhanced. They are not all general techniques for modelling free surfaces and some can not handle for example surface foldings and mergings or very deformed surfaces. The most important alternatives to the VOF method are briefly described in the following.

A free surface can be represented by specifying *its distance from a reference line* as a function of position along this line. In a rectangular grid this could be defined as the height from the bottom of each column of cells to the free surface above. The time evolution of the height function can

quite easily be described by finite difference approximations and be extended to three-dimensional problems. A severe limitation is that only one value for the height is allowed for every position. For this reason bubbles or drops cannot be treated.

A closely related method that overcomes this limitation uses *chains of short line segments*. The system changes in time by moving each point with the local fluid velocity. When two surfaces meet or a surface is folded over itself, the segments must be reordered and some may be deleted or added. This can be a complicated task. In addition, information about each point must be stored - so more storage room is necessary in this method.

Volume tracking methods are a different category of numerical techniques, which have the potential for handling large surface deformations, folding and merging. These use a volumetric variable such as marker particles in the *marker-and-cell technique* (MAC) and volume fractions in the VOF technique. In the MAC method marker particles are spread over all liquid occupied regions and specified to move with the fluid velocity at their location. Free surfaces are in this way described as the boundary between cells with and without marker particles. Based on the distribution of markers in the cells, a more accurate location of the free surface can be computed. One cell can contain several particles. In this method a large number of point coordinates must be stored and computer storage requirements are large.

In the *boundary integral* or *boundary element* method the partial differential equations are in a way re-formulated and thus defined only on the *boundary* of the domain. An equation for example governing a three-dimensional region is transformed into one over its surface. The dimension of the problem is effectively reduced by one, making it computationally efficient.

A relatively new method is the *lattice gas model* (LGM). Here fluid particles (i.e. a large group of molecules) move on the links in an underlying regular grid and the motion evolves in discrete time steps. It is

a comparatively fast method and can be run on parallel computers. There are, however, some difficulties related to the method and various modifications have been made to overcome them. Two offspring are the *lattice Boltzmann model* and the *digital physics model*. Some believe that this group of models will play an important role in fluid modelling in the future.

The *level-set* method is also relatively new and uses a so-called *distance function* to define the interface in two-phase flows. The distance function is always zero at the interface and equations are solved to find where this occurs.

The *moving unstructured boundary conforming grid* methods use various procedures for adjusting the grid in the interface region. *Finite element* methods have also been developed for free and moving boundary problems.

The numerical scheme to choose depends often on the complexity of the physical problem and the accuracy desired for the solution. In some cases intricate details of the interface are important, while in others this is not crucial for predicting the flow behaviour.

4. Analytical Flow Models

4.1 General

Let us consider a vertical circular liquid jet impinging on a horizontal plate. The liquid will spread axisymmetrically over the surface as a *thin film* and if it spreads far enough (i.e. the disk is sufficiently large) will quite noticeably and suddenly increase in thickness. This sudden increase in depth takes place over a narrow annular region and is termed a *hydraulic jump*. Beyond that "point" the liquid moves much slower. The reason for such a jump to occur is still somewhat unclear, but the "energy content "of the flow is certainly of importance. It can be shown that an open flow has a critical depth, which energy-wise is the most economical. If the original flow is a thin film, it will eventually transform to a thicker, more energetically economical flow. This change in energy cannot take place gradually, but appears distinctly as a hydraulic jump. The flow inside the jump is extremely complicated and will not be analysed.

The *specific energy* (total mechanical energy per unit mass of liquid) for an open flow on a horizontal bed may be written as

$$E = hg + \frac{u^2}{2},$$

where h is the depth of the flow, u the mean velocity and g the acceleration of gravity. In a channel of arbitrary cross-section, $u = V/hw_a$, where V is the volumetric flow rate and w_a the width of the flow. For a constant volumetric flow rate it can be shown that E has a minimum value occurring at a so-called *critical depth*, h_c, which may be written as

$$h_c = \left(\frac{V^2}{g w_a^{\,2}} \right)^{\frac{1}{3}} \tag{4-1}$$

In an axisymmetric system the width of the flow varies with the radial location. At location r, we have $w_a = 2\pi r$.

The velocity corresponding to the critical depth is

$$u_c = \frac{V}{w_a h_c} = \sqrt{g h_c} \tag{4-2}$$

u_c is known as the *critical velocity* and has no connection with the critical velocity at which laminar flows become turbulent. u_c also corresponds to the velocity of propagation (relative to the undisturbed liquid) of a small surface wave in shallow liquid. Any small disturbance to the flow can cause a surface wave to be formed. This wave can carry information about the disturbance to the liquid further away. If the flow velocity is less than u_c (*subcritical* or *tranquil flow*), the wave can be propagated upstream against the flow, making it possible for events taking place downstream to influence the behaviour of the liquid upstream. If the flow velocity is greater than the critical (*supercritical* or *rapid* flow), small waves may only be propagated in the downstream direction and no information about downstream-events can be transmitted upstream, i.e. the liquid flow is *not* controlled by downstream conditions.

When the flow is just at the critical velocity a relatively large change of depth will only result in a small change in the specific energy. Small undulations on the surface are easily formed under these conditions. If a small wave is created and attempts to travel upstream, it will make no progress and is known as a *standing wave*. The hydraulic jump is such a stationary wave, through which the depth of flow increases. It is an abrupt change from rapid to tranquil flow, i.e. the depth is less than h_c before the jump and greater afterwards. One method of determining the radial position of a jump is therefore to find the place where the mean cross-sectional flow velocity equals u_c.

The jump position according to the critical velocity method is determined by the following relationship:

$$\frac{V}{2\pi r_j h} = \sqrt{g h} \tag{4-3}$$

This expression is valid for both laminar and turbulent conditions.

In any case the behaviour of open-channel flows depends strongly on whether the velocity is greater or less than the critical velocity.

In any flow where a free surface is present, gravity forces are important. Since the pressure at the surface is constant (usually atmospheric) only gravity forces (overlooking friction) can under steady conditions influence the flow. Disturbances at the surface must raise the liquid against its own weight and thus gravity forces are involved. In free surface flows an important property is therefore the relationship between the inertia force and the gravity force. This is represented as the ratio

$$\frac{inertia\ force}{gravity\ force} \propto \frac{\rho u^2 l^2}{\rho g l^3} = \frac{u^2}{gl},$$

where l is a characteristic length in the flow. In our case it will be natural to define this as the liquid film thickness, h. In practice it is more convenient to use the square root of the above relationship. This ratio is known as the *Froude number*, *Fr* (after William Froude), so

$$Fr = \frac{u}{\sqrt{gh}}$$

This parameter is in the same class as the perhaps more familiar Reynolds number, which relates the inertia force to the viscous force. With $u = V/hw_a$ we see, with the help of equation (4-2), that *Fr* represents the ratio of flow velocity to the velocity of a small surface wave. In critical conditions $u = \sqrt{gh}$ and $Fr = 1$, or alternatively, the critical Froude number may be said to be unity. Consequently, *tranquil flows* have $Fr < 1$ and *rapid flows* $Fr > 1$. If the film thickness, h, after the jump is used in equation (4-3) for determining the jump location, it means that the flow has adapted to a Froude number of unity immediately after the jump.

If the depths of the liquid before and after a jump (so-called *conjugate depths*) are termed h_1 and h_2, it can be shown that the following

relationship is valid for a rectangular channel when the length of the jump is considered infinitesimal:

$$\frac{h_2}{h_1} = \frac{1}{2}\left(\sqrt{1+8Fr_1^{\,2}} - 1\right) \tag{4-4}$$

This based on equation (4-21). Fr_1 is the Froude number before the jump. See also Figure 4.2. It is assumed that the velocities are uniform over the cross-sections of the flow. If a jump is present, h_2 must be greater than h_1, which again implies that Fr_1 must be greater than unity. The value of h_2 is determined by conditions downstream of the jump. The rapid flow before the jump continues until Fr_1 becomes large enough for satisfying equation (4-4).

From experimental observation five classes of jumps, based on the "inlet" Froude number, have been defined:

- $Fr_1 = 1.0$ *to* 1.7: standing wave or *undular jump*. The flow surface does not rise abruptly, but passes through a series of undulations, gradually diminishing in size. Dissipation of inlet kinetic energy is less than 5 percent. For larger values of Fr_1 the jump is more direct, i.e. there is a more abrupt change in height.

- $Fr_1 = 1.7$ *to* 2.5: smooth increase in height, known as a *weak jump*. Energy dissipation is 5 - 15 percent.

- $Fr_1 = 2.5$ *to* 4.5: unstable, *oscillating jump* where the irregular pulsations can create large waves which can travel far downstream. Energy dissipation is 15 - 45 percent.

- $Fr_1 = 4.5$ *to* 9: stable, *steady jump* insensitive to downstream conditions. Energy dissipation is 45 - 70 percent.

- $Fr_1 > 9$: rough, *strong jump*, perhaps pulsating. Energy dissipation is 70 - 85 percent.

The energy loss/dissipation in a jump is

$$\left(\frac{{u_1}^2}{2g}+h_1\right)-\left(\frac{{u_2}^2}{2g}+h_2\right)$$

The final result of the dissipation of energy is a slight increase in the liquid temperature.

In systems not involving thin film flows the length of a jump is usually in the magnitude of five times its height.

4.2 Flow Regions

The whole field of the flow may be divided into five regions, see Figure 4.1.

Region 1 includes the free jet and its deflection into a radial jet. Here there is a stagnation point, whose dimensions are of the order of the jet radius a. The flow velocity grows thereafter rapidly from zero to a value often assumed equal to the undisturbed jet velocity just before impact, U_∞. Because of the acceleration (from nozzle orifice to plate) due to gravity, this velocity may be greater than that in the nozzle itself. It is generally assumed that the jet flow is at a high enough Reynolds number so that the stagnation region is inviscid and that viscous effects occur near the lower boundary as the radial flow is retarded.

In *region 2* the viscous stresses will induce a boundary layer first appearing near the disk surface and then developing further until its external boundary reaches the film surface. The radius where the velocity boundary layer absorbs the whole flow is termed r_v. Outside the boundary layer (region 1), the velocity is often assumed constant and equal to U_∞.

In *region 3* an entirely viscous flow develops throughout the whole film. The boundary layer thickness is equal to the film thickness.

Region 4 is that of the hydraulic jump.

In *region 5* undisturbed fluid flows downstream from the hydraulic jump until it drains down from the disk edge.

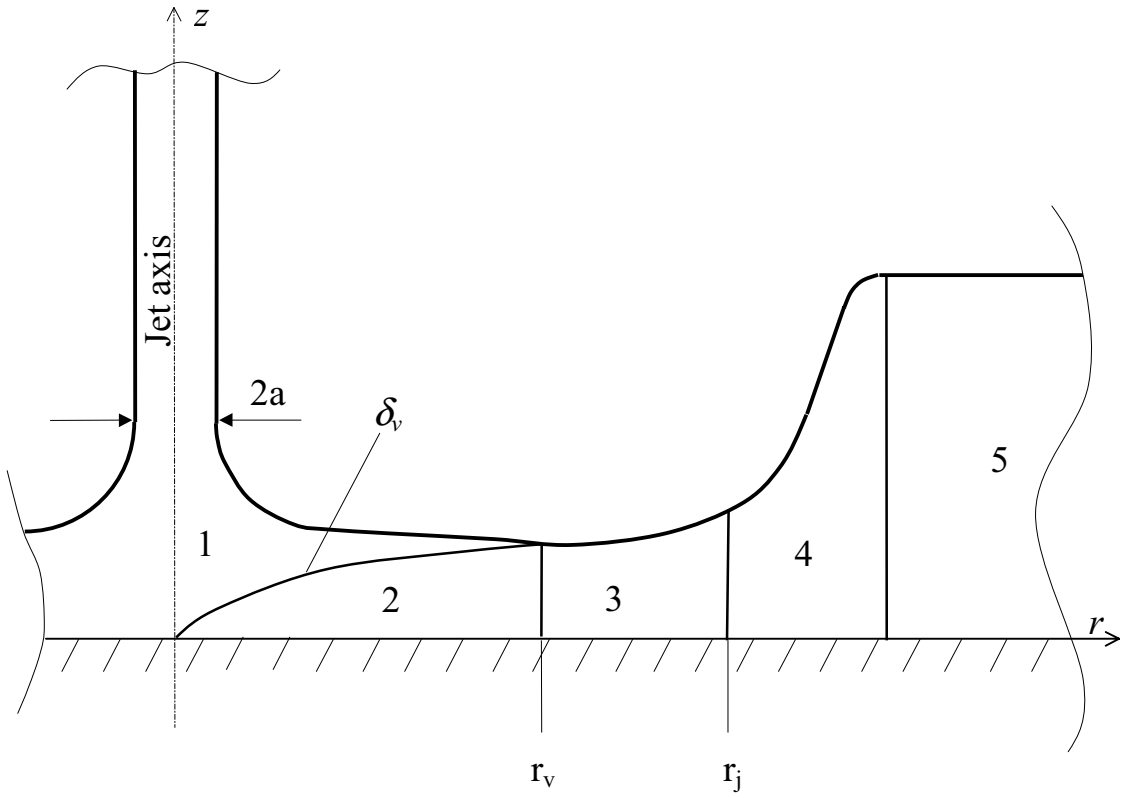

Figure 4.1 Sketch of axisymmetric jet impinging on a horizontal flat surface. Numbers indicate regions used for flow analysis.

Only steady state conditions will be considered. The velocity field is defined by the solution to the conservation equations. In a radial system they are:

Conservation of mass:

$$\frac{\partial(ru)}{\partial r} + \frac{\partial(rw)}{\partial z} = 0 \tag{4-5}$$

and conservation of momentum:

$$u\frac{\partial u}{\partial r} + w\frac{\partial u}{\partial z} = \nu\frac{\partial^2 u}{\partial z^2} \tag{4-6}$$

u is the radial velocity (r-direction) and w the vertical velocity (z-direction)

4.3 Watson (1964)

4.3.1 Laminar Flow

Since the inner layer of fluid (before the jump) is thin, Watson assumed it natural to apply the ideas of boundary layer theory in discussing the motion. No account is taken of gravity or surface tension effects.

Due to friction the liquid will stick to the lower solid boundary (the no-slip condition). This boundary condition is expressed as:

$$u = w = 0 \quad \text{at } z = 0$$

When the viscosity of air is neglected there is no friction (shear stress, τ) along the free surface between the liquid and air above. With $h(r)$ designating the thickness or height of the free surface above the plate, another boundary condition can then be mathematically formulated as:

$$\tau_h = \mu\frac{\partial u}{\partial z}\bigg|_{z=h} = 0$$

This implies $\frac{\partial u}{\partial z} = 0$ a*t z = h(r).*

Watson derived a *similarity solution* for the flow by assuming

$$u = U(r)f(\eta), \tag{4-7}$$

where *U(r)* is the speed at the top of the boundary layer and $\eta = z/\delta_v(r)$. $\delta_v(r)$ is the velocity boundary layer thickness and *z* is the vertical distance from the plate surface to a point in the flow.

A similarity solution is in general a solution to an equation that is transformed from its original form by introducing a new (similarity-) variable. This variable is one that reduces the number of variables by one or more by some analytical means, usually a coordinate transformation merging two or more of the original variables into one. In this problem it can be shown that matters are simplified by the momentum continuity equation being reduced from a partial differential equation to an ordinary differential equation much simpler to solve.

4.3.1.1 The Region $r_v < r < r_j$

First we will consider the region $r > r_v$ before the hydraulic jump, see Figure 4.1. Here $\delta_v(r)$ absorbs the whole flow and is equal to the film thickness, *h(r).* We will therefore in this region use *h* instead of δ_v, so that $\eta = z/h(r)$. At the free surface we have

$$u = U(r) \quad \text{at} \quad \eta = 1 \quad (z = h)$$

The boundary conditions then require that $f(\eta)$ satisfies

$$f(0) = 0, \qquad f(1) = 1, \qquad f'(1) = 0,$$

where $f' = df/d\eta$.

Continuity of the flow requires that

$$2\pi r \int_0^h u dz = V \tag{4-8}$$

where V is the volumetric flow rate from the nozzle. From this equality, equation (4-7) and the fact that $U(r)$ is independent of z, we find:

$$2\pi r U(r) h(r) \int_0^1 f(\eta) d\eta = V$$

A definite integral in an equation is always a constant. Hence $rU(r)h(r)$ must be constant. Making use of this, the equation of mass conservation becomes:

$$Uf' \frac{\partial \eta}{\partial r} - U \frac{h'}{h} f + \frac{\partial w}{\partial z} = 0$$

$h' = \partial h/\partial r = dh/dr$. We have now dropped the arguments r and η and will from now on write U, h, δ_v and f instead of $U(r)$, $h(r)$, $\delta_v(r)$ and $f(\eta)$. For a given radius η varies only through z. Therefore

$$\frac{\partial w}{\partial z} = \frac{\partial w}{\partial \eta}\frac{\partial \eta}{\partial z} = \frac{1}{h}\frac{\partial w}{\partial \eta} \quad \text{and} \quad \frac{\partial \eta}{\partial r} = \frac{\partial \eta}{\partial z}\frac{\partial z}{\partial r} = -\frac{z}{h^2}\frac{\partial h}{\partial r} = -\frac{z}{h^2}h'$$

$$\Downarrow$$

$$Uf'\left(-\frac{zh'}{h^2}\right) - Uf\frac{h'}{h} + \frac{1}{h}\frac{\partial w}{\partial \eta} = 0$$

$$\Downarrow$$

$$Uh'\left(f + f'\eta\right) = \frac{\partial u}{\partial \eta}$$

With $f + f'\eta = d(f\eta)/d\eta$ we can integrate and knowing $u = 0$ for $z = 0$, we get:

$$u = U\, h'\eta\, f$$

The conservation of momentum equation now reduces to

$$\nu f'' = h^2 U'\, f^2 \tag{4-9}$$

If a similarity solution to this equation exists, η can be the only variable. It is therefore necessary that h^2U' is a constant, independent of r. It is convenient to write this requirement as

$$h^2 U' = -\frac{3}{2} c^2 \nu \tag{4-10}$$

where c is some constant not yet determined. This enables us to write equation (4-6) as

$$2f'' + 3c^2 f^2 = 0$$

$$\Downarrow$$

$$2f''\, f' = -3c^2 f^2 f'$$

Integrating once and remembering $f(1) = 1$ and $f'(1) = 0$ (for determining the integration constant), we get:

$$f'^2 = c^2(1 - f^3)$$

$$\Downarrow$$

$$\left(\frac{df}{d\eta}\right)^2 = c^2\left(1-f^3\right)$$

$$\Downarrow$$

$$cd\eta = \frac{df}{\sqrt{1-f^3}}$$

$$\Downarrow$$

$$c\eta = \int_0^f \frac{dx}{\sqrt{1-x^3}}$$

In this format we have x as a dummy variable of integration and a η - f relation is obtained by solving for various f values in the upper limit of the integral. The constant c is unveiled from the condition $f(1) = 1$:

$$c = \int_0^1 \frac{dx}{\sqrt{1-x^3}} \tag{4-11}$$

The solution to this definite integral is listed in mathematical handbooks like Gradshteyn and Ryzhik (1972). More specifically, in this reference as

$$c = \frac{\left(\tilde{u}\left(\frac{1}{3}\right)\right)^2}{2\pi\sqrt{3}\cdot\sqrt[3]{2}} \approx 0.524$$

This result is significantly different from that stated by Watson, namely

$$c = \frac{1}{3}\frac{\tilde{u}\left(\frac{1}{2}\right)\tilde{u}\left(\frac{1}{3}\right)}{\tilde{u}\left(\frac{5}{6}\right)} \approx 1.402\,,\ \Gamma \text{ being the } \textit{gamma} \text{ function.}$$

The first result was assumed to be correct and consequently used while following Watson's deductions. The final outcome was far from promising, being totally unrealistic. A lot of time was spent checking the work over and over again, but to no avail. Finally, a newer edition of Gradshteyn and Ryzhik was located and inspected. The solution to the integral (equation (4-11)) was here listed as

$$c = \frac{\left(\Gamma(\frac{1}{3})\right)^3}{2\pi\sqrt{3}\cdot 2^{\frac{1}{3}}} \approx 1.402 \qquad !!$$

The problem was again encountered when looking up the integral $\int_0^1 \frac{xdx}{\sqrt{1-x^3}} = \frac{1}{\pi}\frac{\sqrt{3}}{\sqrt[3]{4}}\left(\Gamma\left(\frac{2}{3}\right)\right)^2$ in the earlier edition of Gradshteyn and Ryzhik. Again the exponent is 2 instead of 3 and corrected in later editions of the book.

With c determined, $\int_0^1 f(\eta)d\eta = \frac{1}{c}\int_0^1 \frac{xdx}{\sqrt{1-x^3}} = \frac{2\pi}{3\sqrt{3}c^2}$, yielding

$$rUh = \frac{3\sqrt{3}c^2}{4\pi^2}V \tag{4-12}$$

This lets us fairly easy solve equations (4-6) and (4-8) with the result

$$U = \frac{27c^2}{8\pi^4}\frac{V^2}{\nu\left(r^3+b^3\right)} \tag{4-13}$$

and

$$h = \frac{2\pi^2}{3\sqrt{r}}\frac{\nu\left(r^3+b^3\right)}{rV} \tag{4-14}$$

b is a constant of integration and at this point unknown. It can be noted that h goes through a minimum at the radial position

$$r = 2^{-\frac{1}{3}} b$$

with the value

$$h_{\min} = \frac{2^{\frac{1}{3}} \pi^2}{\sqrt{3}} \frac{\nu b^2}{V}.$$

4.3.1.2 The Region $0 < r < r_v$

In this region the so-called momentum integral equation (a momentum-force balance) for the boundary layer flow can be written as

$$\left(\frac{\partial}{\partial r} + \frac{1}{r}\right) \int_0^{\delta_v} \left(U_\infty u - u^2\right) dz = \nu \left(\frac{\partial u}{\partial z}\right)_{z=0}, \qquad (4\text{-}15)$$

In the unretarded fluid outside the boundary layer Watson assumes $u=U_\infty$.

We now state that the velocity u inside the boundary layer has the same form as before, namely $u = Uf(\eta)$. This time with $U = U_\infty$ and $\eta = z/\delta_v$. U_∞ is also the surface velocity which up to r_v is independent of r. With these definitions equation (4-15) ends up as a differential equation for the velocity boundary layer thickness δ_v:

$$\frac{2\left(\pi - c\sqrt{3}\right)}{3\sqrt{3}c^2} U_\infty{}^2 \left(\frac{d\delta}{dr} + \frac{\delta}{r}\right) = \frac{\nu U_\infty c}{\delta_v}$$

After integration of this equation it can be shown that the integration constant safely can be neglected when $r >> a$ (the jet radius), yielding

$$\delta_v^{\,2} = \frac{\pi\sqrt{3}c^3}{\pi - c\sqrt{3}}\frac{\nu r a^2}{V} \tag{4-16}$$

$$\Downarrow$$

$$\delta_v \approx 4.59a\sqrt{\frac{\nu r}{V}} \tag{4-17}$$

At the radial position r_v the boundary layer just reaches the fluid surface and equation (4-8) may be written as

$$r_v U_\infty \breve{u}_v(r_v) = \frac{3\sqrt{3}c^2}{4'^{\,2}}V$$

With δ_v as in equation (4-16), we find

$$r_v^{\,3} = \frac{9\sqrt{3}c\left(\pi - \sqrt{3}c\right)}{16\pi^3}\frac{Va^2}{\nu}$$

$$\Downarrow$$

$$r_v = 0.3155\left(\frac{Va^2}{\nu}\right)^{\frac{1}{3}} \tag{4-18}$$

When $r < r_v$ the volume flow rate is the sum of the flows inside and outside the boundary layer:

$$V = 2\pi r\left[\int_0^{\delta_v} u\,dz + U_\infty(h - \delta_v)\right] \tag{4-19}$$

$$\Downarrow$$

$$V = 2\pi r\left[U_\infty \delta_v \int_0^1 f\, d\eta + U_\infty (h - \delta_v) \right] = \pi a^2 U_\infty$$

Solving for h:

$$h = \frac{a^2}{2r} + \left(1 - \frac{2\pi}{3\sqrt{3}c^2}\right)\delta_v$$

δ_v is again given by equation (4-16).

If we return to the position r_v, the free surface velocity here given by equation (4-13) must just equal the jet velocity U_∞. Subsequently we find

$$b^3 = \frac{9\sqrt{3}c\left(3\sqrt{3}c - \pi\right)}{16\pi^3}\frac{Va^2}{\nu}$$

$$\Downarrow$$

$$b = \frac{3}{\pi}\left(\frac{3\sqrt{3}c^2 - \pi c}{16\sqrt{3}}\right)^{\frac{1}{3}}\left(\frac{Va^2}{\nu}\right)^{\frac{1}{3}} \qquad (4\text{-}20)$$

or

$$b \approx 0.567\left(\frac{Va^2}{\nu}\right)^{\frac{1}{3}}$$

In the theory leading to these results we have neglected the effects of gravity. If the film thickness grows large one can expect that hydrostatic pressure influences the dynamics of the radial flow. Also, the effects of viscosity could be more noticeable in the idealised inviscid region where the jet turns to a radial flow when the Reynolds number of the jet becomes small.

4.3.1.3 Jump Condition

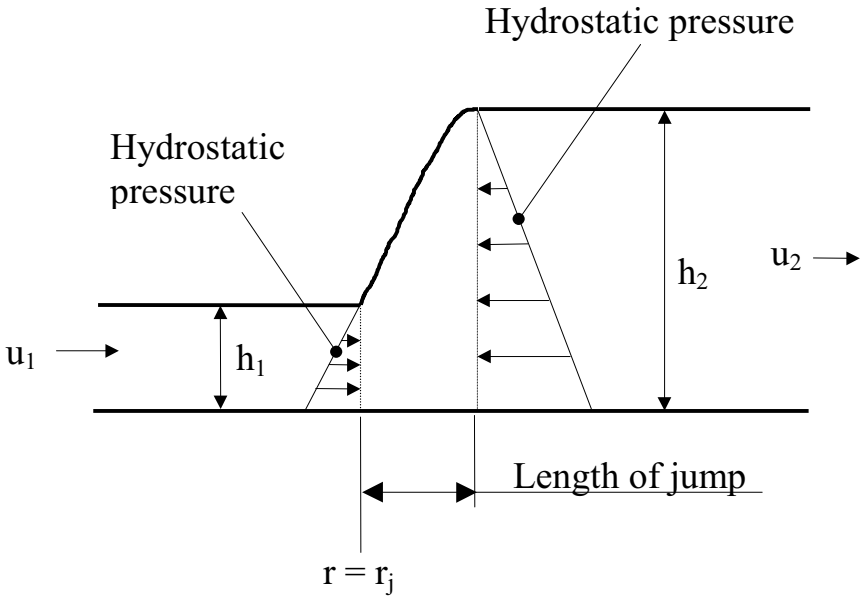

Figure 4.2 Sketch of hydraulic jump. Subscripts 1 and 2 denote conditions before and after the jump.

Until now we have only described the conditions before the hydraulic jump. If the annular region of the jump (measured radially) is small, friction between the liquid and plate can be ignored. Watson prescribed that the thickness of the film after the jump, h_2, is *constant*. This seems to agree well with experiments. The speed of flow immediately outside the jump, u_2, is assumed uniform through the depth. The radial position of the jump, r_j, can be determined by equating the rate of loss of momentum with the pressure thrust in the jump region:

$$\rho \int_0^{h_1} {u_1}^2 dz - \rho \int_0^{h_2} {u_2}^2 dz = \rho g \int_0^{h_2} h\, dh - \rho g \int_0^{h_1} h\, dh \qquad (4\text{-}21)$$

$$\Downarrow$$

$$\rho \int_0^{h_1} {u_1}^2 dz - \rho {u_2}^2 \int_0^{h_2} dz = \frac{1}{2}\rho g {h_2}^2 - \frac{1}{2}\rho g {h_1}^2 \qquad (4\text{-}22)$$

$h_1^2 << h_2^2$ and is neglected by Watson, yielding:

$$\rho \int_0^{h_1} {u_1}^2 dz = \frac{1}{2}\rho g {h_2}^2 + \rho {u_2}^2 h_2 \qquad (4\text{-}23)$$

The left hand side of equation (4-19) must be evaluated separately for r_j larger or smaller than r_v, since the jump may occur at any point in the development of the boundary layer.

- **For the case $r_j \geq r_v$**

We have $$\int_0^{h_1} {u_1}^2 dz = U^2 h \int_0^1 f(\eta)^2 d\eta = \frac{27\sqrt{3}c^3}{16\pi^6} \frac{V^3}{\nu r_j ({r_j}^3 + b^3)}$$

and equation (4-19) may be written as

$$\frac{r_j {h_2}^2 a^2 g}{V^2} + \frac{a^2}{2\pi^2 r_j h_2} = \frac{0.0176}{\left(\frac{{r_j}^3 \nu}{a^2 V} + 0.1826\right)} \qquad (4\text{-}24)$$

provided $r_j \geq 0.3155\left(\frac{V}{\nu a^2}\right)^{\frac{1}{3}}$ from equation (4-18)

- **For the case $r_j < r_v$**

We have:

$$\int_0^{h_1} {u_1}^2 dz = {U_\infty}^2 \delta_v \int_0^1 f(\eta)^2 d\eta + {U_\infty}^2 (h - \delta_v) = {U_\infty}^2 \left(\frac{a^2}{2r_j} - \frac{2\left(\pi - c\sqrt{3}\right)}{c^2 3\sqrt{3}} \delta_v \right)$$

Rearranging, we obtain

$$\frac{r_j {h_2}^2 a^2 g}{V^2} + \frac{a^2}{2\pi^2 r_j h_2} = 0.10132 - 0.1297 \frac{1}{a}\left(\frac{\nu}{V}\right)^{\frac{1}{2}} {r_j}^{\frac{3}{2}} \qquad (4\text{-}25)$$

with $r_j < 0.3155\left(\frac{V}{\nu a^2}\right)^{\frac{1}{3}}$.

4.3.2 Turbulent Flow

Watson predicts the flow on the plate to become unstable (turbulent) at a jet-Reynolds number of $2.57 \cdot 10^4$. However, he states that this is approximate and may be of little value in practice. Watson defines the jet Reynolds number as

$$Re = \frac{V}{\nu a}.$$

In this work it is preferred to be defined as

$$Re = \frac{U_\infty 2a}{\nu} = \frac{2}{\pi}\frac{V}{\nu a}.$$

In that way turbulence occurs at $Re = 1.64 \cdot 10^4$.

The motion is assumed to be turbulent throughout and a similarity solution analogous to that of laminar conditions is proposed. An eddy viscosity, ε, is introduced transforming the momentum continuity equation as follows:

$$u\frac{\partial u}{\partial r} + w\frac{\partial u}{\partial z} = \nu \frac{\partial}{\partial z}\left(\varepsilon \frac{\partial u}{\partial z}\right)$$

with, according to Glauert (1956):

$$u = U(r)F(\eta), \qquad \eta = \frac{z}{\delta_v}$$

$$\varepsilon = \gamma U^{\frac{3}{4}} \delta_v^{\frac{3}{4}} F(\eta)^6$$

γ is a constant.

- **The region $r_v < r < r_j$**

We proceed much as before and find:

$$rUh = \text{constant} = \frac{kV}{2\pi A}$$

$$\tau_w = \frac{\rho k \gamma U^{\frac{7}{4}}}{h^{\frac{1}{4}}} \text{ ; shear stress on plate}$$

$$U = \frac{100}{9(14)^{\frac{1}{4}}(\pi A)^{\frac{5}{4}}} \frac{V}{\nu^{\frac{1}{4}}\left(r^{\frac{9}{4}} + l^{\frac{9}{4}}\right)} \tag{4-26}$$

$$h = \frac{9k}{200}\left(\frac{14\pi A\nu}{V}\right)^{\frac{1}{4}} \frac{\left(r^{\frac{9}{4}} + l^{\frac{9}{4}}\right)}{r} \tag{4-27}$$

$$r_v^{\frac{9}{5}} = \frac{V}{2\pi A U_\infty} \frac{\left(80\left(A - \frac{2}{9}\right)\right)^{\frac{4}{5}}}{\left(\frac{7\nu}{U_\infty}\right)^{\frac{1}{5}}} \tag{4-28}$$

$$l^{\frac{9}{4}} = \frac{20(1-2A)}{(14\pi)^{\frac{1}{4}} A^{\frac{5}{4}}}\left(\frac{V}{\nu}\right)^{\frac{1}{4}} a^2 \tag{4-29}$$

$$A = 0.239$$
$$k = 0.26 \qquad (4\text{-}30)$$
$$\gamma \approx 0.1\nu^{\frac{1}{4}}$$

- **The region $0 < r < r_v$**

We find:

$$h = \frac{a^2}{2r} + \frac{k - A}{\left(80\left(A - \frac{2}{9}\right)\right)^{\frac{4}{5}}}\left(\frac{7\nu}{U_\infty}\right)^{\frac{1}{5}} r^{\frac{4}{5}} \qquad (4\text{-}31)$$

In both cases

$$k\eta = \int_0^F \frac{x^6}{\sqrt{1-x^9}}dx\,.$$

Jump condition

The turbulent jump position is derived as before, giving:

- **For the case $r_j < r_v$**

$$\frac{r_j {h_2}^2 a^2 g}{V^2} + \frac{a^2}{2\pi^2 r_j h_2} = \frac{1}{\pi^2} - \frac{\left(560\pi\left(A - \frac{2}{9}\right)\right)^{\frac{1}{5}}}{40\pi^2}\left(\frac{r_j}{a}\left(\frac{\nu a}{V}\right)^{\frac{1}{9}}\right)^{\frac{9}{5}} \qquad (4\text{-}32)$$

- **For the case $r_j \geq r_v$**

$$\frac{r_j {h_2}^2 a^2 g}{V^2} + \frac{a^2}{2\pi^2 r_j h_2} = \frac{200}{81 \cdot 14^{\frac{1}{4}}(\pi A)^{\frac{9}{4}}} \frac{1}{\left(\frac{r_j}{a}\left(\frac{\nu a}{V}\right)^{\frac{1}{9}}\right)^{\frac{9}{4}} + \frac{40(1-2A)}{(7\pi)^{\frac{1}{4}}(2A)^{\frac{5}{4}}}} \qquad (4\text{-}33)$$

This last expression brought forth quite a few problems as the term $81 \cdot 14^{\frac{1}{4}}$ in Watson's article was presented as $81.14^{\frac{1}{4}}$. Calculations were first carried out according to the original orthography, but results were strange. Watson's work was scrutinized and the misspelling finally detected.

4.4 Buyevich and Ustinov (1994)

Only *laminar* conditions are studied.

The basic theory employed here is the same as that of Watson's, and again surface tension effects are neglected. The major difference is that instead of seeking a similarity solution, Buyecich and Ustinov prefer the *Karman-Pohlhausen polynomial method*, according to which the radial velocity is *approximated* as

$$u = \frac{3}{2} U \left(\eta - \frac{\eta^3}{3} \right). \tag{4-34}$$

As before U (a function of r) is the velocity at the top of the boundary layer and $\eta = z/\delta_v(r)$. This profile satisfies the same boundary conditions as those mentioned in Watson's theory.

4.4.1 The Region $r_v < r < r_j$:

From equation (4-8) and equation (4-34) we find

$$U(r) = \frac{4a^2 U_\infty}{5rh} \tag{4-35}$$

As we know from before $\delta_v = h$ in this region, so the momentum integral equation including the pressure term may be written as:

$$\left(\frac{d}{dr}+\frac{1}{r}\right)\int_0^h u^2\,dz = \nu\left.\frac{\partial u}{\partial z}\right|_{z=0} + \frac{1}{\rho}\int_0^h \rho\frac{\partial p}{\partial r}\,dz \tag{4-36}$$

The pressure, p_0, must be assumed constant above the liquid film so that $p = p_0 + \rho gh$. Further manipulation therefore results in

$$\left(\frac{d}{dr}+\frac{1}{r}\right)\left(\frac{272}{875}a^4 {U_\infty}^2\frac{1}{r^2 h}\right) = \frac{3}{2}\nu\frac{U}{h} + \int_0^h g\frac{dh}{dr}\,dz \tag{4-37}$$

$$\Downarrow$$

$$\frac{272}{875}a^2 U_\infty \frac{d}{dr}\left(\frac{1}{rh}\right) = -\frac{6}{5}\frac{\nu}{h^2} - gh\frac{dh}{dr} \tag{4-38}$$

Neglecting the effect of the hydrostatic pressure variation (last term in equation (4-38)), integration yields:

$$h = \frac{175}{136}\frac{\nu}{U_\infty}\frac{r^2}{a^2} + C\,, \tag{4-39}$$

where C is a constant of integration, temporarily unknown.

4.4.2 The Region $0 < r < r_v$

We have as before

$$V = 2\pi r\left[\int_0^{\delta_v} u\,dz + U_\infty(h-\delta_v)\right],$$

leading to

$$h = \frac{a^2}{2r} + \frac{3}{8}\delta_v \tag{4-40}$$

Equation (4-15) (again neglecting the pressure gradient) leads to

$$\frac{39}{280}\frac{U_\infty}{r}\frac{\partial}{\partial r}(r\delta_v) = \frac{3}{2}\frac{\nu}{\delta_v}$$

$$\Downarrow$$

$$\frac{39}{280}U_\infty d(r\delta_v)^2 = 3\nu r^2 dr$$

$$\Downarrow$$

$$\delta_v = \sqrt{\frac{280}{39}\frac{\nu r}{U_\infty} + \frac{C}{r^2}} \tag{4-41}$$

If we assume that $\delta_v = 0$ at $r = 0$, then $C = 0$ and

$$\delta_v = \sqrt{\frac{280}{39}\frac{\nu r}{U_\infty}} \approx 4.75a\sqrt{\frac{\nu r}{V}} \tag{4-42}$$

At r_v, $\delta_v = h$. Equating equations (4-40) and (4-42)and gives

$$r_v = \sqrt[3]{\frac{78}{875}\frac{U\infty a^4}{\nu}} \approx 0.305\left(\frac{Va^2}{\nu}\right)^{\frac{1}{3}} \tag{4-43}$$

Furthermore equation (4-39) must also equal equation (4-42) at $r = r_v$. This lets us identify the constant C from equation (4-39), namely

$$C = \left(\frac{4}{5} - \frac{39}{340} \right) \frac{a^2}{r} \approx 0.685 \frac{a^2}{r}$$

The film thickness *after* r_v is thus

$$h = \frac{175}{136} \frac{\nu}{U_\infty} \frac{r^2}{a^2} + 0.685 \frac{a^2}{r} \qquad (r_v < r < r_j) \quad (4\text{-}44)$$

4.4.3 Jump Condition and Film Thickness After Jump

The assumptions made in the jump zone are exactly the same as those made by Watson. With the prevalent velocity equation, (4-21) yields

$$\frac{1}{2} g \left(h_2^2 - h_1^2 \right) = \frac{272}{875} \frac{a^4 U_\infty^2}{r_j^2} \left(\frac{1}{h_1} - \frac{1}{h_2} \right) \qquad (4\text{-}45)$$

This equation implicitly relates the jump radius to the film thicknesses before and after the jump. h_1 is given by equation (4-39) or (4-40) and h_2 is found from equation (4-38). Buyevich and Ustinov say that the action of gravity cannot be overlooked after the jump, because however small the gravity forces are, they seem to significantly influence the flow beyond this point. Otherwise the same equations are said to apply after the jump (region 5) as in region 3. Equation (4-38) can be solved numerically if a boundary condition can be provided. An obvious choice is the conditions at the edge of the plate. An alternative to Watson's approach of somehow presupposing a value for h_2 and assuming it constant, can be derived by alleging the liquid flows smoothly down the edge of the disk. According to Buyevich and Ustinov this can mathematically be described by claiming

$$\frac{dh}{dr} \to -\infty \text{ when } r \to R, \qquad (4\text{-}46)$$

R being the disk radius. Actually this statement is physically unrealistic because it requires that the surface of the film is vertical at R, meaning it has no thickness, h_V, down the disk edge. This of course is not possible and a better suggestion might therefore be

$$\frac{dh}{dr} \to -\infty \text{ when } r \to R + h_V . \tag{4-47}$$

Generally when a hydraulic jump occurs $h_V << R$, so that $R + h_V \approx R$. It is therefore unlikely that any significant error is introduced when utilising equation (4-46) after all.

For finite values of r it can be shown that equation (4-46) is satisfied when

$$h(R) = h_R = a\left(\frac{272}{875}\frac{{U_\infty}^2 a}{gR^2}\right)^{\frac{1}{3}}.$$

It is considered beneficial to rewrite this equation in the following form:

$$h_R = \left(\frac{272}{875}\frac{V^2}{g(\pi R)^2}\right)^{\frac{1}{3}} \tag{4-48}$$

To some readers it may seem strange that the derivative of a function has a (negative) infinite value where the function itself has a finite value. This is however mathematically quite reasonable and many functions possess this feature.

Buyecich and Ustinov claim that equation (4-45) can be shown to have either a single physically suitable solution or none at all. There is no solution when R exceeds a maximum value or is smaller than a certain minimum. Naturally these values depend on the original flow conditions in

the jet. In practice this means that for small *R*s the liquid flows down the disk without forming a hydraulic jump. As the disk grows large enough a jump will eventually appear just near the disk edge. Further increasing *R* will move the jump towards the centre of the disk and finally, for a large enough *R*, it merges with the incident jet and vanishes. This behaviour is explained by an increase in hydraulic resistance to the film flow as the disk size increases. The same effect can be experienced by fitting an obstacle in the form of a ring on the disk surface. This is reported to be confirmed by experiments from Nakoryakov et al. (1975).

4.4.4 Remarks for Stagnation Region

The theory reviewed until now, describing the flow before the jump, is not valid in the stagnation region itself. This region is inside a radius r_s, in the same order of magnitude as the jet radius, *a*. The flow here can be described with help of the well-known Blasius series discussed in Schlichting (1979). In the stagnation region the radial velocity near the plate can be approximated by

$$u = 0.383 U_\infty r z \sqrt{\frac{U_\infty}{\nu}} \tag{4-49}$$

Cf. Shach (1934). This is the first term of the Blasius series and is determined with the help of frictionless stagnation theory. r_s can now be evaluated by stating equation (4-49) shall coincide with equation (4-34) for small values of *z* at exactly $r = r_s$. This results in

$$r_s = (2.136)^{\frac{1}{3}} a \approx 1.288 a . \tag{4-50}$$

This is not an exact deduction, but can be improved by increasing the number of terms from the Blasius series.

4.5 Alekseenko et al. (1994)

This analysis is in general similar to the preceding ones. However, two major drawbacks soon became evident, namely obvious printing errors (for example dimensional and exponential errors) and lacking theoretical explanations. This made it difficult to follow the analysis, and to avoid mistakes, it was necessary to painstakingly examine the whole work and repeat all mathematical deductions. To help with this the Academy of Sciences of Russia, Siberian Department, willingly sent a report in Russian (Nakoryakov et al., 1975) which Alekseenko et al. have based much of their work on. Unfortunately some printing errors were apparent here too, making it again necessary to double-check all calculations.

Both laminar and turbulent conditions are studied. The film thickness after the jump is assumed *constant*, equal to the thickness at the plate edge.

4.5.1 Laminar Flow

The governing equations and boundary conditions for the flow are naturally the same as before. The velocity profile is found by the method of *successive approximations*. A guessed *u* velocity enables a *w* velocity to be found from the continuity equation. Thereafter the left-hand side of the momentum-conservation equation is calculated. This is then integrated twice to find a new *u* velocity, and so on.

4.5.1.1 The Region 0 < r < r_v

As an initial guess:

$$u = U_\infty \frac{z}{\delta_v} \tag{4-51}$$

With the continuity of mass equation (4-5), we find

$$w = \frac{U_\infty}{2}\frac{z^2}{{\delta_v}^2}\frac{d\delta}{dz} - \frac{U_\infty}{2z}\frac{z^2}{\delta_v}$$

Using these expressions to evaluate the left-hand side of equation (4-6) and integrating twice with respect to u, employing the appropriate boundary conditions, we find

$$u = -\frac{{U_\infty}^2}{24\nu}\frac{z^4}{{\delta_v}^3}\frac{d\delta_v}{dr} - \frac{U_\infty}{24\nu}\frac{z^4}{r{\delta_v}^2} + \left(\frac{U_\infty}{\delta_v} + \frac{{U_\infty}^2}{24\nu}\frac{d\delta_v}{dz} + \frac{{U_\infty}^2}{24\nu}\frac{\delta_v}{z}\right)z \qquad (4\text{-}52)$$

This result is considered accurate enough and used as the final velocity approximation.

Using $\left.\frac{\partial u}{\partial z}\right|_{z=\delta_v} = 0$, we find a differential equation for δ_v:

$$\frac{{U_\infty}^2}{8\nu}\frac{d\delta_v}{dr} + \frac{{U_\infty}^2}{8\nu}\frac{\delta_v}{r} - \frac{U_\infty}{\delta_v} = 0,$$

which relatively easy can be solved, resulting in

$$\delta_v = \frac{4}{\sqrt{3}}\sqrt{\frac{\nu r}{U_\infty}} \qquad (4\text{-}53)$$

With

$$\frac{d\delta_v}{dr} = \frac{1}{2}\frac{4}{\sqrt{3}}\sqrt{\frac{\nu}{U_\infty}}\frac{1}{\sqrt{r}} = \frac{1}{2}\frac{4}{\sqrt{3}}\sqrt{\frac{\nu r}{U_\infty}}\frac{1}{r} = \frac{1}{2}\frac{\delta_v}{r},$$

equation (4-53) is reduced to

$$u = \frac{U_\infty}{3}\frac{z}{\delta_v}\left(4 - \frac{z^3}{\delta_v{}^3}\right) \tag{4-54}$$

The volume flow rate equation (4-19) can then be solved for *h*, resulting in

$$h = \frac{a^2}{2r} + \frac{2}{5}\delta_v \tag{4-55}$$

This is somewhat different from that obtained by Alekseenko et al., namely

$$h = \frac{a^2}{2r} + 0.065\delta_v \tag{4-56}$$

A suitable explanation for this discrepancy has not been found.

4.5.1.2 The Region $r_v < r < r_j$

A linear velocity profile is again assumed

$$u = Az\,,$$

A being some constant.

With

$$V = \pi a^2 U_\infty = 2\pi r \int_0^h u\,dz\,, \tag{4-57}$$

we can calculate *A* and obtain

$$u = \frac{V}{\pi r h^2} z$$

and progressing as before:

$$w = \frac{V z^2}{\pi r h^3} \frac{dh}{dr}$$

As a second and final approximation for the radial velocity we find

$$u = -\frac{V^2}{12\pi^2 \nu} \frac{z^4}{r^3 h^4} - \frac{V^2}{12\pi^2 \nu} \frac{z^4}{r^2 h^5} \frac{dh}{dr} + \left(\frac{V^2}{3\pi^2 \nu} \frac{1}{r^3 h} + \frac{V^2}{3\pi^2 \nu} \frac{1}{r^2 h^2} \frac{dh}{dr} \right) z$$

Equation (4-57) yields

$$\frac{3}{10} \frac{dh}{dr} + \frac{h}{r} = \frac{10}{3} \frac{\pi \nu r}{V}$$

with the solution

$$h = \frac{10}{9} \frac{\pi \nu r^2}{V} + \frac{C}{r}, \qquad (4\text{-}58)$$

where C is a constant of integration.

At $r = r_v$, $\delta_v = h$. Using equation (4-55) for h and equating this with δ_v itself, results in

$$r_v = \left(\frac{5}{8} \frac{1}{\sqrt{3\pi}} \right)^{\frac{2}{3}} \left(\frac{V}{\nu a} \right)^{\frac{1}{3}} a \qquad (4\text{-}59)$$

or

$$r_v \approx 0.346 \left(\frac{V}{\nu a} \right)^{\frac{1}{3}} a$$

Using this when equating equation (4-57) with (4-55) lets us find the constant of integration in (4-58):

$$C = \frac{595}{864} r_v{}^2 \approx 0.689 r_v{}^2$$

Setting *h* as in (4-56) (in accordance with Alekseenko et al) results in

$$r_v \approx 0.257 \left(\frac{V}{va} \right)^{\frac{1}{3}} a$$

and the constant of integration

$$C \approx 0.476 r_v{}^2$$

4.5.1.3 Jump Condition

No new method for determining the position of the hydraulic jump is proposed. Both Watson's theory and the critical velocity method are referred to for this task.

4.5.2 Turbulent Flow

- **The Region $0 < r < r_v$**

The following velocity profile is assumed

$$u = U_\infty \left(\frac{z}{\delta_v} \right)^{\frac{1}{7}} \qquad (4\text{-}60)$$

This *seventh-root* type of profile is often suggested in turbulent boundary layers.

This velocity profile cannot apply at the plate surface ($z = 0$), since the velocity gradient at that point is infinite $\left(\frac{du}{dz} = \frac{U_\infty}{7 \delta_v^{\frac{1}{7}} z^{\frac{6}{7}}} \right)$. This indicates an infinite shear, which is not physically possible. In the laminar sublayer adjacent to the plate, a linear velocity profile is said to pertain. This becomes tangent to the seventh-root profile at the outer edge of the laminar sublayer.

Blasius developed the following expression for boundary shear stress in a circular pipe, which is also assumed to apply in our flow:

$$\tau_w = \mu \left(\frac{\partial u}{\partial z} \right)_{z=0} = 0.0225 \rho U_\infty{}^2 \left(\frac{\nu}{U_\infty \delta_v} \right)^{\frac{1}{4}} \qquad (4\text{-}61)$$

Nakoryakov et al. (1975) quote this constant as 0.0228.

Equation (4-15) is naturally used for turbulent conditions too, and combined with equation (4-61) we obtain

$$\delta_v = \left(0.0225 \frac{40}{7} \right)^{\frac{4}{5}} \pi^{\frac{1}{5}} \left(\frac{\nu a}{V} \right)^{\frac{1}{5}} a^{\frac{1}{5}} r^{\frac{4}{5}} \qquad (4\text{-}62)$$

$$\Downarrow$$

$$\delta_v \approx 0.244 \left(\frac{\nu a}{V} \right)^{\frac{1}{5}} a^{\frac{1}{5}} r^{\frac{4}{5}}$$

From equation (4-57) we can calculate the film thickness, h:

$$h = \frac{a^2}{2r} + \frac{1}{8}\delta_v$$

Combining equation (4-62) with (4-57) at $r = r_v$ leads to

$$r_v = \left(\frac{4}{7}\pi^{-\frac{1}{5}} \left(\frac{7}{0.0225 \cdot 40} \right)^{\frac{4}{5}} \right)^{\frac{5}{9}} \left(\frac{V}{va} \right)^{\frac{1}{9}} a \qquad (4\text{-}63)$$

$$\Downarrow$$

$$r_v \approx 1.606 \left(\frac{V}{va} \right)^{\frac{1}{9}} a$$

- **The Region $r_v < r < r_j$**

In this region we get from equation (4-57)

$$U = \frac{4}{7\pi}\frac{V}{rh} \qquad (4\text{-}64)$$

The momentum integral equation is

$$\left(\frac{d}{dr} + \frac{1}{r} \right) \int_0^h u(U-u)dz - \int_0^h u \frac{\partial U}{\partial r} dz = \frac{\tau_w}{\rho}$$

which then reduces to

$$\frac{7}{9}\frac{U^2}{r}\frac{d(rh)}{dr} = \frac{\tau_w}{\rho}$$

and with the condition $\delta_v = h$ at $r = r_v$, we obtain

$$h = 0.0225\left(\frac{4}{7}\right)^{\frac{3}{4}}\left(\pi\frac{\nu r}{V}\right)^{\frac{1}{4}} r + \frac{18}{35}\frac{a^2}{r} \tag{4-65}$$

$$\Downarrow$$

$$h \approx 0.0197\left(\frac{\nu r}{V}\right)^{\frac{1}{4}} r + 0.5143\frac{a^2}{r} \tag{4-66}$$

Combining this with equation (4-64) it follows that

$$U = \frac{4}{7\pi}\frac{V}{0.0197\left(\frac{\nu r}{V}\right)^{\frac{1}{4}} r^2 + \frac{18}{35}a^2} \tag{4-67}$$

$$\Downarrow$$

$$U \approx 9.23\frac{V}{\left(\frac{\nu r}{V}\right)^{\frac{1}{4}} r^2 + 26.1a^2} \tag{4-68}$$

The corresponding equations found in the *original paper* have slightly different numerical constants:

- **The Region $0 < r < r_v$**

$$\delta_v \approx 0.246\left(\frac{\nu a}{V}\right)^{\frac{1}{5}} a^{\frac{1}{5}} r^{\frac{4}{5}} \tag{4-69}$$

$$r_v \approx 1.62\left(\frac{V}{\nu a}\right)^{\frac{1}{9}} a \tag{4-70}$$

- **The Region $r_v < r < r_j$**

$$h \approx 0.022\left(\frac{\nu r}{V}\right)^{\frac{1}{4}} r + 0.528\frac{a^2}{r} \tag{4-71}$$

$$U \approx 9.1\frac{V}{\left(\frac{\nu r}{V}\right)^{\frac{1}{4}} r^2 + 24a^2} \tag{4-72}$$

4.6 Bernoulli Model

4.6.1 Introduction

The model to be described here was *developed during this doctoral study* and is based on the much-celebrated Bernoulli's equation for fluid flow. No attention is given to the boundary layer and its development or to surface tension effects. It will be referred to as the *Bernoulli model.*

Between two points (1 and 2) along a single streamline the following relationship exists for a constant-density liquid without friction:

$$p_1 + \frac{\rho u_1^{\,2}}{2} + \rho g h_1 = p_2 + \frac{\rho u_2^{\,2}}{2} + \rho g h_2 \qquad (4\text{-}73)$$

p is the pressure, u the velocity of the streamline and h the vertical distance from a reference level (horizontal datum) to the streamline.

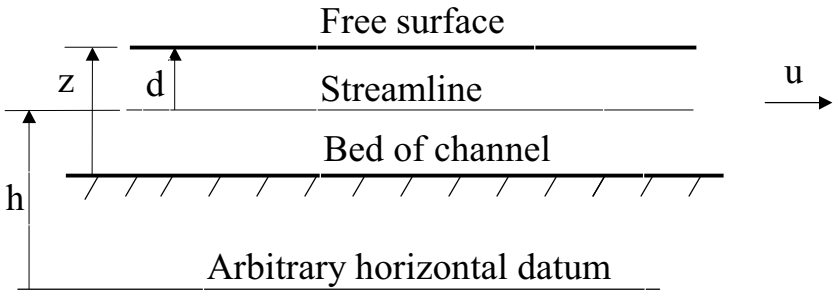

Figure 4.3Streamline and reference datum for an open channel flow.

If the external pressure is neglected and there is no appreciable curvature of the streamlines (not a rapidly varying flow), there is only a *hydrostatic* pressure variation over the cross-section of the flow. In other words, the pressure at any point in the stream is governed only by its depth, *d,* below the free surface. The pressure there will then be $\rho g d$. In our case the bed of

the channel (i.e. the top of the plate) is horizontal and it is natural to choose this as the horizontal datum. Consequently, Bernoulli's expression for a *surface* streamline in a frictionless fluid is simplified to

$$\frac{\rho {u_1}^2}{2} + \rho g z_1 = \frac{\rho {u_2}^2}{2} + \rho g z_2 ,$$

z is the vertical thickness of the fluid. ρgz represents the sum of the hydrostatic pressure, p, and the potential energy term, ρgh. If friction is taken into account:

$$\frac{\rho {u_1}^2}{2} + \rho g z_1 = \frac{\rho {u_2}^2}{2} + \rho g z_2 + w_f \qquad (4\text{-}74)$$

w_f [N/m^2] is the rate of work per unit volumetric flow rate of the fluid due to the frictional forces between positions *1* and *2*. If *the velocity is the same* for all the streamlines and the flow is irrotational, equation (4-74) is valid for the *entire* stream. Due to friction between the liquid and the channel walls and to a certain extent between the free surface and the air above (which is generally neglected), a uniform velocity distribution over the cross-section is never achieved in practice. Bends in the channel and irregularities in the boundaries will also have an effect.

As a result of this non-uniform velocity distribution, the kinetic energy of the fluid per unit weight, $u^2/2$, will have too low a value if calculated from the mean flow velocity, $\overline{u}$, that is the volume flow rate divided by the cross-sectional area of the flow.

Consider an element with area dA in the cross-section of the flow, see Figure 4.4. If it is small enough, the velocity variation over it can be neglected. The discharge through the element is udA and the mass flow rate ρudA. The kinetic energy $\frac{1}{2}(\rho udA)u^2$ passes through the element per

unit time and for the whole cross-section this becomes $\int\frac{1}{2}\rho u^3 dA$. The total mass flow rate is $\int\rho u dA$, so the kinetic energy per unit mass is then

$$\frac{\int\frac{1}{2}\rho u^3 dA}{\int\rho u\, dA} \tag{4-75}$$

For a fluid of constant density this reduces to

$$\frac{1}{2}\frac{\int u^3 dA}{\int u\, dA}$$

Only if u is constant over the entire cross-section is this equal to $\frac{\overline{u}^2}{2}$. To compensate for the error the *kinetic energy correction factor*, α, is introduced so that $\alpha\frac{\overline{u}^2}{2}$ is used in place of $\frac{\overline{u}^2}{2}$. α depends on the flow conditions, and can never be less than unity. It is 2 for a fully developed laminar flow in a circular pipe. Experiments in open channels show that α can vary from 1.03 to 1.6, with the higher values generally occurring in small channels.

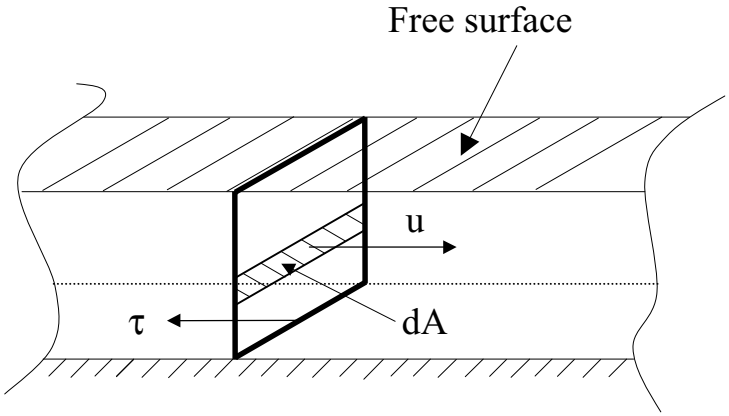

Figure 4.4 Cross-section of free surface flow.

Henri Darcy (1803-58) investigated the flow of water in pipes and suggested that the energy dissipated by friction resulted in a *loss of head*. This head loss, h_f, corresponds to a pressure difference, Δp_f, needed to force fluid through a pipe over the length l.

$$\Delta p_f = \rho g h_f$$

Darcy suggested

$$h_f = \frac{\Delta p}{\rho g} = \frac{4\lambda l}{d}\frac{\bar{u}^2}{2g}, \qquad (4\text{-}76)$$

where d is the pipe diameter and λ the (Darcy- or Moody-) *friction factor*, whose value depends on the roughness of the pipe and the Reynolds number of the flow. It is not uncommon to find the friction factor equal to 4 times that defined by equation (4-76). This is often known as Fanning's friction factor, $f = 4\lambda$, and will be used in this work. The same symbol is often used instead of λ, which can lead to confusion. The friction factor is defined in terms of the shear stress at the pipe wall, τ_w, as follows

$$\tau_w = \frac{1}{2}\rho \bar{u}^2 f$$

Equation (4-76) is also applicable to non-circular channels and channels only partially filled with liquid. In such cases the pipe diameter is replaced by a *hydraulic diameter*, d_h, defined as 4 times the cross-sectional area of the flow divided by the perimeter in contact with the fluid;

$$d_h = 4\frac{A}{S}$$

4.6.2 Laminar Flow

In the case of *laminar* flow between two large parallel plates it can be shown that

$$f = \frac{24}{Re} \tag{4-77}$$

This will be used for the axisymmetric plate flow of our interest. See Figure 4.5.

In the axisymmetric flow

$$d_h = 4\frac{A}{S} = 4\frac{2\pi r z}{2\pi r} = 4z \tag{4-78}$$

and the Reynolds number for the flow on the plate:

$$Re = \frac{\rho \bar{u} d_h}{\mu} = \frac{4\rho \bar{u} z}{\mu}$$

Furthermore

$$w_f = \frac{\tau A_1 \tilde{u}}{V}, \tag{4-79}$$

where A_1 is the area subject to friction forces. Symbols with the ~ embellishment are quantities that represent mean values for a control volume.

$$f = 6\frac{\mu}{\rho \tilde{u} \tilde{z}}.$$

With these definitions:

$$\tau_w = \frac{1}{2}\rho\tilde{u}^2 \frac{6\mu}{\rho\tilde{u}\,\tilde{z}} = \frac{3\mu\tilde{u}}{\tilde{z}}$$

This is coincidentally exactly the same as that calculated by Rahman, Hankey and Faghri (1991) who assumed a parabolic velocity profile across the thickness of the film.

Thus, for a flow between the radial positions r_1 and r_2 (see Figure 4.5):

$$w_f = \frac{3\mu\,\tilde{u}}{\tilde{z}} \frac{\pi(r_2^{\,2} - r_1^{\,2})\tilde{u}}{V} \tag{4-80}$$

In a closed channel w_f would be the equivalent of the pressure drop for the flow between the points 1 and 2. z_1 and z_2 are the thicknesses of the liquid film at r_1 and r_2, and $\tilde{z}$ and $\tilde{u}$ the mean thickness and mean velocity between the same two positions.

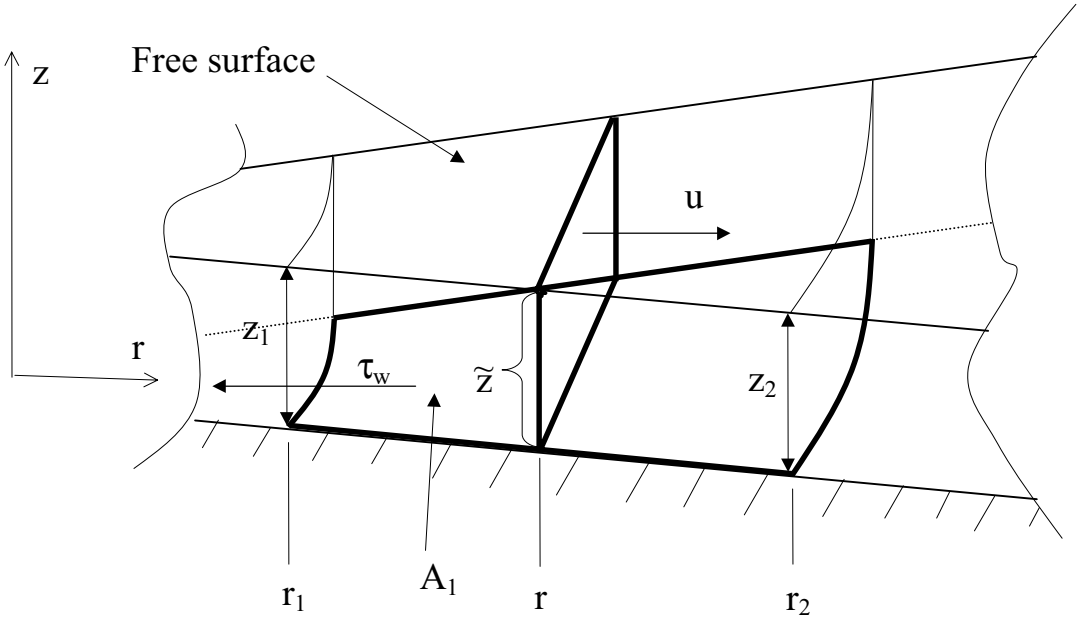

Figure 4.5 Element from axisymmetric flow

The simplest way of defining $\tilde{y}$ and $\tilde{u}$ is:

$$\tilde{u} = \frac{\bar{u}_2 + \bar{u}_1}{2}, \qquad \tilde{z} = \frac{z_2 + z_1}{2},$$

giving

$$w_f = \frac{3\mu\pi(\bar{u}_1 + \bar{u}_2)^2(r_2^{\,2} - r_1^{\,2})}{2(z_1 + z_2)V}. \tag{4-81}$$

If the flow is considered to be purely radial, continuity requires that

$$2\pi r_1 z_1 \bar{u}_1 = 2\pi r_2 z_2 \bar{u}_2$$
$$\Downarrow$$
$$\bar{u}_2 = \frac{r_1 z_1 \bar{u}_1}{r_2 z_2} \tag{4-82}$$

The Bernoulli equation now becomes

$$\alpha_1 \frac{\bar{u}_1^{\,2}}{2} + gz_1 = \alpha_2 \frac{V^2}{8\pi^2 r_2^{\,2} z_2^{\,2}} + gz_2 + \frac{3}{2}\nu\pi \frac{\left(\bar{u}_1 + \dfrac{V}{2\pi r_2 z_2}\right)^2 (r_2^{\,2} - r_1^{\,2})}{(z_1 + z_2)V} \tag{4-83}$$

This is a fourth order equation for z_2. α_1 and α_2 are the kinetic energy correction factors at positions 1 and 2.

This equation describes the flow from a random position (index 1) to another position (index 2). If the conditions at position 1 are known, the film thickness, z_2, at position 2 is the only unknown. If position 1 is taken

to be near the centre of the plate, then z_2 can be found at a chosen distance from this location. If this value is used as z_1, a new z_2 can be found further outwards, etc. In this way the film thickness and mean velocity can be calculated *stepwise* from the centre to the edge of the plate.

Exactly the same technique can be used for calculating the flow from the edge of the plate towards the centre. In this case the film thickness at the edge of the plate can be used as a boundary condition. This acts as a start value for z_2 and a z_1 value can be found at a specified distance (r_2 - r_1) upstream of this. The following equation, analogous to equation (4-83), pertains to this flow:

$$\alpha_1 \frac{V^2}{8\pi^2 r_1^2 z_1^2} + g z_1 = \alpha_2 \frac{\bar{u}_2^2}{2} + g z_2 + \frac{3}{2} \nu \pi \frac{\left(\frac{V}{2\pi r_1 z_1} + \bar{u}_2 \right)^2 (r_2^2 - r_1^2)}{(z_1 + z_2) V} \tag{4-84}$$

Equations (4-83) and (4-84) can be said to describe the flow *before* and *after* the hydraulic jump, but information about the jump itself and where it occurs is still wanting.

4.6.3 Jump Condition

Neglecting friction in the jump area, the *momentum balance* for the jump is generally the same as before - mentioned first in relation with Watson's theory:

$$\rho g 2\pi r_1 \frac{z_1^2}{2} - \rho g 2\pi r_2 \frac{z_2^2}{2} = \beta \rho V (\bar{u}_2 - \bar{u}_1) \tag{4-85}$$

The only new factor introduced is β, the *momentum correction factor*. In a flow with a constant-density fluid and a non-uniform velocity profile, the true rate of momentum flow perpendicular to the cross-section is not $\rho\ \overline{u}^2 A$ but $\beta\,\rho\ \overline{u}^2 A$. $\overline{u}$ is the mean velocity. For fully developed flow in a circular pipe, β can vary from 4/3 in a laminar flow to 1.02 for the turbulent case. In a given situation β is always less than α, the kinetic energy correction factor.

$$\beta = \frac{\int \rho u^2 dA}{\rho \overline{u}^2 A} \tag{4-86}$$

Gerhart et al. (1992) report the width or length of the to be as in Figure 4.6.

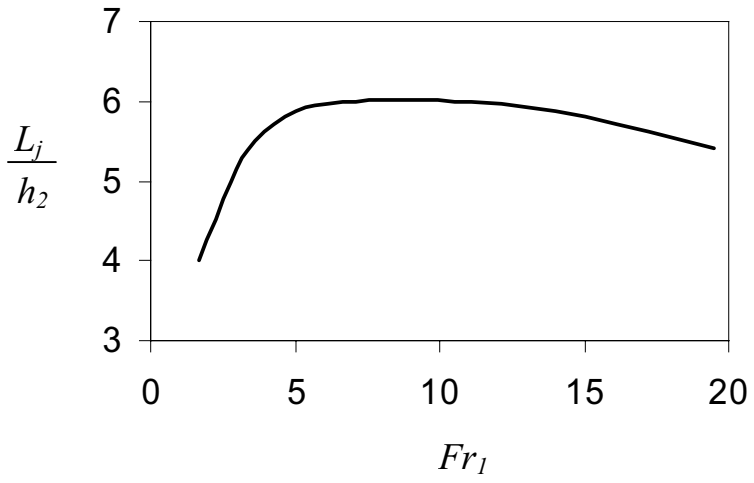

Figure 4.6 Experimentally determined length of hydraulic jump, L_j, as function of Froude number at jump. h_2 is film thickness after jump.

For the flows encountered in this study, we would from Figure 4.6 expect L_j to be about 5 to 6 times the film thickness after the jump. Compared with the experiments, this seemed to overestimate the length of the jump and it was decided to use $L_j = 2h_2$. It was in any case later confirmed that the length of the jump has little influence on the computed jump position.

Equation (4-85) now takes the form

$$2\pi(r_2 - 2z_2)g\frac{z_1^2}{2} - 2\pi r_2 g\frac{z_2^2}{2} = \beta V(\bar{u}_2 - \bar{u}_1) \qquad (4\text{-}87)$$

This equation shows the relation between the thickness of the film before (z_1) and after (z_2) the jump and the radial location of the jump, r_2. Equations (4-83) and (4-84) describe the film thicknesses before and after the jump, but we still do not know the exact position of the jump, i.e. where equation (4-83) takes over for equation (4-84) in describing the flow.

These equations are solved independently of each other. Subsequently one starts marching inwards from the edge of the plate, and z_1 is solved from equation (4-87) for every position used in equation (4-84) and compared to the film thickness at that position obtained from equation (4-83). Where these two values coincide we have a jump.

Although the equations derived here have several solutions, only one solution to each equation is physically suitable.

4.6.4 Turbulent Flow

The turbulent flow model is very similar to the laminar one, the only difference being the expression for the shear stress. A great amount of theoretical and practical work is done on flows in closed circular ducts. Results from this work can be used for different geometric shapes. The hydraulic diameter of these shapes can simply be used in place of a circular pipe diameter. However, this is not very accurate for laminar flows, but for turbulent flows it works remarkably well, being accurate to ±10%. It is therefore decided that this approach will be used in the turbulent Bernoulli model. One of the simplest (and earliest) attempts to correlate data on turbulent friction factors in smooth pipes is one by Blasius, namely:

$$f = \frac{0.0791}{Re^{\frac{1}{4}}} \tag{4-88}$$

This is reasonably accurate for Reynolds numbers between 4000 and 10^5, i.e. shortly after turbulence sets in. Equation (4-79) now takes the form:

$$w_f = \frac{\rho \tilde{u}^2}{2} \frac{0.0791}{\left(\frac{4\tilde{u}\,\tilde{z}}{\nu}\right)^{\frac{1}{4}}} \frac{\pi(r_2{}^2 - r_1{}^2)\tilde{u}}{V} \tag{4-89}$$

and with

$$\tilde{u}^2 = \alpha \frac{\bar{u}_1{}^2 + \bar{u}_2{}^2}{2} \tag{4-90}$$

we get:

$$\alpha_1 \frac{\bar{u}_1{}^2}{2} + g\,z_1 = \alpha_2 \frac{V^2}{8\pi^2 r_2{}^2 z_2{}^2} + g\,z_2 +$$

$$0.0791\alpha\pi^{\frac{5}{4}}\left(\frac{(r_1 + r_2)\nu}{4}\right)^{\frac{1}{4}} \frac{\left(\bar{u}_1{}^2 + \left(\frac{V}{2\pi r_2 z_2}\right)^2\right)\left(\bar{u}_1 + \frac{V}{2\pi r_2 z_2}\right)(r_2{}^2 - r_1{}^2)}{4V^{\frac{5}{4}}} \tag{4-91}$$

A general expression for the turbulent shear stress on a smooth wall can be approximated as follows:

$$\tau = \rho \frac{\widetilde{u}^2}{400} \tag{4-92}$$

This corresponds to a friction factor of 0.005.

Equation (4-89) now takes the form:

$$w_f = \frac{\rho}{400} \frac{\widetilde{u}^2 \pi ({r_2}^2 - {r_1}^2)\widetilde{u}}{V}$$

and with equation (4-90) we get

$$\alpha_1 \frac{{\overline{u}_1}^2}{2} + g\, z_1 = \alpha_2 \frac{V^2}{8\pi^2 {r_2}^2 {z_2}^2} + g\, z_2 + \frac{\alpha\pi}{1600} \frac{\left({\overline{u}_1}^2 + \left(\frac{V}{2\pi r_2 z_2} \right)^2 \right) \left(\overline{u}_1 + \frac{V}{2\pi r_2 z_2} \right) ({r_2}^2 - {r_1}^2)}{V} \tag{4-93}$$

Likewise, from the plate edge and inwards:

$$\alpha_1 \frac{V^2}{8\pi^2 {r_1}^2 {z_1}^2} + g\, z_1 = \alpha_2 \frac{{\overline{u}_2}^2}{2} + g\, z_2 + \frac{\alpha\pi}{1600} \frac{\left(\left(\frac{V}{2\pi r_1 z_1} \right)^2 + {\overline{u}_2}^2 \right) \left(\frac{V}{2\pi r_1 z_1} + \overline{u}_2 \right) ({r_2}^2 - {r_1}^2)}{V} \tag{4-94}$$

The method for estimating the jump position is the *same* as that for laminar flows.

4.6.5 Starting Conditions

In order to traverse the plate from the centre and outwards, an initial condition for the film thickness and velocity near the centre must be set. Near the stagnation point the impinging jet at some point starts to turn into a radial flow. One suggestion is to specify an angle, ϕ, for the flow at one point, say at a distance from the centre equal to the radius of the jet. The radial component of the velocity here ($u\cos\phi$) is then used to calculate the corresponding film thickness, z_i. See Figure 4.7.

$$z_i = \frac{V}{2\pi r_i u \cos\phi}$$

u is based on the nozzle outlet velocity and its acceleration due to gravity before the jet strikes the plate. If the calculated z_i is larger than the distance between the nozzle and the plate, this latter value is used for z_i.

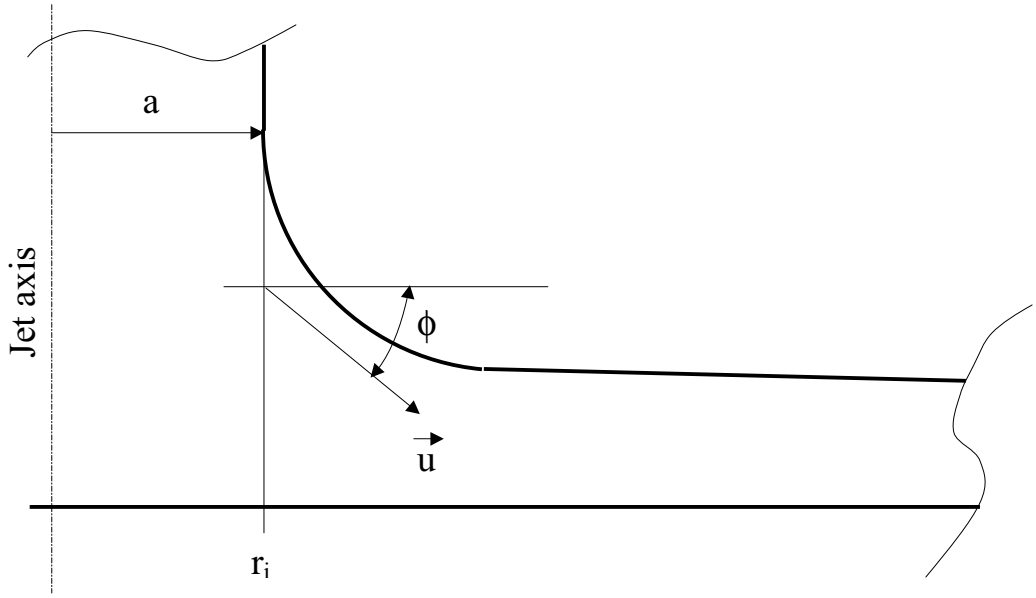

Figure 4.7 Sketch of initial conditions for Bernoulli calculations. r_i is position for initial conditions, a is jet radius, ϕ is angle describing the velocity direction.

4.6.6 Film Thickness at Plate Edge

The problem that now must be dealt with, is how to obtain a value for h_R, the film thickness at the edge of the disk. This is an essential boundary condition for the solution of the problem. Three theories for estimating this value have been found in the literature:

i) Buyevich and Ustinov, equation (4-48). For a water flows of $4.25 \cdot 10^{-5}$ and $2.29 \cdot 10^{-4}$ m^3/s on a plate with radius 0.315 m, the thicknesses are computed to 0.4 and 1.2 mm, respectively.

ii) The second theory states that the flow must pass through critical conditions near the outfall (edge of plate). It is found that this occurs a little upstream of the brink and that the film thickness at the brink itself is about 71% of this critical value. With reference to equation (4-1), with $w_a = 2\pi R$, we compute the edge thicknesses to be 0.4 and 1.1 mm for the cases mentioned above. This theory yields answers very similar to **i)**.

iii) If a laminar flow is assumed and viscous dissipation of energy is neglected as the liquid turns over the edge, there will be no change in velocity or film thickness as the liquid "turns the corner". The flow down the outer face of the plate will be very similar to a laminar film falling along a vertical surface. The thickness of such a flow, h_V, is thought to equal h_R , and according to Bird et al. (1960):

$$h_R = h_V = \left(\frac{3}{2} \frac{\nu V}{\pi g R} \right)^{\frac{1}{3}} \tag{4-95}$$

For the same cases as in **i)** and **ii)**, the edge thicknesses with this formula equate to 0.2 and 0.4 mm.

These predictions for the film thickness at the plate edge are too small (close to an order of magnitude) compared with experimental studies. They are in fact even smaller than the thickness of stagnant water on a plate, which is believed to be the absolute minimum thickness of a water film flow (measured to about 2.5 mm). In the relatively thin liquid films encountered in this work, it is not improbable that *surface tension* may affect the film thickness. If a drop of liquid is laid to rest on a plane, horizontal surface, mechanical equilibrium is obtained by balancing the pressure inside, p_i, and outside p_o, of the drop with the surface tension between the liquid and the surrounding atmosphere (in our case air). The following equation describes this relationship:

$$\Delta p = p_i - p_o = \sigma \kappa \tag{4-96}$$

σ is the surface tension and κ the *curvature* of the drop. The radius of curvature, R, is $1/\kappa$. The mathematical definition of κ for a curve $y = f(x)$ is as follows:

$$\kappa = \frac{1}{R} = \frac{\left|\frac{d^2 y}{dx^2}\right|}{\left[1 + \left(\frac{d^2 y}{dx^2}\right)^2\right]^{\frac{3}{2}}} \tag{4-97}$$

A 3-dimensional surface has two radii of curvature, i.e. κ is $1/r_1 + 1/r_2$. For a sphere of radius r, κ is $2/r$. The smaller the sphere, the greater its curvature. Figure 4.8 shows a stagnant liquid film on a horizontal plane. In a coordinate system with ξ as the variable, $f(\xi)$ is the function describing its surface and h the maximum equilibrium thickness of the film, appearing at some distance from the "edge" of the film. The volume of the fluid is not important, as long as it is large enough to allow the fluid to spread out

evenly. It is believed that a large volume will spread out further than a smaller one, but adjust itself to the same equilibrium height.

θ is the contact angle (*wetting angle*) the fluid makes with the body it rests on. It is determined by the particular liquid-solid combination. If θ is less than 90°, the liquid is *wetting*; if greater than 90°, it is *nonwetting.* In the latter case, drops of liquid will tend to move about easily on the surface. *Complete* wetting occurs at an angle of zero degrees.

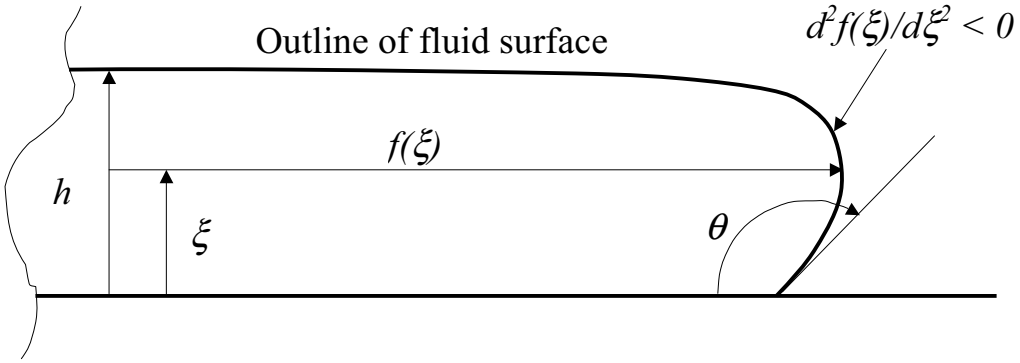

Figure 4.8 Sketch of stagnant liquid film on a horizontal surface.

In this case it can be deduced that $\frac{d^2 f(\xi)}{d\xi^2}$ is always negative, making it legitimate to write equation (4-97) as:

$$\kappa = \frac{1}{R} = \frac{-\frac{d^2 f}{d\xi^2}}{\left[1+\left(\frac{d^2 f}{d\xi^2}\right)^2\right]^{\frac{3}{2}}} = -\frac{d}{d\xi}\left[\frac{\frac{df}{d\xi}}{\sqrt{1+\left(\frac{df}{d\xi}\right)^2}}\right], \quad f = f(\xi) \qquad (4\text{-}98)$$

The boundary conditions pertaining to $f(\xi)$ are:

1): $f'(\xi) \rightarrow -cot(\theta)$ when $\xi \rightarrow 0$ and

2): $f'(\xi) \rightarrow -\infty$ when $\xi \rightarrow h$

We have $p_i = \rho g(h - \xi) + p_o$, and combining with equation (4-96) results in:

$$\frac{\rho g}{\sigma}(h-\xi) = -\frac{d}{d\xi}\left[\frac{\frac{df}{d\xi}}{\sqrt{1+\left(\frac{df}{d\xi}\right)^2}}\right] \tag{4-99}$$

This can easily be integrated once, and from boundary condition 1), we evaluate the constant of integration to $-cos\theta$.

Boundary condition 2) yields:

$$\frac{\rho g}{\sigma}(h^2 - \frac{1}{2}h^2) = 1 - cos\theta$$

$$\Downarrow$$

$$h = \sqrt{\frac{2\sigma}{\rho g}(1-\cos\theta)} \tag{4-100}$$

The above expression can be interpreted as the minimum thickness a stable liquid film will conform to when let to rest on a horizontal plane. The idea is now to add this thickness to one of the other theoretical thicknesses referred to previously, for example, equation (4-95), and thereby obtain a new total film thickness for a *tranquil* flow at the plate edge. Of course the mechanics of a stagnant and moving fluid are not the same, but anyhow a credible suggestion is:

$$h_R = \left(\frac{3}{2} \frac{\nu V}{\pi g R} \right)^{\frac{1}{3}} + \sqrt{\frac{2\sigma}{\rho g}(1 - cos\,\theta)} \qquad (4\text{-}101)$$

Wetting angles

To make use of equation (4-101) the surface tension and the wetting angle of the fluid/surface combination in question must be known. The surface tension for both water and tin are fairly well documented, but references on these fluids' wetting angles on different materials are sparse.

Various commercially available optical equipment can be used to measure contact angles, but none was available for this study. However, it is fairly easy to indirectly obtain a contact angle by measuring the thickness of a stagnant liquid on a plane surface and add this directly to equation (4-95). The thickness of water on a glass plate was in this way found to be about 2.5-3 mm - indicating a contact angle of around 50°.

As mentioned later in Chapter 6, tin's contact angle on stainless steel is evaluated to 155 to ±10°. Using the average value of 155°, the calculated stagnant film thickness from equation (4-100) is 5.9 mm, which agrees very well with the experimental observations.

If the wetting angle is varied between its two extremes (0 and 180^o), the stagnant thickness from equation (4-100) will vary from 0 to 5.6 mm for water and from 0 to 5.7 mm for tin. The close relation between these values is due to the fact that the material dependent term, $\frac{\sigma}{\rho}$, is nearly the same for water and tin.

4.6.7 Model Testing

In both models the kinetic energy correction factor is kept constant throughout the equations describing the flow before and after the jump. It would however seem natural to experiment with different (constant)

factors before and after the jump, since the flows in these regions are dissimilar in character.

4.6.7.1 Laminar Flow

The velocity angle at the plate centre was varied in steps of 15° - from 15° to 75° (from the horizontal). A large angle produces a low radial velocity and subsequently a large initial film thickness. Except for the differences here, the angles seem to have negligible influence on the surface profile from the impingement region up to the jump. The profile after the jump is of course completely independent of this. Angles above 45° markedly stretch the curves upwards, but only at the start. 45° is chosen as the general initial velocity angle. Figure 4.9 shows an example of results obtained by varying this angle.

Increasing β, the momentum correction factor, moves the jump outwards. Using 1.3 as a maximum value, it moves about 10%, i.e. from 44 mm to 49 mm for the lowest flow rate. The maximum distance moved is about 10 mm, for the highest flow rate. The effect is most noticeable with small flow rates.

The jump position is also moved outwards if the energy correction factor before the jump is increased. At the same time the film thickness in this region is reduced. Setting the factor to 2 can move the jump up to 35% (equivalent to 10 mm and 55 mm for the lowest and highest flow rates). Manipulation of this factor after the jump has little or no influence on the jump position.

The length of the jump has only a slight effect on the jump position. A longer jump tends to shift the start of the jump outwards.

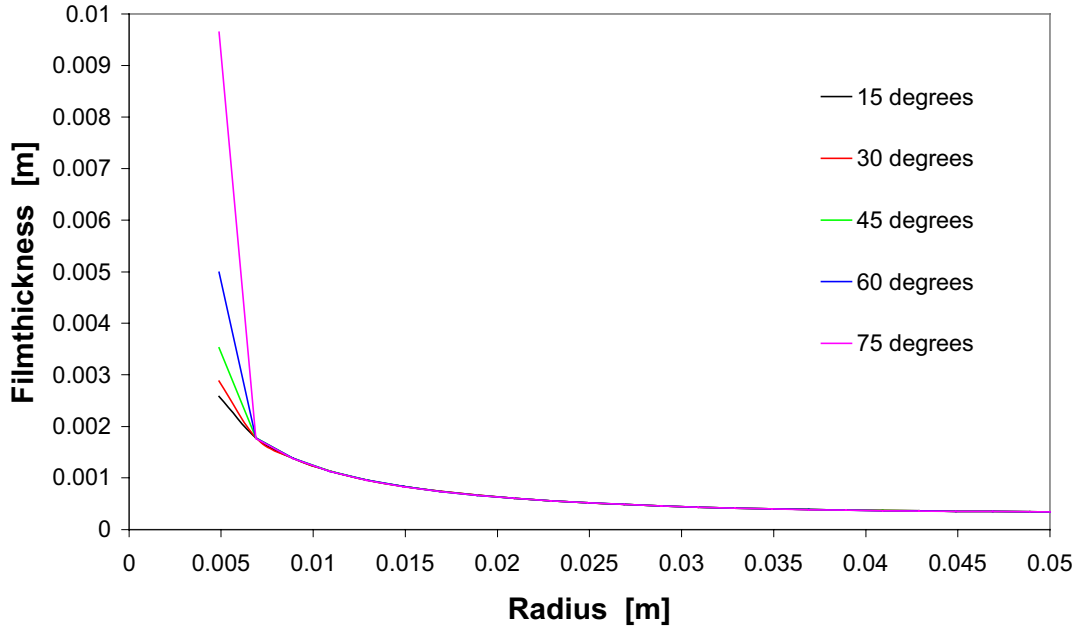

Figure 4.9 Surface profiles of water flow near impingement point due to variation of initial velocity. V=1.55·10^{-4} m^3/s, 10 mm nozzle, free fall height =10 mm, laminar calculation, plate radius=0.21 m.

The most uncertain element in the Bernoulli model is probably the friction term. Reducing the friction reduces the film thickness before the jump and shifts it outwards, as one might naturally assume. Halving the original shear stress before the jump can move it up to 25% (10 mm and 45 mm for the lowest and highest flow rates). The effect of varying this parameter is also greatest before the jump. Altering the shear stress after the jump has little influence on its position, but changes only the appearance of the profile in this region. The profiles before and after the jump are as a rule turned upwards with increasing shear stress. The reason for this is that friction slows down the flow, and in order to conserve the flow, the thickness must increase. A point worth noting is that the model calculates a flow downstream of the jump that can either increase or decrease in thickness towards the specified height at the plate edge, depending on the magnitude of the shear stress. For low shear stresses the height increases slightly from the jump to the edge. As the friction factor is made larger, the film profile first grows in thickness, reaches a maximum and becomes thinner as it reaches the plate edge. After a certain value of the friction factor, the maximum point vanishes, and the thickness is found to decrease

steadily from the jump to the edge. This is probably due to the fact that in order to overcome these relatively large friction forces, a height difference is needed to maintain the flow. For lower shear stress values, the thrust or momentum of the flow prior to the jump is sufficient to drive the flow outwards.

As a whole the flow is assumed to be radial in character, i.e. any possible vertical velocity components have been neglected. A test was performed where the velocity was given a direction of 30° from horizontality. This shifted the surface profile a little upwards and the jump position a little inwards, but to no great extent. Figure 4.10 shows the effect of altering the friction factor and velocity direction. The effects are the same for other flow rates.

Radial step sizes of 1 to 5 mm were tested. No difference in the surface profiles were noted. The only deviation is that the position of the jump could change a little, but only within the limits of the largest step. For example if a jump position is calculated with a step of 5 mm, this position would shift less than 5 mm when calculated with a step of 1mm. In other words the “resolution” in the calculation is increased with smaller steps.

The manner in which one factor influences the flow seems to be stable regardless of the other factors’ value.

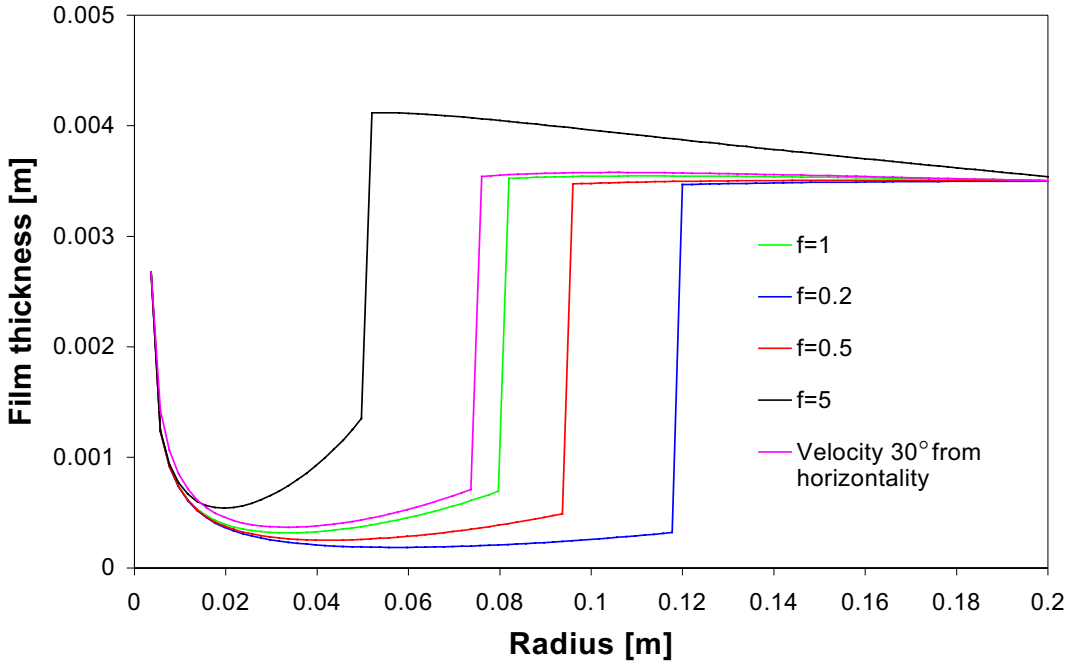

Figure 4.10 Effect of varying friction factor and velocity angle on surface profile. $V=1.10\cdot10^{-4}$ m^3/s, 8 mm nozzle, free fall height=52 mm, laminar flow, plate radius=0.21 m. *f* is friction factor relative to original value of *24/Re*.

4.6.7.2 Turbulent Flow

As mentioned earlier, the only difference between the laminar and turbulent model is the expression for the shear stress. The discussion in the preceding section applies here as well, and no further comments are found necessary.

However, one point worth mentioning is that for low flow rates, the turbulent friction against the plate is lower than for laminar flow. This is also the case if turbulent friction factors are used in place of the appropriate laminar ones (in laminar flows) in for example pipes. This can either indicate that the criterion used for the onset of turbulence or the expressions for the respective friction factors are inaccurate.

4.7 Discussion of Analytical Flow Models

When comparing results from the various analytical models, the jet impingement velocity used is identical and as described under the Bernoulli model; i.e. the acceleration of the jet during its fall is taken into account. In the experiments the position of the hydraulic jump increased with increasing plate to nozzle spacings. Generally the models do not seem to reflect this feature particularly well, and are subsequently considered most suitable for small nozzle to plate spacings. The theoretical predictions agree well with the experiments regarding the minimal influence plate size seems to have on the jump position. Table 4-1 to 4-6 show the experimental jump positions for water along with the results from the theoretical models. The Bernoulli model was used with a radial step size of 2 mm. The experiments themselves are described in Chapter 6. Analogous results for tin are presented at the end of Chapter 6.

The film thickness at the edge of the plate is as mentioned a critical parameter for the jump position. The theories of Watson and Alekseenko et al. require that this value is by some means *known and stays constant* all the way in to the jump. At the same time no consideration is taken regarding plate size and its possible influence on the jump position. The theory of Buyevich and Ustinov and the Bernoulli model are *superior in this manner*. Both these models, however, predict only slight variations in the film thickness after the jump - *agreeing well with practical observations*.

The edge thicknesses according to equations (4-1), (4-48) and (4-95) are substantially lower than what was experimentally observed. The correlation developed under the Bernoulli model is considered a useful improvement.

Since no variations in the post-jump flow thickness were discerned in the experiments, the thickness at the plate edge was consistently set to 3.5 mm for water and 5.5 mm for tin.

At low flow rates and fall heights the laminar Watson and Buyevich/Ustinov models seem to be the most correct in predicting the jump position. The laminar Bernoulli model underestimates this position

and is at the most 10% off. As the flow rates increase, the two former models overestimate the jump position, rendering the Bernoulli model as the most accurate. The jump radius determined by the critical velocity condition (equation (4-1)) can be combined with all theoretical flow models. It is computed by equating the mean flow velocity before the jump with the critical velocity in the flow after the jump. This implies that a wave cannot propagate further upsrteam than the jump. As an example this jump position was computed based on the theory of Alekseenko et al. and is certainly the largest and most inaccurate. In addition the method does not in any way account for varying conditions after the jump (which certainly affects its position), since it contains no force balance for the jump. See Table 4-1 to Table 4-6 for jump positions.

In the flow conditions considered here, the laminar Bernoulli model always displays the smallest jump radii. By manipulating the momentum- and energy correction factors, there would be no problem computing the exact experimentally acquired jump radius for each case. However, this seems inconsistent and is of dubious benefit for other flows where a jump position is not experimentally established. An alternative is to find a flow-rate dependent correlation, but this is left unattempted in this study. All in all, correction factors of *unity* are the simplest to use, and as an average for the experiments carried out here, seem to work quite well. This is also the usual practice elsewhere.

With water and the flow rates studied in this work the turbulent Bernoulli model predicts a jump position outside the laminar alternative. The observed jump positions lie in between. With tin the turbulent model predicts jump positions inside laminar calculations.

It can also be noted that the surface profiles and jump positions according to the laminar Watson and Buyevich/Ustinov models are the two that coincide most with each other. The model of Alekseenko et al. yields the smallest film thickness before the jump in laminar conditions. The Bernoulli model's thickness in this region lies initially below Watson and Buyevich/Ustinov's, but after a period increases and rises above these. When comparing all profiles before the jump, the most noticeable feature observed is the increase in thickness of the laminar Bernoulli model as the jump is approached. This means that the Bernoulli flow loses its

momentum quickest and therefore produces an earlier jump than the other models.

An attribute common to all models is that the film thickness after the impingement point first decreases, reaches a *minimum* and increases towards the jump. It may seem peculiar that the thickness can increase when the flow is spreading radially. This is because the friction effect after the minimum point is greater than the spreading effect. The shear stress (friction) against the plate slows down the flow and increases its thickness. Depending on inlet and outlet conditions it is possible that not all flows will display such a minimum in film thickness.

In the experiments carried out, only two flow rates can be characterised as turbulent according to Watson's theory. Figure 4.12 shows there is little difference in both the development of the surface profiles and jump positions for the three turbulent models and Buyevich and Ustinov's laminar model. The laminar Bernoulli model distinguishes itself with the smallest jump radius, but not further off than the others are from the observed jump position. It is therefore proposed that the laminar Bernoulli model can be used in laminar conditions and the turbulent alternative in turbulent conditions.

In Buyevich/Ustinov's and Watson's work the width of the jump is as earlier noted ignored. If allowance for this were made, there would be additional friction forces at the base of the fluid in the force balance for the jump, and the hydrostatic pressure outside the jump would have a greater area on which to work (also affecting this force balance). If these effects were taken into account, the theoretical jump positions in both models would be drawn inwards. Also, all models assume a straight line for the surface profile through the jump and that no air is entrained in the jump (which would affect the pressure distribution).

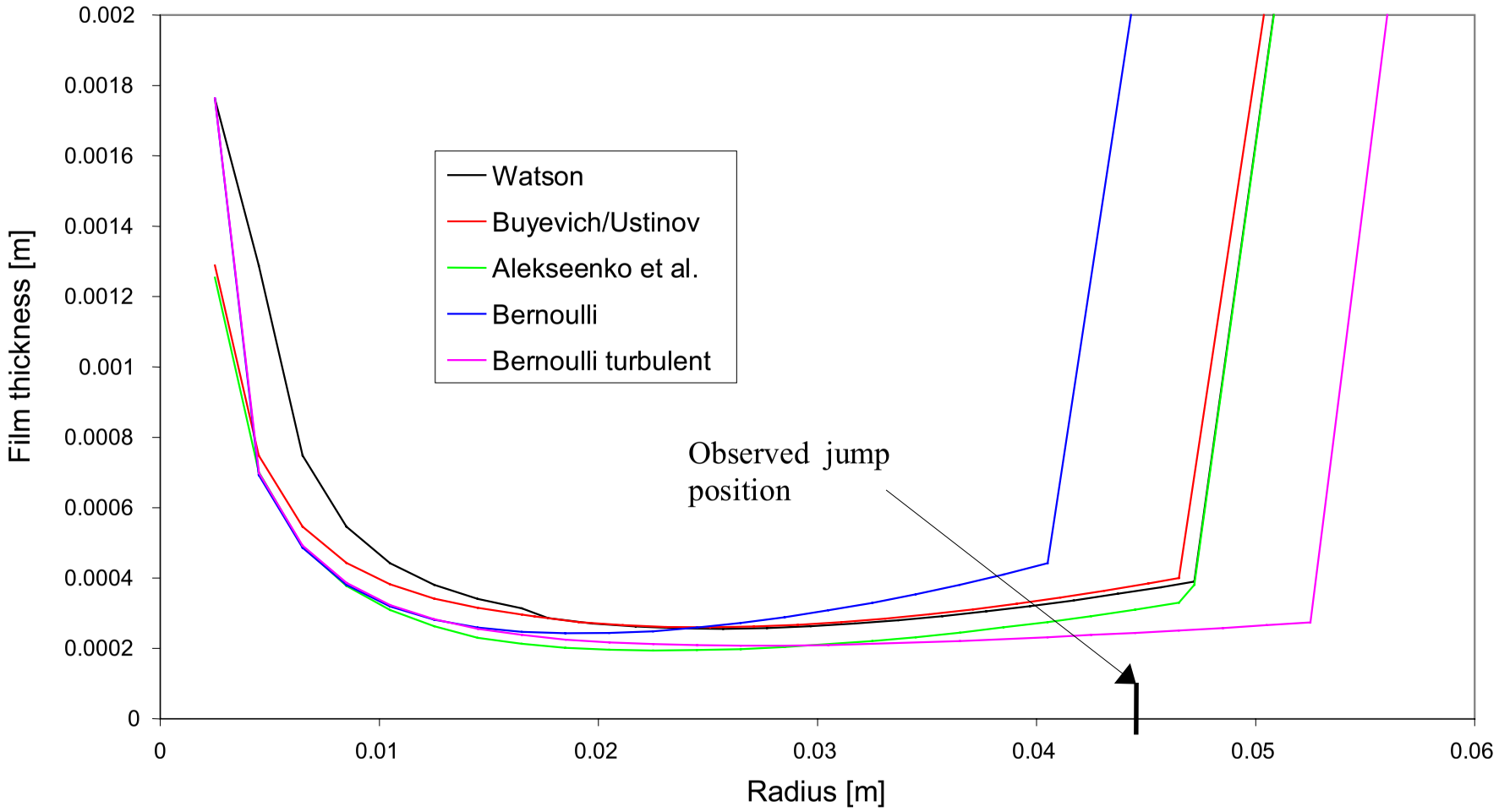

Figure 4.11 Analytical surface profiles for water. 5 mm nozzle, flow rate $4.25 \cdot 10^{-5}$ m^3/s, *Re* in nozzle 11,333, 3 mm free fall height.

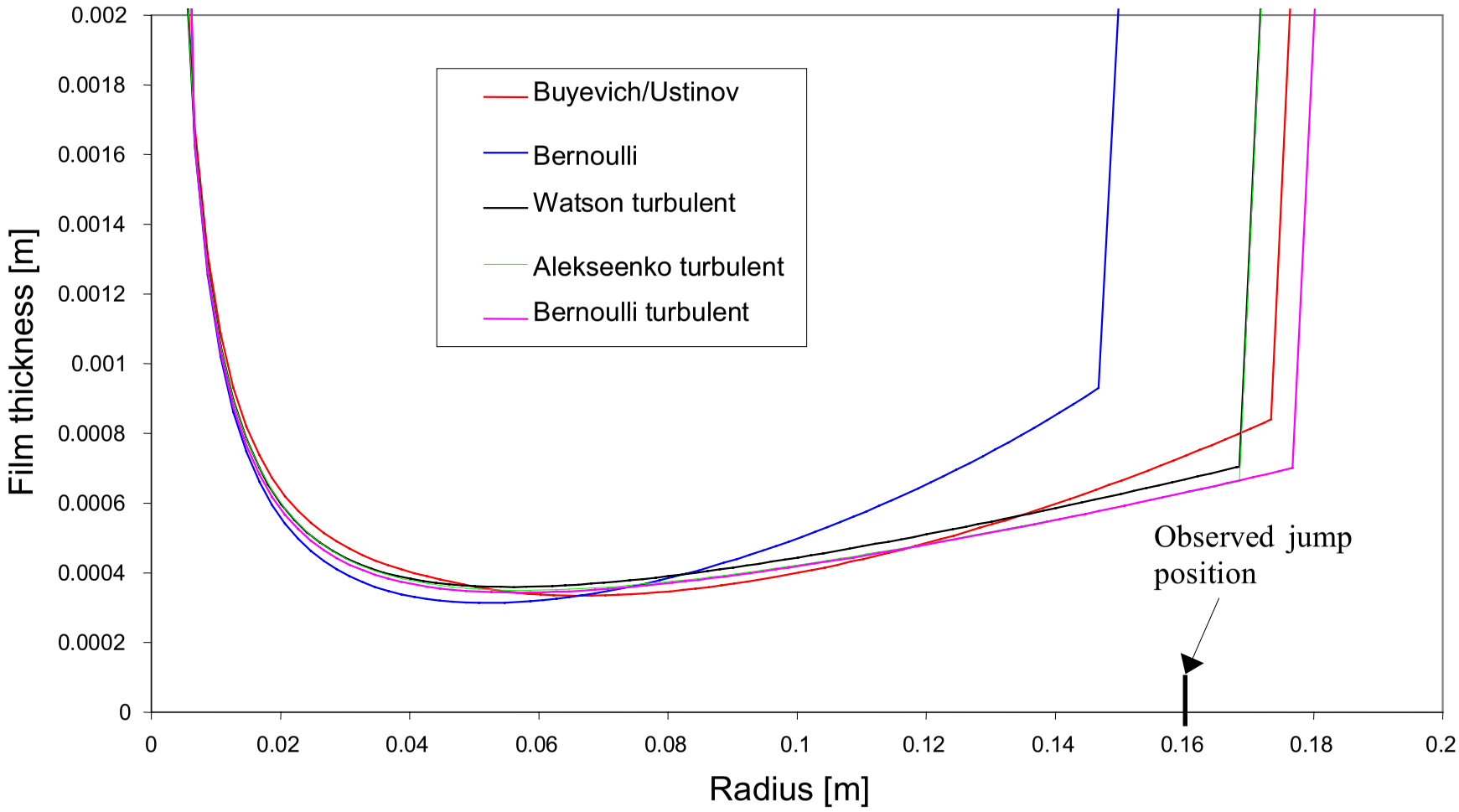

Figure 4.12 Analytical surface profiles for water. 10 mm nozzle, flow rate $42.42 \cdot 10^{-4}$ m^3/s, *Re* in nozzle 32267, 158 mm free fall height.

Radius of plate	Free fall height	Observed jump position	Watson	Critical velocity method *	Buyevich and Ustinov	Bernoulli	Fr at jump start (Bernoulli model)
0.105	0.003	0.045	0.047	0.065	0.047	0.040	5.74
0.210	0.003	0.045	0.047	0.065	0.047	0.040	5.74
0.315	0.003	0.045	0.047	0.065	0.047	0.040	5.74
0.105	0.040	0.047-0.048	0.047	0.065	0.047	0.040	5.88
0.210	0.040	0.047	0.047	0.065	0.047	0.040	5.88
0.315	0.040	0.049	0.047	0.065	0.047	0.040	5.88
0.105	0.090	0.046-0.047	0.048	0.065	0.047	0.040	6.05
0.210	0.090	0.047	0.048	0.065	0.047	0.042	6.05
0.315	0.090	0.04-0.05	0.048	0.065	0.046	0.040	6.05
0.105	0.140	0.046-0.048	0.048	0.065	0.046	0.040	6.19
0.210	0.140	0.048-0.049	0.048	0.065	0.046	0.042	6.19
0.315	0.140	0.051-0.052	0.048	0.065	0.046	0.040	6.19

Table 4-1 Jump positions for 5 mm nozzle. Flow rate $4.25 \cdot 10^{-5}$ m^3/s. *Re* in nozzle = 7220. All measurements are in meters. * based on the theory of Alekseenko et al.

Radius of plate	Free fall height	Observed jump position	Watson	Critical velocity method *	Buyevich and Ustinov	Bernoulli	Fr at jump start (Bernoulli model)
0.105	0.003	0.063-0.065	0.066	0.086	0.064	0.056	4.69
0.210	0.003	0.063-0.065	0.066	0.086	0.065	0.056	4.69
0.315	0.003	0.063-0.065	0.066	0.086	0.065	0.055	5.34
0.105	0.040	0.065	0.066	0.086	0.065	0.056	4.73
0.210	0.040	0.065	0.066	0.086	0.065	0.056	4.73
0.315	0.040	0.065	0.066	0.086	0.065	0.054	5.39
0.105	0.090	0.067	0.066	0.086	0.065	0.056	4.78
0.210	0.090	0.067	0.066	0.086	0.065	0.056	4.78
0.315	0.090	0.067	0.066	0.086	0.065	0.054	5.44
0.105	0.140	0.070	0.066	0.086	0.065	0.056	4.82
0.210	0.140	0.070	0.066	0.086	0.065	0.056	4.82
0.315	0.140	0.070	0.066	0.086	0.066	0.054	5.49

Table 4-2 Jump positions for 5 mm nozzle. Flow rate $6.38 \cdot 10^{-5}$ m^3/s. *Re* in nozzle = 10835. All measurements are in meters. * based on the theory of Alekseenko et al.

Radius of plate	Free fall height	Observed jump position	Watson	Critical velocity method *	Buyevich and Ustinov	Bernoulli	Fr at jump start (Bernoulli model)
0.105	0.003	0.087-0.089	0.09	-	0.088	0.078	3.75
0.210	0.003	0.087-0.089	0.09	0.115	0.089	0.076	4.08
0.315	0.003	0.087-0.089	0.09	0.115	0.089	0.076	4.12
0.105	0.040	0.090	0.091	-	0.089	0.078	3.86
0.210	0.040	0.09-0.091	0.091	0.115	0.09	0.076	4.23
0.315	0.040	0.092	0.091	0.115	0.088	0.076	4.23
0.105	0.090	0.092	0.091	-	0.089	0.078	3.96
0.210	0.090	0.090	0.091	0.116	0.089	0.078	3.96
0.315	0.090	0.095	0.091	0.116	0.089	0.078	3.96
0.105	0.140	0.095	0.091	-	0.089	0.078	4.04
0.210	0.140	0.093-0.095	0.091	0.116	0.089	0.077	4.04
0.315	0.140	0.097-0.099	0.091	0.116	0.090	0.077	4.04

Table 4-3 Jump positions for 8 mm nozzle. Flow rate $1.01 \cdot 10^{-4}$ m^3/s. *Re* in nozzle = 10720. All measurements are in meters. * based on the theory of Alekseenko et al.

Radius of plate	Free fall height	Observed jump position	Watson	Critical velocity method *	Buyevich and Ustinov	Bernoulli	Fr at jump start (Bernoulli model)
0.105	0.006	-	-	-	-	-	
0.210	0.006	0.112-0.114	0.126/0.125	0.177	0.124	0.106/0.130	3.49/4.75
0.315	0.014	0.113-0.115	0.126/0.125	0.177	0.125	0.106/0.132	3.49/4.57
0.105	0.050	-	-	-	-	-	
0.210	0.050	0.117-0.119	0.127/0.125	0.177	0.124	0.106/0.130	3.52/4.79
0.315	0.050	0.120-0.122	0.127/0.125	0.177	0.125	0.106/0.132	3.52/4.60
0.105	0.100	-	-	-	-	-	
0.210	0.100	0.119	0.127/0.125	0.177	0.125	0.106/0.132	3.55/4.64
0.315	0.100	0.122-0.123	0.127/0.125	0.177	0.125	0.106/0.132	3.55/4.64
0.105	0.140	-	-	-	-	-	
0.210	0.140	0.120	0.127/0.125	0.177	0.125	0.106/0.132	3.58/4.68
0.315	0.140	0.124-0.126	0.127/0.125	0.177	0.126	0.106/0.132	3.58/4.68

Table 4-4 Jump positions for 8 mm nozzle. Flow rate $1.55 \cdot 10^{-4}$ m^3/s. *Re* in nozzle = 16455. Where two values separated by slashes are given, the first is based on a *laminar* model and the second on a *turbulent* model. All measurements are in meters. * based on the theory of Alekseenko et al.

Radius of plate	Free fall height	Observed jump position	Watson	Critical velocity method *	Buyevich and Ustinov	Bernoulli	Fr at jump start (Bernoulli model)
0.105	0.008	-	-	-	-	-	-
0.210	0.008	0.115-0.117	0.130	0.160	0.127	0.111	3.18
0.315	0.008	0.120	0.130	0.160	0.128	0.109	3.39
0.105	0.060	-	-	-	-	-	
0.210	0.060	0.117-0.118	0.131	0.160	0.128	0.111	3.26
0.315	0.060	0.117-0.118	0.131	0.160	0.129	0.109	3.48
0.105	0.110	-	-	-	-	-	
0.210	0.110	0.123	0.131	0.161	0.129	0.111	3.33
0.315	0.110	0.123	0.131	0.161	0.128	0.109	3.56
0.105	0.150	-	-	-	-	-	
0.210	0.150	0.125	0.132	0.161	0.128	0.110	3.39
0.315	0.150	0.125	0.132	0.161	0.129	0.108	3.63

Table 4-5 Jump positions for 10 mm nozzle. Flow rate $1.65 \cdot 10^{-4}$ m^3/s. *Re* in nozzle 14015. All measurements are in meters. * based on the theory of Alekseenko et al.

Radius of plate	Free fall height	Observed jump position	Watson	Critical velocity method *	Buyevich and Ustinov	Bernoulli	Fr at jump start (Bernoulli model)
0.105	0.008	-	-	-	-	-	
0.210	0.008	0.145	0.175/0.168	-	0.172	0.147/0.175	2.88/3.77
0.315	0.008	0.150	0.175/0.168	0.226	0.173	0.145/0.177	3.03/3.66
0.105	0.060	-	-	-	-	-	
0.210	0.060	0.156-0.157	0.176/0.168	-	0.173	0.147/0.177	2.91/3.70
0.315	0.060	0.156-0.157	0.176/0.168	0.227	0.174	0.145/0.177	3.07/3.70
0.105	0.110	-	-	-	-	-	
0.210	0.110	0.155	0.176/0.168	-	0.173	0.147/0.177	2.93/3.72
0.315	0.110	0.156-0.158	0.176/0.168	0.227	0.172	0.145/0.177	3.09/3.73
0.105	0.150	-	-	-	-	-	
0.210	0.150	0.160	0.176/0.169	-	0.173	0.147/0.177	2.95/3.75
0.315	0.150	0.160	0.176/0.169	0.227	0.172	0.145/0.177	3.11/3.75

Table 4-6 Jump positions for 10 mm nozzle. Flow rate $2.42 \cdot 10^{-4}$ m^3/s. *Re* in nozzle = 20550. Where two values separated by slashes are given, the first is based on a *laminar* model and the second on a *turbulent* model. All measurements are in meters. * based on the theory of Alekseenko et al.

5. Analytical Heat Transfer Model

5.1 Introduction

Studies regarding heat transfer in radially spreading flows due to an impinging jet have been published before. These findings, however, relate to fluids with Prandtl numbers in the region of unity and higher, and are thus *not* applicable to liquid metals. In this chapter a *new theory* for such flows with $Pr << 1$ is proposed.

The high thermal conductivity of liquid metals account for their very low Prandtl number, since the viscosity and specific heat do not differ greatly from other common fluids. The high thermal conductivity is also the basis for the unusual heat transfer characteristics of liquid metals. Molecular conduction is the dominant heat transfer mechanism, even in fully turbulent flows. The effect of eddy diffusivity becomes smaller as Pr approaches zero. As a result of this, heat transfer in liquid metals has many characteristics of a laminar flow.

This means that the effective conductivity, $\rho c_p(\alpha+\varepsilon)\approx\rho c_p\alpha$, is fairly constant throughout a thermal boundary layer, even though the effective viscosity may vary considerably. This again leads to only slight variations in the temperature gradient throughout this boundary layer.

As in laminar flows, the Nusselt number for a liquid metal is often low, but due to the high molecular thermal conductivity, heat transfer coefficients tend to be high. This is a main reason why such fluids are of great interest as heat transfer media, often where large energy quantities must be removed from a relatively small space (e.g. nuclear reactors). In casting, heat flow is of course in the opposite direction, i.e. *from* the liquid metal. The greatest disadvantage of using liquid metals is the hazards involved in case of equipment failure.

With such high heat transfer coefficients involved, surface contamination and wetting problems can easily and noticeably affect the heat transfer. These facts have reportedly led to *difficulties* and *large uncertainties* in experiments. As is fairly commonly known, theoretical expressions do not

always match the values found in experiments. It is not improbable that such disagreements are augmented with liquid metals. Theory in this work, of course, applies to clean systems with ideal wetting of the surfaces involved.

5.2 Analysis

Only *laminar* conditions are studied.

A jet impinging on a horizontal surface leading to a radially spreading flow incorporating a hydraulic jump, is for clarity divided into *seven regions* for studying *heat transfer*, see Figure 5.1. After the jump δ_v and δ_T are envisioned to develop in two different manners. In the first, they develop from the value they have immediately before the jump. In the second, the jump is thought to disturb the flow so much that the boundary layers are completely broken down and must be built up from scratch.

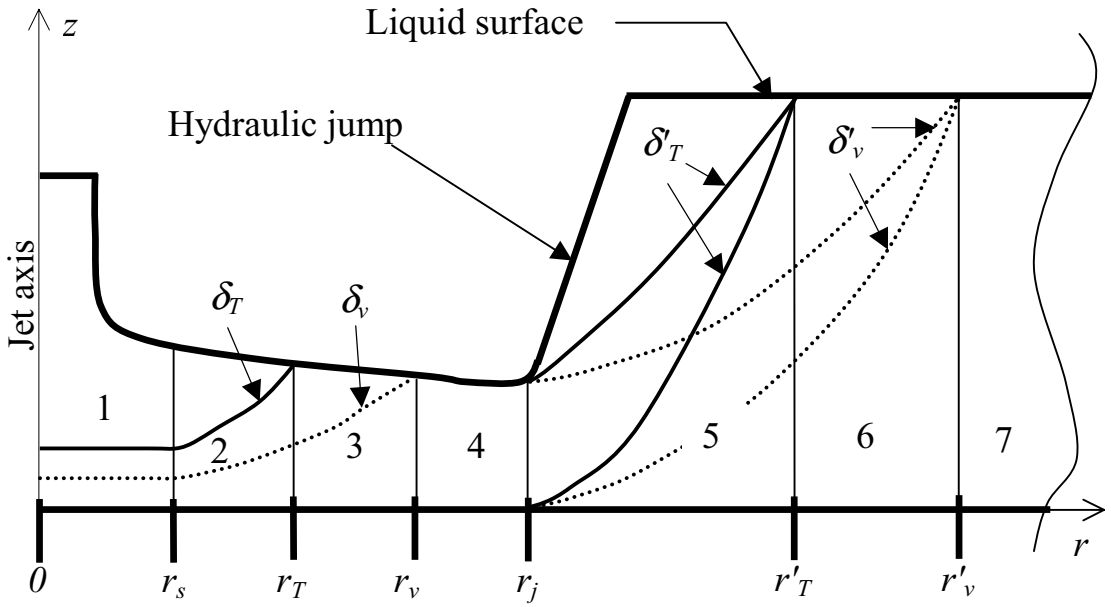

Figure 5.1 Regions for theoretical heat transfer analysis. The boundary layers are envisioned to develop in two different ways after the jump. Symbols marked ' refer to conditions after jump.

The seven regions will not be treated in numerical order.

5.2.1 Region 2, $r_s < r < r_T$

In a radial system, the integral energy equation may be written as:

$$\frac{1}{r}\frac{\partial}{\partial r} r \int_0^{\delta_T} (T_\infty - T) u dz = -\alpha \left.\frac{\partial T}{\partial z}\right|_{z=0} \tag{5-1}$$

T is the fluid temperature and a function of z. T_w is the wall temperature. As in Chapter 2 we will assume a third order polynomial for the radial velocity and the temperature inside their respective boundary layers:

$$u = U_\infty \left[\frac{3}{2}\frac{z}{\delta_v} - \frac{1}{2}\left(\frac{z}{\delta_v}\right)^3 \right] \tag{5-2}$$

$$\frac{T - T_w}{T_\infty - T_w} = \frac{3}{2}\frac{z}{\delta_T} - \frac{1}{2}\left(\frac{z}{\delta_T}\right)^3 \tag{5-3}$$

When the thermal boundary layer is thicker than the velocity boundary layer, the integral must be split in two parts, for it must be remembered that the radial velocity is defined by equation (5-2) for $z < \delta_v$, and is U_∞ from δ_v up to the surface (until the velocity boundary layer reaches the surface). For the case $Pr < 1$, equation (5-1) becomes

$$\frac{1}{r}\frac{\partial}{\partial r}\left[r\int_0^{\delta_v}(T_\infty - T_w)\left(1-\frac{3}{2}\frac{z}{\delta_T}+\frac{1}{2}\left(\frac{z}{\delta_T}\right)^3\right)U_\infty\left(\frac{3}{2}\frac{y}{\delta_v}-\frac{1}{2}\left(\frac{z}{\delta_v}\right)^3\right)dz \right.$$

$$\left. + r\int_{\delta_v}^{\delta_T}(T_\infty - T_w)\left(1-\frac{3}{2}\frac{z}{\delta_T}+\frac{1}{2}\left(\frac{z}{\delta_T}\right)^3\right)U_\infty dz\right] = -\alpha\left.\frac{dT}{dz}\right|_{z=0}$$

$$\Downarrow$$

$$\frac{1}{r}\frac{\partial}{\partial r}\left[rU_\infty(T_\infty - T_w)\delta_T\left(\frac{3}{8}-\frac{3}{8}\frac{\delta_T}{\delta_v}+\frac{3}{20}\left(\frac{\delta_T}{\delta_v}\right)^2-\frac{3}{280}\left(\frac{\delta_T}{\delta_v}\right)^4\right)\right]$$

$$= \alpha\frac{3}{2}\frac{(T_\infty - T_w)}{\delta_T}$$

Introducing the relationship $\varsigma = \dfrac{\delta_T}{\delta_v}$ (constant, regarded independent of r), we arrive at

$$\left(1-\varsigma+\frac{2}{5}\varsigma^2-\frac{1}{35}\varsigma^4\right)\frac{1}{r}\frac{\partial}{\partial r}(r\delta_T) = 4\frac{\alpha}{U_\infty\delta_T} \tag{5-4}$$

If δ_v is known and both the thermal and velocity boundary layers are assumed to be of zero thickness at the plate centre, we can proceed with the differentiation of equation (5-4). So, with the results from Chapter 4, equation (4–42) for δ_v gives:

$$\delta_T = \varsigma\delta_v = \varsigma\sqrt{\frac{280}{39}\frac{\nu r}{U_\infty}},$$

and

$$1-\varsigma+\frac{2}{5}\varsigma^2-\frac{1}{35}\varsigma^4 = \frac{13}{35}\frac{1}{\mathrm{Pr}}\frac{1}{\varsigma^2} \tag{5-5}$$

This is *not* the same as given by Buyevich and Ustinov, where ς^2 is written as the numerator on the right hand side of the equation. That is concluded to be a *printing error*.

It is easy to see that equation (5-5) has the root $\varsigma = 1$ precisely at $Pr = 1$. *In this work a correlation for the ς - Pr relationship for small Prandtl numbers is sought. Mathematical analysis demonstrates that the general solution for ς can be correlated by*

$$\varsigma = 0.728\,\mathrm{Pr}^{-0.48} \qquad (Pr<<1) \qquad (5\text{-}6)$$

The maximum deviation from the exact solution is less than 8% for $0.00015 < Pr < 0.1$ and less than 2% for $0.00015 < Pr < 0.02$. Alternatively, several, piecewise more accurate correlations could be composed for various Prandtl number intervals.

Remembering that

$$q = -k\left.\frac{\partial T}{\partial z}\right|_{z=0} = \frac{3}{2}k\frac{(T_\infty - T_w)}{\delta_T} = h_c(T_\infty - T_w)$$

we find

$$h_c = \frac{3}{2}\frac{k}{\varsigma}\sqrt{\frac{39}{280}\frac{U_\infty}{\nu r}} \qquad (5\text{-}7)$$

Utilising equation (5-6), the following *correlation for small Pr is presented*:

$$Nu_r = \frac{h_c r}{k} = \frac{3}{2}\sqrt{\frac{39}{280}}\sqrt{Re_r}\,1.374\,Pr^{0.48} \qquad (5\text{-}8)$$

$$\Downarrow$$

$$Nu_r \approx 0.769\,\mathrm{Re}_r^{0.5}\,\mathrm{Pr}^{0.48},$$

with $Re_r = \dfrac{U_\infty r}{\nu}$.

The radial position at which the thermal boundary layer reaches the surface of the film, r_T, is found with equation (4–40), using $h = \delta_T$. The result is

$$r_T = \left(\frac{39}{280}\frac{U_\infty}{\nu}\right)^{\frac{1}{3}}\left(\frac{4a^2}{8\varsigma - 3}\right)^{\frac{2}{3}} = \left(\frac{5}{8\varsigma - 3}\right)^{\frac{2}{3}} r_v \qquad (5\text{-}9)$$

In Buyevich and Ustinov's article 8ς is replaced by $8/\varsigma$. This must be another printing error.

For the free stream over a flat plate, we saw in Chapter 2 that ς was proportional to $Pr^{-0.5}$, compared to $Pr^{-0.48}$ for the film flow. These are very close and it is therefore tempting to try out a correlation like equation (5-6) with $Pr^{-0.5}$. The result obtained is

$$\varsigma = 0.618\,\mathrm{Pr}^{-0.5} \quad (Pr<<1) \qquad (5\text{-}10)$$

For $0.00015 < Pr < 0.02$ the maximum deviation from the exact result is less than 9%. For $0.00015 < Pr < 0.005$ it is about 4%, i.e. the exponent -0.5 seems to be more accurate for lower Prandtl numbers.

An other method of solving equation (5-4) is to *assume* a value for ς. Brdlik and Savin (1965) followed this scheme and used the relation $\varsigma = Pr^{-\frac{1}{3}}$ for *all* values of *Pr*. This is identical to equation (2–26), which was the result for $Pr = 1$. For $Pr < 1$, we just found a relationship where ζ is proportional to $Pr^{-\frac{1}{2}}$. A more prudent solution is therefore to use *this*

proportionality factor instead. Following that thought, we obtain an ordinary differential equation for δ_T, with the solution

$$\delta_T = 2\sqrt{\frac{2}{3}\frac{\nu}{U_\infty}\frac{r}{\mathrm{Pr}\left(1-\sqrt{\frac{35}{13}\mathrm{Pr}}+\frac{14}{13}\mathrm{Pr}-\frac{35}{169}\mathrm{Pr}^2\right)}}+C \qquad (5\text{-}11)$$

If we again state that $\delta_T = 0$ at $r = 0$, then $C = 0$.

Proceeding as before, we find

$$Nu_r = \sqrt{\frac{27}{32}}\sqrt{\left(1-\sqrt{\frac{35}{13}\mathrm{Pr}}+\frac{14}{13}\mathrm{Pr}-\frac{35}{169}\mathrm{Pr}^2\right)\mathrm{Pr}\,\mathrm{Re}_r} \qquad (5\text{-}12)$$

or $$Nu_r = 0.919\sqrt{\left(1-1.641\sqrt{\mathrm{Pr}}+1.077\,\mathrm{Pr}-0.207\,\mathrm{Pr}^2\right)\mathrm{Pr}\,\mathrm{Re}_r}$$

$$(Pr \ll 1)$$

In order to achieve these results, we have assumed that the velocity outside the velocity boundary layer is constant and equal to U_∞ up to the point r_v. This is an assumption made in many theoretical studies. Experiments, however, have shown that this not always holds true. Measurements (Stevens and Webb, 1993) indicate that the surface velocity can be up to 25% higher than the jet velocity. This is a maximum and occurs around the position $r = 2.5a$. Thereafter it decreases, but is reported generally to be higher than the jet velocity.

The value to use for U_∞ is open to discussion. Brdlik and Savin (1965) used a value for U_∞ equal to twice the jet velocity. In this work U_∞ is for simplicity set equal to the jet velocity. This can easily be modified later by multiplying the free-stream velocity everywhere with a factor (for example based on experiments) larger than unity.

For comparison, Brdlik and Savin's result will be presented, namely

$$Nu_r = 0.82\sqrt{\left(2.5 - 2.5\,\mathrm{Pr}^{\frac{1}{3}} + \mathrm{Pr}^{\frac{2}{3}}\right)\mathrm{Pr}\,\mathrm{Re}_r} \qquad (5\text{-}13)$$

It is worth mentioning that higher order polynomials naturally can be used for the assumed velocity and temperature profiles. Additional boundary conditions must then be declared in order to correctly evaluate the numerical constants involved. The method is as mentioned *approximate* and it is of limited benefit to use polynomials of much higher order.

5.2.2 Region 1, $0 < r < r_s$

It is not strictly true that the velocity and thermal boundary layers are zero in the stagnation point (axis of impinging jet), but in reality do have a finite thickness also here. This means that the constants of integration in equation (5-11) and (4–41) are not zero. A detailed solution to the flow problem in this region (Shach, 1934) yields

$$\delta_{vs} = 2.985\sqrt{\frac{\nu a}{U_\infty}} \qquad (5\text{-}14)$$

It can be noted that this expression is independent of radial location, and is valid up to a certain radial position, which we may call r_s. This position can for example be determined by requiring that the velocity boundary layers inside and outside the stagnation region must be equal there;

$$\delta_{vs} = \delta_v \quad \text{at} \quad r = r_s$$

A second condition ensuring a smooth transition between the two expressions is

$$\frac{d\delta_{vs}}{dr} = \frac{d\delta_v}{dr} \quad \text{at } r = r_s$$

This gives us the following two equations for the unknowns, r_s and C (using equation (4–41) for the velocity boundary layer):

$$\sqrt{\frac{280}{39}\frac{\nu r_s}{U_\infty} + \frac{C}{r_s{}^2}} = 2.985\sqrt{\frac{\nu a}{U_\infty}}$$

and

$$\frac{280}{39}\frac{\nu}{U_\infty} - \frac{2C}{r_s{}^3} = 0$$

with the solution

$$r_s = 2.985^2\,\frac{13}{140}a, \;\; C = \frac{2.985^6}{3}\left(\frac{13}{140}\right)^2\frac{\nu}{U_\infty}a^3, \qquad \text{(5-15)}$$

or

$$r_s = 0.83a, \quad C = 2.03\frac{\nu}{U_\infty}a^3$$

$$\Downarrow$$

$$\delta_v = \sqrt{\frac{\nu}{U_\infty}\left(\frac{280}{39}r + 2.03\frac{a^3}{r^2}\right)} \qquad \text{(5-16)}$$

Wang et al. (1989) have used the same line of action, but with a fourth order polynomial for the velocity and temperature profiles. Their result is

$$\delta_v = \sqrt{\frac{\nu}{U_\infty}\left(\frac{420}{37}r + 0.81\frac{a^3}{r^2}\right)}, \qquad r_s = 0.52a \qquad (5\text{-}17)$$

It might be remembered that in Chapter 4 (equation (4–50)), Buyevich and Ustinov derived another expression for r_s:

$$r_s = 1.288a$$

This was achieved by equating the velocities inside and outside the stagnation region at r_s and is regarded as less exact.

For $r = 3a$, the velocity boundary layer described by equation (4–42), with the integration constant = 0, is about 0.5% smaller than equation (5-16). So for $r > 3a$, equation (4–42) can be used with negligible error.

The stagnation region energy equation may in dimensionless form be written as

$$\xi\frac{\partial\phi}{\partial\eta}\frac{\partial\theta}{\partial\xi} - 2\phi\frac{\partial\theta}{\partial\eta} = \frac{1}{\mathrm{Pr}}\left(\frac{\partial^2\theta}{\partial\xi^2} + \frac{1}{\xi}\frac{\partial\theta}{\partial\xi} + \frac{\partial^2\theta}{\partial\eta^2}\right) \qquad (5\text{-}18)$$

θ, ξ and η are dimensionless variables defined as

$$\theta = \frac{T - T_\infty}{T_w - T_\infty} \qquad \text{(temperature)}$$

$$\xi = \frac{r}{\sqrt{\frac{\nu a}{0.44U_\infty}}} \qquad (r\text{-coordinate})$$

$$\eta = \frac{z}{\sqrt{\frac{\nu a}{0.44U_\infty}}} \qquad (z\text{-coordinate})$$

The conditions equation (5-18) must satisfy are:

1) $\dfrac{\partial\theta}{\partial\xi}=0$ at $\xi=0$
2) $\theta=\theta_s(\eta)$ at $\xi=\xi_s$
3) $\theta=\theta_w(\xi)$ at $\eta=0$
4) $\theta=0$ at $\eta=\infty$

The indexes *s* and *w* stand for values at the edge of the stagnation region and at the plate surface (wall).

The radial and vertical velocities in the stagnation region are (Schlichting, 1979 and Shach, 1934):

$$u=\sqrt{0.44\frac{\nu U_\infty}{a}}\,\xi\,\phi'(\eta), \qquad w=-2\sqrt{0.44\frac{\nu U_\infty}{a}}\,\xi\,\phi(\eta) \qquad (5\text{-}19)$$

where $\phi(\eta)$ is a transformation function defined by the non-linear ordinary differential equation

$$\phi'''+2\phi\phi''-\phi'^2+1=0,$$

with the boundary conditions

$$\phi(0)=\phi'(0)=0, \quad \phi'(\infty)=1$$

The energy equation (5-18) can be simplified if radial convection and/or radial conduction is neglected. It is nevertheless a cumbersome and time-consuming task to obtain the correct temperature distribution in the fluid (and subsequent Nusselt correlation). This is done by Wang et al. (1989) for radially varying heat flux from the plate to the fluid and for a radially varying prescribed plate temperature. These results are not particularly user-friendly and will not be reported here.

In a casting process it is assumed that the temperature of the mould surface (against the liquid metal) does not vary steeply radially outwards from the

impinging metal jet. If the temperature or heat flux in fact is assumed to be constant, a manageable expression for the local Nusselt number can be obtained:

$$Nu = \frac{0.9381\sqrt{Re_j}}{\int_0^{\infty} exp\left[-2\,Pr\int_0^{q}\phi\,dq\right]dq}, \tag{5-20}$$

which, by the way, is identical to the result of Sibulkin (1952).

The Nusselt number is here defined as

$$Nu = \frac{2ah_c}{k} \tag{5-21}$$

In deriving equation (5-20), radial conduction was neglected. This may seem risky, knowing that liquid metals usually conduct heat quite well. However, the error resulting from neglecting the conduction term, can be shown to be small for mild radial variations in wall heat flux and temperature.

Equation (5-20) can be solved numerically. In this study, this was carried out, but in addition a *more explicit or practical Nu-Pr correlation of a more familiar form for small Prandtl numbers, was sought.* The correlation derived is:

$$Nu = 0.904\,Re_j^{0.5}\,Pr^{0.48}, \tag{5-22}$$

$$h_c = \frac{Nu\,k}{2a} \qquad 0 < r < r_s$$

This expression is found to deviate from the "exact" solution by maximum 2.5% for $0.001 < Pr < 0.05$. It is noted that the result is independent of radial location.

5.2.3 Region 4, $r_v < r < r_j$

Here we can define a third order temperature distribution slightly different from before:

$$T = a + bz + cz^2 + dz^3$$

with the boundary conditions

1) $T = T_w$ at $z = 0$

2), 3) $\frac{\partial T}{\partial z} = \frac{\partial^2 T}{\partial z^2} = 0$ at z = h

4) $k\frac{\partial T}{\partial z} = q$ at $z = 0$

This gives:

$$T = T_w + \frac{q}{k}(z - \frac{z^2}{h} + \frac{z^3}{3h^2}), \quad 0 < z < h$$

The *mixed mean temperature* of the film, T_m, is defined as

$$T_m = \frac{\int_0^h c_{pm}\rho u_r T dA}{c_{pm}\int_0^h \rho u_r dA} = \frac{\int_0^h u_r T dz}{\int_0^h u_r dz}$$ (with constant material properties)

With our temperature profile we get

$$T_m = T_w + \frac{31}{105}\frac{qh}{k} \qquad (5\text{-}23)$$

By defining the convective heat transfer coefficient, h_c, as $h_c = \frac{q}{T_m - T_w}$,

we get

$$h_c = \frac{105}{31}\frac{k}{h} \tag{5-24}$$

and the local Nusselt number, defined in the terms of the local fluid film thickness

$$Nu = \frac{h_c h}{k} = \frac{105}{31} \approx 3.39 \tag{5-25}$$

In the two preceding sections the Nusselt numbers utilised the jet radius (via the jet Reynolds number) as the characteristic length, whereas now the film thickness is used. The jet radius could be used in other regions of the flow, but this would make the correlations much more complicated. Near the stagnation point there is no film flow, so a film thickness there has no sensible meaning.

If no heat is lost from the surface of the fluid, a method for estimating the temperature evolution in the fluid can be presented. An energy balance for the fluid film may be written as

$$\rho c_p V dT_m = -h_c (T_m - T_w) 2\pi r dr \tag{5-26}$$

$$\Downarrow$$

$$\frac{dT_m}{T_m - T_w} = -\frac{2\pi\alpha}{V}\frac{105}{31}\frac{rdr}{\frac{175}{136}\frac{\nu}{U_\infty}\frac{r^2}{a^2} + 0.685\frac{a^2}{r}} \tag{5-27}$$

If T_w is assumed constant we can estimate the difference between the mixed mean temperature at two different points (1 and 2) by directly integrating equation (5-27):

$$\frac{T_{m2}-T_w}{T_{m1}-T_w}=\left[\frac{\frac{175}{136}r_2{}^3+0.685\frac{U_\infty}{\nu}a^4}{\frac{175}{136}r_1{}^3+0.685\frac{U_\infty}{\nu}a^4}\right]^{-\frac{2}{3}\frac{105}{31}\frac{136}{175}\frac{1}{Pr}} \tag{5-28}$$

or, converting to decimal format

$$\frac{T_{m2}-T_w}{T_{m1}-T_w}=-\left[\frac{r_2{}^3+0.532\frac{U_\infty}{\nu}a^4}{r_1{}^3+0.532\frac{U_\infty}{\nu}a^4}\right]^{\frac{1.755}{\mathrm{Pr}}}$$

In a real casting process, T_w is most probably not constant, but the temperature of a cooling medium underneath the mould, for example ambient air or water in a water-cooled system, can without loss of accuracy, be assumed constant. An *overall heat transfer coefficient*, U, may then be defined as

$$\frac{1}{U}=\frac{1}{h_{cm}}+\frac{1}{h_{ca}}+\frac{t_m}{k_m}$$

h_{cm} and h_{ca} are the heat transfer coefficients from the liquid metal to the mould and from the mould to cooling medium. h_{ca} can for the appropriate conditions be found in heat transfer handbooks. t_m and k_m is the thickness and thermal conductivity of the mould. The cooling medium holds a temperature T_a. In this way, the energy balance in place of equation (5-26) becomes

$$\rho c_p V dT_m = -U(T_m - T_a)2\pi r\, dr \tag{5-29}$$

and we can present another expression for the estimated temperature evolution:

$$\frac{dT_m}{T_m - T_a} = -\frac{2\pi}{V\rho c_p} \frac{rdr}{\frac{31}{105}\frac{1}{k}\left(\frac{175}{136}\frac{\nu}{U_\infty}\frac{r^2}{a^2} + 0.685\frac{a^2}{r}\right) + \frac{1}{h_{ca}} + \frac{t_m}{k_m}}$$

This expression cannot be integrated directly, but can easily be solved numerically on a computer. A simplified and more approximate solution can be obtained by the method of partial fractions. For the sake of simplicity we write

$$A = \frac{2\pi}{\rho c_p V}$$

$$B = \frac{31}{105}\frac{175}{136}\frac{\nu}{U_\infty k a^2}$$

$$C = 0.685\frac{31}{105}\frac{a^2}{k}$$

$$D = \frac{1}{h_{ca}} + \frac{t_m}{k_m}$$

and get

$$\frac{dT_m}{T_m - T_a} = -A\frac{rdr}{Br^2 + \frac{C}{r} + D} \qquad (5\text{-}30)$$

$$\Downarrow$$

$$\ln\frac{T_{m2}-T_a}{T_{m1}-T_a}=-\left[\frac{A}{3B}\ln\left(Br^3+Dr+C\right)+\frac{AD}{18B^2\gamma^2+6BD}\ln\frac{r^2+\gamma r+\gamma^2+\dfrac{D}{B}}{(r-\gamma)^2}\right.$$

$$\left.-\frac{AD\gamma}{3B\gamma^2+D}\frac{1}{\sqrt{3B^2\gamma^2+4BD}}\arctan\left(\frac{2Br+B\gamma}{\sqrt{3B^2\gamma^2+4BD}}\right)\right]_{r1}^{r2}$$

(5-31)

γ is a (real) root to the equation $B\gamma^3+D\gamma+C=0$ - a basis for splitting equation (5-30). For small values of γ(which is right and proper for liquid metals), it can be deduced that if $\frac{BC^2}{D^3}<<1$, then γ can, without much error, be approximated by $\gamma\approx-\frac{C}{D}$. This condition was tested for a wide variety of the parameters involved, and it can be concluded that it holds true in practical casting techniques. Equation (5-31) can therefore be approximated by

$$\ln\frac{T_{m2}-T_a}{T_{m1}-T}=-\frac{A}{3B}\left[\ln\left(Br^3+Dr+C\right)\right.$$

$$+\frac{1}{2}\ln\frac{BD^2r^2-BCDr+D^3}{B(Dr+C)^2}$$

$$\left.+\frac{3}{2}\frac{BC}{D\sqrt{BD}}\arctan\left(\frac{2BDr-BC}{2D\sqrt{BD}}\right)\right]_{r1}^{r2}$$

(5-32)

5.2.4 Region 3, $r_T < r < r_v$

For the region $r_T < r < r_v$ the same procedure can be used, but the task is complicated somewhat because the expression for T_m must be split in two, due to the fact that the velocity boundary layer is still developing. We have

$$T_m = \frac{\int_0^{\delta_v} uTdz + \int_{\delta_v}^{h} U_\infty Tdz}{\int_0^{\delta_v} u\,dz + \int_{\delta_v}^{h} U_\infty dz} \tag{5-33}$$

giving

$$h_c = \frac{k(168h^6\text{-}168\delta_v h^5\text{+}126\delta_v{}^2 h^4\text{-}21\delta_v{}^4 h^2)}{(42h^7\text{-}84\delta_v{}^2 h^5\text{+}140\delta_v{}^3 h^4\text{-}77\delta_v{}^4 h^3\text{+}14\delta_v{}^6 h\text{-}4\delta_v{}^7)}$$

which also may be written as

$$h_c = \frac{k}{h} f(\eta), \tag{5-34}$$

where we have introduced

$$f(\eta) = \frac{-21\eta^4 + 126\eta^2 - 168\eta + 168}{-4\eta^7 + 14\eta^6 - 77\eta^4 + 140\eta^3 - 84\eta^2 + 42} \quad \text{and} \quad \eta = \frac{\delta_v}{h} \tag{5-35}$$

h is the film thickness. These are rather ponderous expressions, but can be simplified by *approximating f (η)*. The type of function to chose for such an approximation depends on the accuracy desired. *f (η)* is plotted in Figure 5.2. Here η varies between 0 and 1. In reality the lowest value is problem-dependent, but nonetheless located at the radial position 3*a.* As

one might remember, this is the position from which the simplified expression for the velocity boundary layer is used - equation (4–42).

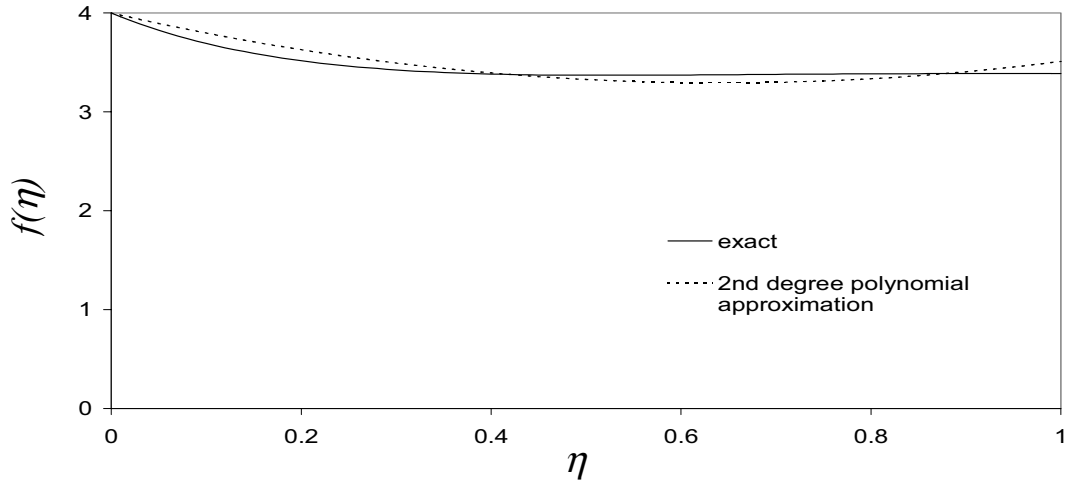

Figure 5.2 Function $f(\eta)$ describing heat transfer coefficient according to equation (5-35) between r_T *and* r_v.

It is evident that $f(\eta)$ is a *slowly varying* function of η. At $\eta \approx 0.3$ the function flattens out to a value of about 3.4. The absolute simplest and most tempting option is to use the average value for $f(\eta)$ over the interval $0 < \eta < 1$ as an approximation for $f(\eta)$ itself. This value is found to be 3.46. The maximum deviation from the exact function is about 15% at $\eta = 0$. For values of η near zero, correlations for the convective heat transfer coefficient by the way do not involve $f(\eta)$ (inside $r = 3a$). Based on the average value, we get

$$h_c = 3.46\frac{k}{h} \tag{5-36}$$

Another alternative is to use a second order polynomial for the function $f(\eta)$. The best fit according to this suggestion is

$$h_c = \frac{k}{h}\left[4 - 2.2\frac{\delta_v}{h} + 1.71\left(\frac{\delta_v}{h}\right)^2\right] \tag{5-37}$$

Higher order polynomials can be used, but due to the slowly varying characteristic of $f(\eta)$, the increased accuracy would be small, accompanied by markedly increased complexity.

We can also define a Nusselt number related to the film thickness, h:

$$Nu = h_c\frac{h}{k} = f(\eta) \tag{5-38}$$

In the simplest case, Nu is constant and equal to 3.46. This is remarkably close to the value found for the region $r_v < r < r_j$ $\left(= \frac{105}{31} \approx 3.39\right)$.

A heat balance for the two cases (again without heat transfer at the liquid surface) incorporating a constant T_w, yields:

i) $f(\eta) = 3.46$:

$$\frac{dT_m}{T_m - T_w} = \frac{2\pi\alpha}{V}3.46\frac{rdr}{\frac{a^2}{2r} + \frac{3}{8}\sqrt{\frac{280}{39}\frac{vr}{U_\infty}}} \tag{5-39}$$

$$\Downarrow$$

$$\ln\frac{T_{m2} - T_w}{T_{m1} - T_w} = -\frac{4\pi\alpha}{3V}3.46\left[\frac{s}{k_3} - k_2\frac{\ln(k_2 + k_3 s)}{{k_3}^2}\right]_{s1}^{s2} \tag{5-40}$$

ii) $f(\eta) = 4 - 2.2\eta + 1.71\eta^2$:

$$\ln\frac{T_{m2}-T_w}{T_{m1}-T_w} = -\left[\frac{1}{2}\frac{a_2 {k_1}^2 {k_2}^3}{{k_3}^4(k_2+k_3 s)^2} - \sum_{n=0}^{2}\left(\frac{4\pi\alpha}{3V}\frac{a_n s}{{k_3}^{n+1}}\right.\right.$$

$$\left.\left. -(n+1)a_n {k_1}^n k_2 \frac{\ln(k_2+k_3 s)}{{k_3}^{n+2}} - \frac{n(n+1)}{2}\frac{a_n {k_1}^n {k_2}^2}{{k_3}^{n+2}(k_2+k_3 s)}\right)\right]_{s1}^{s2} \tag{5-41}$$

We have substituted r with a new variable $s = r^{\frac{3}{2}}$. In addition

$$a_0 = 4,\ a_1 = -2.2,\ a_2 = 1.71,\ k_1 = \sqrt{\frac{280}{39}\frac{\nu}{U_\infty}},\ k_2 = \frac{a^2}{2},\ k_3 = \frac{3}{8}\sqrt{\frac{280}{39}\frac{\nu}{U_\infty}}$$

The accuracy of these two approximations has been evaluated by integrating their respective h_c-expressions between the limits r_T and r_v and comparing this to the exact integration. The second order polynomial approach is as expected in best agreement with the exact result. The accuracy is to a very small degree problem-dependent and is for all practical applications less than 0.3%. The mean value approach deviates at most 2.3% from the exact value. It is concluded that this latter approximation is of sufficient accuracy for most applications.

A heat balance with a constant ambient temperature underneath the mould results in:

$$\frac{dT_m}{T_m - T_a} = -\frac{2\pi}{V\rho c_p}\frac{rdr}{\frac{1}{3.46k}\left(\frac{a^2}{2r} + \frac{3}{8}\sqrt{\frac{280}{39}\frac{\nu r}{U_\infty}}\right) + \frac{1}{h_{ca}} + \frac{t_m}{k_m}} \tag{5-42}$$

This equation does not have an explicit analytical solution. This can however, be obtained if δ_v is *linearised* with respect to r between r_T and r_v.

The film thickness incorporating this linearisation is negligibly different from the original value. If we write

$$\delta_v = \frac{\delta_v(r_v) - h_c(r_T)}{r_v - r_T} r + \frac{\delta_v(r_T) r_v - \delta_v(r_v) r_T}{r_v - r_T},$$

equation (5-42) can be integrated, giving

$$\ln \frac{T_{m2} - T_a}{T_{m1} - T_a} = -\frac{2\pi}{\rho c_p V B} \left[r - \frac{C}{2B} \ln(A + Cr + Br^2) \right.$$

$$\left. + \frac{C^2}{B\sqrt{4BA - C^2}} \arctan\left(\frac{2Br + C}{\sqrt{4BA - C^2}} \right) - \frac{2A}{\sqrt{4BA - C^2}} \arctan\left(\frac{2Br + C}{\sqrt{4BA - C^2}} \right) \right]_{r1}^{r2}$$

with

$$A = \frac{a^2}{6.92 k_l}$$

$$B = \frac{3}{8 \cdot 3.46 k_l} \frac{\delta_v(r_v) - \delta_v(r_T)}{r_v - r_T}$$

$$C = \frac{3}{8 \cdot 3.46 k_l} \frac{\delta_v(r_T) r_v - \delta_v(r_v) r_T}{r_v - r_T} + \frac{1}{h_{ca}} + \frac{t_k}{k_k}$$

If it assumed that the fluid surface temperature equals T_∞ all the way up to the jump, a rough approximation for the Nusselt number between r_v and the jump position can easily be obtained. The thickness of the thermal boundary layer in this region is equal to the thickness of the velocity boundary layer, and occupies the whole fluid film. With reference to equation (4–44) for the film thickness, we get

$$q = k\left.\frac{\partial T}{\partial z}\right|_{z=0} = \frac{3}{2}k\frac{(T_\infty - T_w)}{\delta_T} = \frac{3}{2}\frac{k(T_\infty - T_w)}{\left(\frac{175}{136}\frac{\nu r^2}{a^2 U_\infty} + 0.685\frac{a^2}{r}\right)} \qquad (5\text{-}43)$$

$$\Downarrow$$

$$Nu = \frac{3}{2}\frac{r}{\left(\frac{175}{136}\frac{\nu r^2}{a^2 U_\infty} + 0.685\frac{a^2}{r}\right)} \approx \frac{Vr^2}{2.675\nu r^3 + 1.435 a^4 U_\infty} \qquad (5\text{-}44)$$

This expression is independent of *Pr*.

5.2.5 Region 5, $r_j < r < r'_T$

In connection with the jump the fluid flow must reorganize, involving new development of the boundary layers. One possible scenario is that both boundary layers have reached the surface of the flow before the jump and will develop further from this thickness. Matters are, however, simplified if the boundary layers are assumed to have been broken down completely and start developing from zero thickness at the jump. Since the film thickness is an order of magnitude greater after the jump than before, this simplification is considered to have little effect on the final results.

The smoothing out of the flow gradients (over the cross-section of the flow) with respect to velocity and temperature cannot of course occur abruptly at r_j, but must in reality take place over a finite interval Δr. The theory outlined below will therefore not be applicable at exactly r_j (just as in the case of free-stream boundary layer flow over a flat plate, where the theory breaks down at the tip of the plate, i.e. $x = 0$).

The conditions after the jump are hopefully somewhat simplified by the fact that the film thickness in this region varies little and can be regarded as constant, equal to the thickness at the plate edge, h_R. The reasoning and line of action is otherwise almost identical to that carried out prior to the jump.

In general we now have, similar to equation (4–42) before the jump:

$$\delta'_v = \sqrt{\frac{280}{39}\frac{\nu(r-r_j)}{u_{mj}}}, \qquad \delta'_T = \varsigma\delta'_v \tag{5-45}$$

u_{mj} is the mean velocity of the liquid fluid immediately preceding the jump

$$u_{mj} = \frac{V}{2\pi r_j h_{j1}}$$

It is assumed that the velocity outside the velocity boundary layer after the jump is equal to u_{mj}. h_{j1} is the film thickness immediately before the jump.

As before the jump, we can determine r'_T by equating δ'_T with h_R, which gives

$$r'_T = \frac{280}{39}\frac{u_{mj}}{\nu}\frac{h_R^2}{\varsigma^2} + r_j \tag{5-46}$$

and

$$r'_v = \frac{280}{39}\frac{u_{mj}}{\nu}h_R^2 + r_j \tag{5-47}$$

Analogous to velocity, a reasonable assumption is that the temperature outside the new thermal boundary layer is equal to the mean temperature of the fluid, T_{mj}, just in front of the jump. We then have for the heat flow from the fluid to the mould (cf. equation (5-43)).

$$q = \frac{3}{2}k\frac{T_{mj}-T_w}{\delta'_T} = h_c(T_{mj}-T_w), \tag{5-48}$$

which gives

$$h_c = \frac{3}{2}\frac{k}{\varsigma}\sqrt{\frac{39}{280}\frac{u_{mj}}{\nu(r-r_j)}} \tag{5-49}$$

or $$h_c \approx 0.769k\sqrt{\frac{u_{mj}}{\nu(r-r_j)}}\,\mathrm{Pr}^{0.48}$$

and a local Nusselt number

$$Nu_r = \frac{h_c h_R}{k} = \frac{3}{2}\frac{h_R}{\varsigma}\sqrt{\frac{39}{280}\frac{u_{mj}}{\nu(r-r_j)}} \tag{5-50}$$

5.2.6 Region 6, $r'_T < r < {}'_v$

As in the corresponding region before the jump we may write

$$h_c = \frac{k}{h_R} f(\eta), \qquad \eta = \frac{\delta'_v}{h_R}$$

$f(\eta)$ is the same function as introduced before the jump, and employing its *average* value for $0 < \eta < 1$ equal to 3.46, we get

$$h_c = 3.46\frac{k}{h_R} \tag{5-51}$$

$$Nu = \frac{h_c h_R}{k} = 3.46 \tag{5-52}$$

and in the case of a *constant wall temperature*, T_w, the decrease of the mean temperature with r is

$$\ln\frac{T_{m2}-T_w}{T_{m1}-T_w}=-3.46\frac{\pi\alpha}{Vh_R{}^2}(r_2^2-r_1^2)$$

For a *constant ambient temperature*, T_a, the corresponding relation is

$$ln\frac{T_{m2}-T_a}{T_{m1}-T_a}=-\frac{\pi}{\rho c_p V}\frac{1}{\frac{h_R}{3.46k_l}+\frac{1}{h_{ca}}+\frac{t_k}{k_k}}(r_2^2-r_1^2) \qquad (5\text{-}53)$$

5.2.7 Region 7, $r > r'_v$

Much as before the jump, we have for the heat transfer coefficient

$$h_c=\frac{105}{31}\frac{k}{h_R} \qquad (5\text{-}54)$$

$$Nu=\frac{105}{31}\approx 3.39 \qquad (5\text{-}55)$$

and for the temperature development

$$\ln\frac{T_{m2}-T_w}{T_{m1}-T_w}=-\frac{105}{31}\frac{\pi\alpha}{Vh_R{}^2}(r_2^2-r_1^2)\ ,\ T_w \text{ constant} \qquad (5\text{-}56)$$

$$\ln\frac{T_{m2}-T_a}{T_{m1}-T_a}=-\frac{\pi}{\rho c_p V}\frac{1}{\frac{31h_R}{105k_l}+\frac{1}{h_{ca}}+\frac{t_k}{k_k}}(r_2^2-r_1^2)\ ,\ T_a \text{ constant} \qquad (5\text{-}57)$$

5.3 Summary and Example

The formulas derived in the preceding sections are important results of this study. Succinctly, the convective heat transfer coefficients for the radially spreading liquid metal flow may be summarised as follows:

Region	Equation no.	h_c [W/m^{2}K]
1, $0 < r < r_s$	5–22	$0.904\,Re_j^{0.5}\,Pr^{0.48}\,\frac{k}{2a}$
2, $r_s < r < r_T$	5–7	$0.769\,Re_r^{0.5}\,Pr^{0.48}\,\frac{k}{r}$
3, $r_T < r < r_v$	5–36	$3.46\frac{k}{h}$
4, $r_v < r < r_j$	5–24	$\frac{105}{31}\frac{k}{h}$
5, $r_j < r < r'_T$	5–49	$h_c \approx 0.769k\sqrt{\frac{u_{mj}}{\nu(r-r_j)}}\,Pr^{0.48}$
6, $r'_T < r < r'_v$	5–51	$3.46\frac{k}{h_R}$
7, $r > r'_v$	5–54	$\frac{105}{31}\frac{k}{h_R}$

Table 5-1 Summary of local heat transfer coefficients for radially spreading liquid metal.

Figure 5.3 shows a plot of the theoretical heat transfer coefficient computed from the preceding formulas. After the *constant value* in the stagnation region, it *increases* to a local peak where a new correlation takes over. The peak arises because these two correlations do *not exactly match* at the point r_s. Outside of this point the convection coefficient *decreases* to a local minimum where the thermal boundary layer reaches the fluid surface, r_T. This *reduction* in the heat transfer coefficient due to the *increasing* thickness of the thermal boundary layer is a *general trend*,

also attributable to other flows. After r_T this boundary layer is equal to the film thickness, which in this region ($r_T < r < r_v$) *decreases*, manifesting itself as an *increase* in the convection coefficient. There is a sudden change in the development of the thermal boundary layer at r_T and the curves for h_c before and after this point cannot (again) be evenly merged. After r_v the film thickness continues to decrease, reaches a *minimum* and *increases* towards the hydraulic jump. This is reflected as a continuing *increase* in h_c till it reaches a *maximum.* Towards the hydraulic jump it then *decreases* due to the increased thermal boundary layer (following the film thickness). At the jump it *drops sharply*, for so to *decrease* inversely proportional to the square root of its radial location, up to r'_T. In this theory there is no influence from any possible increase of turbulence associated with the hydraulic jump. Finally, at r'_T it adjusts to a an almost *constant value* (since the film thickness is almost constant) which changes minutely at r_v.

The value of the local convective heat transfer coefficient is in the same order of magnitude as experienced in rapid solidification processes. Contrary to what was initially believed, it is *not maximum in the stagnation region, but at the point of minimum film thickness*. Mathematically it can be shown that this lies *between* r_v and r_j when a third order polynomial is assumed for the velocity profile (equation (4–34)). This feature remains true for all practical purposes. Analysis yields that the stagnation heat transfer coefficient is largest only in flows with extremely high Reynold numbers, which one in practice doubtfully will achieve. Hypothetically, for tin flow through an 8 mm nozzle the heat transfer coefficient is greatest in the stagnation region when the nozzle velocity increases to about 16000 m/s ($Re_j = 5.5 \cdot 10^8$).

Wang et al. (1993) have also confirmed that the heat transfer coefficient can be greatest outside the stagnation region. This was, however, for gas jets at low flow rates ($Re_j < 10$) where natural convection becomes preponderant.

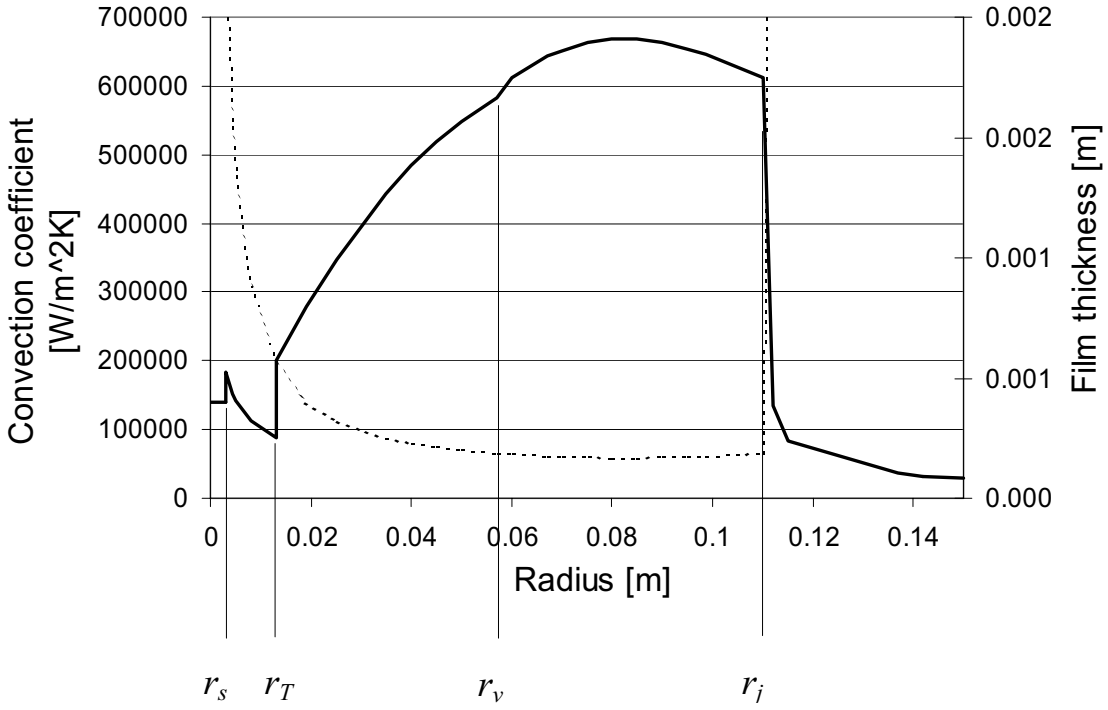

Figure 5.3 Example of analytically computed local convective heat transfer coefficient (solid line) for tin at 341 °C impinging on a flat horizontal plate and corresponding film thickness (dashed line). Flow through 8 mm nozzle, $1.0464 \cdot 10^{-4}$ m^3/s, 92 mm free fall. Values are related to the *local* bulk tin temperature (a function of radial location).

For the flow in Figure 5.3 we have:

Before jump:

$$r_s = 0.003 \text{ m}$$
$$r_T = 0.013 \text{ m}$$
$$r_v = 0.057 \text{ m}$$
$$r_j = 0.110 \text{ m}$$

After jump:

$$r'_T = 9.59 \text{ m}$$
$$r'_v = 351 \text{ m}$$

One can see that both boundary layers need a fairly long distance to reach the fluid surface after the jump.

Comparison of Heat Transfer in Water and Liquid Metal

For sake of comparison, some heat transfer coefficients for *water* and *liquid tin* will be calculated.

First we consider an impinging flow on a flat, horizontal plate and restrict the study to *region 4,* $r_v < r < r_j$, in Figure 5.1, i.e. after both boundary layers have reached the fluid surface. The wall temperature is assumed constant and there is no heat transferred from the liquid surface. The jet has a diameter of 10 mm and a velocity of 2 m/s. The temperature profile through the cross-section of the fluid is described by the now familiar third order polynomial.

For *water* at 50 °C we have from equation (5-24) and (4-44)

$$h_c = \frac{105}{31}\frac{k}{h} = \frac{105}{31}\frac{0.641}{\frac{175}{136}\frac{5.54\cdot 10^{-5}}{0.01^2\cdot 2}r^2} \approx \frac{6.1}{r^2} \quad W/m^2K$$

For *liquid tin* at 300 °C we accordingly have

$$h_c = \frac{105}{31}\frac{k}{h} = \frac{105}{31}\frac{32.6}{\frac{175}{136}\frac{2.41\cdot 10^{-7}}{0.01^2\cdot 2}r^2} \approx \frac{7120}{r^2} \quad W/m^2K$$

In order to display definite values, these coefficients can for example be evaluated at the location $r = r_v$. For water we then get

$$r_v = 0.032 \text{ m}, \qquad h_c = 6020 \text{ W/m}^2\text{K}$$

and for tin

$$r_v = 0.195 \text{ m}, \qquad h_c = 187560 \text{ W/m}^2\text{K}$$

For a fully developed laminar flow in a pipe (2 m/s, 10 mm diameter pipe), we have Nu = 3.66 (regardless of diameter and velocity).

With liquid tin under the same conditions, the flow is turbulent and the following correlation can be used (Seban and Shimazaki, 1951):

$$Nu = 5 + 0.025(\mathrm{Re}\,\mathrm{Pr})^{0.8}$$

In both cases $h_c = \dfrac{Nu \cdot k}{d}$ (d is the pipe diameter), which gives

h_c = 235 W/m^2 K for water

h_c = 38170 W/m^2 K for tin

This clearly shows that liquid metal flows are endowed with qualities that lead to unsurpassed convective heat transfer coefficients. It is also clear that impinging jets, regardless of fluid, exhibit high heat transfer coefficients compared to other flows (at least before a hydraulic jump).

Another point worth mentioning is that for fully developed *laminar* flows - region 4 (the boundary layers occupy the whole cross-section of the flow) - liquid metals *show the same characteristics as other fluids*. From a practical point of view this means that their heat transfer coefficients can be calculated using *general correlations* (*Nu = f(Re, Pr)*) for the specific flow type hopefully found in a heat transfer handbook. *Turbulence*, however, influences the flow in a manner heavily dependent on fluid properties. The turbulent contribution to the effective thermal conductivity, for example, is different in flows with water and liquid metal, even if the Reynold numbers are the same.

5.4 Turbulent Heat Transfer

Due to their low viscosities, liquid metal flows are often turbulent. The heat flux (in the *y*-direction) in a fluid can, with the exception of large-scale convection ($\rho c_p \overline{v}\,\overline{T}$), in such cases be described as

$$q = -k\frac{\partial \overline{T}}{\partial y} + \rho c_p \overline{v'T'} \tag{5-58}$$

k is the usual molecular thermal conductivity. General theory on turbulence was addressed in Chapter 3.

The first term in this equation is the heat flux due to ordinary molecular conduction or thermal diffusion (as in laminar flow) and the second the heat transported by the turbulent motion of eddies, which also can be described as small-scale convection. The difficulty is to now find some method for handling this last term (similar to turbulent momentum). One theory introduces an *eddy diffusivity for heat transfer*, ε_H, analogous to the eddy diffusivity for momentum, proposing that

$$\overline{v'T'} = \varepsilon_H \frac{\partial \overline{T}}{\partial y}\ , \quad \text{so that}$$

$$q = -(k + \rho\, c_p \varepsilon_H)\frac{\partial \overline{T}}{\partial y} = -(k + k_t)\frac{\partial \overline{T}}{\partial y} \tag{5-59}$$

k_t is a *turbulent* or *eddy conductivity* = $\rho c_p \varepsilon_H$. The two thermal conductivities can be integrated into one *effective conductivity*:

$$k_{eff} = k + k_t \quad \text{and} \quad q = -k_{eff}\frac{\partial \overline{T}}{\partial y} \tag{5-60}$$

It is also possible to introduce the concept of a *turbulent Prandtl number*, Pr_t:

$$\mathrm{Pr}_t = \frac{\mu_t c_p}{k_t} = \frac{\varepsilon_M}{\varepsilon_H} \tag{5-61}$$

μ_t is the turbulent dynamic viscosity and ε_M the eddy diffusivity for momentum. The corresponding molecular quantity is the kinematic viscosity, ν $(=\mu/\rho)$. This enables us to obtain the following form for the turbulent boundary layer energy conservation equation

$$\overline{u}\frac{\partial \overline{T}}{\partial x} + \overline{v}\frac{\partial \overline{T}}{\partial y} = \frac{\partial}{\partial y}\left[\left(\alpha + \frac{\varepsilon_M}{\mathrm{Pr}_t}\right)\frac{\partial \overline{T}}{\partial y}\right]$$

If the boundary layer momentum equation has been solved so that ε_M is known, the thermal boundary layer problem can be solved if information about Pr_t is known. Various models for Pr_t have been developed. The oldest and simplest one was by Reynolds, concluding that $Pr_t = 1$.

Later work has shown that things are not so simple as $Pr_t = 1$, although this is not far off the mark in many cases. Experiments with liquid metals in pipes indicate Pr_t greater than 1. This means that an eddy can lose a substantial amount of heat by conduction before it has travelled the distance of a mixing length. In other words, eddies (following the onset of turbulence) *do not greatly enhance heat transfer in fluids with high thermal conductivities*. To realistically predict heat transfer in turbulent liquid metal flows by solution of the energy differential equation, one must consequently assume $Pr_t > 1$.

The turbulent Prandtl number also increases when nearing a wall. This indicates that the mechanisms of momentum and heat transfer differ in this area compared to other regions of the flow. Both ε_M and ε_H will decrease towards a wall, but they can *decrease at different rates*, producing an *increase* in Pr_t. Taking this factor into account is critical for the calculation of thermal boundary layers with moderate and high Prandtl numbers.

An equation for Pr_t that fits experiments reasonably well for fluids with $Pr < 1$ is

$$Pr_t = \frac{1}{\frac{1}{2\,Pr_{t\infty}} + C\,Pr\left(\frac{\varepsilon_M}{\nu}\right)\sqrt{\frac{1}{Pr_{t\infty}}} - C^2\,Pr^2\left(\frac{\varepsilon_M}{\nu}\right)^2\left[1 - exp\left(-\frac{\nu}{C\varepsilon_M\sqrt{Pr_{t\infty}}}\right)\right]} \tag{5-62}$$

C is an experimental constant and $Pr_{t\infty}$ the turbulent Prandtl number far from the wall - also an experimental value.

If we assume Pr_t =1 and apply the same concepts as in kinetic gas theory, we can write

$$q = -k\frac{\partial \overline{T}}{\partial y} + \rho c_p \nu_t \frac{\partial \overline{T}}{\partial y},$$

$$\nu_t = l \cdot v'$$

l is the so-called *mixing length* (a theory suggested by Prandtl) and is thought of as the length over which an imaginary particle moves before changing its momentum due to the turbulence. l and v' are small relative to other dimensions in the system. A crude assumption is that l and v' are an order of magnitude less than some characteristic length and velocity in the problem, for example *the film thickness* and *mean film velocity*. Before the hydraulic jump this velocity can be approximated by the jet velocity. This gives

$$q = -(k + \rho c_p \cdot (0.1U_\infty) \cdot (0.1 \cdot h))\frac{\partial \overline{T}}{\partial y} = -k_{eff}\frac{\partial \overline{T}}{\partial y}$$

To illustrate the magnitude of k_{eff} we can use a flow with a jet velocity of 3 m/s and a film thickness of 0.1 mm (in the same order of magnitude as the thickness of the flow before the jump), and find for liquid tin with k = 33 W/mK at 300 °C

$$k_{eff} = 33 + 6900 \cdot 257 \cdot 0.1 \cdot 3 \cdot 0.1 \cdot 0.0001$$

$$\Downarrow$$

$$k_{eff} = 38.3 \ \ W / mK$$

In this case the heat conductivity was increased about 16%. This is an exaggerated value because the mean film velocity becomes much less than the jet velocity as the flow moves outwards.

Generally a relationship for l is obtained by reasoning and adjusted with experimental data. Such theory will not be dealt with here, but can be found in various textbooks.

Turbulence is an active area of research and new models are frequently presented.

5.5 Heat Transfer From Fluid Surface

In the foregoing theory heat transfer from the fluid surface by radiation and convection has been neglected. Depending on the emissivity of the substance involved and cooling conditions on the surface, this heat transfer can be of considerable importance. It is however, quite complicated to theoretically take this into consideration, and in this work, time will not allow it. Some remarks on this will anyway be made.

Heat flow from the surface will result in the development of an additional thermal boundary layer propagating into the fluid from its surface. Depending on the general cooling conditions, both at the liquid surface and its underside, the two thermal boundary layers may eventually meet. Their further development is also dependent on the cooling conditions. The top boundary layer can be described by a second order polynomial with boundary conditions similar to the lower boundary layer. See Figure 5.4.

If the two boundary layers after some time are said to meet at the radial location $r = r_{Tm}$ at a vertical distance from the plate equal to h_T and at a temperature T_T , we can prescribe the following conditions that must be fulfilled by the temperature profiles for $r > r_{Tm}$:

Lower boundary layer:

1) $T = T_w$ at $z = 0$
2) $q = k\frac{\partial T}{\partial z}$ at $z = 0$
3) $T = T_T$ at $z = h_T$
4) $\frac{\partial T}{\partial z} = 0$ at $z = h_T$

Upper boundary layer:

1) $T = T_T$ at $z = h_T$
2) $\frac{\partial T}{\partial z} = 0$ at $z = h_T$
3) $-k\frac{\partial T}{\partial z} = \varepsilon\sigma T_s^{\,4}$ at $z = h$

Condition 3) describes the thermal radiation from the liquid surface. Convection can alternatively be included. ε is the emissivity and σ is the Stefan-Boltzmann constant.

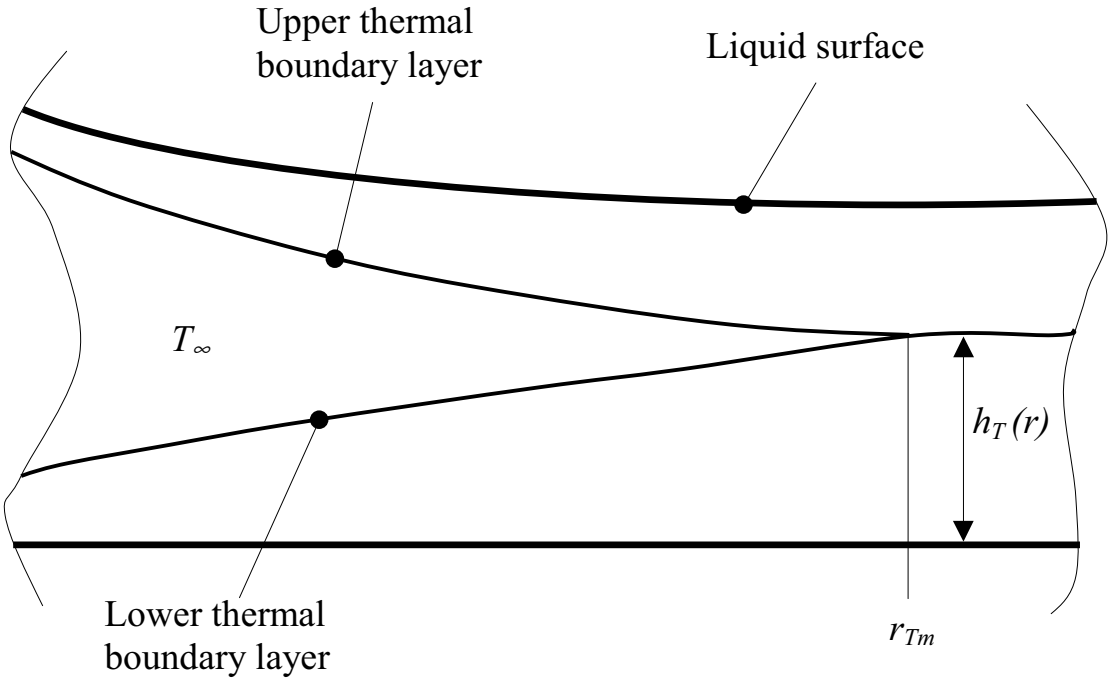

Figure 5.4 Sketch of upper and lower thermal boundary layers in radially spreading flow.

6. Experimental Procedures and Introductory Results

6.1 Experiments With Water

6.1.1 Apparatus

The apparatus for the water experiments consisted of a 40-liter cylindrical tank with an outlet nozzle at the bottom forming the jet. Underneath was a disk of plate glass, 10 mm thick. Initially plexiglass was used, but the surface of this material proved not to be completely level. Plates of three different diameters were tested; 210, 420 and 630 mm. This was to investigate how plate size influenced the flow. The plates rested on a tray, which neatly collected the water and guided it to a drain. The tray was supported by three legs incorporating adjustable screws, making it possible to level the plate accurately.

The water tank was supported in an adjustable rack so that the free fall height of the water, i.e. the distance between the nozzle orifice and the glass plate, could be altered. The tray and plate were arranged so that the jet would strike the plate vertically at its centre. See Figure 6.1.

Three nozzle sizes were used, with diameters of 5, 8 and 10 mm. These sizes were chosen as they are of the same proportions as that used in the *CTS* equipment. The nozzles were made of brass and their orifices machined as sharp as possible and perpendicular to the nozzle axis. No attempt was made to study the effects of different orifice geometries. Originally the nozzles were 50 mm long, but the water jets seemed unsteady and the nozzle lengths were increased to 200 mm. This resulted in much steadier jets but they were still not acceptable. Between the nozzle and the tank was a ball valve. This was removed and the nozzles screwed directly to the tank. The jets were now satisfactory and this set-up was consequently used.

Water was supplied to the tank through a 1-inch hose. Its momentum created vigorous stirring in the tank, which was thought to disturb the jet. Different angles of impact, submerged and not-submerged hose, a high-

speed nozzle in the hose and a horizontal, circular "deflection plate" in the tank, which the water struck vertically and decelerated against to ensure a tranquil flow into the tank, were all tried in order to study if the conditions in the tank affected the jet. The conclusion was that they did not. The hose was therefore simply submerged in the tank without any further bother.

Two different flow rates for each nozzle was achieved by using two different water levels in the tank. This was arranged with two overflow pipes; 290 and 670 mm above the nozzle opening. The lowest one was blocked when the highest level was in use and vice versa. The rate of flow was found by measuring the volume of water leaving the tank in a known period of time. No systematic variation of dimensionless groups was carried out.

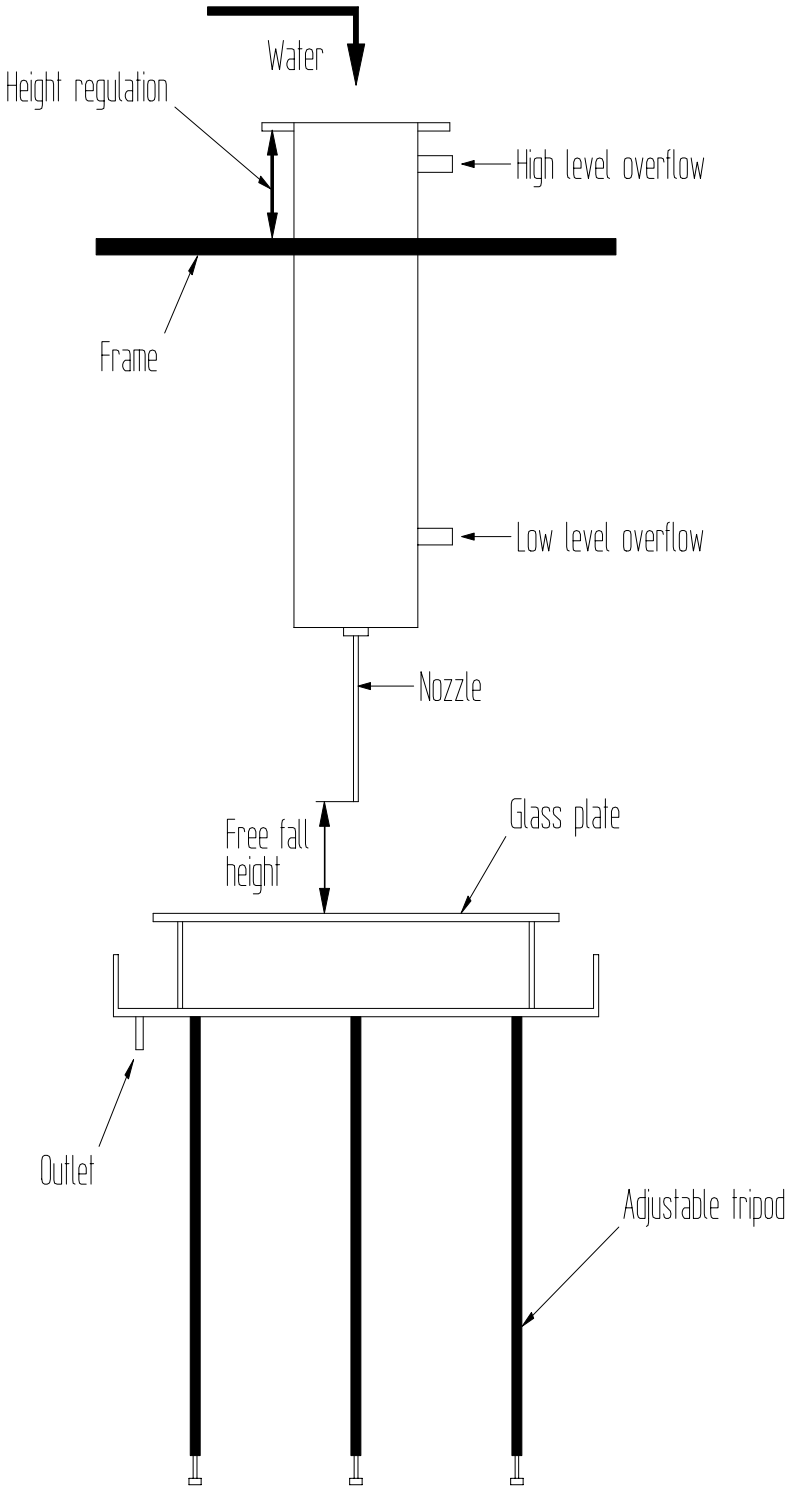

Figure 6.1 Apparatus for water experiments.

6.1.2 The Laser-Doppler Method

Fluid velocities were measured with a laser-Doppler instrument. The operating principle is that a single laser beam is split into two. These resulting coherent beams are at an angle to each other and will intersect at a fixed point, or more precisely, an intersection *volume* is formed containing interference fringes, see Figure 6.2 If a particle traverses this volume, light consisting of two components (one for each beam) will be reflected. A photo detector is arranged to receive the scattered light. Both components will have a Doppler shift due to the velocity of the particle, but as the two beams are at an angle, they will be different. This results in a pulsating light intensity noticed by the photo detector. This pulsation has a frequency that is directly proportional to the velocity component of the particle perpendicular to the fringes. For a correct measurement it is therefore important that the probe is aligned so that the beams and the particle trajectory are in the same plane.

The system used for the velocity measurements was a FlowLite integrated laser-optics system from Dantec Measurement Technology A/S, Denmark. This consists of a probe emitting laser light connected to a signal processor. This again is controlled by Dantec's FLOware software, which runs on a personal computer under DOS. A wide variety of measuring parameters can be set.

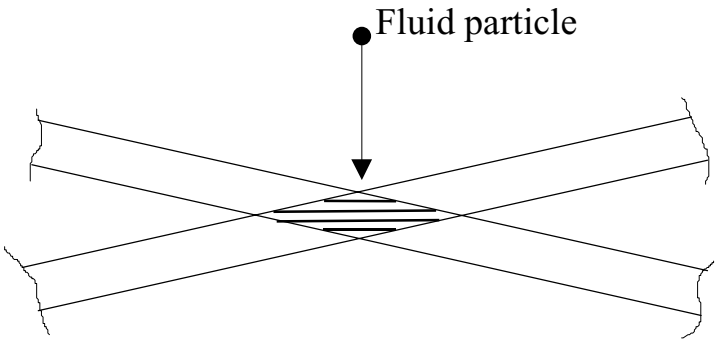

Figure 6.2 Fringes formed at intersection of two coherent beams.

6.1.3 Measurements

The plate was marked with a ruler on the lower face making it easy to confirm where the jump occurred. The laser-Doppler instrument was placed in an adjustable frame beneath the plate so it could smoothly traverse the water film vertically at a selected radius. An attached micrometer was used to determine the vertical position of the measuring point of the laser beams. The instrument was manually moved to measure at different radii on the plate.

A problem experienced almost immediately after trying the apparatus was the condensation of vapour on the lower side of the plate, due to the cold water (5-6 °C). This disturbed the laser-Doppler measurements and had to be eliminated. An electric pump was obtained and the water from the tray was led to a new tank. It was then pumped to the first tank and recirculated. The hose from the water main was now redundant. Eventually the water reached room temperature and the condensation ceased. The room temperature was not measured during the experiments, but an estimated variation of ±5 °C is considered to have negligible effect on the water properties.

At large flow rates and free-fall distances splashing from the jet occurred and no observations could be made. The smaller these values were, the smoother the jump and the flow on the plate seemed to be. Generally the flow formed a nice circular jump, which radially fluctuated about ±5 mm around a given point. Ripples in the water film were evident, especially after the jump, and seemed to increase in size with increasing flow rates and jet velocities. These most probably disturbed the laser-Doppler measurements. In some cases ripples were visible to the naked eye along the whole plate, but a high-speed camera revealed others, especially before the jump, that initially were not apparent.

In all tests the film thickness in the region after the jump seemed independent of all variables inherent to the impinging jet. At large jet Reynolds-numbers the jump region appeared to grow in size, making the transition from a thin to a stable thicker flow less abrupt. At the most the jump region extended to about 30 mm. In these cases the thickness rose quite quickly to about 2 mm and thereafter used approximately 30 mm to

develop to the typical value of 3.5 mm. Mostly the jump length was 5 to 10 mm.

The film depth was measured with both a micrometer and by reading off the distance traversed by the laser-Doppler measuring volume from the plate surface to the water surface. These two positions were determined by sight. A reliable measurement before the jump was unattainable, again due to the uneven fluid surface. No differences between the water depths in the different flow rates could be ascertained. The film thickness in the pre-jump region is estimated to be in the order of 1/10th millimetre. Beyond the jump the thickness seemed to be stable at around 3 to 4 mm, with, as mentioned, no differences between the flow rates being evident. The height of the ripples could not be measured with any degree of accuracy.

Velocities in the jet itself were also measured. The values recorded here were in agreement with the mean values obtained in the "manual" method of measuring flow rates earlier described.

It was generally difficult to obtain reliable velocity measurements of the fluid flow on the plate and it was thought that this might be due to a low particle concentration in the water. An additive with particles was mixed in, and the situation improved somewhat. The velocity profiles acquired were however quite unexpected, see Figure 6.3 and Figure 6.4. A common feature to all velocity measurements is that the flow velocity at the plate is not zero. Additionally, contrary to what may seem natural, the majority of the measurements did not show the maximum velocities to be at, or in the vicinity of the fluid surface. Another feature often experienced was that the average of the measured velocities over a cross-section was higher than the calculated bulk velocities for that position and film thickness. These observations proved to be a general trend in the experiments.

The inconsistencies could originate from limitations in the apparatus, incorrect use of the apparatus or the nature of the flow. The measurements were regularly double-checked, but no significant variances were detected. According to results reported by Stevens and Webb (1993), the maximum velocity in the film before the jump does not necessarily occur at its surface, which, by the way, invalidates the assumptions of many analytical models (see Chapter 4). Near the jet they actually found the maximum

velocity to be close to the plate. Following the radially spreading stream, the maximum velocity moves upwards and at $r/a \approx 2.5$ reaches the free surface. Other experimental studies have shown that the flow just *behind* the jump can separate and create a recirculating eddy attached to the plate. These were corroborated by dropping small particles into the fluid immediately after the jump. They were initially dragged downstream, but after 20 to 70 mm returned back to the jump, disclosing a recirculation zone.

Depending on the flow conditions this separation region can be quite long and can display very complex flow patterns. In addition, air bubbles can be trapped in the flow. It is quite probable that such conditions can affect the laser-Doppler measurements carried out in this work.

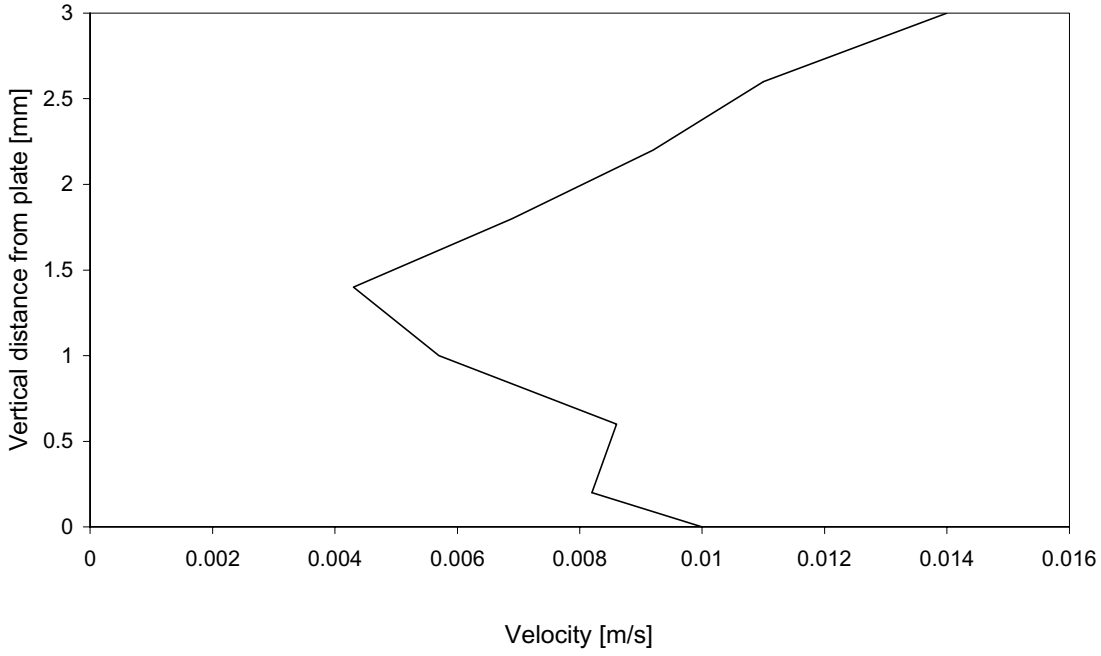

Figure 6.3 Example of velocity profile obtained by laser-Doppler measurements at a position of 235 mm from plate centre. Nozzle diameter: 5mm, free fall height: 50 mm, plate diameter: 630 mm, flow rate: $4.52 \cdot 10^{-5}$ m^3/s. Calculated bulk velocity is 0.01 m/s.

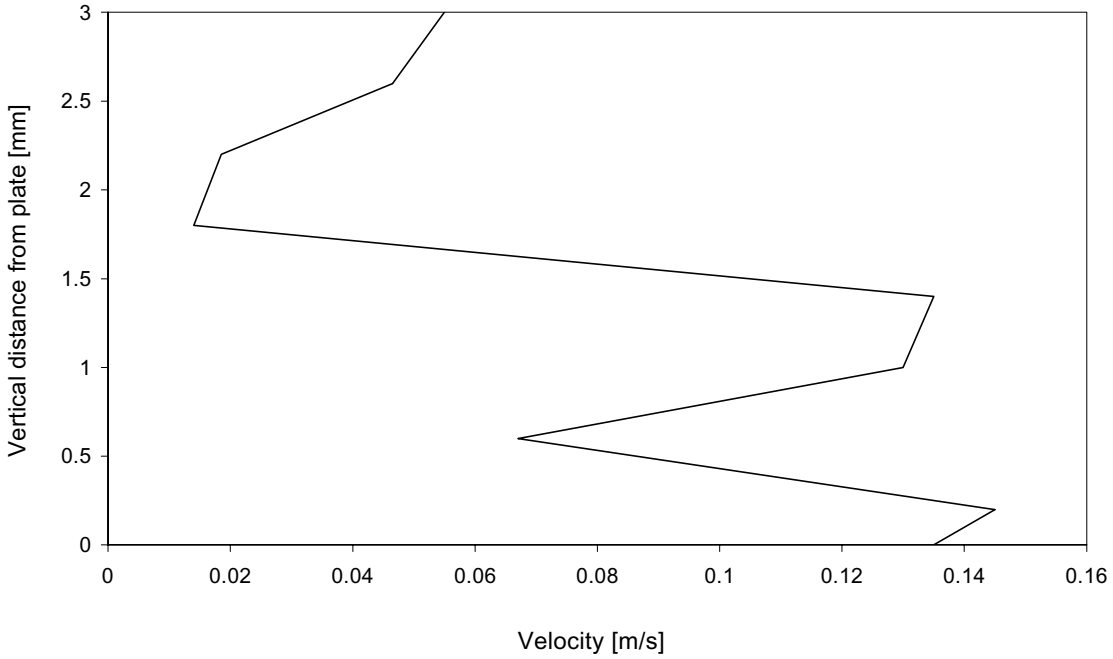

Figure 6.4 Example of velocity profile obtained by laser-Doppler measurements at a position of 160 mm from plate centre (after jump). Nozzle diameter: 10 mm, free fall height: 50 mm, plate diameter: 630 mm, flow rate: $1.42 \cdot 10^{-4}$ m^3/s. Calculated bulk velocity is 0.047 m/s.

An attempt was also made to measure the surface velocity of the water film along the plate. Figure 6.5 shows typical results. The surface-velocity curves for other conditions are of similar shape. After a maximum, 10-40 mm from the centre, the velocities decrease more or less rapidly towards the jump position and thereafter adjust to a minimum.

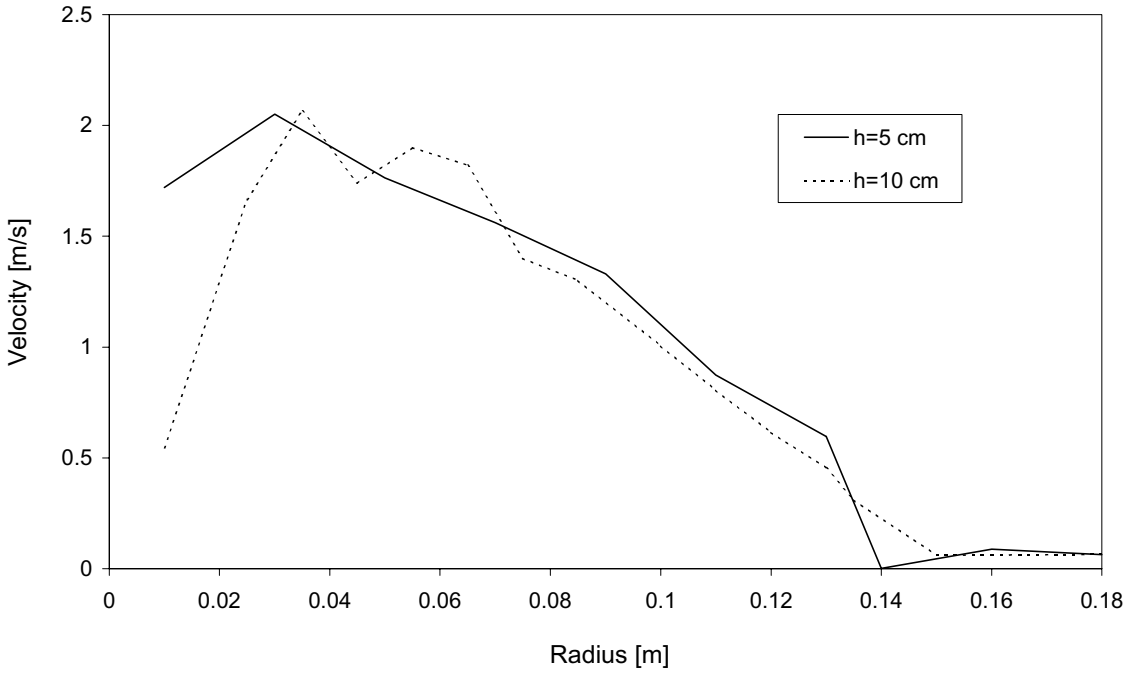

Figure 6.5 Laser-Doppler measurements of surface velocity for water on a glass plate. Flow is $1.42 \cdot 10^{-4}$ m^3/s through a 10 mm nozzle at two different free-fall heights.

The source for the uneven film surface is not completely understood. It is perhaps an innate characteristic of the flow and will occur even with an ideal, perfectly smooth jet. It was anyhow decided to study the existing jet more closely in order to investigate how "ideal" it in reality was. This was done with high-speed photography. Figure 6.6 to Figure 6.8 are pictures taken from the experiments at two different shutter speeds. The slowest resembles what is perceived by the human eye. Here the jet, liquid surface and jump position seem smooth and stable. The others show an unsteady surface full of ripples and waves, confirming that the real situation is not as initially envisaged. This clearly explains many of the difficulties and inconsistencies in the Laser-Doppler measurements. It is highly probable that the uneven jet influences the flow, leading to an uneven fluid surface.

Filming with a *high-speed* video camera with the jet impinging on a *dry* plate revealed that the hydraulic jump develops *before* the water flow reaches the edge of the plate. Its location does *not* seem to change while the fluid (after the jump) flows towards the plate edge or when steady state

conditions eventually are established. This is a strong indication that the jump position is not heavily influenced by plate size, which by the way validates the theory in the Bernoulli model and that of Buyevich and Ustinov. During testing of the Bernoulli model it was seen that friction and plate size (in a way a sign of the total friction force working on the flow) did not greatly affect the jump position.

The laser-Doppler system used has a measuring-point volume with a height of approximately 0.6 mm. It seems apparent that this dimension is too large to measure variations in velocities in the water film encountered in our experiments, at least prior to the jump. One does not know if the particles traverse at the lower or upper part of the volume, making it impossible to record any velocity variations over the cross-section of the flow. In our scale a difference of 0.6 mm is considerable. Inwards of the jump the best one can expect to obtain is a sort of average film velocity, but the values found are not reliable. Outside the jump a little more accuracy should have been expected, but also here the measurements are dubious. Small ripples on the water surface were visible, especially for the larger volume flows. These can have a marked effect on measurements in the vicinity of the surface.

Even clear water from the tap will contain some particles invisible to the human eye but large enough for the laser light to be reflected. As already mentioned, seeding particles can be mixed in the fluid to increase the measuring data rate. Various additives were tried, and latex paint proved to be the simplest and most effective. It is assumed that this did not alter the viscosity of the water significantly.

The suppliers of the equipment were contacted and felt that better measurements could be made. A meeting with them was subsequently arranged, but was unfortunately cancelled.

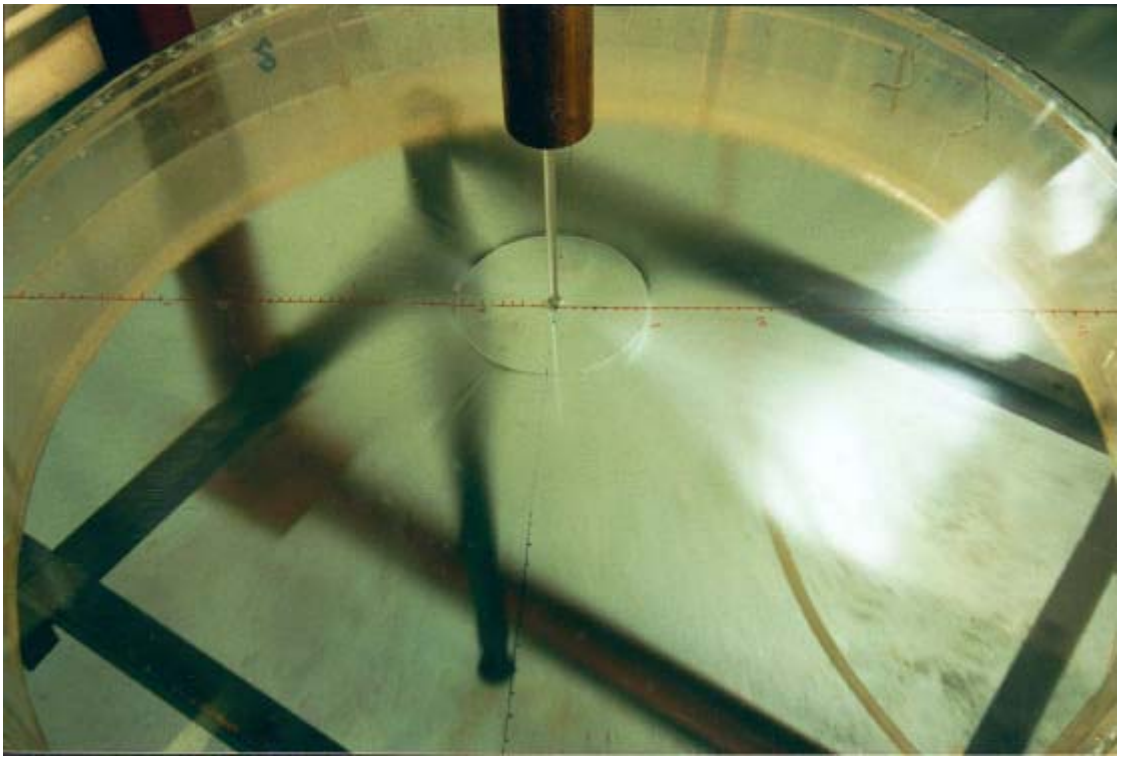

a)

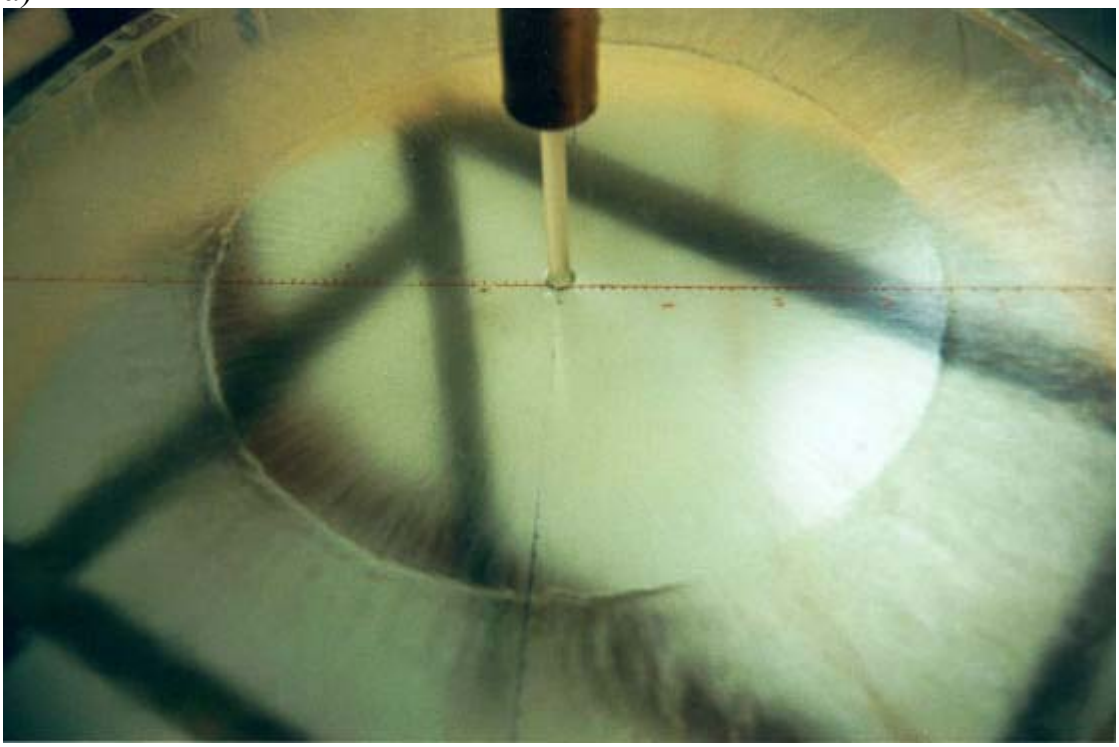

b)

Figure 6.6 Photographs of water experiments with "normal" shutter speed, i.e. as seen by the human eye. a) 5 mm nozzle, b) 10 mm nozzle.

a)

b)

Figure 6.7 Same as Figure 6.6, but higher shutter speed.

a) b)

Figure 6.8 Photographs of impinging water jet. Nozzle diameter is 10 mm.
a) low shutter speed and resembles what is perceived by the human eye
b) high shutter speed.

6.1.4 Jump Form and Effect of Surface Tension

In the thin liquid films experienced in these experiments, surface tension presumably plays an important role. These forces most likely act in the direction of stabilising the flow, but when turbulence in the flow becomes large enough, they are too small to suppress the (surface-) disturbances observed. Various chemicals such as paraffin, methyl isobutyl carbinol and glycerol were added to the water to modify the surface tension in order to

see how this affected the flow. Undiluted soap was also tried. No improvements of any importance were noted. The surface tension reducing additives tended to increase the disturbances and draw the jump position towards the plate centre. Also, the difference between the thicknesses before and after the jump seemed to decrease.

6.2 Experiments with Tin

6.2.1 Apparatus

For verifying the heat transfer calculations in the flow, a new apparatus was designed. It is essentially the same as that for the water experiments, but *tin* was in this case used as the liquid medium. Around the upper tank a 13 kW heating element was mounted. A pump was used to circulate the tin.

The plate the metal was poured onto (referred to as the *casting plate*, although casting is not really taking place here) was equipped with thermocouples. Experiments were conducted using an uncooled plate and thereafter a cooled plate with both air and water as cooling media. Figure 6.9 shows the experimental set-up.

As mentioned before, the viscous properties of water and liquid metals are quite similar, making it possible to simulate the flow of liquid metals with water. The thermal properties, on the other hand, are notably different, making it hopeless to compare temperature related behaviour in liquid metals and water. Liquid metals have a high thermal conductivity and a low viscosity, resulting in a Prandtl number at least an order of magnitude smaller than that for water. All liquid metals, however, are similar in this respect, and tin was chosen to simulate the flow of ferroalloys because of its comfortably low melting point, simplifying the experimental equipment and procedures.

6.2.1.1 Tin Circulation System

The simplest set-up for tin flow would be to fill the tank, seal it, and use pressurised gas (for example argon) to drive the tin out through a nozzle. If

the pressure were sufficiently high, the variation in hydrostatic pressure in the tank as it was emptied, would become unimportant. It is not certain whether thermal steady-state conditions in the plate would be obtained, but temperatures could still be measured reliably in a transient case.

A better method, which would make it possible to obtain steady-state conditions (regarded as the most favourable to work with), is to somehow circulate the tin. Several suppliers of different types of pumps were contacted, but none had the experience of pumping liquid tin and would not guarantee a system that worked. The pump project was therefore practically abandoned when it was discovered that Norsk Hydro's magnesium plant in Porsgrunn, Norway was using centrifugal pumps for conveying liquid magnesium. They were contacted and proved willing to lend a pump to the project. A pipe from the pump outlet to the upper tank was designed and the equipment was ready for testing.

Initially the pumping was not successful; i.e. no tin at all came out of the pipe. It was thought that the pump was not powerful enough to pump the tin the two vertical meters up to the tank. A test pipe of one meter in length was made to see if the pump then would work, but not so. The problem lay therefore somewhere else. The pump had previously been preheated with a gas burner for about 15 minutes before it was submerged in the tin. It was hoisted out of the metal and a new thorough preheating of approximately 30 minutes was carried out. After this the system worked as hoped.

The pump motor was connected to a frequency converter, making it possible to adjust the pump speed and obtain a correct, steady flow rate. Before the experiments started, the tin in the pump tank was heated to approximately 350 °C in a separate heating chamber and forklifted to the casting rig. The upper tank was heated to the same temperature.

6.2.1.2 Casting Plates

The first experiments were conducted using a 12 mm thick mild steel plate 630 mm in diameter, insulated on the bottom side. In this way the transient temperature evolution in the plate could be recorded. These measurements

were unsatisfactory, mainly because the tin did not fully wet the plate, especially towards the edge. It was decided to design a cooled plate where steady-state conditions could be measured.

To enhance complete wetting of the plate, the new design was reduced to a diameter of 300 mm. In addition it was cooled underneath by means of cooling channels, 20 x 20 mm in cross-section, resulting in a heat flow through the plate. Thermocouples were positioned in a radial direction from the centre of the plate along the central cooling channel, see Figure 6.10. They were fixed on the bottom, top and in the middle of the plate. Temperatures were also measured at the inlet and outlet of the cooling system.

All surfaces exposed to the surroundings were insulated with glass wool and the pipe from the lower to the upper tank and the container around the casting plate were fitted with hot-wires.

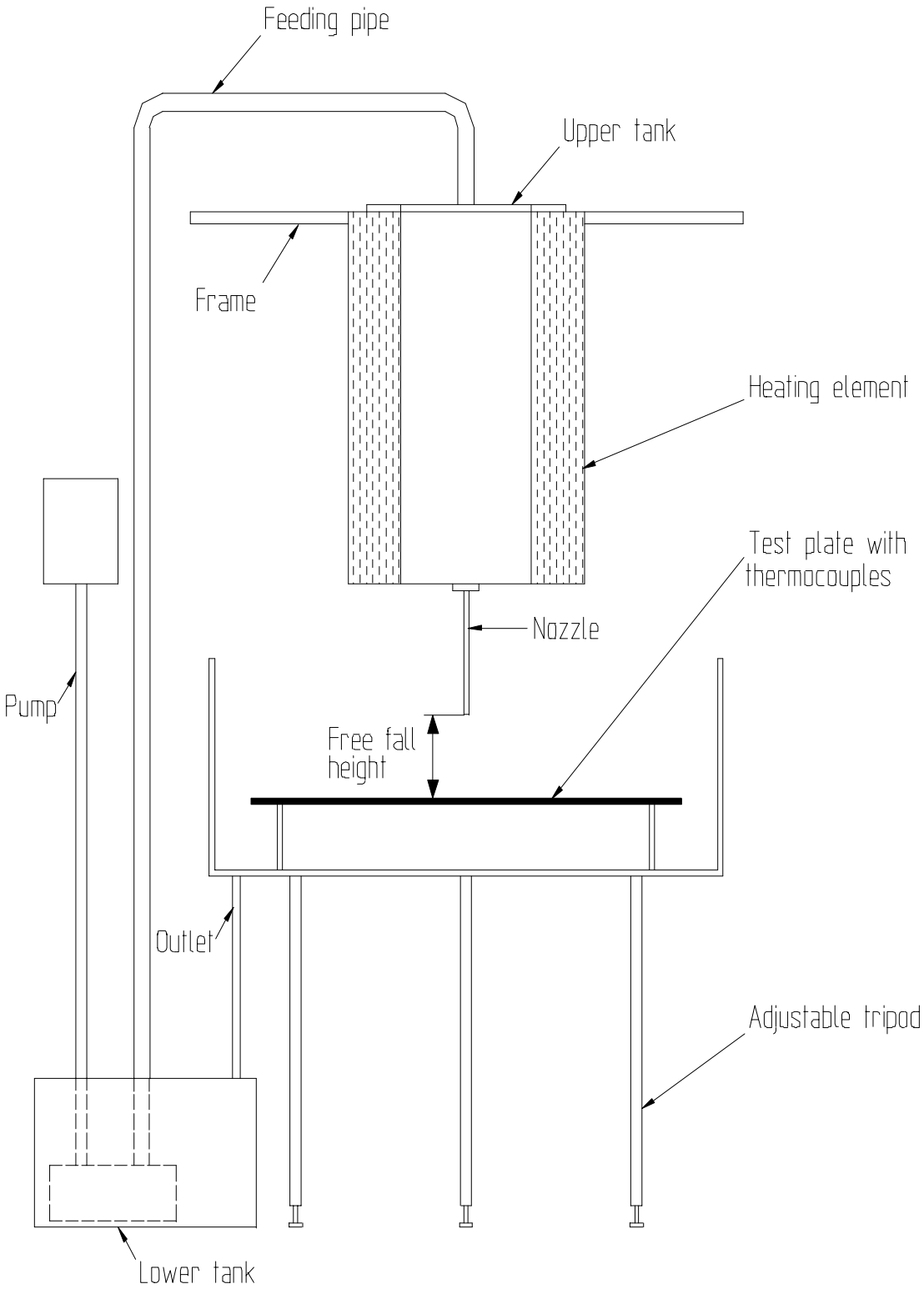

Figure 6.9 Set-up for tin experiments.

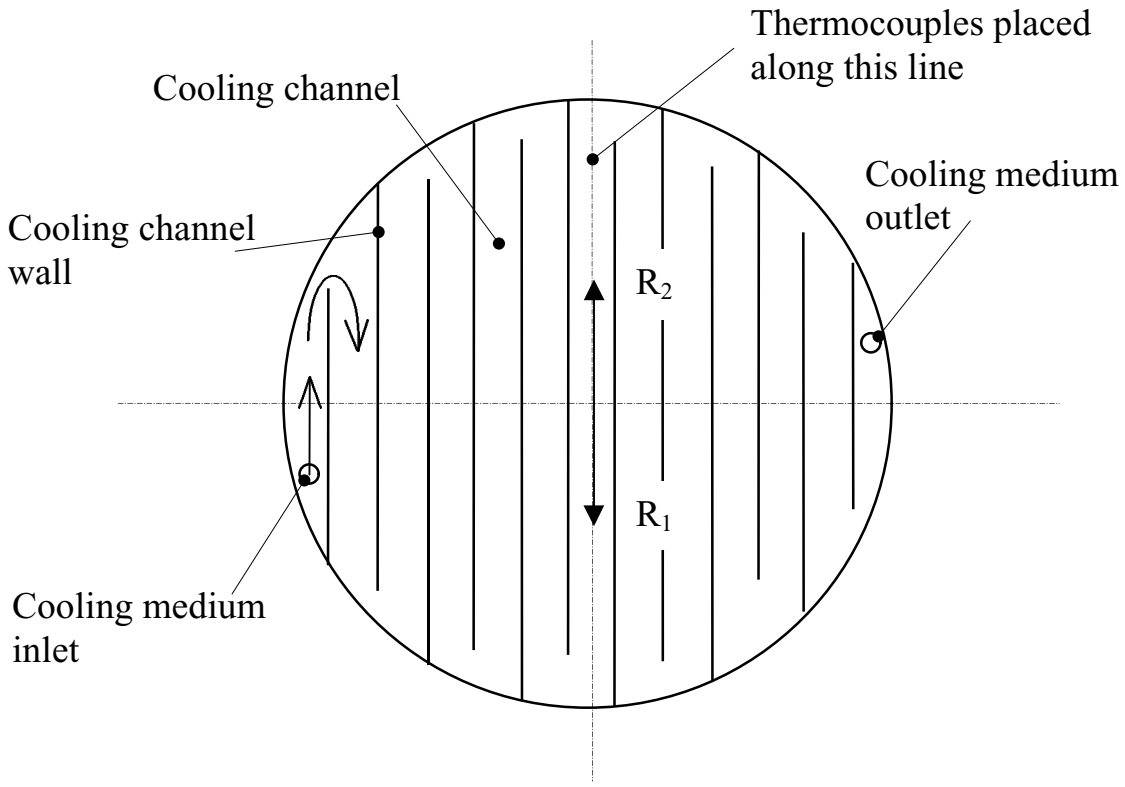

Figure 6.10 Sketch of cooling system. Casting plate removed. R_1 and R_2 are directions for thermocouple positioning, see

Table 6-1.

As seen in Figure 6.11, the thermocouples were installed in recesses machined in the plate surfaces. In this way not only the tip of the thermocouple (where the temperature is recorded) will be in touch with the media whose temperature is of interest. This ensures a better temperature measurement because the thermocouple sheath can, in some circumstances, draw heat away from the measuring point (or, when the temperature to be measured is lower than that of the surroundings, can draw heat *to* the measuring point). Grådahl and Johansen (1992) have investigated various positionings of thermocouples and how this affects the values of the measured temperatures. The recesses were cut with a small mill and the thermocouples were clamped or pinned in place by centre-punching the plate several spots at the edge of the recesses. The thermocouples were drawn out through holes in the plate. These were afterwards filled to

prevent coolant leaking to the atmosphere. This sealant has to adhere to the steel and withstand the temperature and internal pressure involved. It proved difficult to find a suitable material for this purpose. After testing various candidates, a two-component adhesive was chosen. It was not a perfect solution, as it had to be repaired twice during the experiments.

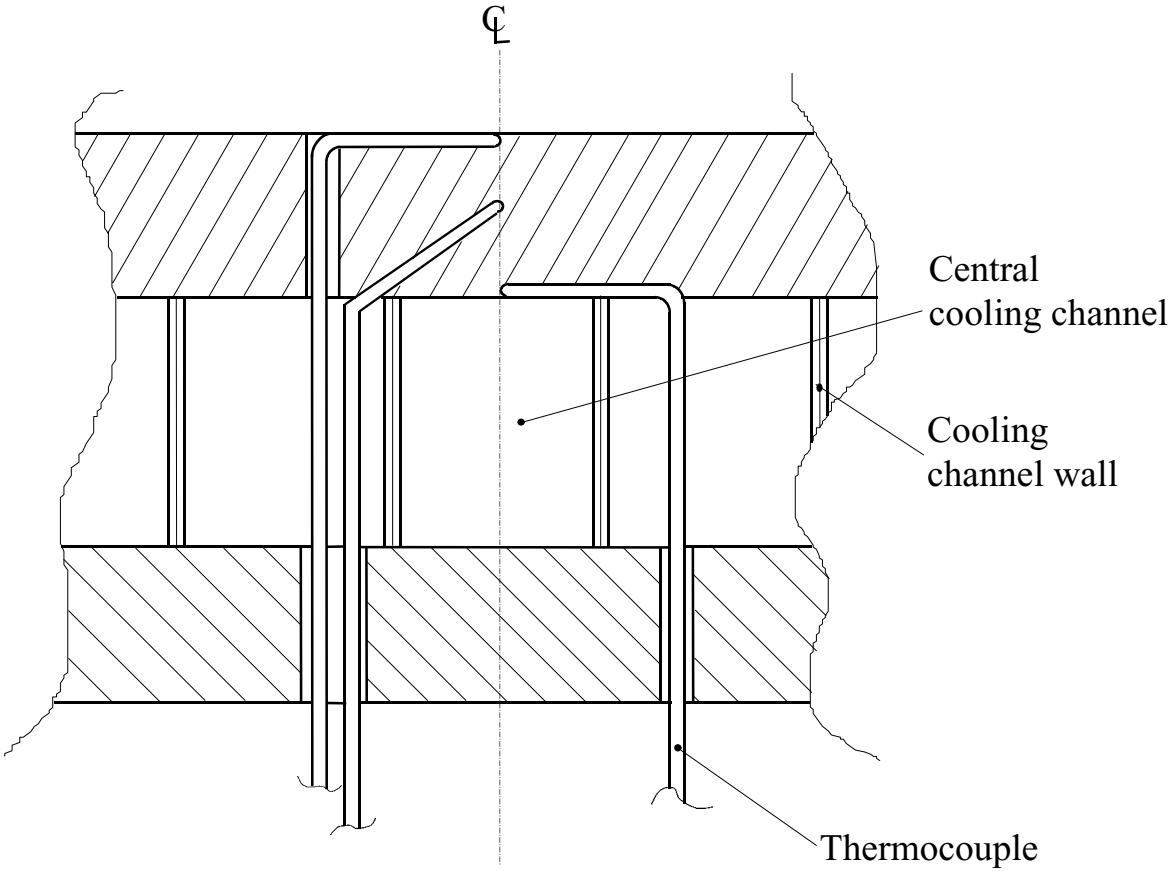

Figure 6.11 Section of casting plate with three thermocouples through its thickness.

Figure 6.11 shows three thermocouples through the thickness of the plate. To measure the heat flux from the tin to the coolant only two are strictly necessary, for example on the top and bottom surface. In some places the one in the middle was used as an additional check. The heat flux from the top to the centre thermocouple should, in a one-dimensional system, be equal to the flux from the centre to the bottom one.

The temperature of the impinging tin was measured by manually sticking in a thermocouple. The same was done to measure the tin temperature at the plate edge.

Three nozzles of 5, 8 and 10 mm in diameter were used with a heat resistant ball valve for closing the flow, mounted between them and the upper tank.

From a practical point of view, the new experiments were quite successful. The temperature measurements, however, were dubious. The calculated heat fluxes from some of the top to the middle thermocouples did not agree with those from the middle to the ones on the bottom. Also, the radial temperature distribution at the surface of the plate seemed puzzling. It was later found out that some vital thermocouples had been damaged and therefore were recording erroneous values. In addition, it is difficult to be certain of how well the middle thermocouples were in contact with the bottom of their holes. It is probable that some of them were not bottoming correctly.

Choice of New Casting Plate Material

Due to the above difficulties a third set of experiments was arranged. In connection with this, the casting plate was slightly revised. It was considered favourable that the plate's thermal conductivity was reduced somewhat. The temperature difference between the top and bottom surfaces of the plate would then increase, and possible inaccurate temperature measurements would have a smaller influence on the temperature difference (and calculated heat flux) between these two positions. A natural choice would then be stainless steel. It was not known how liquid tin wetted this material, i.e. if it would flow evenly over the plate surface or along preferred paths leaving parts of the plate dry. To investigate this, four small plates of mild steel, zinc-plated mild steel, stainless steel and copper-plated stainless steel were made and liquid tin carefully poured over them. No variations in wetting properties were evident.

Afterwards the plates were placed in an oven with identical pieces of solid tin on them. The idea was to melt the tin on the plates, turn off the oven to

let them solidify, and ultimately study their geometries. The thicknesses of the tin specimens were measured with a gauge and observed not to vary significantly amongst the samples. In each sample it varied between 4.7 and 5.5 millimetres. Secondly, the samples were magnified and projected onto paper, where outlines of their surfaces were drawn and the contact angle measured. This method is not absolutely precise, but does give an impression of the contact angles involved. There was no obvious variation between the different specimens. The contact angle is estimated to vary from 145 to 165^{o}. Besides the uncertainty of the angle measurements, the angle itself can shift during the phase change from liquid to solid. Also, the geometries of the specimens may be altered if there is a volume change when going from liquid to solid or if a sample is cooled unevenly.

Since no distinct differences in theses tests were observed, it was decided to use a plain *stainless steel plate* (AISI 316L) in the next experiments.

Stainless steel has a lower thermal conductivity than the mild steel formerly used. The plate thickness was reduced to 10 mm, but the diameter remained unchanged. The middle thermocouples (Figure 6.11) were omitted, so that measurements now were taken only at the top and bottom surface of the plate.

The thermocouples were still located along the middle cooling channel. Table 6-1 shows their exact positions. Additional thermocouples for logging coolant temperatures were placed at the outlet and inlet of the cooling system and at the ends and in the centre of the central cooling channel. By that means 51 thermocouples were connected to the plate and cooling system. Figure 6.12 to Figure 6.14 show pictures of the casting plate and cooling system.

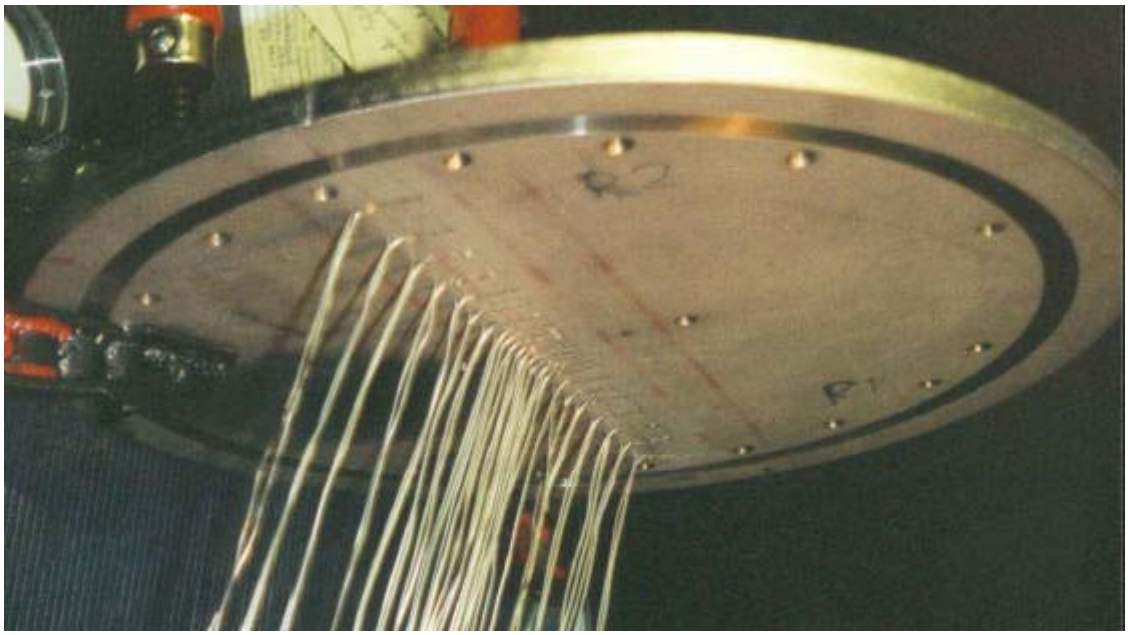

Figure 6.12 Bottom view of casting plate with thermocouples.

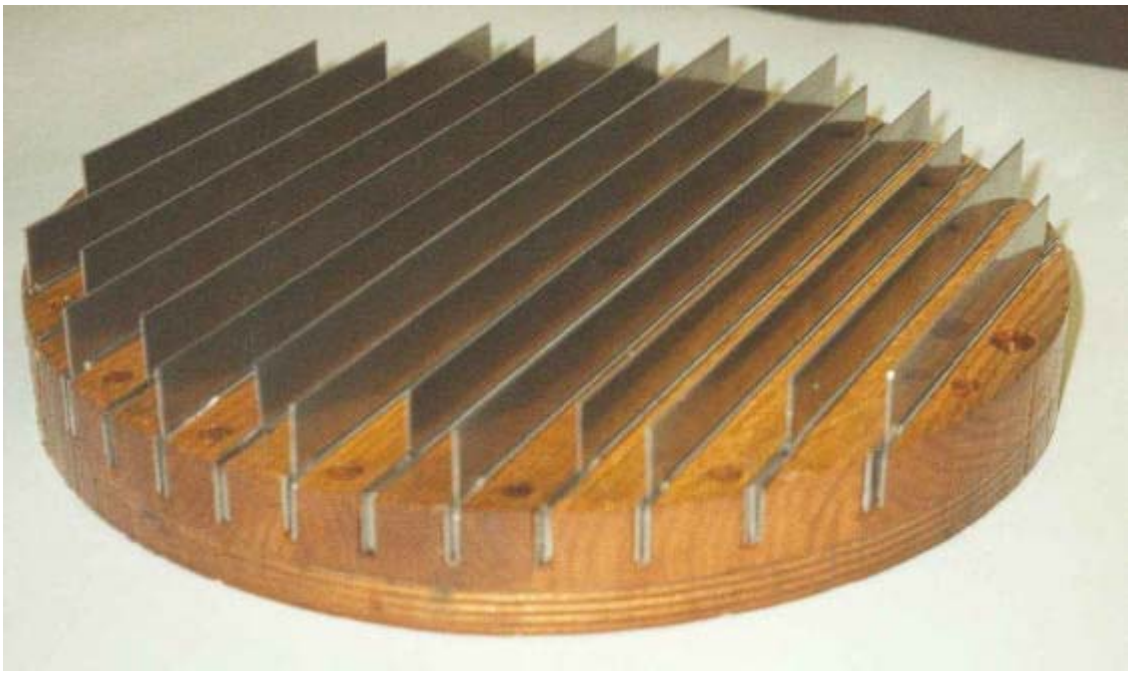

Figure 6.13 View of cooling channels under casting plate.

Figure 6.14 Assembly of casting plate and cooling system.

R_1 direction		R_2 direction	
Thermocouple #	Distance [mm]	Thermocouple #	Distance [mm]
12	0	12	0
11	5	13	2.5
10	10	14	7.5
9	15	15	12.5
8	20	16	17.5
7	30	17	25
6	40	18	35
5	50	119	45
4	65	20	57.5
3	80	21	72.5
2	95	22	87.5
1	120	23	107.5

Table 6-1 Distance from centre and numbering system for thermocouples in casting plate. R_1 and R_2 are defined in Figure 6.1.

6.2.1.3 Cooling Media

Separate experiments were conducted with air and water as cooling agents. The water flow was simply measured by a stopwatch and bucket technique. The air was taken from a compressor outlet and though a flowmeter before running through the casting plate. This meter is permanently coupled to the air system in the laboratory. After some time it was decided to check this meter for accuracy by hooking on another one before the plate. It was discovered that the fixed flowmeter showed an airflow only 60% of the new measurement. The new instrument was checked and found reliable and was thereafter permanently connected to the apparatus.

After a while leaks in the plate cooling system were detected. Some coolant leaked out by the thermocouple holes. Application of aluminium oxide cured most of this problem. It was appreciably worse on the bottom where the "cooling channel part" mated with the plate itself. Various

remedies were tried to seal the plate, but none succeeded in resolving the problem completely. As a result a certain leakage had to be endured. Due to the more or less permanent affixing of the thermocouples, the system could not be disassembled completely for more thorough repair and alteration.

To obtain knowledge of the magnitude of the leaks, it was decided to measure the airflow also at the outlet of the plate. The gauges available to meter this are not designed to withstand the temperatures appearing in the system - approximately 180 °C. The air must therefore be cooled before entering this gauge. A counter-flow heat exchanger was specially designed and built for this task. Water was used for cooling and both water and air inlets and outlets were equipped with thermocouples. In this way the heat absorbed by the cooling air could be measured, which could act as a check for the heat flow through the plate calculated from the plate temperature measurements.

6.2.2 Thermocouples and Data Acquisition

The thermocouples were all type K with Inconel (stainless steel) sheath material and a diameter of 1 mm. The temperatures were recorded with three Campbell Scientific 21X microloggers. One of these was connected to a model AM32 32-channel multiplexer (relay scanner). Each logger has eight channels, so that in total 55 temperatures (one channel in the third logger is for the multiplexer) could be logged simultaneously. Data is stored in the loggers' internal memories and regularly transferred to a PC for processing in a worksheet. Temperatures were recorded every 10 seconds.

6.2.3 Results

First of all, cooling with water was too forceful, in the way that tin solidified on the plate. Hot water from the tap (~60 °C) was also tried, but results were similar. Secondly, the flow from the 5 mm nozzle was not adequate to wet the entire plate. After the jump, the flow seemed to

accumulate in streams, leaving parts of the casting plate dry. Subsequently the experiments were continued with only 8 and 10 mm nozzles at two different nozzle to plate spacings: around 30 and 90 mm. Above 90 mm there was too much splashing. The flow rate could not be altered with overflow systems as with water, but attempts were made to vary the tin level in the upper receptacle (and thus the flow) by regulating the pump speed.

The impinging jet seemed more irregular with tin than with water. This may be due to the ball valve, as the water jet became steadier without it. Coinciding with water, the tin film thickness after the jump appeared to be constant all the way to the plate edge. This thickness was measured to 5-5.5 mm. No dependency on nozzle size and nozzle to plate spacing was noticed.

Quite soon *oxide formation* in the tin became evident. On the plate it was visible as a thin layer on the tin surface, but only after the jump. In the pump container stirring of the tin was more vigorous and heavy oxidation took place. In fact, after 15-20 minutes of running there was so much oxide that the experiments had to be stopped and continued the next day with a fresh supply of tin. Excessive clearance between the pump shaft and its housing created violent stirring and contributed strongly to the oxidation. A new seal was made, which reduced the problem somewhat, but not sufficiently to eliminate it. Some places on the plate (after the jump), the oxide stayed still, with tin flowing beneath. It was regularly scraped off. Other places it followed the tin off the plate. Oxide formation seemed to take place quite soon after scraping. It is not clear exactly how this oxide affects the tin flow, but observations indicate that it shifts the jump a little inwards.

Generally the tin seemed to flow off the casting plate in a pulsating manner. Also, the jump was not as circular in appearance as with water, but more irregular around its circumference. It is not known if this feature is inherent to the system and flow variables or has to do with the oxide formation. Marcussen and Hansen (1998) have with ethylene glycol found that the regular ring-shaped hydraulic jump can change its shape spontaneously into stationary polygons with four to eight corners. Their work is still in progress.

An attempt to reduce the tin oxidation was made by trying to flush the three major parts of the system with inert argon gas; the upper and lower receptacles and the casting plate. It is impossible to enclose these sufficiently to make them air tight, so constant flushing with gas was necessary. This cooled the tin, but most importantly the gas flow around the casting plate disturbed the flow of the tin. The experiments were therefore forced to continue without gas purging, but with the unfortunate oxide formation. Figure 6.15 shows pictures from the tin experiments.

Figure 6.15 Photographs of tin experiments with 10 mm nozzle.

Figure 6.16 to Figure 6.19 show samples of temperature recordings from the tin experiments. One may notice that the temperature does not always regularly decrease with increasing radius. The distinct dips in the curves are disturbances from the jet temperature measurements. The scraping of the oxide did not noticeably affect the temperatures.

Table 6-2 and Table 6-3 compare the theoretical and observed jump positions for all tin experiments. The critical velocity method is based on the surface profile predicted by Alekseenko et al., and, as for water, predicts a jump position far outward of that observed. Watson's turbulent jump position is nearest the plate centre with the turbulent Bernoulli position just outside. The results from the laminar Watson and Buyevich/Ustinov models are very similar results, with Watson's jump position consistently furthest out. The laminar Bernoulli model predicts jump positions a little inward of these. The Froude numbers at the jump are two to three times larger than those experienced with water.

With tin the laminar calculations seem to give the best results regarding the jump position. All models appear equally accurate in this connection.

Flow rate [10^{-4} m^3/s]	Free fall height [m]	*Re* in jet	Observed jump position [m]	Watson	Critical velocity method	Buyevich and Ustinov	Bernoulli	*Fr* at jump start (Bernoulli model)
1.000	0.081	79560	0.11	0.107/0.077	0.152	0.105	0.096/0.082	19.42/14.17
1.044	0.090	83150	0.11-0.12	0.112/0.080	0.150	0.110	0.100/0.086	19.20/13.69
0.959	0.028	72630	0.11	0.100/0.073	0.147	0.099	0.092/0.080	18.60/13.36
1.132	0.089	98140	0.10	0.120/0.086	0.164	0.118	01.06/0.092	19.23/13.16
1.093	0.048	83620	0.10-0.11	0.115/0.083	0.160	0.113	0.104/0.088	18.23/13.37
1.070	0.088	84800	0.10	0.114/0.082	0.159	0.112	0.102/0.088	19.01/13.45
1.100	0.089	86950	0.10-0.11	0.116/0.084	0.161	0.115	0.104/0.090	19.13/13.30
1.046	0.092	83490	0.10	0.112/0.080	0.152	0.110	0.100/0.086	19.30/13.75
1.051	0.037	79830	0.10-0.11	0.110/0.080	0.156	0.108	0.100/0.086	18.41/13.19

Table 6-2 Jump positions for tin in 8 mm nozzle. Plate radius 150 mm. Where two values separated by slashes are given, the first is based on a laminar model and the second on a turbulent model. The critical velocity method is based on the turbulent theory of Alekseenko et al. The Buyevich and Ustinov model is laminar.

Flow rate [10^{-4} m^3/s]	Free fall height [m]	*Re* in jet	Observed jump position [m]	Watson	Critical velocity method	Buyevich and Ustinov	Bernoulli	*Fr* at jump start (Bernoulli model)
1.368	0.085	89250	0.13-0.14	0.135/0.096	0.180	0.132	0.120/0.102	16.66/11.55
1.193	0.028	73480	0.12	0.114/0.083	0.165	0.112	0.105/0.091	16.32/11.37
1.325	0.089	87290	0.13-0.14	0.131/0.093	0.177	0.129	0.118/0.100	16.58/11.61
1.399	0.048	87240	0.12-0.13	0.136/0.096	0.182	0.133	0.123/0.103	16.00/11.35
1.365	0.088	89370	0.13	0.135/0.096	0.180	0.132	0.120/0.102	16.67/11.55
1.374	0.085	89560	0.13	0.136/0.096	0.181	0.133	0.120/0.102	16.89/11.60
1.442	0.092	93870	0.13	0.142/0.100	0.186	0.139	0.126/0.106	16.49/11.45
1.484	0.037	90860	0.13	0.143/0.101	0.188	0.140	0.129/0.107	15.66/11.20

Table 6-3. Jump positions for tin in 10 mm nozzle. Plate radius 150 mm. Where two values separated by slashes are given, the first is based on a laminar model and the second on a turbulent model. The critical velocity method is based on the turbulent theory of Alekseenko et al. The Buyevich and Ustinov model is laminar.

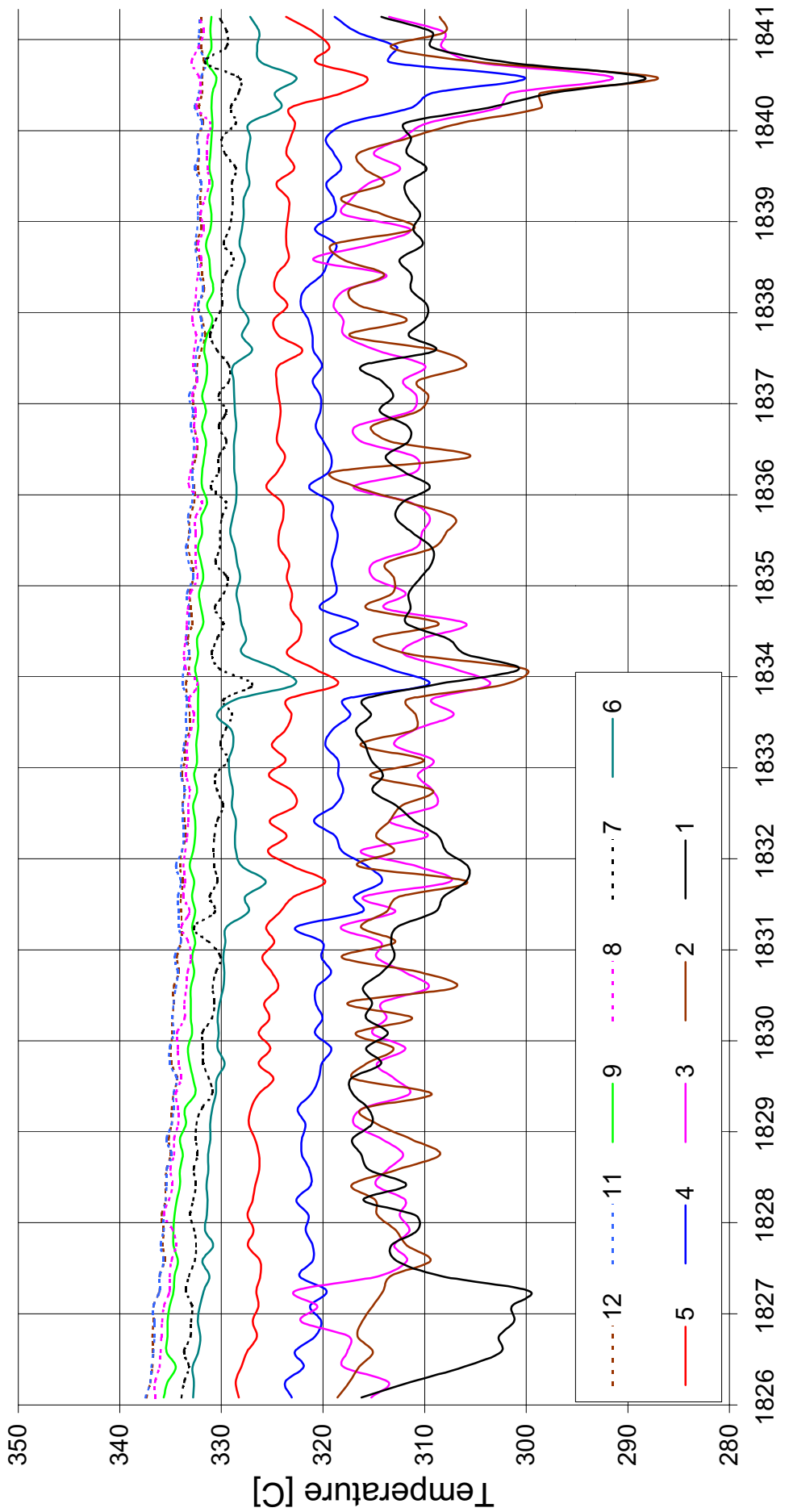

Figure 6.16 Temperature curves for thermocouples 1 to 12 in top surface of casting plate. Tin flow through 8 mm nozzle, $1.07 \cdot 10^{-4}$ m^3/s, 88 mm free fall height. Thermocouple 10 is defective.

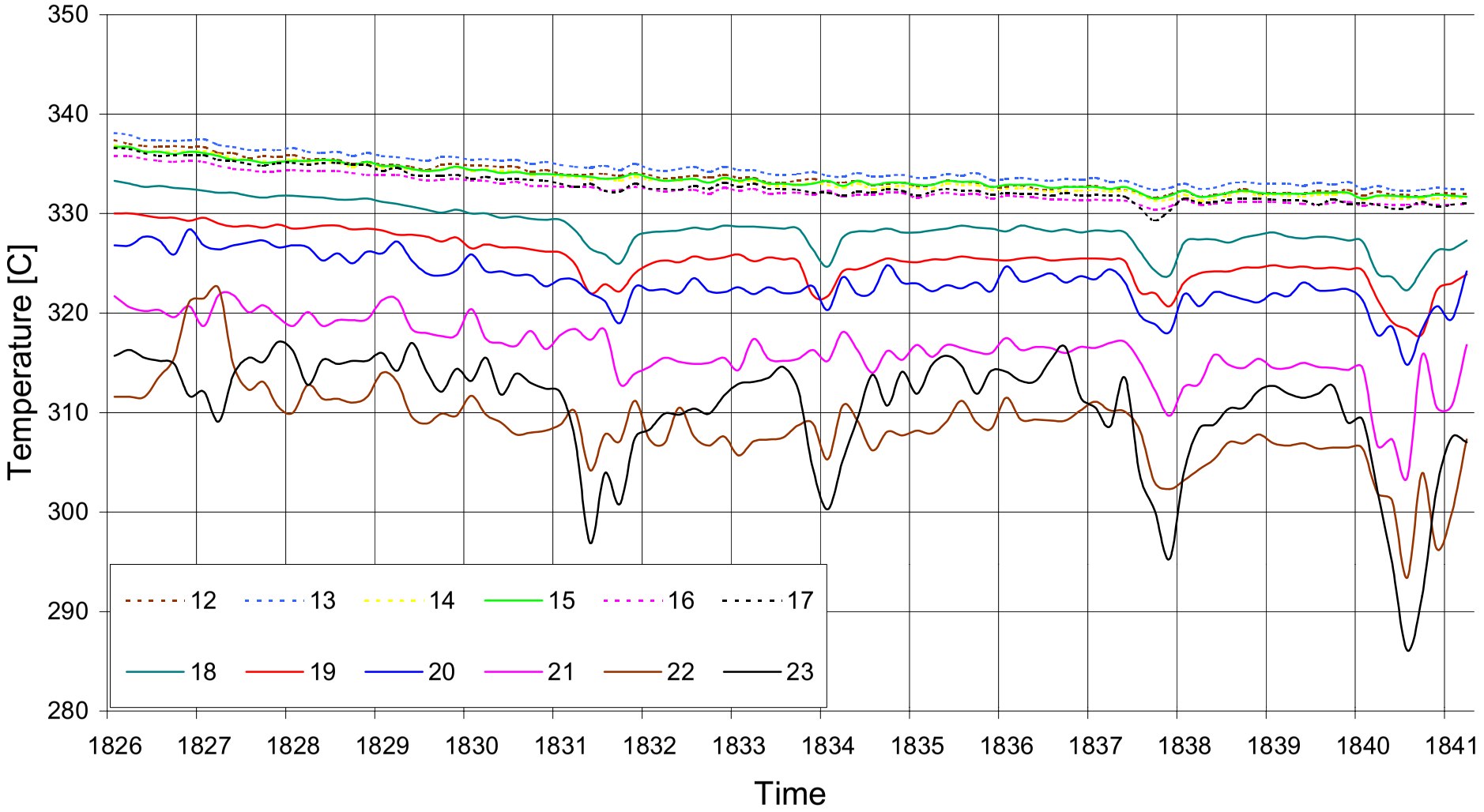

Figure 6.17 Temperature curves for thermocouples 12 to 23 in top surface of casting plate. Tin flow through 8 mm nozzle, $1.07 \cdot 10^{-4}$ m^3/s, 88 mm free fall height.

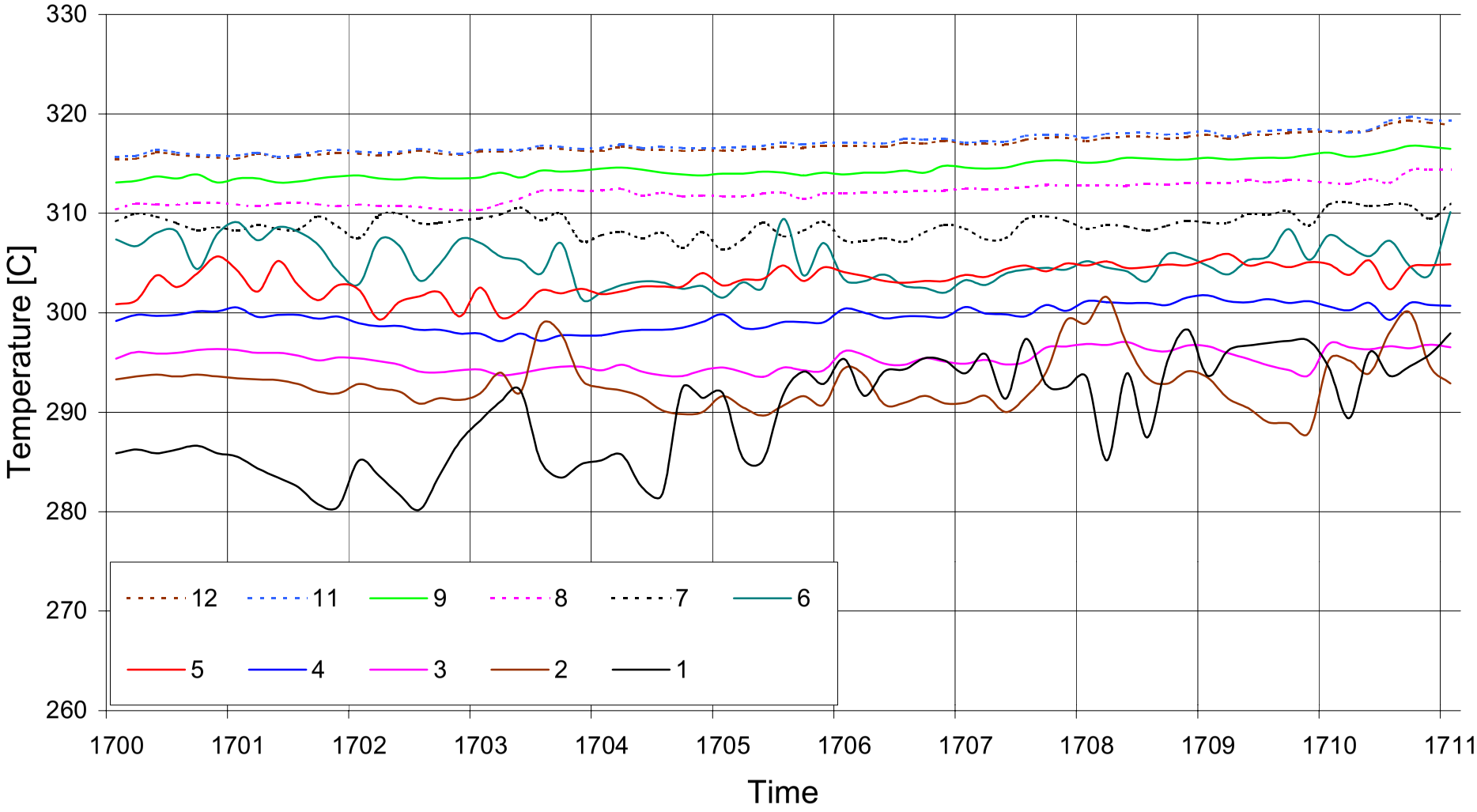

Figure 6.18 Temperature curves for thermocouples 1 to 12 in top surface of casting plate. Tin flow through 10 mm nozzle, $1.48 \cdot 10^{-4}$ m^3/s, 37 mm free fall height. Thermocouple 10 is defective.

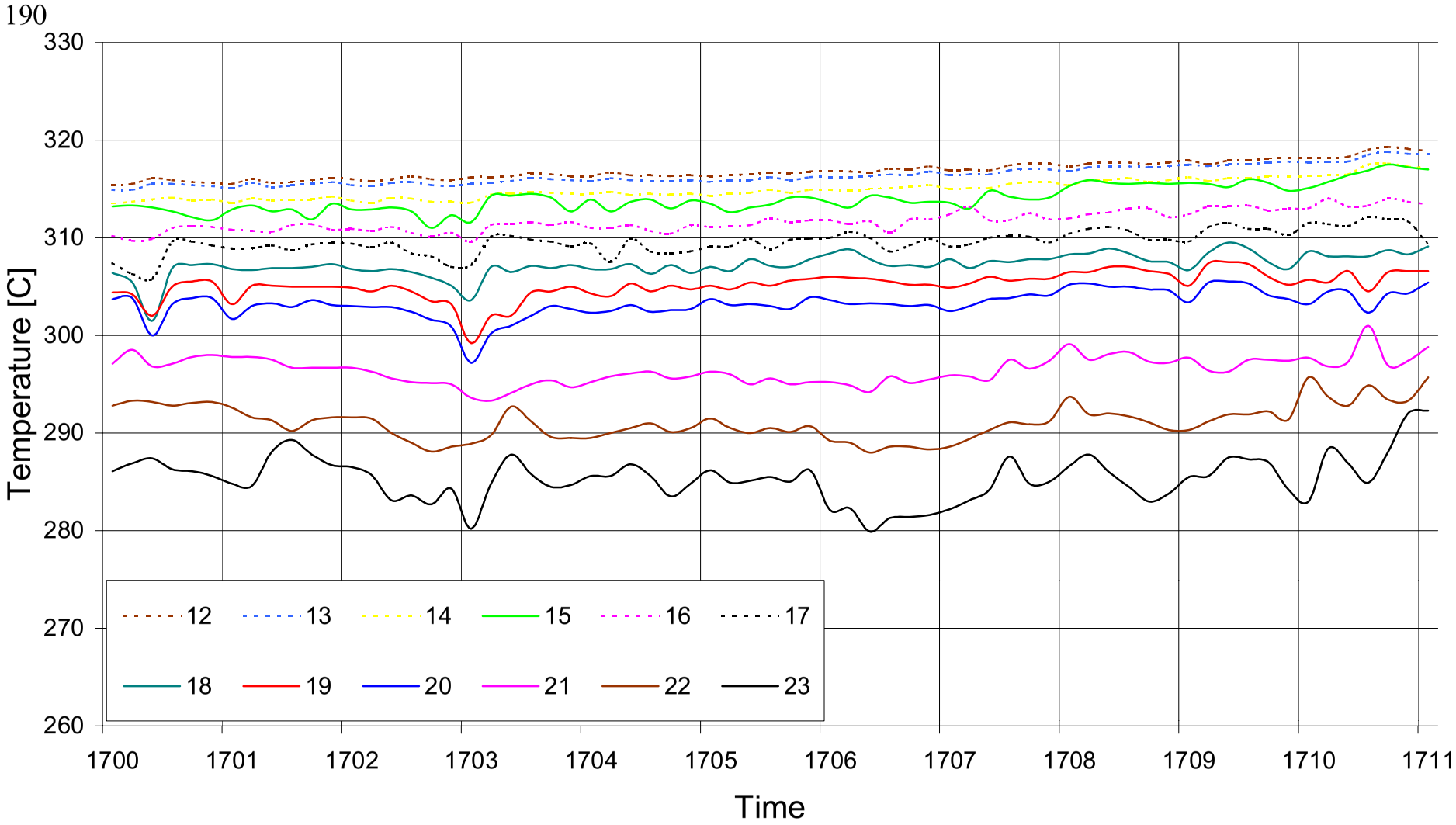

Figure 6.19 Temperature curves for thermocouples 12 to 23 in top surface of casting plate. Tin flow through 10 mm nozzle, $1.48 \cdot 10^{-4}$ m^3/s, 37 mm free fall height.

6.2.4 Error Analysis

The 21X micrologger determines a thermocouple temperature by first measuring a reference temperature. This is usually the logger's own temperature, measured with a built-in thermistor. The logger then calculates the voltage that a thermocouple of the specified type would output with respect to a reference temperature of 0 °C. This voltage is added to the measured thermocouple voltage. The temperature at the measuring point is then calculated according to an international temperature-voltage scale.

The error in a thermocouple temperature measurement is the sum of the errors in the reference junction temperature, the thermocouple output, the voltage measurement in the logger, and the error involved when converting voltage to temperature (this computation is managed by the logger). Table 6-4 shows estimated errors in a thermocouple at approximately 400 °C.

Source	**Error** [°C]
Thermocouple	±3
Compensation leads (at room temperature)	±0.3
Reference temperature	±0.2
Micrologger*	±0.2
Sum of individual errors	±3.7
Correct uncertainty analysis error	±3.5

* This error consists of voltage measurement and voltage to temperature conversion uncertainty.

Table 6-4 Estimated errors in thermocouples.

In Table 6-4 the correct uncertainty value is calculated by the following method, cf. Grådahl (1999):

$$2\sqrt{\left(\frac{3}{\sqrt{3}}\right)^2+\left(\frac{0.3}{\sqrt{3}}\right)^2+\left(\frac{0.2}{\sqrt{3}}\right)^2+\left(\frac{0.2}{\sqrt{3}}\right)^2}=3.5\ ^\circ\mathrm{C}$$

Additional errors that may exist are:

- ageing of the thermocouples
- thermocouples exposed to radiation from nearby equipment (increases the registered temperature)
- only exposing the tip of the thermocouple to the temperature of interest
- variations in ambient temperature (affects reference temperature in datalogger)

These factors are estimated to be of no importance in this work.

A temperature uncertainty of ±3.5 °C is not acceptable in his study, making it necessary to calibrate the thermocouples. With the equipment available the uncertainty could then be reduced to ±0.9 °C. Due to already booked workshop time, the thermocouples could not be calibrated before they were fixed in position. Following the experiments, the thermocouples were dismantled from the casting plate for calibration. Some could not be removed without breaking them, and in these the two leads were welded together. The effect of this on the calibration was tested by calibrating a few thermocouples twice - first as whole ones and thereafter cut and welded. The difference was negligible.

The calibration was performed at five different temperatures: 100, 200, 250, 300 and 380 °C. This was in the operating range of all thermocouples, except the four measuring water temperatures in the heat exchanger, the inlet temperature of the cooling air and the air temperature out of the heat exchanger.

The indicated temperatures proved to be above the reference temperature for practically all thermocouples. The highest indicated value was 3.76 °C

above reference and the lowest 0.7 °C below. The deviation was in general least at the lowest reference temperature. At 200 °C and above most of the thermocouples displayed a relatively constant error of about +3 °C.

6.3 Experiments with Silicon Metal

It is of course desirable to perform experiments with ferroalloys, which after all are the materials this study is aimed towards. The existing set-up for tin can not be used due to the high temperatures involved (up to 1600 °C). Also, these metals are excellent solvents for many other materials. An important task is therefore to find a material that can withstand such an environment. It is also of great importance that the material can be machined so that a smooth "casting plate" can be created and equipped with thermocouples. In addition their thermal shock resistance should be good and their conductivity not too "high" or too "low" in order to achieve satisfactory temperature measurements. As in the tin experiments, a suitable value would be 10 to 40 W/mK. Finally they must be available in large enough pieces and be of reasonable cost.

It was planned that a rig be made and installed at Elkem's silicon plant in Kristiansand, Norway and 99% silicon-metal be used in the experiments.

No well-suited materials for this specific application were known of and a literature study was initiated in order to find possible candidates. Afterwards simple experiments could be conducted to test their thermal and chemical properties.

First the natural elements were investigated, then oxides, silicates, borides, carbides, nitrides, ceramics and some refractory materials. Phase diagrams between silicon and the other elements were studied to check the solubilities. Based on these and other properties and availability, it was decided to test the following materials in liquid silicon metal:

- tungsten with 2% thorium oxide, ThO_2

- boron nitride, BN

- titanium with 2% boron

- partly stabilised zirconium oxide, PSZ

- titanium boride, TiB_2

- silicon carbide saturated on silicon, SiSiC

- silicon nitride, Si_3N_4

- aluminium oxide, Al_2O_3

The samples were of different sizes and shapes and as it is beneficial to have them all alike, they were all made equal to the smallest one, i.e. 4x5x10 mm in size. They were then cleaned and weighed.

The test was intended to somehow expose the specimens to liquid silicon metal, preferably with a relative velocity between the two. The resulting design for a testing system consisted of a rod with two discs at one end. The specimens could be pressed between the discs and lowered into a crucible with silicon metal. The other end of the rod was fitted to an electric motor mounted in a rack. See Figure 6.20. The test was determined to last for about one half hour, which is a likely duration for the actual casting experiments with silicon.

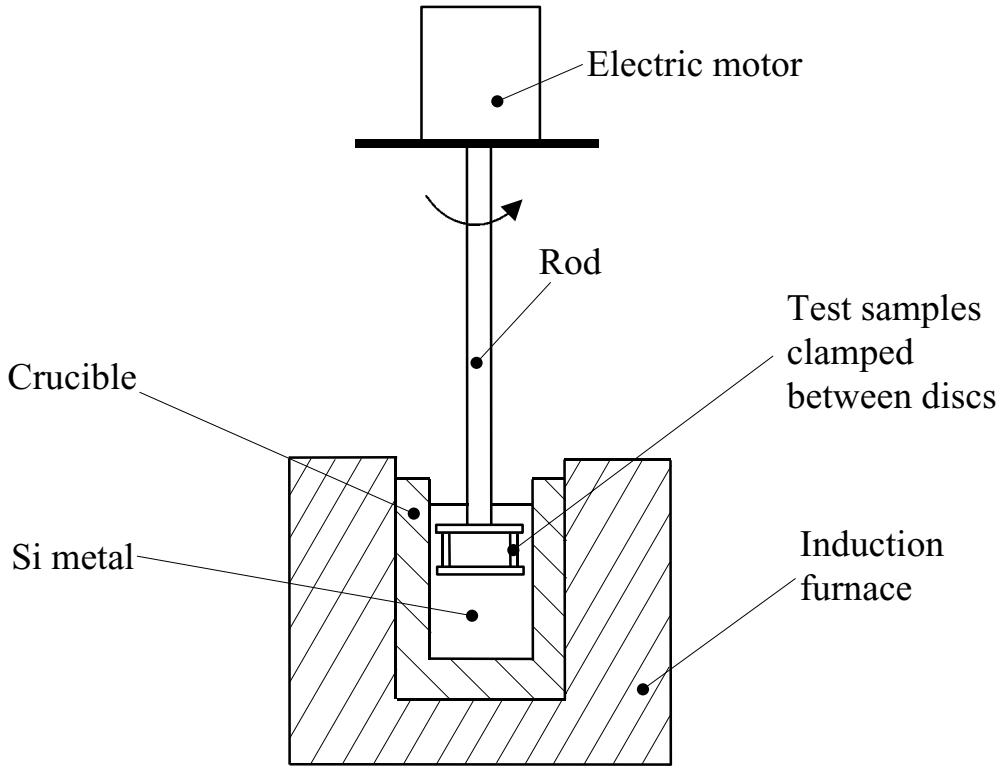

Figure 6.20 Set-up for testing material samples in liquid silicon-metal.

The samples were fastened between the two discs by means of a screw, which forced the discs towards each other, clamping the samples in between. The crucible, rod, discs and screw were all machined in graphite. This is a material known to withstand liquid silicon. The reason it can not be used in the casting experiments is that it disintegrates quite rapidly in air when heated. The rod was designed thick enough to last through the test and its disintegration would not disturb the test.

The crucible was first filled with crushed silicon, then placed in an induction furnace for melting. Afterwards, the samples would be lowered into the melt and the motor started to induce a rotation, providing a relative motion between the samples and the melt. Due to its low electric conductance (and of course contact resistance between the crushed pieces), solid silicon metal will not permit efficient heating of itself by induction. Since the furnace produces heat in this manner, a graphite crucible is used.

This crucible can be heated by induction and will conduct heat to the silicon inside. Although the system is a little time consuming it works perfectly well.

After melting the silicon, the rod with discs and samples was lowered into the melt. Soon afterwards the rod broke completely off just above the upper disc. The cause of the fracture is most probably temperature gradients inducing stresses in the rod. There is also a substantial notch in this region accentuating the stresses further.

Owing to lack of time, a new, improved system could not be built. A simplified test was therefore decided upon as an alternative. The discs with samples (everything still intact) were now to be submerged in liquid silicon with no relative motion. A new crucible was machined and the discs with samples put inside and covered with crushed silicon. The discs were wedged in place because they are of lower density than silicon metal and would otherwise float to the top of the melt, perhaps leaving the samples dry. The crucible and its contents was put in an inductive vacuum furnace and let to stand for one hour after the silicon had melted. The reason for this furnace being used is that we now could create an oxygen-free atmosphere that would prevent unwanted oxidation of the metal.

Finally the crucible was removed from the furnace and the metal poured out. The crucible has to be cracked open to get at the discs with samples, as they had become stuck to the crucible wall. Quite surprisingly only one sample was left, namely *siliconcarbide saturated on silicon* (SiSiC). All the other specimens had completely vanished. With the limitations in the number of material samples tested, a rudimentary conclusion is that SiSiC is the only material suitable for the silicon casting experiments.

Unfortunately time and cost would not allow for experiments with silicon metal to be implemented in this study.

7. Computational and Experimental Results

7.1 FLUENT Simulations

Various types of FLUENT simulations have been carried out, both with and without the VOF method.

There are no remarks in the FLUENT manual of any limitations in the program's capabilities of simulating a free-surface impingement flow, and it was more or less taken for granted that that this was achievable. However, in the long run, this proved to be impossible.

A free-surface flow test was also performed with another simulation code, but these results were disappointing as well. Lack of time and money made it impossible to pursue the problem any further by trying other codes.

7.1.1 Boundary Conditions

7.1.1.1 Symmetry

The geometry of the problem is axisymmetric, making it logical to impose such boundary conditions along the jet axis. This greatly reduces computational time. Mathematically this means there is zero normal velocity and zero normal gradients of all variables at the axis.

7.1.1.2 Inlet

In order to minimise the number of cells, the inlet (impinging jet) was modelled as close to the plate as possible, taking into account the acceleration and contraction of the jet from the nozzle. In calculations involving turbulence, FLUENT requires input of a *turbulence intensity* and a *characteristic length* for turbulent fluctuations at the inlet in order to derive values for the turbulent kinetic energy and its dissipation rate there. These were set to 5% and 1 mm (~1/10 of the nozzle diameter), respectively - empirically derived values for pipe flows. These parameters

and the velocity were distributed evenly over the cross-section of the inlet. Swirl was not included in the computations.

7.1.1.3 Flow Exit

When details of the flow at its exit from the computational domain are unknown prior to a computation, outlet boundary conditions must be used. A flow exit can be modelled with either *outlet* or *inlet* cells. The first uses a zero normal gradient for all properties except pressure. With inlet cells the user specifies appropriate velocity or pressure values.

FLUENT's outlet cells are provided with an overall mass balance correction feature. This accelerates convergence and the correction is zero in a converged solution where mass balance is obeyed locally in each control volume. Unfortunately this disposition also means that fluid can be *pulled into* the domain through the outlet. Even if this inflow persists, a converged solution with perfect mass balance can be obtained. However, the mass flow through the domain is now *undefined*, i.e. all control over incoming fluid is lost, naturally leading to invalid results. In addition, the scalar properties of the "pulled-in" fluid, such as temperature, are not defined. FLUENT uses the temperature of the cell adjacent to the outlet. As said in the manual*: "you should view all calculations that involve flow entering the domain through an outlet boundary with scepticism*".

The thickness of the tin film at the plate edge did not vary significantly between the different experiments. Subsequently, in all simulations with a pre-defined surface profile, it was specified to 5.5 mm - as measured experimentally.

7.1.1.4 Free Surface of Liquid

The VOF model includes shear stress between the liquid and the air above. In simulations with a prescribed surface profile, a wall boundary exerting *no shear stress* on the fluid was defined. This simplification has negligible effect on the final results because the viscosity of the liquid is much larger than the viscosity of air. A frictionless wall is incidentally identical to a symmetry boundary condition.

Either a fixed heat convection coefficient (for both radiation and convection) or no heat transfer at all was set at the free surface. The latter was used when comparing FLUENT simulations with analytical results involving heat transfer only from the underside of the fluid.

7.1.1.5 Underside of Fluid

A no-slip (zero fluid velocity at the fluid/wall interface) wall condition was used for the plate beneath the fluid. The roughness parameter is set as for a smooth wall, which in FLUENT is specified with a roughness height of zero. To reduce the number of nodes, the plate itself was not modelled. The heat flow to the cooling medium through the plate was taken care of by specifying an overall heat transfer coefficient. The convective heat transfer coefficient for the cooling air was based on measurements of the air flow rate and temperature and the following correlation for turbulent flow in closed channels (Rogers and Mayhew (1967)):

$$h_c = 0.023 \frac{k}{D_h} \mathrm{Re}^{0.8} \mathrm{Pr}^{0.33}$$

7.1.2 VOF Simulations

The free surface simulations in FLUENT with the VOF method were encumbered with problems. The first simulations (with version 3.03) seemed initially to produce reasonable results. For verification, a *subroutine* that checked the mass-balance in the domain *was programmed* and implemented. A *large inconsistency* between the mass entering the domain and the sum of that accumulated and exiting was noticed. Numerous combinations of numerical procedures, boundary conditions and grid structures were experimented with. Both impinging jets and "jets" parallel to the plate surface were tried in axisymmetric and rectangular coordinates. No alternative set-up would correct the severe imbalance of mass.

Later versions of FLUENT have rectified this error, but in return seem to contribute with new ones. The dominant problem now was that drops of liquid emerged at the strangest places, resulting in highly unrealistic flow fields. This is believed to originate from the innate characteristics of FLUENT's outlet condition, i.e. fluid being brought into the domain via the outlet. At the beginning of the simulation, the jet seemed to strike the plate nicely and spread radially as a thin film towards the plate edge. The problems commenced when the flow reached the outlet at the edge. See Figure 7.1 for details. The last version of FLUENT used was 4.51.

Various locations of the outlet were tested, but none made any real difference to the results. See Figure 7.2.

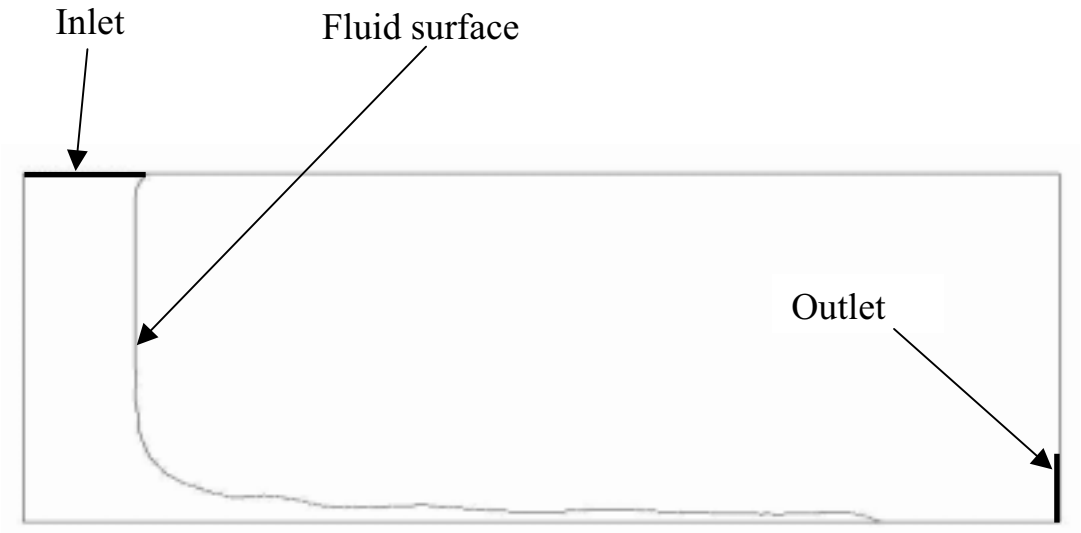

a)

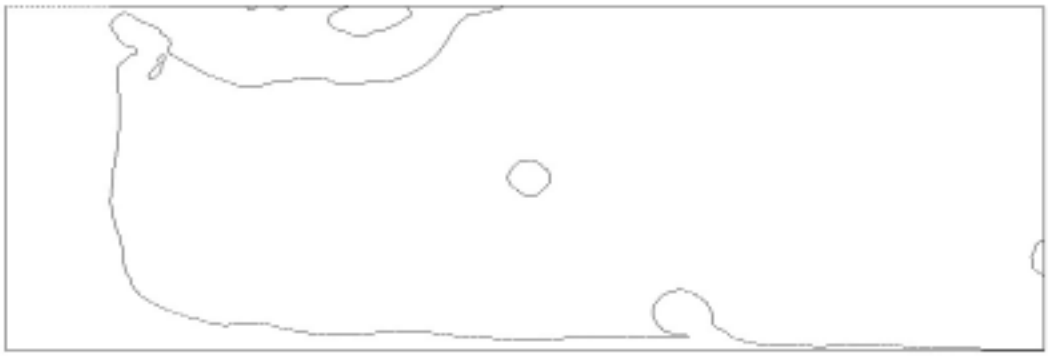

b)

Figure 7.1 Example of VOF calculation with water flowing through an 8 mm nozzle and impinging on a flat plate. Domain size is 15x40 mm.

a) fluid surface after 0.02 seconds.
b) fluid surface after 0.055 seconds.

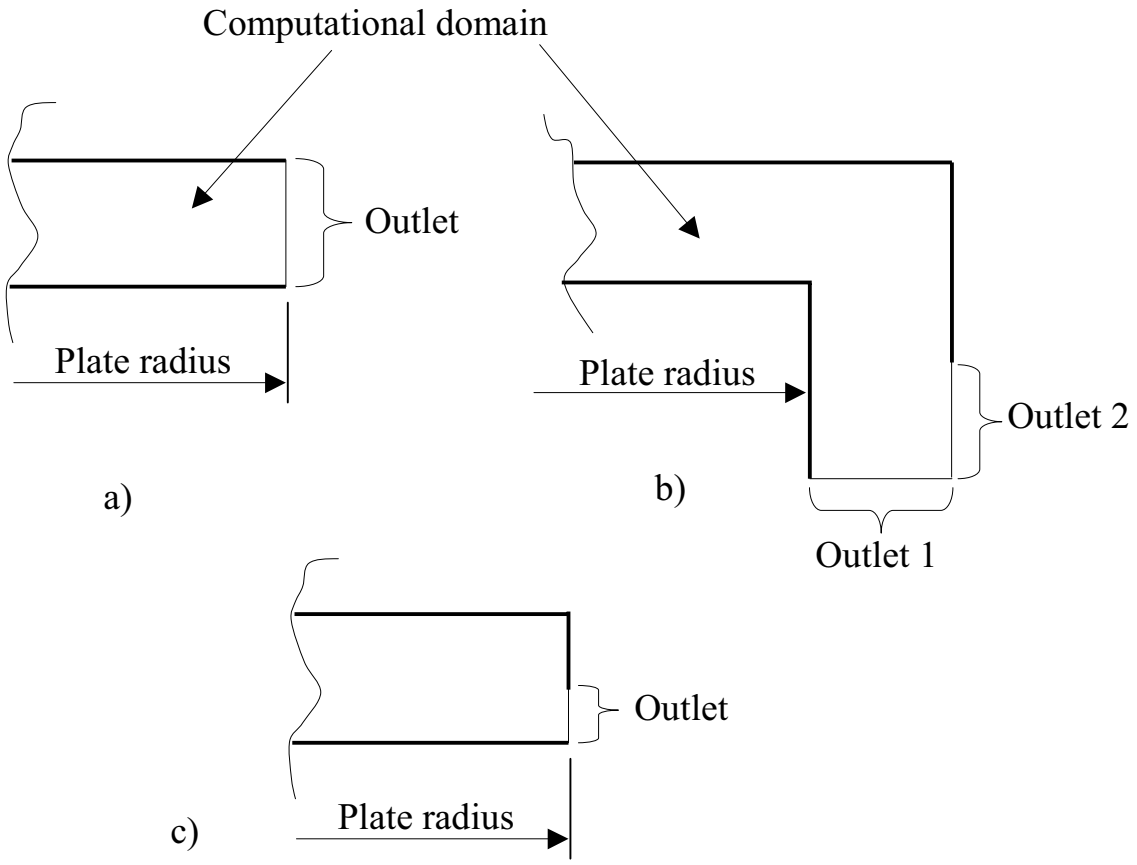

Figure 7.2 Three examples of model configurations for VOF simulations. a) - outlet over the whole domain height at edge of plate. b) - domain extends beyond edge of plate and fluid "turning the corner" is modelled. Flow is emptied into basin with two alternative outlet locations. c) - size of outlet is set equal to expected film thickness at plate edge.

Figure 7.3 shows results from another VOF simulation with set-up similar to Figure 7.2 b).

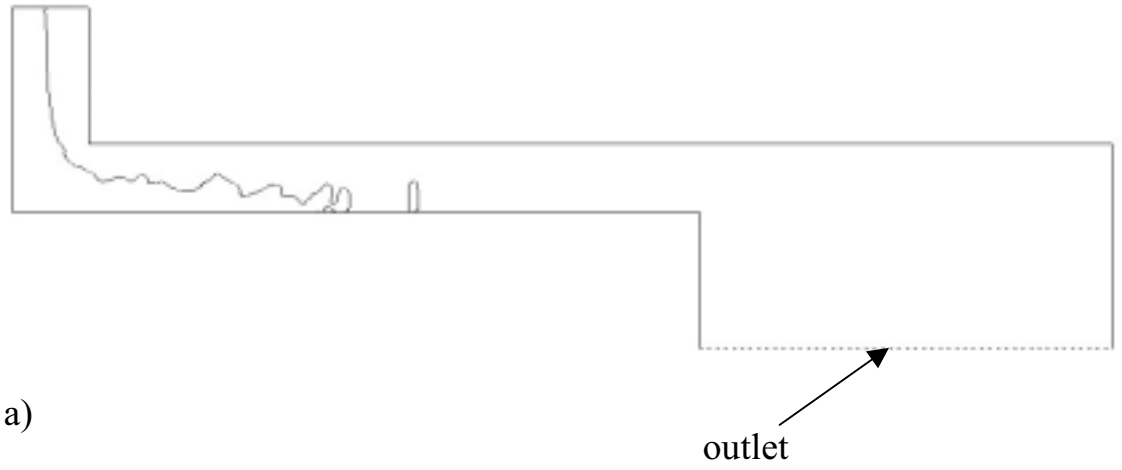

a)

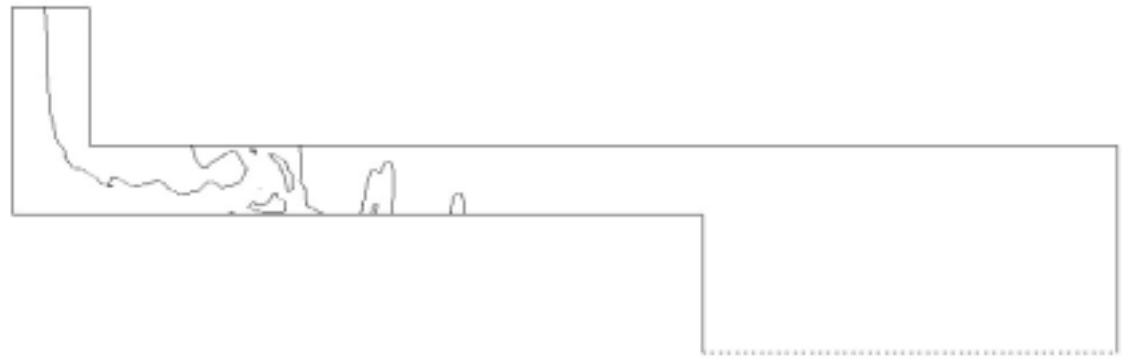

b)

Figure 7.3 Example of VOF calculation with water flow through an 8 mm nozzle impinging on a flat plate. Domain size is 10 x 160 mm. Figures are scaled 5 times in vertical direction for better visualisation.

a) shows fluid surface after 0.04 seconds.

b) shows fluid surface after 0.06 seconds.

Finally, attempts were made to help the liquid spread radially to the plate edge, thinking that this would lead to better results. This included manipulating the contact angle between the fluid and surface beneath, manipulating the surface tension, specifying a frictionless surface beneath the fluid and imposing a thin liquid film on the plate from the jet to the edge. The latter was thought to be a better starting point for a simulation than a completely dry plate.

Variations of the numerical grid were of course also tried. In order to maintain tolerable simulation times, a very fine grid was constructed that incorporated only a region of 80 mm in diameter, i.e. well inside a hydraulic jump. Figure 7.1 is from such a simulation. This was like all other VOF simulations unsuccessful. However, results seemed to indicate the surface profile inside an even smaller diameter of 40 mm was stable, irrespective of what happened further away. It is therefore believed that the VOF simulations are correct in that region. Figure 7.4 compares one such VOF simulation with four analytical calculations. The VOF simulated surface profile is the thinnest, but correlates otherwise well with the analytical results.

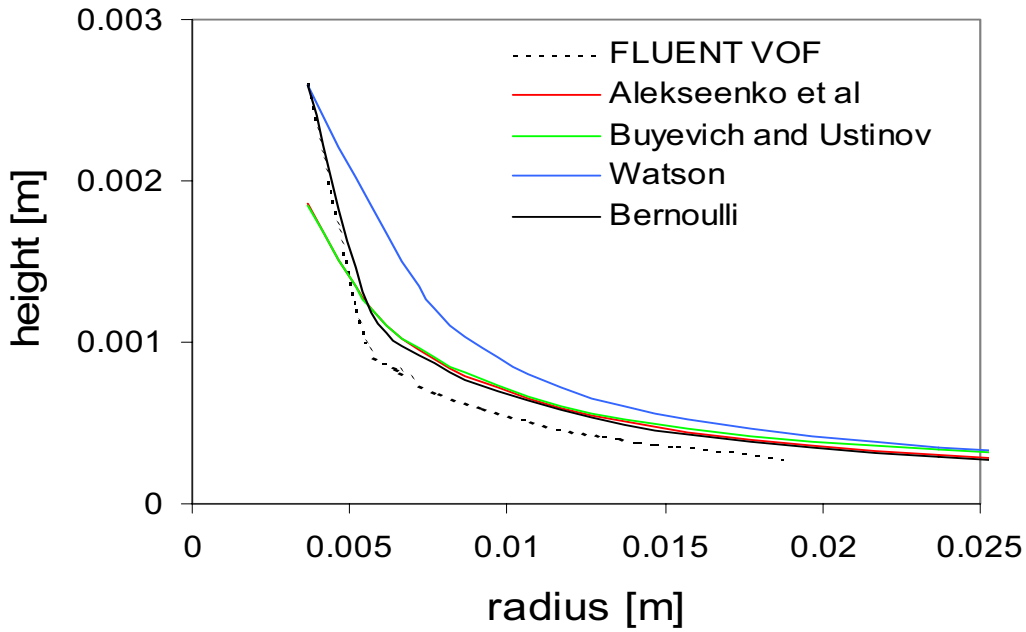

Figure 7.4 Comparison of surface profiles in stagnation region. Water flow through 8 mm nozzle. All computations are laminar.

7.1.3 Numerical Simulations with Prescribed Surface Profiles

7.1.3.1 Procedure

After spending an immense amount of time and effort on laborious VOF simulations, it must unfortunately be concluded that FLUENT (at least up to version 5) can not reliably simulate the flow of a free jet impinging on a plate, with the fluid exiting the domain at the plate edge. It was therefore necessary to find other ways of computing the surface profile, see Chapter 4. FLUENT was then used for flow and heat transfer calculations inside these profiles. The computer code GAMBIT was used as a pre-processor for constructing this finite-difference grid.

The isothermal flow was first computed, and afterwards, "on top" of this converged flow field, the calculation of the energy equation was performed. This is permissible in our case, since the temperature variation is small (maximum 20 °C) and the physical properties influencing the flow are not heavily temperature dependent. Thus there is a coupling from the flow field to the temperature field, but not vice versa. Constant properties simplify both the numerical and analytical calculations. Viscous heating is considered negligible and omitted in all simulations.

The VOF method is in nature a time dependent scheme. The other simulations were initially attempted run as steady-state cases. None of these converged acceptably. Better results were achieved when they were run *time-dependently*. This is unfortunately believed to increase the computational time noticeably.

Both laminar and various turbulence models were used, combined with different meshes.

The final mesh comprised 25 nodes evenly spaced across the film thickness before the jump and around 50 after (refined towards the plate). Around 300 nodes were used in the radial direction. Refining this mesh did not seem to influence any results. The plate beneath the liquid was not modelled. Based on the simulated heat flux, the temperature anywhere in this plate can easily be computed manually.

Laminar flow simulations could take up to 40 CPU hours on a Silicon Graphics Indigo 2 computer. Turbulent flow simulations could take up to half of this, whereas thermal simulations used up to 15 CPU hours. An effort was made to reduce this time by splitting the model at the jump and running separate simulations for the flow before and after the jump. As the inlet boundary condition for the post-jump region, a linear velocity distribution across the cross-section of the flow was specified immediately before the jump.

The "split-model" yielded reliable results before the jump, but the flow after the jump seemed to be different from the equivalent flow computed in the complete model. Subsequently it was decided to simulate the system only as one, complete model. FLUENT's outlet cells were specified as the boundary condition at the plate edge. The time steps used varied between $1 \cdot 10^{-2}$ and $1 \cdot 10^{-6}$ seconds, increasing with time - convergence permitting. Some models were extremely sensitive to variations in time steps and under-relaxation factors. Example: a time step of $5 \cdot 10^{-5}$ seconds and a velocity under-relaxation of 0.4 make for good convergence, whereas increasing the time step to $6 \cdot 10^{-5}$ seconds or the under-relaxation to 0.5 drastically worsens the situation. In some thermal simulations, divergence was encountered when too small time-steps were used.

Four cases were chosen for the tin simulations, see Table 7-1.

Case	Nozzle diameter [mm]	Flow rate [m^3/s]	Free fall height [mm]	Tin inlet temperature [°C]	Cooling air temperature [°C]	U
1	8	$0.959 \cdot 10^{-4}$	28	320	154	205
2	8	$1.046 \cdot 10^{-4}$	92	341	177	204
3	10	$1.193 \cdot 10^{-4}$	28	339	140	218
4	10	$1.442 \cdot 10^{-4}$	92	323	167	204

Table 7-1 Overview of FLUENT simulations with tin in prescribed surface profile. *U* is overall heat transfer coefficient at underside of fluid, [W/m^2K].

The results were compared with the corresponding experiments and analytical computations. The 5 mm nozzle was not simulated due to the experimental difficulties encountered with this nozzle size (i.e. incomplete wetting of the plate).

Case 2 with the turbulent Bernoulli flow model was used as basis for comparing the various laminar and turbulent features available in FLUENT, see Table 7-2. This was also the only case used for simulating the flow under all four theoretical surface profiles (Watson, Alekseenko et al, Buyevich/Ustinov, Bernoulli). The other cases were simulated only with the turbulent Watson and Bernoulli profiles. These computations were performed with both the laminar and the standard k-ε turbulence models, which are considered to be the two extreme alternatives.

Case	Computational model	
	Flow	Heat Transfer
a	laminar	laminar
b	standard k-ε	standard k-ε
c	RNG, nonequilibrium	RNG, nonequilibrium
d	RNG, nonequilibrium	laminar
e	RNG two-layer	RNG, two-layer
f	RNG, standard wall function	RNG, standard wall function
g	RNG, standard wall function	RNG, no wall function
h	RNG, nonequilibrium Differential viscosity model *off* (*on* in all other cases)	RNG, nonequilibrium

Table 7-2 Summary of test computations performed in FLUENT for tin flow through 8 mm nozzle, $1.046 \cdot 10^{-4}$ m^3/s, 92 mm free fall. Surface profile is from the *turbulent Bernoulli model.*

Case *d* in Table 7-2 is an unlikely choice for any simulation, but was included to investigate how sensitive the results are to the thermal model employed.

The Reynolds Stress Model is not considered to possess any advantages over the other schemes for an impingement flow. It is more suitable for highly swirling flows (which is considered not to be the case here), and as mentioned in the FLUENT manual, it can be more prone to stability and convergence problems than the other models. Also, it requires more computer resources and was for these reasons not tried.

There was in general some difficulties involved in making the simulations converge. As mentioned, both the flow and thermal simulations had to be performed time-dependently, often with small time steps. Manipulation of time steps and underrelaxation factors was also necessary for satisfactory convergence. The computer's response to these manipulations was fairly slow, making the simulations a tedious job.

The computational difficulties are believed to hail from two different sources. First, the mesh used is not optimal, but a compromise between accuracy and CPU time. A rather fine mesh through the thickness of the film was chosen at the sacrifice of more cells in the radial direction. This led to long thin cells in some areas and subsequently anisotropic coefficients in the discretization equations, which in turn impedes convergence.

Secondly, the very nature of the flow itself leads to numerical problems. The abrupt increase of the flow's cross-section at the jump results in eddies and complete reorganisation of the flow. This reorganisation may need to take place over a longer distance than that available between the jump and the plate edge (outlet boundary). Radial gradients can in such a case still be large at the outlet and fluid can also be pulled into the FLUENT domain, which greatly affects the results. See Figure 7.5. In some situations the calculation will not converge at all.

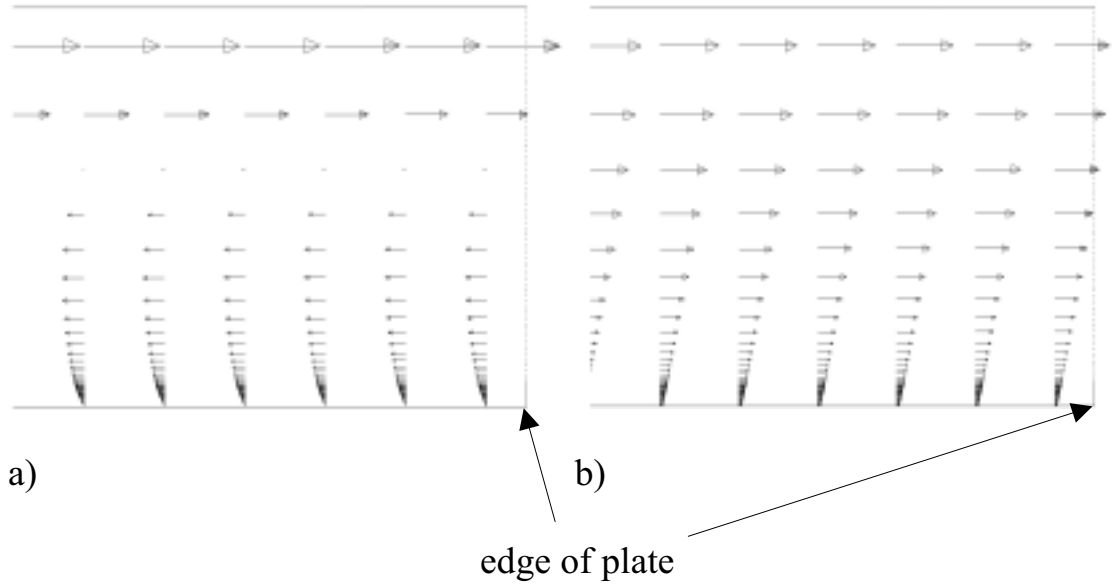

Figure 7.5 Steady-state FLUENT-derived velocity vectors in turbulent Bernoulli profile near outlet. Fluid is tin, flow rate $1.05 \cdot 10^{-4}$ m^3/s through 8 mm nozzle. a) is laminar flow calculation and b) turbulent (standard k-ε). The first produces inflow of fluid through the outlet. b) is believed to be a more realistic flow field.

All of the laminar computations resulted in some degree of inflow at the outlet, whereas this was not evident in any turbulent computation. Similar to the VOF simulations, various attempts were made to resolve this problem. First, a sensible velocity profile, incorporating the correct mass flow, was specified at the edge of the plate. Three cells, either near the surface of the fluid or by the plate, were left as conventional outlet cells so FLUENT could adjust the mass balance if necessary. The same set-ups as in Figure 7.2 were also tried, but these computations produced inflow problems too.

Laminar computations were also performed starting from a converged turbulent computation. After a while, inflow once more started up and stabilised itself at the outlet.

Thinking that problems in the laminar computations were due to insufficient space for the flow to re-establish itself after the jump, a

computation was performed on a plate of radius 0.25 m (opposed to 0.15 m previously). The results were rather disappointing; showing a flow with consecutive eddies between the breakdown of jet entering the jump and the outlet. Inflow through the outlet was just as obvious as before. Specifying a pressure-inlet as the outlet made no difference.

None of the laminar flow fields are believed to be realistic after the breakdown of the incoming jet after the jump.

Laminar flows generally need longer space to become fully developed than turbulent flows, due to the higher effective viscosity in the latter. The situation is the same for reorganisation of the flow after a hydraulic jump. The simulations show that the thin film before the jump acts more or less like a jet forced into the thicker film after the jump. It is clearly seen that this jet is damped or broken down much faster with a turbulent simulation model, see Figure 7.6. The problems at the outlet are eliminated if a turbulence model is employed. This was confirmed by the fact that turbulent calculations in most cases converged better and faster than laminar calculations, also resulting in shorter CPU times. This is contrary to many other problems, where solving the additional turbulence equations leads to increased CPU times.

Figure 7.6 shows regions with recirculating fluid immediately after the jump. This is usual in channels with abrupt changes in cross-section and agrees well with observations in the water experiments. It is mentioned in various literature, but it is beyond the scope of this work to study it more profoundly. The laminar computation shows the typical additional recirculation zone stretching all the way to the outlet, where inflow occurs.

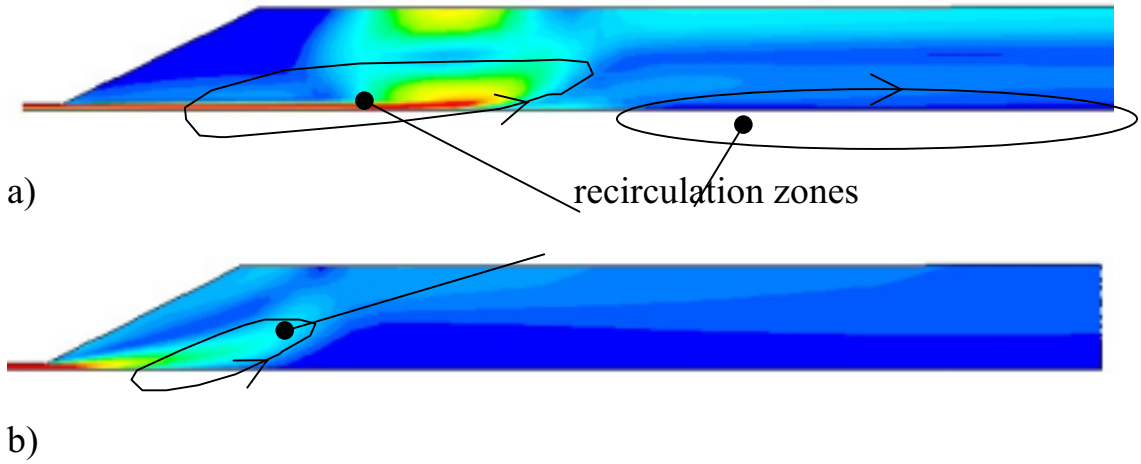

Figure 7.6 Contour plots of steady-state FLUENT-derived velocity magnitudes after hydraulic jump. Same conditions as in Figure 7.5. **a)** is laminar flow calculation. **b)** is turbulent. The turbulent "jet" entering the jump is broken down more rapidly than the laminar counterpart. The colours, from dark blue to red, indicate velocity magnitudes. The former represents 0 m/s, while 0.5 m/s and more is red.

As mentioned earlier, only the *stationary* conditions in the system are of interest. These were concluded to have been established when further calculation in time had no influence on the flow and temperature fields. It is impossible to beforehand predict when this occurs. It was therefore often necessary to continue calculations from an initially finished job where stationary conditions had not been obtained. The last results where then naturally used as input for the new computer run.

Following this routine it gradually became clear that such a "stop and start" process in itself influenced the results. The results seemed to change immediately after a restart. This was fully investigated by running a turbulent case long enough on the computer for it to reach steady state in the first attempt. Afterwards a new simulation was started based on this converged solution. This second run converged to a new steady-state solution, different from the first. This was repeated twice more, ending in

two new solutions, i.e. all four, well-converged steady-state solutions *differed among themselves*.
All the differences appeared after the jump, in areas where recirculation was evident. In magnitude the velocity differences were not large, but the relative changes could be up to 100%, for example from 0.05 m/s 0.1 m/s in one place. The changes in these relatively low velocities are assumed to have insignificant effect on the temperature distribution.

The reason for the inconsistency in the flow simulations is not completely understood. One theory is that when a job is completed, some numerical information stored temporarily in the computer during the run is lost. When the job is started again, the less-than-optimal grid makes it difficult to reach this former steady-state condition again. Another possible explanation is that the system *does not have one, absolutely stable solution*. Disturbances - either numerical or physical - may lead to an unstable flow fluctuating around a time-averaged steady-state flow situation. These problems added of course to the overall time spent on the simulations. It is difficult to say if the first converged solution is any more accurate than the others.

7.1.3.2 Results of Flow Simulations

All FLUENT simulations show a maximum flow velocity *very near the plate surface* (distance ~ 0.1 mm) at a distance of 1.2 to 1.5 jet radii from the symmetry axis. It is noted that the magnitude of this maximum film velocity is *greater* than the average jet velocity. All this agrees well with the water experiments and with the work of Stevens and Webb (1993). The latter mention that in some cases the radial flow can achieve a velocity 30% greater than the jet. In the computer simulations the film velocities were, in some cases, seen to reach twice the jet velocity. See Table 7-3. All laminar flow computations predicted slightly higher maximum velocities than the corresponding turbulent options. The maximum velocities in the FLUENT simulations of the Bernoulli surface profile seem to agree best with the experimental studies of Stevens and Webb.

Case	Surface profile model	Jet velocity [m/s]	Maximum FLUENT-derived velocity [m/s]	
			Laminar	Turbulent (standard k -ε)
1	Watson Bernoulli	2.0	4.0 3.0	3.8 2.8
2	Alekseenko et al. Buyevich/Ustinov Watson Bernoulli	2.4	4.9 5.3 5.4 3.8	4.5 4.8 4.7 3.4
3	Watson Bernoulli	1.6	3.4 2.4	3.2 2.3
4	Watson Bernoulli	2.3	4.7 3.5	4.3 3.3

Table 7-3 Comparison of maximum velocities in FLUENT simulations with tin in prescribed surface profiles. All surface profiles are calculated turbulently, except Buyevich/Ustinov. Case numbers are as in Table 7-1.

The calculated turbulent velocities near the surface of the flow all exhibit a minimum at a distance of about 1.4 jet radii from the centre. A pronounced maximum is then relatively quickly obtained at a distance of 5 to 6 jet radii from the centre.

The common assumption made in many theoretical studies that $u = U_\infty$ outside the boundary layer is contradicted by both the water experiments and the computer simulations - this again being consistent with the work of Stevens and Webb.

The nozzle-to-plate spacing has no apparent effect on the flow, at least within the range used in these simulations.

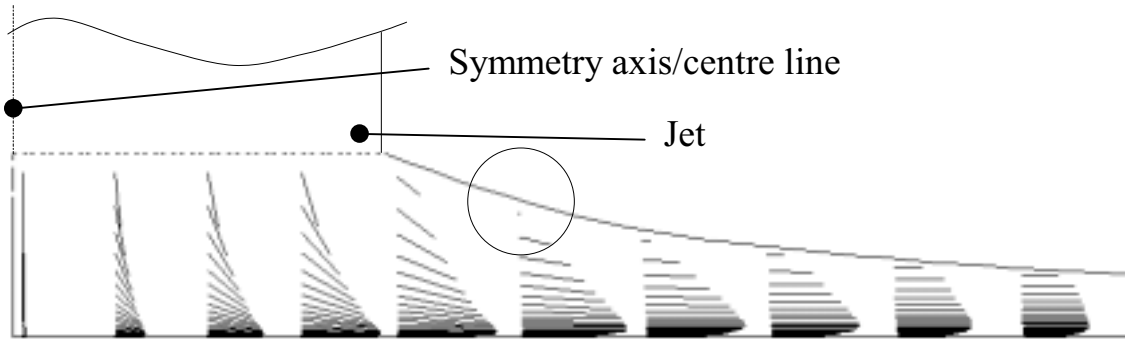

a) Alekseenko et al.'s turbulent surface profile

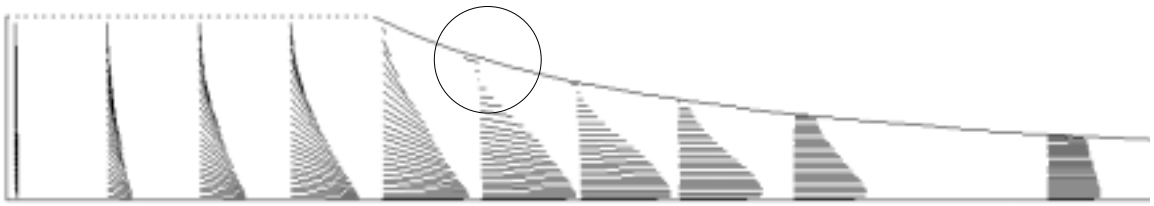

c) Buyevich and Ustinov's laminar surface profile

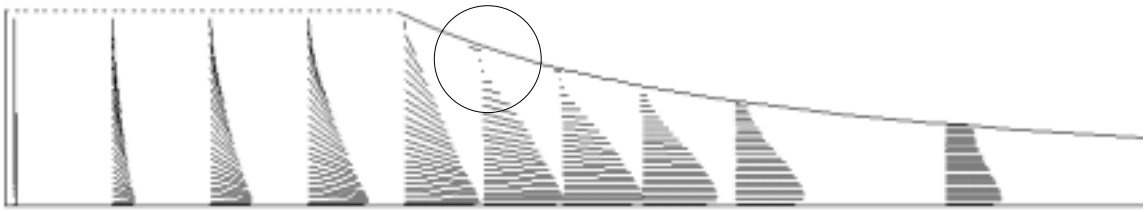

c) Watson's turbulent surface profile

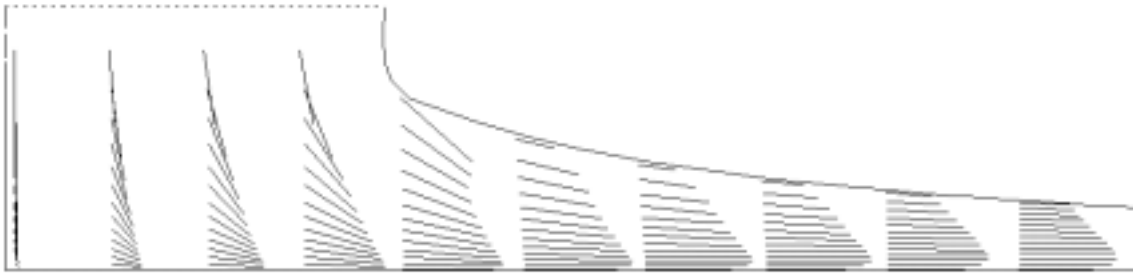

d) Bernoulli model turbulent surface profile

Figure 7.7 Comparison of FLUENT-derived steady-state velocity vectors near stagnation region. FLUENT's standard k-ε turbulence model is used in all computations. Fluid is tin, flow rate $1.05 \cdot 10^{-4}$ m^3/s through 8 mm nozzle and 92 mm free fall. Arrowheads on vectors are removed for better visualisation. Vector lengths are not consistent between the four cases and can therefore not be used for velocity comparisons. Circles mark regions with recirculating fluid.

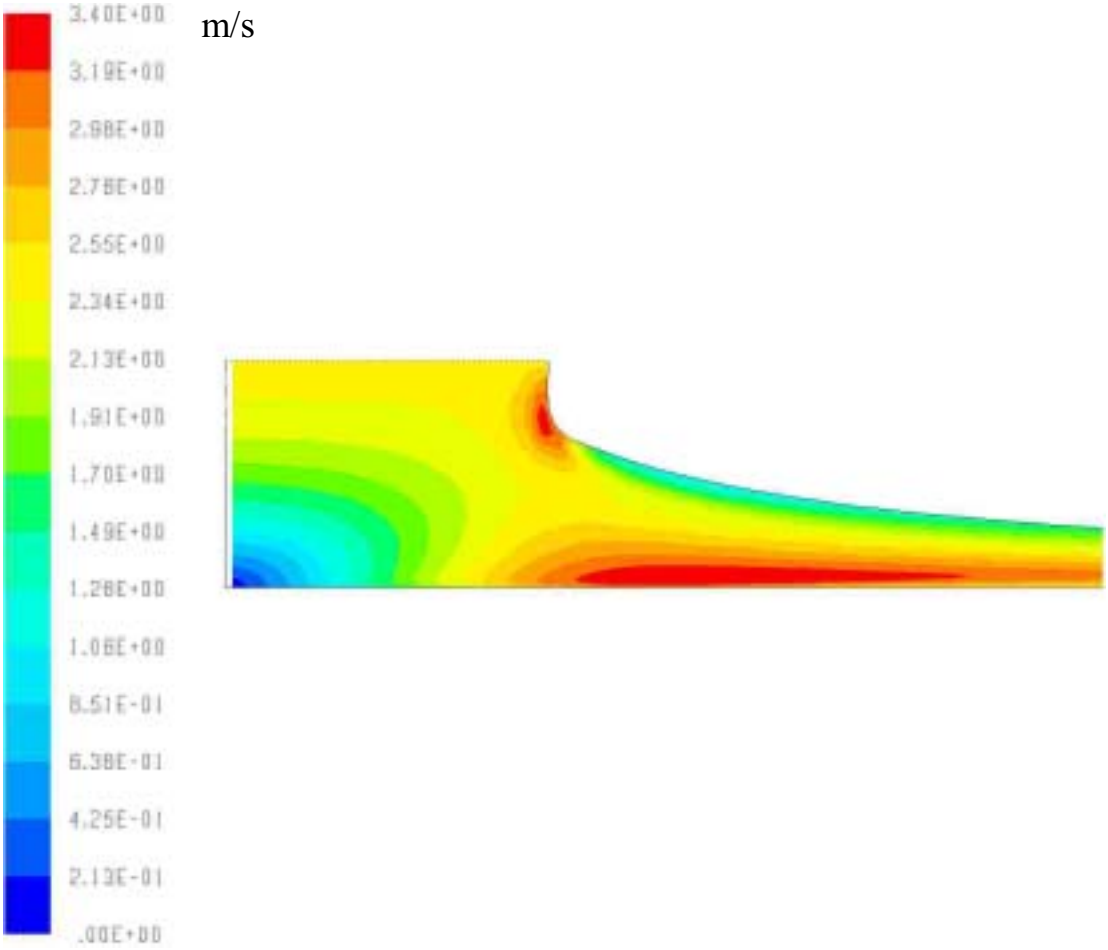

Figure 7.8 Plot of steady-state velocity magnitude for tin flow in Bernoulli surface profile. Conditions are as in Figure 7.7.

As expected, there are no major disagreements between the FLUENT-derived flows in the four different prescribed surface profiles. Some discrepancies are however noted. The Bernoulli profile seems to give a "smoother" and intuitively more convincing profile in the impingement region. The other models show a sharper, almost immediate transition from the vertical jet to the radial film flow. In most cases they also reveal a recirculation zone near the surface in this region, with fluid flowing "against" the jet. This is believed to be unphysical. The reason for this recirculation is probably that the imposed theoretical surface profiles have too large a cross-section near the "turning point" of the jet, leaving a redundant area near the surface, with a stationary eddy occupying the space. As this occurs near the surface, the heat transfer to the plate is most

probably unaffected. See Figure 7.7 for details. In all fairness it must be mentioned that Watson and Buyevich/Ustinov mention that their theories can not be expected to hold when $r \approx a$. Figure 7.9 compares the surface profiles from the four theoretical models.

As mentioned before, all turbulent flow simulations displayed a quicker breakdown of the "jet" entering the post-jump region than the equivalent laminar calculations, furthermore leading to quicker reorganisation of the flow after the jump. This correlates well with flow in closed channels with sudden expansions where laminar flows often need six times longer than turbulent flows to regain fully developed conditions.

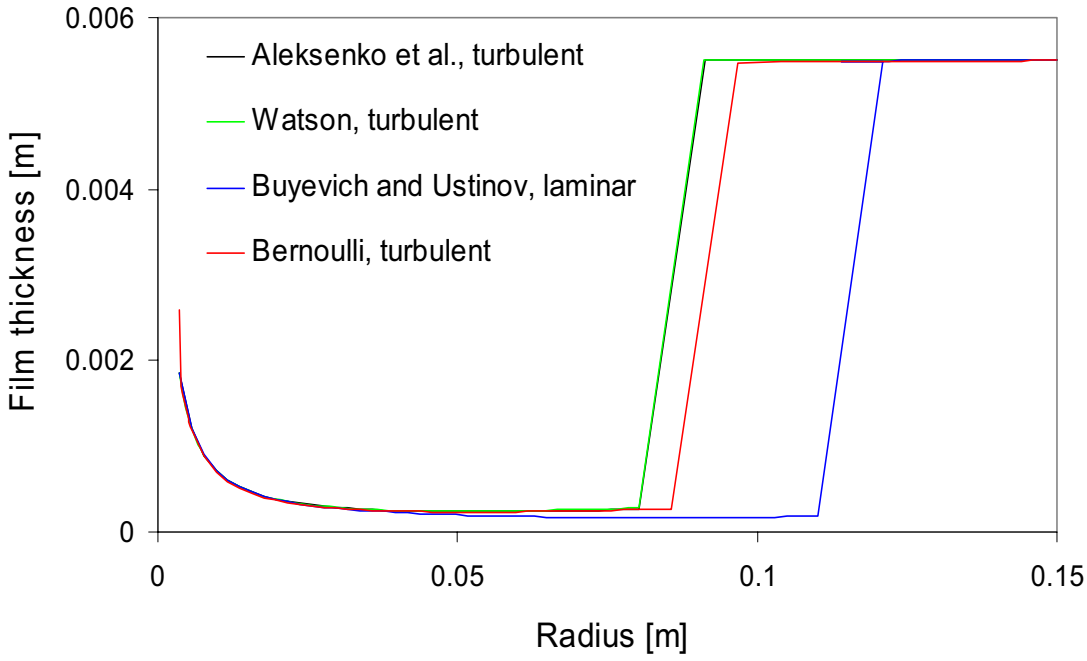

Figure 7.9 Comparison of theoretical surface profiles. Fluid is tin, flow rate $1.05 \cdot 10^{-4}$ m^3/s through 8 mm nozzle and 92 mm free fall.

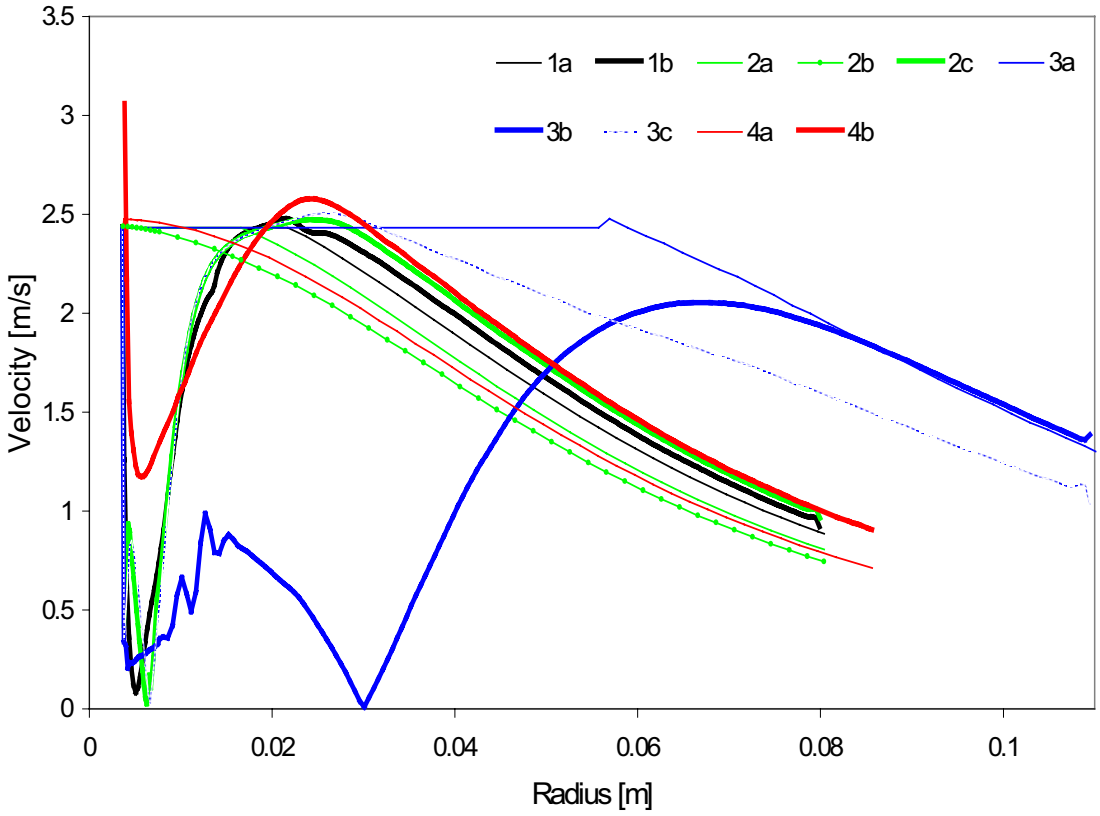

Figure 7.10 Steady-state velocity magnitude (absolute value) in surface cells up to hydraulic jump, as computed by FLUENT in prescribed surface profiles. Fluid is tin, flow rate $1.05 \cdot 10^{-4}$ m^3/s through 8 mm nozzle and 92 mm free fall Jet velocity before impingement is 2.43 m/s.

1a: Analytical turbulent solution from Alekseenko et al. **1b**: standard k - ε turbulence model in FLUENT used in turbulent surface profile from Alekseenko et al. **2a**: Analytical turbulent solution from Watson. **2b**: FLUENT's standard k - ε turbulence model used in turbulent surface profile from Watson. **2c**: Mean velocity according to Watson's turbulent solution. **3a**: Analytical (laminar) solution from Buyevich and Ustinov. **3b**: Laminar FLUENT solution in Buyevich and Ustinov's surface profile. **3c**: FLUENT's Standard k - ε turbulence model used in Buyevich and Ustinov's surface profile. **4a**: FLUENT's standard k - ε turbulence model used in turbulent Bernoulli surface profile. **4b** Mean velocity in turbulent Bernoulli model.

Figure 7.11 compares FLUENT-derived laminar and turbulent velocity profiles in a prescribed surface profile before the jump. There is very little difference between the turbulent velocities, and as in other geometries, the turbulent profile is "flatter" in its shape over the cross-section of the fluid than its laminar counterpart, with a steeper gradient next to the plate.

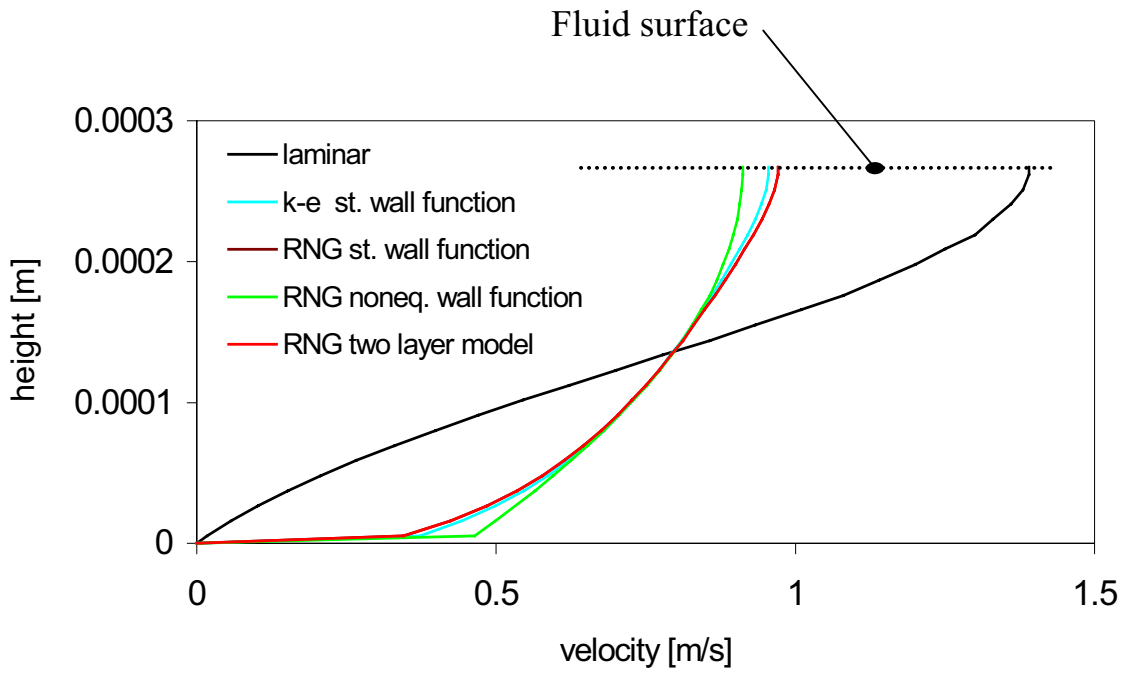

Figure 7.11 Comparison of FLUENT derived velocity profiles (steady state) in turbulent Bernoulli model surface profile 0.0825 m from plate centre (before hydraulic jump). Fluid is tin, flow rate $1.05 \cdot 10^{-4}$ m^3/s through 8 mm nozzle and 92 mm free fall. Curves for RNG standard wall function and two layer models are coincident.

It might be remembered that when the two-layer zonal model is employed, y^+ at the wall adjacent cell most ideally should be near unity, but that up to 5 is acceptable. Figure 7.12 shows that y^+ is less than 5 from about one jet radius from the plate centre and outwards. Even if it is as high as 18 near the axis, this does not seem to have any perceptible effects on the velocity and temperature calculations in that region.

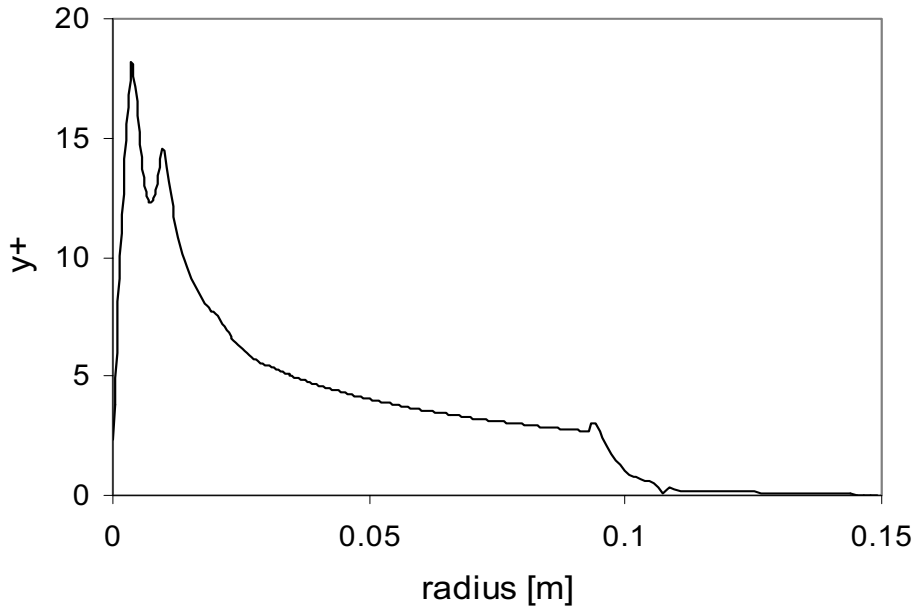

Figure 7.12 y^+ as function of radius as computed in the RNG two-layer model. Fluid is tin, flow rate $1.05 \cdot 10^{-4}$ m^3/s through 8 mm nozzle and 92 mm free fall, and surface profile used is from the turbulent Bernoulli model.

One noticeable difference could be observed between the various flow patterns in the turbulent simulations, namely the occasional existence of *two* recirculation zones after the jump. All laminar and turbulent computations predict *one* such zone in the jump region between the incoming "jet" and the fluid surface. As mentioned earlier, all laminar flows show an additional zone after the breakdown of the jet, extending to the outlet. *Some* turbulent simulations exhibit a similar zone, but more locally confined - not extending to the outlet. See Figure 7.13 for an example. This feature is not always existent, but seems to depend on the surface profile and jump position, or more specifically the flow rate and the ratio of the conjugate depths.

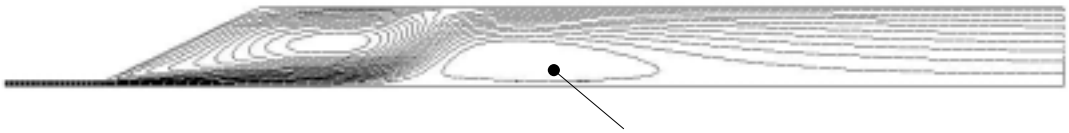

a) Watson turbulent surface profile

b) Bernoulli turbulent surface profile

Figure 7.13 Stream functions (steady state) from FLUENT simulations of prescribed surface profiles, case 3, Table 7-1. Computations are with the k - ε turbulence model.

7.1.3.3 Results of Heat Transfer Simulations

The temperature fields, on the other hand, exhibited no equivalent distinct signs indicative of turbulent or laminar computations. The results from the thermal computations were reported as wall temperatures (temperatures in top surface of the plate beneath the flow) and heat fluxes from the fluid to the plate. The test cases listed in Table 7-2 showed practically identical wall temperatures prior to the jump. See Figure 7.14. There is no distinct drop in the temperatures where the jump occurs, contrary to what might be expected due to the abrupt increase in film thickness and subsequent decrease in bulk velocity, which again is thought to decrease the heat transfer. The reason for this is that the thin-film flow (the afore-mentioned "jet") continues to a certain degree into the thicker film following the jump, where it gradually breaks down.

The temperature curve based on the RNG two-layer flow field is smooth, with only a slight disturbance from the jump, all the way to the plate edge. The other curves based on turbulent flow fields exhibit a more pronounced break a little after the jump. All these computations predict the additional

recirculation zone close to the plate, after the jump. This eddy prevents new, hot fluid from flowing along the plate in this region. The heat must therefore travel from the hotter fluid near the surface of the flow and through the eddy before it reaches the plate. This barrier leads to a somewhat cooler plate in the vicinity of the eddy. After the eddy, "new" fluid can again flow across the plate, evidenced by the temperature falling in with the RNG-two-layer curve. This feature is also seen in some of the other simulations and is always attributed to the recirculating fluid near the plate. Since it is a fairly local phenomenon, it does not significantly affect the total heat loss from the fluid.

The wall temperatures based on laminar flow fields dip after the turbulent ones. This is because the laminar jet in the jump is broken down slower. This temperature curve also falls further down because the recirculation zone extends to the plate edge, where fluid (obviously of a lower temperature) is drawn into the domain. The result can not be relied upon.

Some other differences are also noticed among the turbulent-flow-based temperature curves after the jump (excluding the RNG two-layer curve). The standard k-ε flow and heat simulation agrees with theory by predicting the highest temperatures in that region.

Very little difference is seen between the RNG nonequilibrium wall function-based flow field with RNG (equilibrium) wall function heat transfer and laminar heat transfer (cases c and d). The only point worth mentioning is that the laminar heat transfer model yields a marginally lower wall temperature, again agreeing with turbulent theory.

The option of abandoning the law-of-the-wall for temperature in the RNG model is as good as identical to the standard wall function alternative. Only the latter is plotted. These two predict the lowest temperatures in the post-jump region.

Before the jump the fluid temperature varies insignificantly across its cross-section (from the plate to the free surface). The variation is in tenths of degrees and there is no visible difference between the cases in Table 7-2. This confirms the fact that turbulence has negligible effects on the computed heat transfer.

From this test case it can be concluded that different procedures for calculating heat transfer on an already established flow field *do not* result in significantly different heat flows from the fluid to the surface beneath. The temperatures in the system are more *dependent* on the technique used for calculating the *flow field*. Supercritical flows (before the jump) seem to be the exception, yielding practically no variation in temperature, *regardless* of flow or heat transfer model chosen.

It is possible that more pronounced differences can appear in other conditions with higher or lower flow rates.

Figure 7.15 shows the wall temperatures as computed by FLUENT in the four theoretical surface profiles. The wall temperatures before the jump are as good as identical for all surface profiles. Some differences are evident after the jump. These are due to the differences in the jump positions predicted by the various models. The temperatures calculated in the Buyevich and Ustinov profile are the highest, agreeing well with the fact that the jump position in this model is furthest from the plate centre. The temperature in the Bernoulli profile shows a dip after the jump, but near the plate edge once again "meets up" with the other curves. This simulation stands out by the fact that it in this case is the only one with two recirculation zones after the jump, and as explained earlier, contributes to a somewhat cooler plate.

Figure 7.16 shows the computed heat fluxes to the plate. Since there is no radial variation of the cooling conditions, these curves follow exactly the development of the temperature curves.

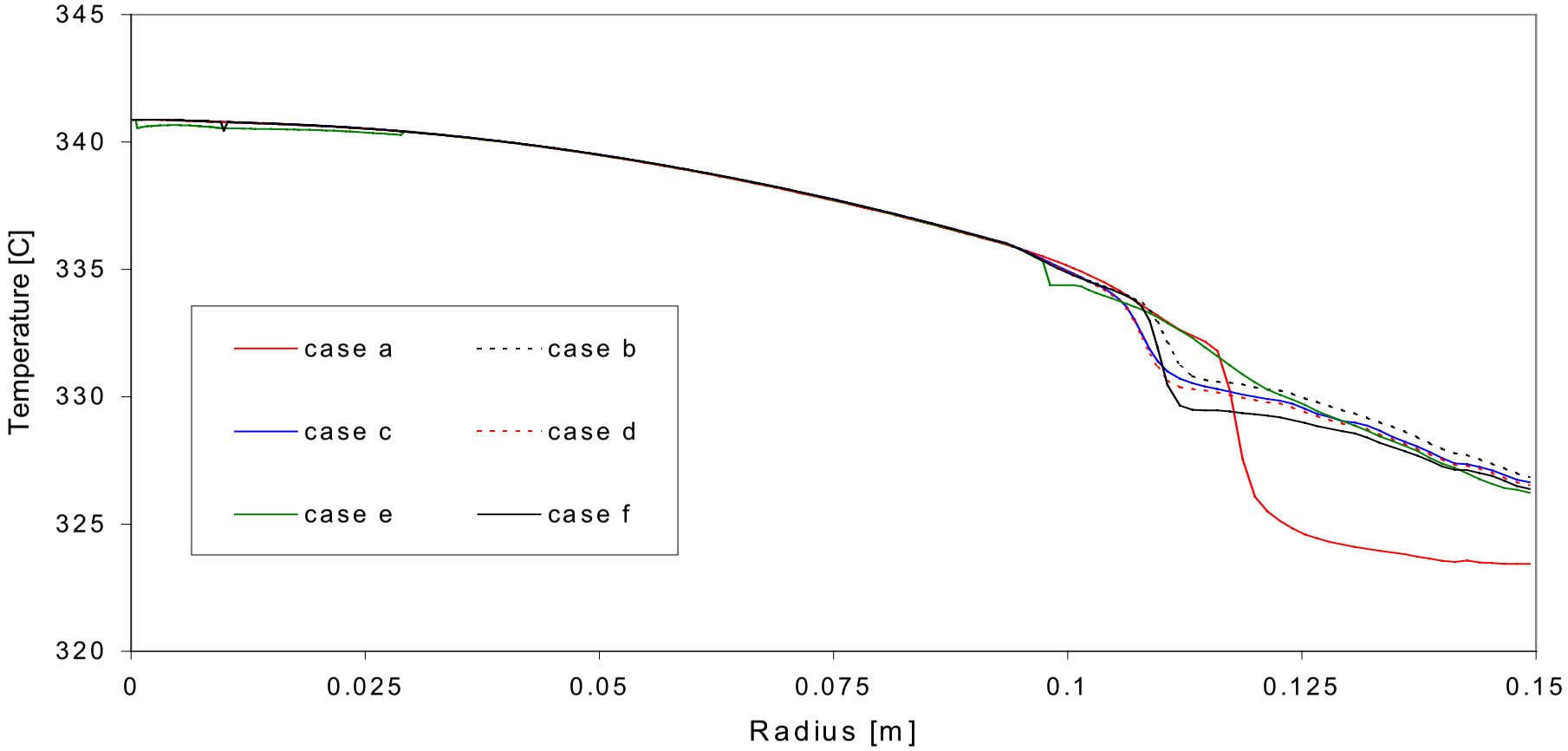

Figure 7.14. Comparison of plate temperatures computed according to Table 7-2.

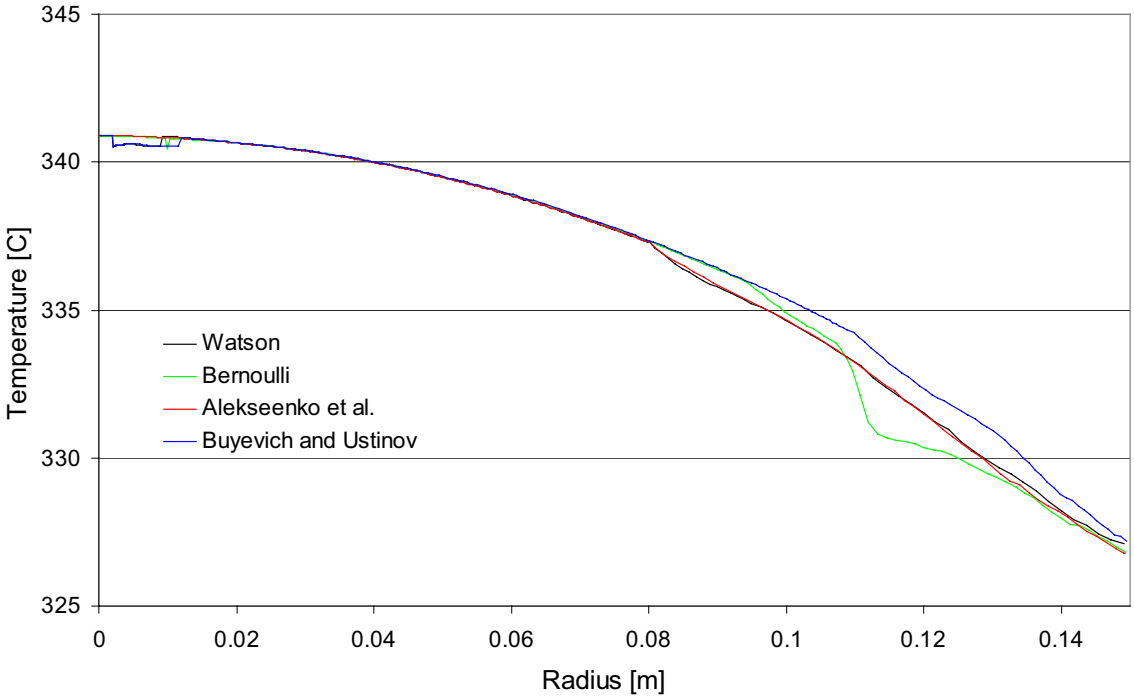

Figure 7.15. Comparison of FLUENT-simulated surface temperatures in plate. The standard k - ε turbulence model is used for both flow and heat transfer. Surface profiles are all computed turbulently, except that of Buyevich and Ustinov. Tin flow through 8 mm nozzle, $1.0464 \cdot 10^{-4}$ m^3/s, 92 mm free fall. Calculations do not include heat transfer from fluid surface. Cooling air temperature is 177 °C with an overall heat transfer coefficient at the underside of the fluid of 204 W/m^2K.

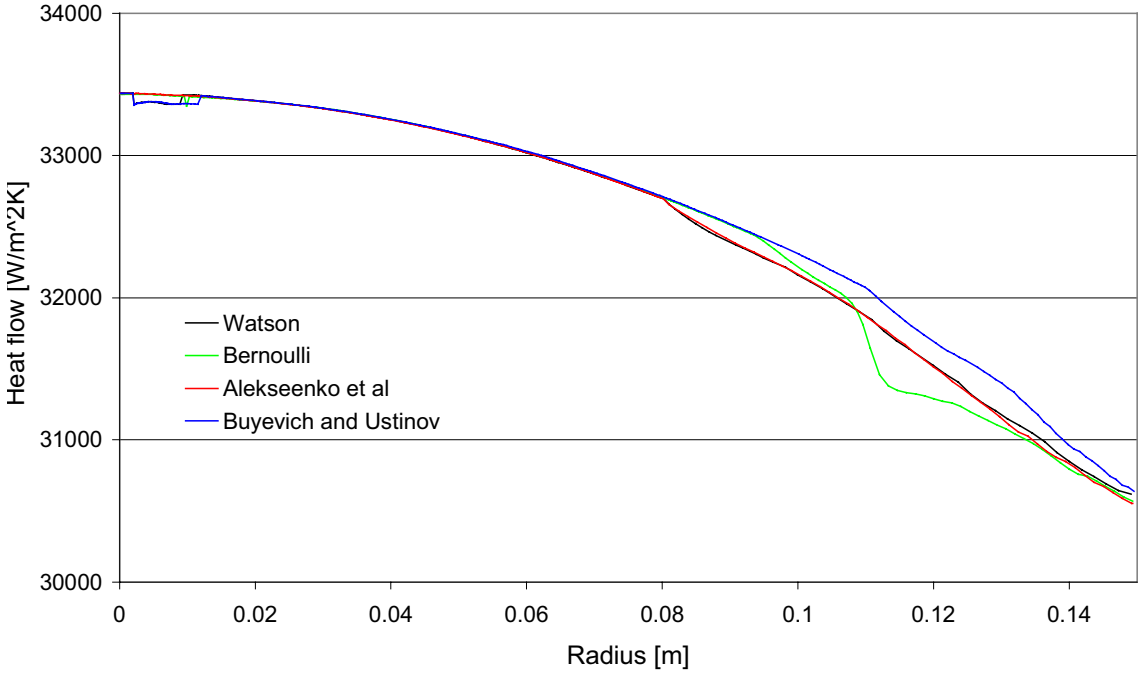

Figure 7.16. Comparison of FLUENT-simulated heat flux from fluid to plate. Conditions are identical to those in

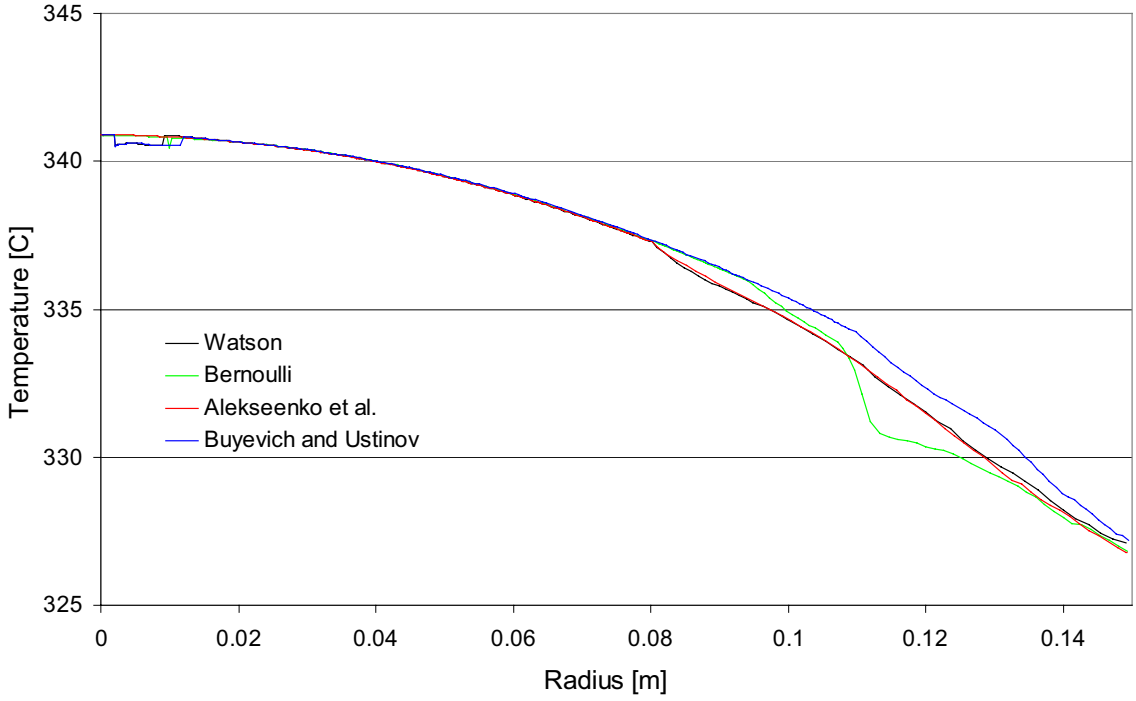

Figure 7.15.

7.2 Analytical Heat Transfer Calculations

Simple analytical calculations for temperature and heat flux can easily be performed with the help of the theory from Chapter 5. The convective heat transfer coefficients are known from the plate centre to the edge and the problem is solved by iteration. The major difficulty is to find an expression for the fluid's bulk temperature as a function of radial distance from the plate centre. One simple suggestion is to use a *linear* variation of the bulk temperature with radius, i.e. from the known inlet temperature to the (initially) unknown outlet temperature. The outlet temperature is the only unknown and is found by equating the total heat flow to the plate with the heat loss in the tin. This simplifies analytical calculations and it is assumed that it does not greatly affect the correctness of the final results. The total heat flow to the plate can be found by dividing the plate into annular regions, individually computing the heat received by these and finally adding them together.

Another method - also in better accordance with the theoretical deductions - is to assume a linear temperature variation only from r_T . Up to this point the bulk temperature is then equal to the inlet temperature. This procedure yields practically identical heat losses and outlet temperatures compared to the first. There are, however, some local differences in heat transfer and wall temperatures up to r_T, due to the somewhat increased fluid temperature in this region

Two other methods not employed here will also be mentioned. Instead of using the same linear bulk temperature profile for the fluid along the whole plate, separate linear profiles could be used for each of the annular regions. The second method involves the same annular regions. In the central region the heat loss can be computed with the bulk temperature of the fluid equal to the jet temperature. The second region uses the outlet temperature of the first region as its bulk temperature, and so on. The total fluid heat loss is the sum of the loss in the individual sections. The difference between the various methods will not be large if the total temperature change in the fluid is small compared to the average temperature difference between the fluid and its surroundings.

The heat transfer theory was originally developed on the basis of Buyevich and Ustinov's flow theory. Although this theory deviates from the other three analytical models, it is possible to implement the obtained convective heat transfer coefficients in another flow model. This was done with the Bernoulli model using the expressions for r_v and r_T from Buyevich and Ustinov to demarcate the flow regions.

7.3 Comparison of Results

Figure 7.17 compares some analytical results with FLUENT simulations. Figure 7.18 gives an idea of the convective heat transfer coefficients involved.

The heat and temperature losses from the test cases in Table 7-2 are shown in Table 7-4. The results from the other computations are presented in Table 7-5 to Table 7-8. Even though the laminar computations are dubious, the results from these are also included.

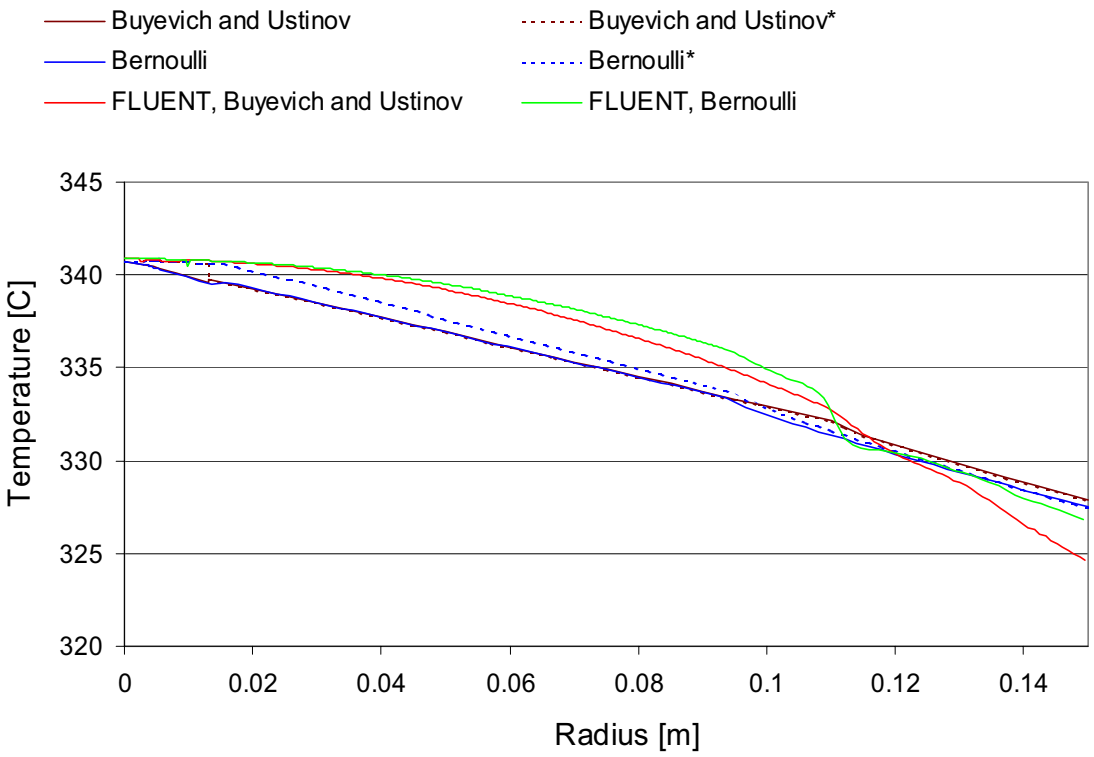

Figure 7.17 Comparison of calculated steady state temperatures in top surface of plate as in case 2, Table 7-1. Curves marked * use a linear variation of tin temperature from r_T (others are linear variation from plate centre). FLUENT simulations are with the standard k - ε turbulence model. Bernoulli surface profile is turbulent.

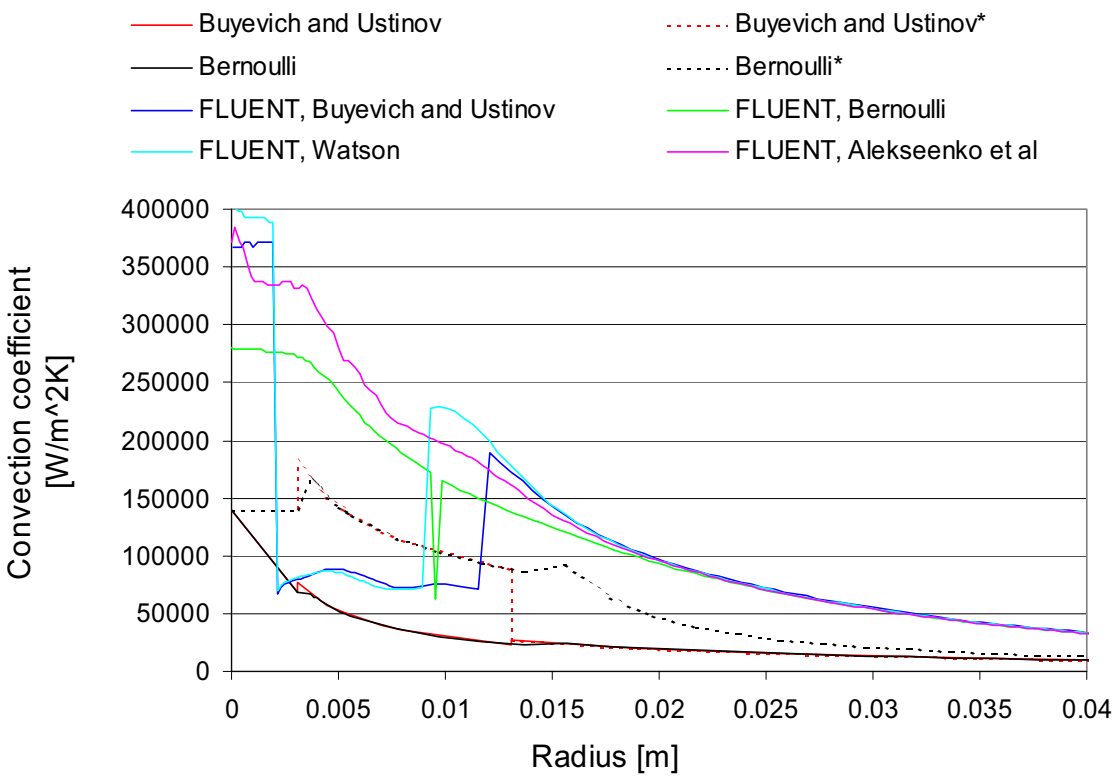

Figure 7.18 Comparison of calculated convective heat transfer coefficients from tin to plate as in case 2, Table 7-1. Values refer to *jet temperature*. Curves marked * use a linear variation of tin temperature from r_T (others are linear variation from plate centre). FLUENT simulations are with the standard k - ε turbulence model. All surface profiles are turbulent except Buyevich and Ustinov's.

Case	Computed outlet temperature [°C]	Heat loss [W]
a	329.2	2189.6
b	328.9	2245.3
c	328.9	2245.3
d	328.9	2245.3
e	328.4	2338.0
f	328.8	2263.8
g	328.8	2263.8
h	328.9	2245.3

Table 7-4 Comparison of results from test simulations in FLUENT. Steady state tin flow as in case 2, Table 7-1 Surface profile is from the turbulent Bernoulli model.

Surface profile	Computational model for flow and heat transfer	Temperature [°C]		Heat loss in tin [W]
		Inlet	Outlet	
Bernoulli, turbulent	laminar	320	306.7	2262
	standard k - ε		306.5	2296
Watson, turbulent	laminar		306.6	2279
	standard k - ε		306.8	2245
Buyevich and Ustinov, laminar	analytical		306.9	2232
Bernoulli, turbulent	analytical		306.7	2265
experimental measurements		321	307.0	2381

Table 7-5 Comparison of results from FLUENT simulations, analytical computations and measurements. Tin flow through 8 mm nozzle, $0.959 \cdot 10^{-4}$ m^3/s, 28 mm free fall. Calculations do not include heat transfer from fluid surface. Cooling air temperature is 154 °C with an overall heat transfer coefficient at the underside of the fluid of 205 W/m^2K.

Surface profile	Computational model for flow and heat transfer	Temperature [°C]		Heat loss in tin [W]
		Inlet	Outlet	
Buyevich and Ustinov, laminar	laminar	341	329.1	2213
	standard k - ε		328.8	2264
Bernoulli, turbulent	laminar		329.2	2190
	standard k - ε		328.9	2245
Watson, turbulent	laminar		328.8	2264
	standard k - ε		328.8	2264
Alekseenko et al	laminar		328.8	2264
	standard k - ε		329.0	2236
Buyevich and Ustinov, laminar	analytical		328.9	2237
Bernoulli, turbulent	analytical		328.9	2240
experimental measurements		341	327.0	2598

Table 7-6 Comparison of results from FLUENT simulations, analytical computations and measurements. Tin flow through 8 mm nozzle, $1.0464 \cdot 10^{-4}$ m^3/s, 92 mm free fall. Calculations do not include heat transfer from fluid surface. Cooling air temperature is 177 °C with an overall heat transfer coefficient at the underside of the fluid of 204 W/m^2K.

Surface profile	Computational model for flow and heat transfer	Temperature [°C]		Heat loss in tin [W]
		Inlet	Outlet	
Bernoulli, turbulent	laminar	339	325.3	2898
	standard k - ε		325.1	2940
Watson, turbulent	laminar		325.4	2877
	standard k - ε		325.2	2919
Buyevich and Ustinov, laminar	analytical		325.2	2918
Bernoulli, turbulent	analytical		325.2	2912
experimental measurements		342	323.0	4019

Table 7-7 Comparison of results from FLUENT simulations, analytical computations and measurements. Tin flow through 10 mm nozzle, $1.1928 \cdot 10^{-4}$ m^3/s, 28 mm free fall. Calculations do not include heat transfer from fluid surface. Calculations do not include heat transfer from fluid surface. Cooling air temperature is 140 °C with an overall heat transfer coefficient at the underside of the fluid of 218 W/m^2K. The inlet tin temperature varied somewhat in the experiments and the instantaneous value shown here does not exactly match the time-averaged value used in the computations.

Surface profile	Computational model for flow and heat transfer	Temperature [°C]		Heat loss in tin [W]
		Inlet	Outlet	
Bernoulli, turbulent	laminar	323	314.7	2122
	standard k - ε		314.5	2174
Watson, turbulent	laminar		314.7	2122
	standard k - ε		314.5	2174
Buyevich and Ustinov, laminar	analytical		314.5	2167
Bernoulli, turbulent	analytical		314.5	2162
experimental measurements		319	307	3069

Table 7-8 Comparison of results from FLUENT simulations, analytical computations and measurements. Tin flow through 10 mm nozzle, $1.442 \cdot 10^{-4}$ m^3/s, 92 mm free fall. Calculations do not include heat transfer from fluid surface. Cooling air temperature is 167 °C with an overall heat transfer coefficient at the underside of the fluid of 204 W/m^2K.

The results show good agreement between the predicted total heat losses in all computations.

From Figure 7.18 one can see that the FLUENT-derived heat transfer coefficients are higher than the analytically computed ones before the jump. After the jump all curves seem to eventually merge together. There is also some variation between the FLUENT-values inside the stagnation region. The analytical curve based on the surface profile of Buyevich and Ustinov with a linear temperature variation from r_T is initially practically identical to the corresponding curve based on the Bernoulli model. At r_T the former drops due to a lower wall temperature. The curves using a linear variation in fluid temperature all the way from the plate centre are initially lower than the ones maintaining the inlet temperature up to r_T and then

varying linearly to the plate edge. This is obvious as the heat flow in this region increases with the higher temperature, and since the *local* heat transfer coefficients still are the same, the coefficient related to the inlet temperature must increase in order to support the increased heat flow. In this case there is very little difference between the analytical convection coefficients based on a surface profile from Buyevich and Ustinov and the Bernoulli model.

The peaks in the analytical curves are due to the fact that the theories for the various regions do not exactly match at their connecting points.

It can be noted that the difference in convective heat transfer coefficients is greater than the difference in plate temperatures in the various computations. This is due to the fact that the main resistance to heat transfer from the fluid through the plate and to the cooling system is in the stainless steel plate. Variations in the high heat transfer coefficients from the fluid to the plate will in this case therefore hardly influence the plate temperature.

None of the computations predict an increase in the coefficients after the jump as originally presumed in Chapter 2. It was then believed that the jump would disturb the flow, leading to increased turbulence and enhanced heat transfer. As seen earlier, the flow before the jump enters the post-jump region more or less as a jet. This is gradually broken down with a recirculation zone above it and sometimes another one near the plate after the jet is broken down. There is no apparent increase in turbulent properties in the jump region.

7.3.1 Heat Transfer From Fluid Surface

To investigate the effect radiation and convection from the fluid surface has on the temperature field, a FLUENT computation involving these features was performed. The radiative heat transfer was handled by introducing a radiative heat transfer coefficient, h_r, in the following manner.

$$h_r = \varepsilon\sigma(T_s + T_a)(T_s^2 + T_a^2)$$

ε is the emissivity of the surface, σ is Stefan-Boltzmann's constant, T_s is the surface temperature of the fluid and T_a the ambient temperature. For tin ε is estimated to 0.5 and T_s is for simplicity considered constant and equal to the average temperature of the fluid on the plate. This temperature is initially unknown, but can be found iteratively. In our problem radiation does not have a great influence on the fluid temperature and the average temperature without radiation was used. For Case 2 in Table 7-1 we then get:

$$h_r = 0.5 \cdot 5.67 \cdot 10^{-8} (606 + 323)(606^2 + 323^2) = 12.7 W / m^2 K$$

T_a is estimated to 50 °C. Taking into account convective heat transfer from the surface and exaggerating a little to be on the safe side, we say

$$h_r = 25\ W / m^2 K$$

Radiative heat loss from the fluid surface is relatively easy incorporated in the analytical calculations. As in the FLUENT simulations, the absolutely simplest way is to use a radiative heat transfer coefficient. Its value is temperature dependent, but for simplicity 25 W/m^{2}K was used in all tin computations. Case 2 in Table 7-1 was simulated with FLUENT, while the other cases were only calculated analytically. Results along with measurements are shown in Table 7-9 to Table 7-12, Figure 7.19 and Figure 7.20. There are two curves for the measurements - one in each direction from the plate centre.

Surface profile	Computational model for flow and heat transfer	Temperature [°C]		Heat loss in tin [W]
		Inlet	Outlet	
Buyevich and Ustinov, laminar	analytical	320	304.3	2679
Bernoulli, turbulent	analytical		304.1	2699
experimental measurements		321	307.0	2381
heat gain in cooling air		3263 W		

Table 7-9 Comparison of results from FLUENT simulations, analytical computations and measurements. Tin flow according to case 1, Table 7-1. Radiation and convection from the fluid surface is included by heat transfer coefficient of 25 W/m^{2}K towards an ambient temperature of 50 °C.

Surface profile	Computational model for flow and heat transfer	Temperature [°C]		Heat loss in tin [W]
		Inlet	Outlet	
Buyevich and Ustinov, laminar	standard k - ε	341	326.1	2765
Buyevich and Ustinov, laminar	analytical		326.4	2716
Bernoulli, turbulent	analytical		326.4	2712
experimental measurements		341	327.0	2598
heat gain in cooling air		3592 W		

Table 7-10 Comparison of results from FLUENT simulations, analytical computations and measurements. Tin flow according to case 2, Table 7-1. Radiation and convection from the fluid surface is included by heat transfer coefficient of 25 W/m^{2}K towards an ambient temperature of 50 °C.

Surface profile	Computational model for flow and heat transfer	Temperature [°C]		Heat loss in tin [W]
		Inlet	Outlet	
Buyevich and Ustinov, laminar	analytical	339	323.0	3387
Bernoulli, turbulent	analytical		323.0	3381
experimental measurements		342	323.0	4019
heat gain in cooling air		3705 W		

Table 7-11 Comparison of results from FLUENT simulations, analytical computations and measurements. Tin flow according to case 3, Table 7-1. Radiation and convection from the fluid surface is included by heat transfer coefficient of 25 W/m^{2}K towards an ambient temperature of 50 °C.

Surface profile	Computational model for flow and heat transfer	Temperature [°C]		Heat loss in tin [W]
		Inlet	Outlet	
Buyevich and Ustinov, laminar	analytical	323	312.8	2620
Bernoulli, turbulent	analytical		312.8	2615
experimental measurements		319	307	3069
heat gain in cooling air		3221 W		

Table 7-12 Comparison of results from FLUENT simulations, analytical computations and measurements. Tin flow according to case 4, Table 7-1. Radiation and convection from the fluid surface is included by a heat transfer coefficient of 25 W/m^{2}K towards an ambient temperature of 50 °C.

The heat gain in the cooling air is computed from its measured inlet and outlet temperatures. Properties are used for dry air at the average of these two values. The results do not agree completely with the heat loss from the tin. They seem to vary from 8% less to 50% more. In a perfect system the cooling air should gain less heat than the tin loses, because additional heat is transported from the tin to the surroundings by radiation and convection. The bottom face and vertical sidewall (about 5 cm high) of the cooling circuit are very close to the channel carrying off the tin to the lower container. The sidewall was thermally insulated, but there is nonetheless bound to be some heat exchange between the channel and cooling circuit. The so-called outlet temperatures of the tin are at the plate edge and were measured by manually moving a thermocouple in the tin around the periphery of the plate. A variation of ± 5 °C was experienced.

The cooling air comes from a central compressor via a drier. The humidity in the air can however vary, affecting its cooling properties. Later, in another connection, water vapour was clearly seen in the compressed air. At that time the drier was malfunctioning. It is not known if this problem was present during the experiments.

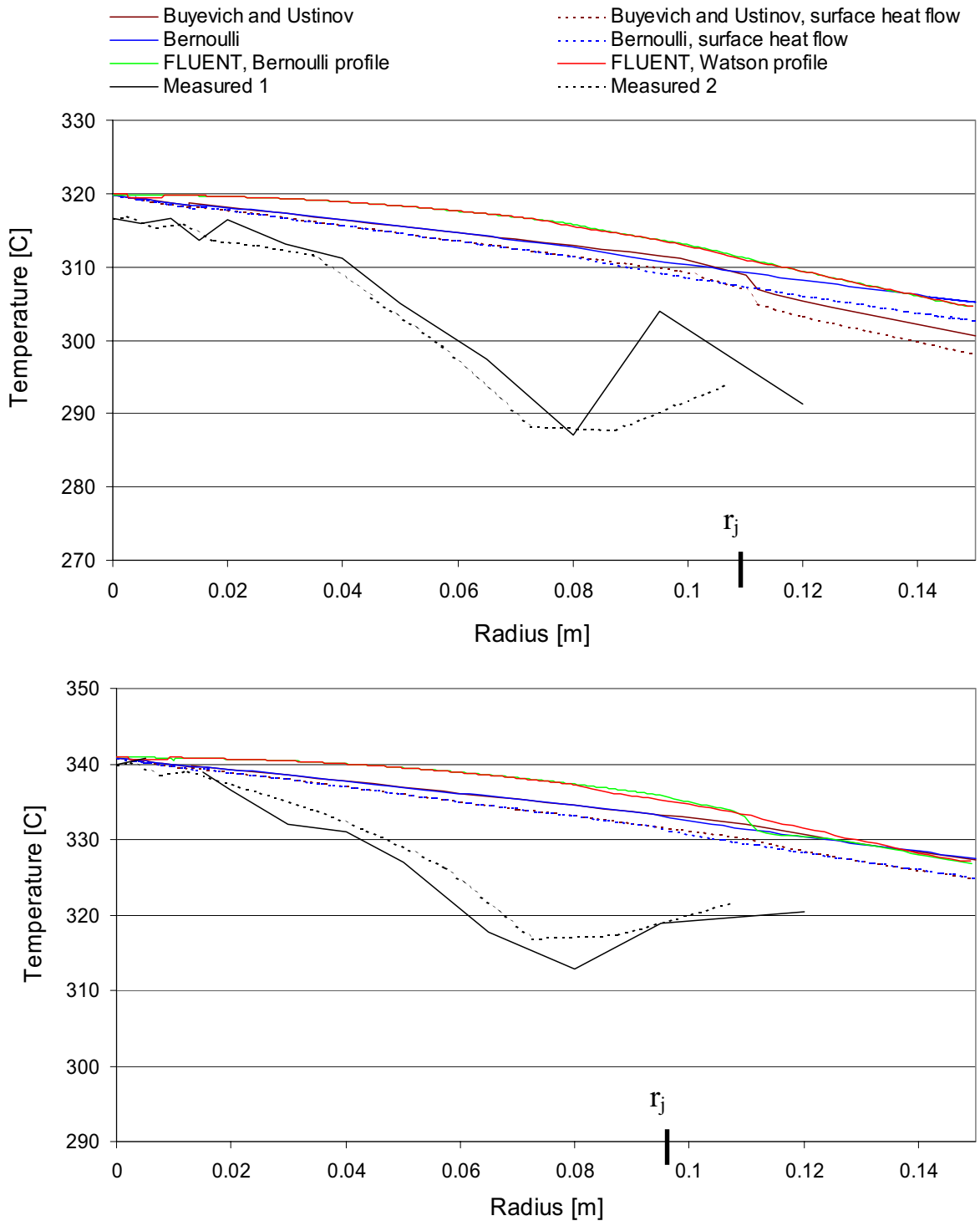

Figure 7.19 Comparison of analytical, steady state FLUENT-simulated and measured wall temperatures for case 1 (top) and case 2 (bottom), Table 7-1.

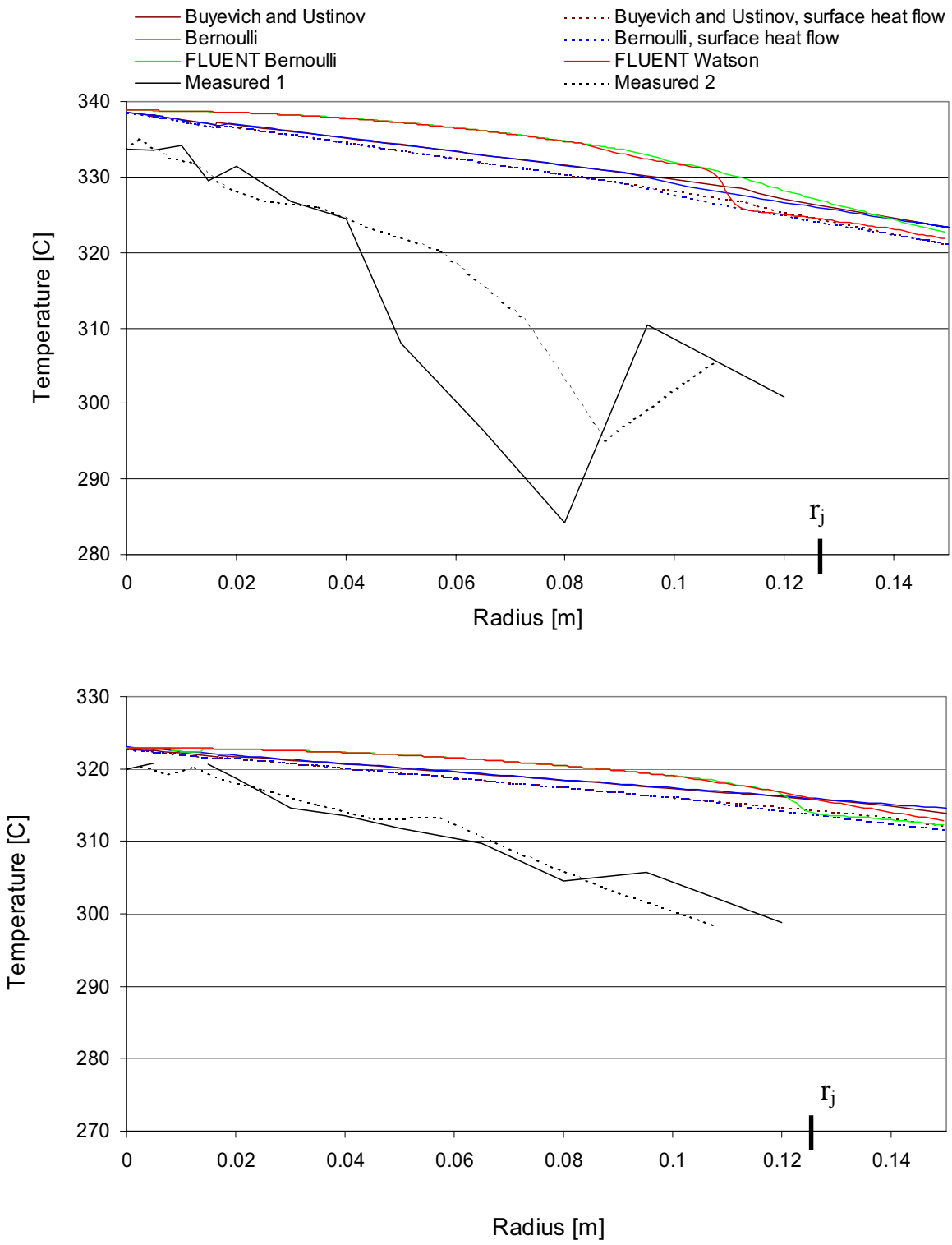

Figure 7.20 Comparison of analytical, steady state FLUENT-simulated and measured wall temperatures for case 3 (top) and case 4 (bottom), Table 7-1.

FLUENT's standard k-ε model yields a somewhat colder plate when taking into account heat loss from the metal surface. The mixed mean temperature is also a little lower.

All the experimentally determined temperatures are lower than calculated. In addition they all show a local minimum around 8 cm from the plate centre. After this they increase more or less pronouncedly to a local maximum, and then seem to decrease again. This has been experienced in other, similar flows, although with water, where it is attributable to instabilities in the flow bringing about a transition to turbulence. This increases the convective heat transfer coefficient. Since there is so little difference between the laminar and turbulent FLUENT simulations before the jump, it is hard to believe that such a transition can cause this distinct effect in liquid metals. Neither can the temperature increase be caused by the hydraulic jump, as this appears further out.

Figure 7.21 and Figure 7.22 show the computed and measured heat fluxes from the tin to the plate. The computations use an average cooling air temperature, although it in reality varies along the plate. The measured heat fluxes in the two directions are therefore averaged; in order to comply best with the computations.

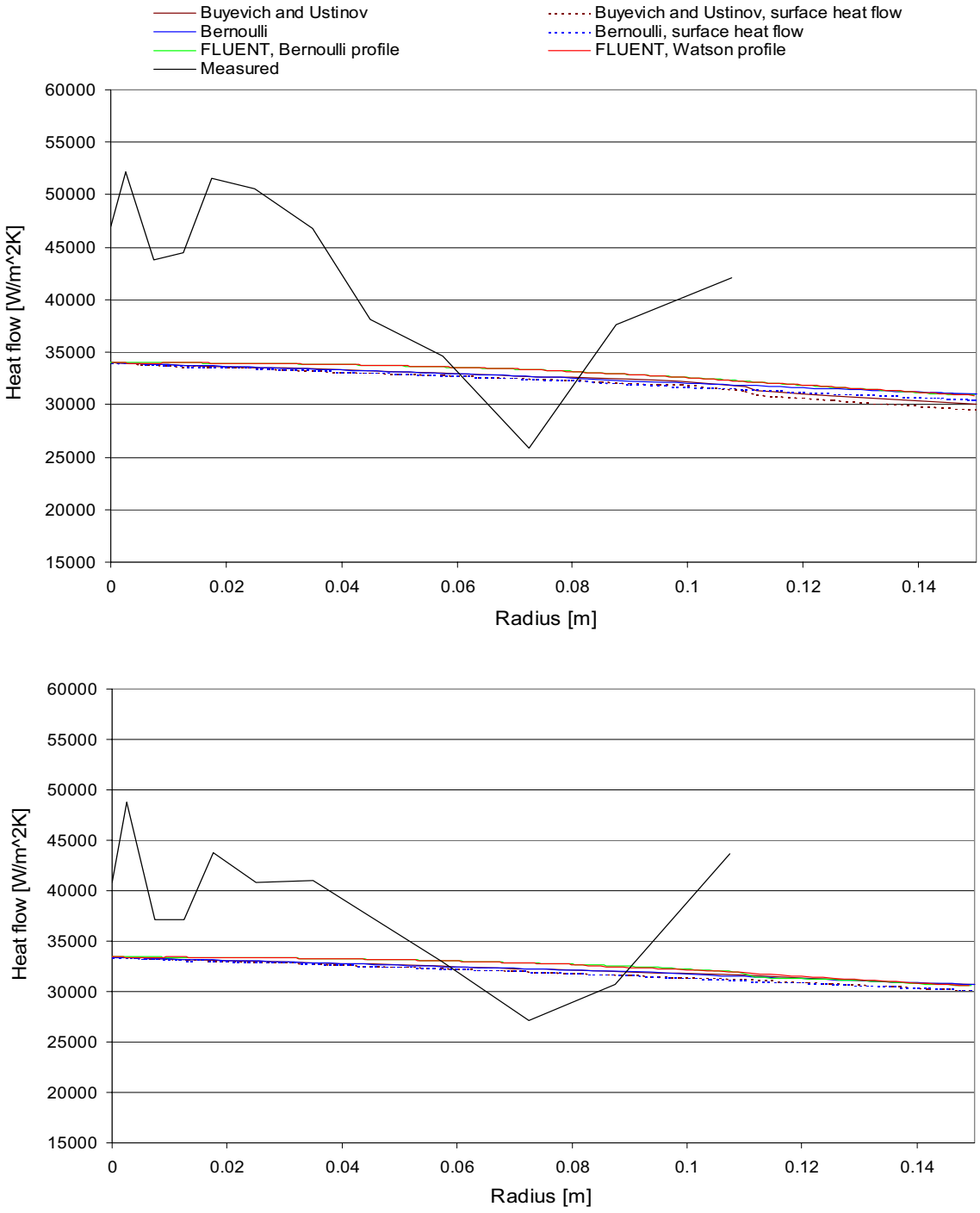

Figure 7.21. Comparison of analytical, steady state FLUENT-simulated and measured heat flow from liquid to plate for case 1 (top) and case 2 (bottom), Table 7-1.

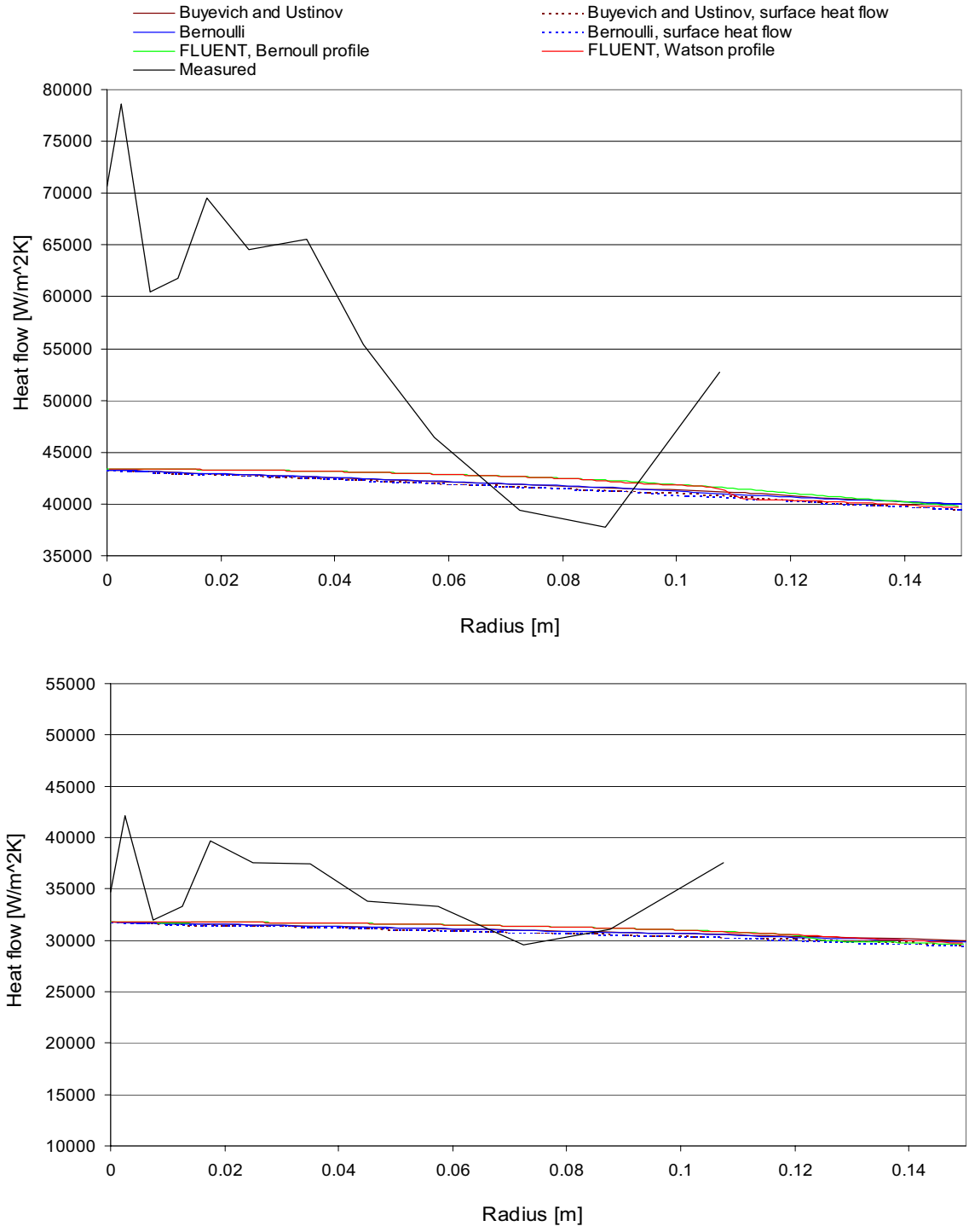

Figure 7.22 Comparison of analytical, steady state FLUENT-simulated and measured heat flow from liquid to plate for case 3 (top) and case 4 (bottom), Table 7-1.

The FLUENT simulations always predict a slightly higher wall temperature than the analytical calculations, except near the plate edge. This can be associated with the fact that the latter are based on an *imposed linear temperature drop* in the fluid. Such a simple assumption is most likely not correct, and will affect the local heat flow and resultant wall temperatures. A slacker temperature drop will increase the wall temperature (remember that the convective coefficients are temperature independent). If the computed convection coefficients from the fluid to the plate are too low, the wall temperatures will also be too low. Downstream of the jump, the analytical temperatures tend to cross the "FLUENT temperatures". The overall heat loss from the fluid can for this reason turn out very similar in all computations.

7.3.2 Computations with Ferrosilicon

Since this project is aimed at heat transfer in ferroalloys, corresponding simulations to those described in the preceding sections were performed with ferrosilicon (FeSi75). Time limited the number of cases to simulate, so only case 2 in Table 7-1 was investigated. In order to save time, the same surface profile as for tin was used, but the flow within it was simulated with the material properties of ferrosilicon. The error introduced here is considered to be small, since the viscosities of the two metals are in the same order of magnitude, thus giving similar surface profiles.

The jet temperature is set to 1450 °C, which is a plausible casting temperature for this metal. Computations with and without heat transfer from the fluid surface were performed. The overall heat transfer coefficient from the surface is estimated to 215 W/m^2K. Other conditions are kept identical to the tin computations. See

Table 7-13 and Figure 7.23 for results.

Surface profile	Computational model for flow and heat transfer	Temperature [°C]		Heat loss From fluid [W]
		Inlet	Outlet	
Buyevich and Ustinov, laminar	standard k - ε	1450	1392.8 1329.5*	17851 37605*
Buyevich and Ustinov, laminar	analytical		1393.3 1330.7*	17683 37220*
Bernoulli, turbulent	analytical		1393.3 1330.9*	17696 37171*

Table 7-13 Comparison of results from FLUENT simulations, analytical computations and measurements. Ferrosilicon flow through 8 mm nozzle, $1.0464 \cdot 10^{-4}$ m^3/s, 92 mm free fall. Surface profiles are as for the equivalent case with tin. Cooling air temperature at the underside is 177 °C with an overall heat transfer coefficient of 204 W/m^2K. Figures marked * include radiation and convection from the fluid surface by a heat transfer coefficient of 215 W/m^2K to an ambient temperature of 50 °C.

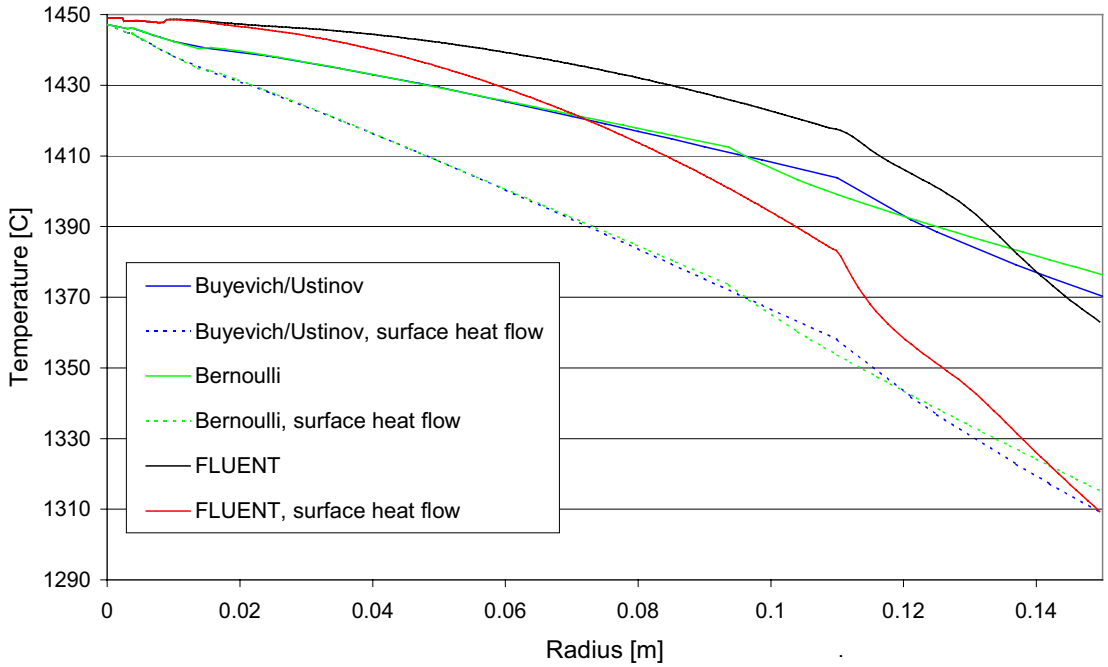

Figure 7.23 Comparison of computed steady state temperature curves in casting plate surface with ferrosilicon flow as in case 2, Table 7-1, with and without heat flow from fluid surface. FLUENT simulations are with the k-ε turbulence model in the surface profile computed for tin with Buyevich and Ustinov's theoretical model. The other computations are analytical.

These computations follow the same general trends as those with tin.

7.4 Discussion

The measured wall temperatures are in general lower than all computations. Compared with these, the analytic and FLUENT-derived temperatures agree well with each other. The latter are, however, always highest. The heat fluxes, on the other hand, behaved in the opposite manner. Near the plate centre these fluxes measured up to 75% more than calculated. From here they decreased outwards and at around 7 cm from the centre crossed the computed fluxes and then again increased above the calculated values - similar to the evolution of wall temperatures. The

measurements stop 12.5 cm from the centre and how they progress further is therefore not known.

Since the measured wall temperatures are lower than calculated, while the fluxes at the same time are higher, means that the measured temperatures on the down-facing side of the plate must be considerably lower than calculated. Figure 7.24 shows this to be true.

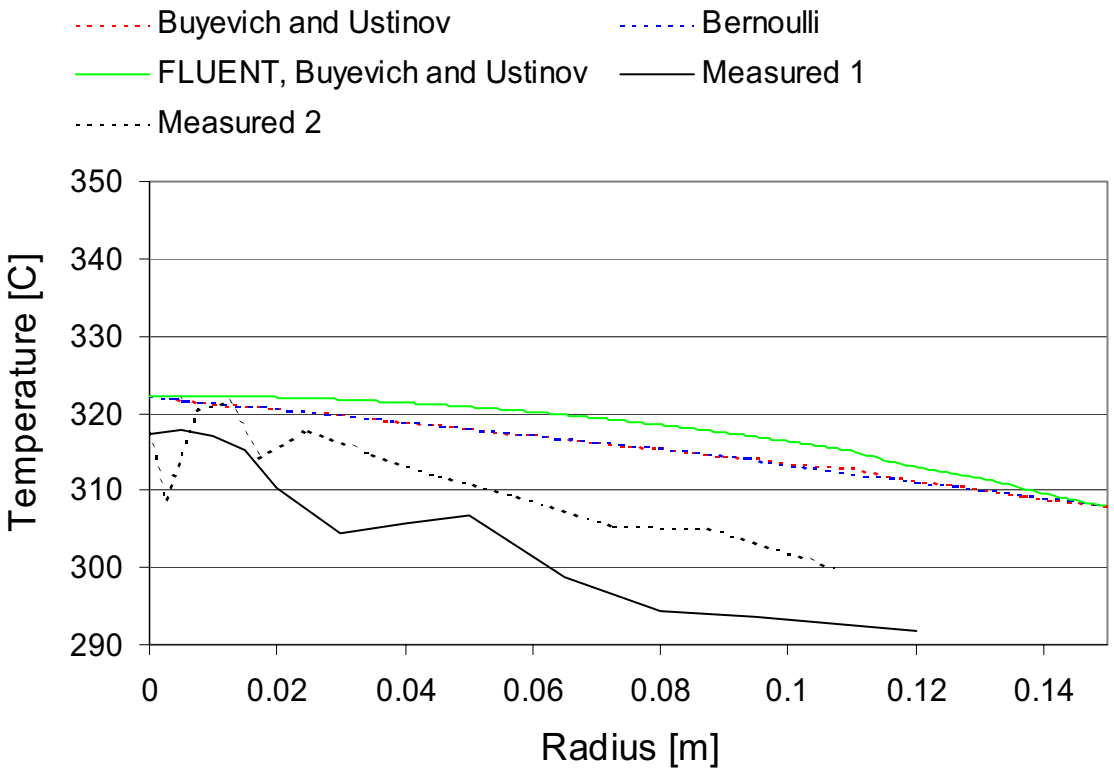

Figure 7.24 Comparison of temperatures on bottom side of plate, case 2, Table 7-1. Computations include heat transfer from fluid surface.

After calibrating the thermocouples, it is believed that the measured temperatures are correct. The disagreement with the calculations can rely on various factors:

- Positioning of thermocouples. A thermocouple lacking proper contact with the plate will on the top face report temperatures exceeding the plate temperature. The opposite will be the case on the bottom face. Inspection of the thermocouples' location, combined with the fact that

the topside temperatures are lower than calculated, indicates that this is not a likely explanation. The thermocouples are also regarded to have been placed flush with the plate surface, ruling out the possibility of comparing temperatures at different levels in the plate with each other.

- Radial heat flow. The computations assume a one-dimensional heat flow through the plate. A noticeable radial heat flow will of course affect the comparisons. Based on the experiments, the radial heat flow is calculated to maximum 0.1% of the transverse heat flow, i.e. the one-dimensional simplification does not introduce significant error.
- Heat conductivity in plate. A value lower than the true conductivity will in the computations lead to a higher temperature on the topside of the plate, but will reduce the heat flow through the plate. This can therefore not alone explain the disagreements.
- Oxide on tin surface. It is not completely understood how this affects the flow of the tin. In any case it was only visible after the hydraulic jump and can not explain the discrepancies before this point. In the experiments the oxide layer seemed to flow slower than the tin, but how this influences the tin flow and heat transfer is not certain. The oxide layer is not as shiny as the tin and will therefore radiate heat more effectively. At the same time it can act as an insulating layer regarding conduction.
- Flow pattern. It is possible that the thermocouples disturb the flow in such a way that the tin does not perfectly wet all thermocouples. A possibility is that the tin somehow splits up and "goes around" some thermocouples, afterwards merging into one flow again. This can explain the local dips and peaks in the wall temperature. Insulating air pockets and/or oxide formation can theoretically also obstruct the heat transfer to the thermocouples.

  Warping in the plate can disturb the flow and measurements. Inspection of the plate after the experiments revealed it was slightly concave - about 1 mm out of plane. The horizontal position of the plate during experiments was checked with a level and is considered satisfactory.
- The calculations assume a perfectly symmetric and even tin jet. In reality it was uneven and sometimes sputtering. This extra turbulence may increase the heat transfer in the stagnation region. Experiments with water (Vader et al., 1991) show that heat transfer is sensitive to free stream turbulence. An increase in free stream turbulence intensity

from 0 to 3% can cause an 80% increase in stagnation heat transfer for a cylinder in cross flow. Similar results are reported for the stagnation region of impinging gas jets. Al-Sanea (1992) concludes that impingement heat transfer is sensitive to the velocity distribution in a slot jet. Nusselt numbers for a parabolic velocity distribution at the jet exit are much higher than those produced by a uniform velocity profile. No studies are found relating to liquid metals, and the coinciding results from turbulent and laminar FLUENT simulations in the whole region before the jump, suggests that liquid metals are practically insensitive to these parameters.

- Material properties. These are fairly well documented for the materials in question. The tin may pick up some impurities, but this is thought to have little effect on heat transfer.
- Cooling air temperature, flow rate and humidity. Divergent values will affect computed plate temperatures. The error in temperature measurements is considered to be small, see next section. Leakage of cooling air was evident in some experiments. Flow measurements before and after the plate indicate that this was in the region of 10%. A decrease in air flow will reduce the heat transfer through the plate. As mentioned earlier, the humidity in the air may have varied during the experiments. Increased humidity will increase heat transfer.
- Heat exchange with surroundings. The upper tin container with heating elements is shielded at the bottom in order to minimise radiation to the casting plate. The walls around the plate are also heated, but the view factor is unfavourable, reducing the amount of heat absorbed by the plate and the tin. Some heat will certainly be exchanged, leading to a slight increase in the plate and cooling air temperature.

Measured Cooling Air Temperature

One reason why the calculated temperatures are higher than measured, can be that the cooling air temperature is lower than actually reported. This is due to heat gained in the thermocouple by radiation from the plate above it. In steady-state conditions this heat is lost to the cooling air by convection. See Figure 7.25.

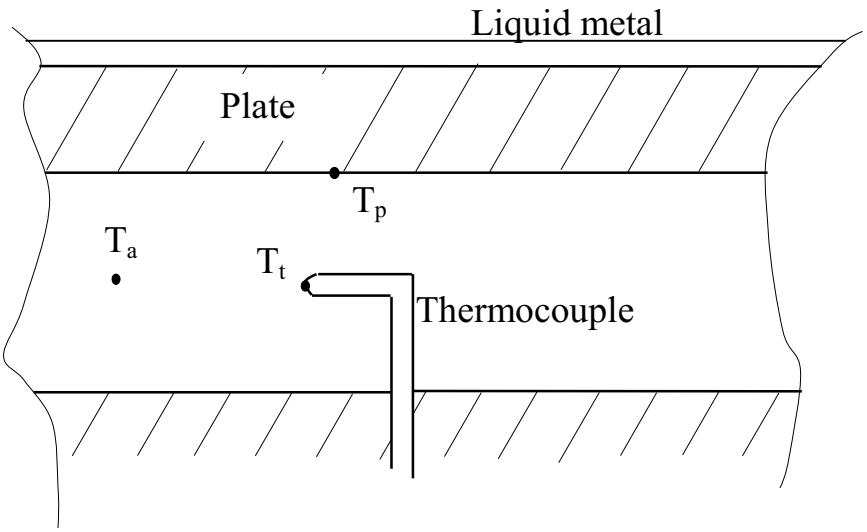

Figure 7.25 Sketch of thermocouple in cooling channel and ambient temperatures. T_a is cooling air temperature, T_t is thermocouple temperature and T_p temperature on bottom surface of casting plate.

The bottom plate in the cooling channel is considered thermally insulated with temperature T_p. The heat balance between the radiation gain and convection loss can then be written as

$$h_c(T_t - T_a) = F\varepsilon\sigma({T_p}^4 - {T_t}^4)$$

h_c is the convection coefficient between the thermocouple and the cooling air. F is the geometric view factor for the system. For a sphere in a turbulent air flow, Nu is given by Wong (1977).

$$Nu = 0.37\, Re^{0.6} \qquad \text{for } 17 < Re_{sphere} < 7\cdot 10^4$$

This correlation is used for the thermocouple, which is 1 mm in diameter and shiny in appearance. ε for the thermocouple is estimated to 0.2 and it is (conservatively) thought to be enclosed by a black body. Hence

$$h_c(T_t - T_a) = \varepsilon\sigma({T_p}^4 - {T_t}^4)$$

For case 2 in Table 7-2, T_a = 177 °C, T_p = 311 °C (average over plate) and the air flow rate is 41.5 Nm^3/h. We find

$$h_c = 1510 W / m^2 K$$

The true air temperature is thus

$$T_a = 177.6\ ^O C,$$

It can safely be concluded that the temperatures indicated by the thermocouples are acceptably accurate.

8. Conclusions and Recommendations for Further Work

8.1 Conclusions

As mentioned in the introduction, the primary aim of this thesis was to find a reliable tool for simulating fluid flow and heat transfer during casting of ferroalloys into open moulds, with special focus on the impingement region. This is believed to be where heat-, mass transfer and shear stress is greatest. FLUENT's *volume of fluid* (VOF) model designed for such free surface flows proved incapable of simulating such a flow reliably.

This made it necessary to attack the problem from a different angle. Theoretical models describing the surface profile of the flow, including a hydraulic jump, were studied. In addition, a *new, simple model* based on Bernoulli's equation was developed. Results based on this model were in *good agreement* with the other theories and practical experiments.

FLUENT simulations of the flow inside these profiles showed that the maximum velocity in the liquid film near the stagnation region is not at the free surface, but near the plate surface. This invalidates the assumptions made for the velocity profile in many analytical models and corroborates the measurements of Stevens and Webb.

Flow simulations with FLUENT must be performed turbulently in order to obtain sensible flow patterns after the jump. Laminar simulations predicted a recirculation zone extending to the plate edge where fluid was *pulled into* the computational domain, resulting in erroneous temperature calculations. Laminar results before the jump, however, are believed to be realistic. There is generally very little difference between the thermal results in this *region regardless of flow and heat transfer model employed*. After the jump, some variations in the flow field were observed dependent on the computational flow model used. However, results from different thermal computations performed on one and the same flow field, varied insignificantly. In other words, the choice of thermal model - laminar or

turbulent - seems *unimportant*. Thus, for liquid metals, only obvious *large-scale* variations, such as recirculation zones, seem to affect the final temperature field. There is no great difference in the FLUENT simulations of the four surface profiles analysed here.

Measured temperatures in experiments with liquid tin were consistently lower than simulated. Measured heat flow usually exceeded predicted values, particularly in the stagnation region. Similar results have been widely reported in systems with gas and water, and are found to vary significantly with free stream turbulence intensity. This does not seem to be valid for liquid metal simulations. The reasons for the deviations between experiments and computations are not fully understood. The flow may be too complex for a two-dimensional model to handle, which additionally of course is an idealization/simplification of a real flow. Systems involving liquid metal heat transfer are vulnerable to disturbances and if such exist, measurements can easily deviate from calculations.

An analytical model for heat transfer was also developed. Wall temperatures calculated in this way were a little lower than the numerically simulated temperatures, but still higher than those predicted by FLUENT. The comparison of results shows good promise that this analytical method can act as a *useful alternative* to the much more demanding numerical simulations. The model was developed on the basis of laminar flow, but numerical simulations show it is just as applicable to turbulent flows. It can be further developed to include inclined jets and jets impinging on moving surfaces, as in strip casting.

The analytical model shows that in all practical flows with liquid metals the heat transfer coefficient is largest where the film thickness is at a minimum and *not* in the stagnation region. The heat flow rate is all the same greatest in this region, due to the bulk temperature of the fluid being highest there. In traditional casting methods (not rapid solidification) the resistance to heat flow from the liquid metal will be in the mould and from the mould to the surroundings or a cooling system and not from the metal to the mould. The convective heat transfer coefficients from the metal to the mould are very high, and it will thus not be critical which theoretical flow model is used for thermal computations.

Measurements of an impinging water jet with a laser-Doppler instrument were performed. This is an unacceptable method due to the roughness of the free surface and the large measuring volume in relation to the film thickness before the jump.

Experiments show that the hydraulic jump develops before the flow reaches the edge of the plate and remains quite steady at this position even after steady-state conditions are established. This indicates that plate size does not heavily influence the jump position, agreeing well with the theory of Buyevich and Ustinov and the Bernoulli model developed in the course of this study.

Only steady state impingement flows were considered, and transient conditions, such as filling a mould, must (at least temporarily) be simulated numerically. It is, however, believed that these flows resemble the conditions at the start of the casting in an empty mould, when the strain on the mould is greatest. During the filling period, the heat flow is probably a little different.

8.2 Recommendations for Further Work

8.2.1 Experiments

The main deficiency of the water experiments is the velocity measurements. In subsequent work a much smaller laser-Doppler measuring volume must be used in order to accurately investigate the thin film flows experienced in this study.

Experiments with tin proved difficult, mainly due to its oxidation. This most probably influenced the flow and heat transfer in the tin. In later work it would be beneficial to use a metal that does not oxidate so easily in air, preferably still with a relatively low melting point. A thorough study of various alternatives must be carried out. The pump design can also be improved, with a better sealing between the housing and the shaft in order to reduce stirring and entrainment of air. The shaft diameter should, for the same reasons, be reduced to a minimum. Alternatively, the whole set-up

could be enclosed in an inert atmosphere. This will of course increase the costs significantly.

The flow characteristics of liquid metals and water are very similar and therefore water can quite reliably be used to simulate liquid metal flows. There are some methods available for the measurement of velocity in liquid metals, but due to their opacity and the small film thickness of interest here, it is extremely difficult to measure velocity variations over the cross-section of the flow. The possibility of using probes or hot wire methods should be investigated. For measuring velocities close to the free surface photographic methods, with or without tracer particles, could be used.

Even though the thermocouples for measuring casting plate temperatures were countersunk to lie flush with its surface, it is inevitable that they to some extent influence the film flow. To reduce this to a minimum, a better-suited filler around them than used in the experiments, should be investigated. The best solution is to afterwards somehow coat the surface of the plate with a thin layer of highly conducting material (higher than the plate) that does not chemically react with the liquid metal in use. It must of course be checked that the surface is still plane.

It is also a good idea to use a thermocamera to measure the temperature on the liquid metal surface.

8.2.2 Mathematical Simulations

Other CFD codes should be studied to see if they can reliably simulate the axisymmetric impingement flow with a hydraulic jump, including heat transfer. Alternatively, the refining of FLUENT's VOF method should be continued. A last resort is to tailor-make a new code for this specific flow.

It is possible that the flow after the hydraulic jump consists of three-dimensional eddies. This is too complex for a two-dimensional numerical model to reproduce and a more thorough investigation of the flow characteristics in this region should be carried out. It is strongly recommended that three-dimensional simulations be looked into.

Appendix: Material Properties

The following material properties have been used in the various calculations:

	T °C	ρ kg/m^3	c_p J/kgK	ν m^2/s	k W/mK	Pr	σ N/m
Water	5	1000	4200	$1.5 \cdot 10^{-6}$	0.578	10.9	0.075
Air	20	1.2	1005	$1.51 \cdot 10^{-5}$	0.026	0.713	
	80	1.0	1009	$2.09 \cdot 10^{-5}$	0.030	0.708	
	150	0.83	1015	$2.86 \cdot 10^{-5}$	0.035	0.694	
	160	0.82	1017	$2.99 \cdot 10^{-5}$	0.036	0.693	
	180	0.78	1022	$3.23 \cdot 10^{-5}$	0.037	0.690	
	200	0.83	1026	$3.46 \cdot 10^{-5}$	0.039	0.685	
Tin	20	7168	222	-	62.5	-	
	232	6950	257	$3.90 \cdot 10^{-7}$	33.0	0.021	
	298	6940	257	$2.39 \cdot 10^{-7}$	33.0	0.013	
	409	6840	257	$2.02 \cdot 10^{-7}$	33.0	0.011	0.621 *
FeSi75	liquid state	3200	932	$3.40 \cdot 10^{-7}$	10.0	0.101	
Stainless steel - AISI 316	20	7850	470		15.0		
	100	7850	500		16.0		
	200	7850	530		17.5		
	400	7850	600		20.0		

FeSi75 is ferrosilicon with 75 weight% Si.

T - temperature, ρ - density, c_p - specific heat capacity, ν - kinematic viscosity, k - heat conductivity, Pr - Prandtl number, σ - surface tension.

- Tin:

Melting point: 232 °C
Boiling point: 2270 °C

*From 400 to 800 °C, $\sigma = 700 - 0.17T + (25 + 0.015T)$. T is in K. From Metals Handbook, 1990.

For sake of simplicity it was decided to use constant material properties, chosen as following for liquid tin:

$\rho = 6900$, $c_p = 257$, $k = 33$, $\nu = 2.174 \cdot 10^{-7}$, $Pr = 0.012$, $\sigma = 0.61$.

- Stainless steel

A constant value of 18 W/mK was used for the thermal conductivity.

References

Al-Sanea, S.: A numerical study of the flow and heat transfer characteristics of an impinging laminar slot-jet including crossflow effects, Int. J. Heat Mass Transfer, Vol. 35, pp. 2501-2513 (1992).

American Society for Metals: Metals Handbook, 10th ed. Metals Park, Ohio, 1990.

Alekseenko, S. V., Nakoryakov, V. E., Pokusaev, B. G.: Wave Flow of Liquid Films, Begell House, New York, 1994.

Argylopoulos, S.A., Mikrovas, A.C.: A generic technique to estimate velocity in high temperature liquid metals and its adaption to reactive metals, Scandinavian Journal of Metallurgy, Vol. 23, pp. 48-53 (1994)

Bakken, J. A.: Metallurgiteknikk 2, Norwegian University of Science and Technology, Trondheim, 1993 (in Norwegian).

Bird, R. B., Stewart, W. E., Lightfoot, E. N.: Transport Phenomena, Wiley, New York, 1960.

Bowles, R.I., Smith, T.F.: The standing hydraulic jump: theory, computations and comparisons with experiments, J. Fluid Mech., Vol. 242, pp. 145-168 (1992).

Brackbill, J. U., Kothe, D. B., Zemach, C.: A continuum method for modelling surface tension, Journal of Comp. Physics, Vol. 100, pp. 335-354 (1992).

Brdlik, P.M., Savin, V.K.: Heat transfer between an axisymmetric jet and a plate normal to the flow, Inzhenerno-Fizicheskii Zhurnal, Vol. 8, pp. 156-155 (1965).

Buick, J. M.: Lattice Boltzmann Methods in Interfacial Wave Modelling,

Ph.D. thesis, the University of Edinburgh, Scotland, 1997

Buyevich, Y. A., Ustinov, V. A.: Int. J. Heat Mass Transfer, Vol.37 No. 1, pp. 165-173 (1994).

Buyevich, Y. A., Mankevich, V. N.: J. Eng. Physics, Vol 61, pp 71-81 (1991).

Chaudhury, Z.H., Heat transfer in a radial liquid jet. J. Fluid Mech., Vol 20, pp. 501-511 (1964).

Downs, S.J., James, E.H.: Jet Impingement Heat Transfer-a Literature Survey, ASME paper 87-HT-35 (1987).

Fluent Inc.: Fluent User's Guide, version 2.9, Fluent Incorporated, USA, 1992.

Fluent Inc.: Fluent User's Guide, version 4.5. Fluent Incorporated, USA, 1996.

Fluent Inc.: Fluent User's Guide, version 5. Fluent Incorporated, USA, 1998.

Gerhart, P.M., Gross, R.J., Hochstein, J.R.: Fundamentals of Fluid Mechanics; Addison Wesley, 1992.

Glauert, M.B.: The wall jet, J. Fluid Mech. Vol 1, pp. 625-643 (1956).

Gradshteyn, I. S., Ryzhik, I. M.: Tables of Integrals, Series and Products, Academic Press, New York, 1972.

Grådahl, S., Johansen, S.T.: Måleprogram for valseblokk, del II, SINTEF report no. STF34 F92132, Trondheim, 1992 (in Norwegian).

Grådahl, S.: Prosedyre for kalibrering av termometre, SINTEF note dated 16/11 1999, Trondheim, 1999 (in Norwegian).

Higuera, F.J., The hydraulic jump in a viscous laminar flow, J. Fluid Mech., Vol 274, pp. 69-92 (1994).

Hirt, C. W., Nichols, B. D.: Volume of Fluid (VOF) Method for the Dynamics of Free Boundaries, Journal of Comp. Physics, Vol. 39, pp. 201-225 (1981).

Holmberg, N.A.: Metal Feeding in Horizontal Belt Strip Casters, Licenciate thesis, Luleå University of Technology, Sweden 1996.

Incropera, F., P., DeWitt, D., P.: Fundamentals of Heat Transfer; J. Wiley and Sons, 1996.

Kakaç, S., Shah, R.K., Aung, W.: Handbook of Single Phase Convective Heat Transfer, John Wiley , New York, 1987.

Kakaç, S., Yaman, Y.: Convective Heat Transfer, 2nd ed., CRC Press, Boca Raton, 1995.

Kays, W. M., Crawford, M. E. : Convective Heat and Mass Transfer, McGraw-Hill, New York, 1993.

Kothe, D. B., Mjolsness, R. C., Torrey, M. D., RIPPLE: A Computer Program for Incompressible Flows With Free Surfaces; Los Alamos Report LA-12007-MS, 1991.

Liu, X., Lienhard V, J.H.: The hydraulic jump in circular jet impingement and in other thin film flows, Experiments in Fluids, Vol. 15, pp. 108-116 (1993).

Lyon, R.N., Liquid-Metals Handbook: Bureau of Ships, Washington, 1954.

Massey, B. S.: Mechanics of Fluids, 4th ed., Van Nostrand Reinhold, New York, 1979.

Ellegaard, C., Hansen, A.E., Haaning, A., Hansen, K., Marcussen, A., Bohr, T., Hansen, J.L., Watanabe, S.: Creating corners in kitchen sinks, Nature, Vol. 392, pp. 767-768 (1998)

Johansen, S.T.: Personal communication, 1995-1999.

Middleman, S.: Modeling Axisymmetric Flows, Academic Press, San Diego, 1995.

Nakoryakov, V. E., Pokusaev, B. G., Troyan, E. N., Alekseenko, S.V.: Wave Processes in Two-Phase Systems (in Russian), Novosibirsk, pp. 129-206 (1975).

Nakoryakov, V. E., Pokusaev, B. G., Troyan, E. N.: Int. J. Heat Mass Transfer, Vol. 21, pp. 1175-1184 (1978).

Nos, P. O., Experimental Study of a Rectangular Evaporation Cooler Operating on Synthetic Heat Transfer Fluids. Dr. ing. thesis, Norwegian University of Science and Technology, Norway, 1993.

Olsson, R.G., Turkdogan, E.T.: Radial spread of a liquid stream on a horizontal plate, Nature, Vol. 211, pp. 813-816 (1966).

Patankar, S. V.:Numerical Heat Transfer and Fuid Flow, Hemisphere Publishing Corp., Washington DC, 1980.

Rahman, M.M., Faghri, A., Hankey, W.L., Swanson, T.D.: Prediction of heat transfer to a thin liquid film in plane and radially spreading flows, Transactions of the ASME, Vol. 112, pp. 822-825 (1990).

Rahman, M.M., Hankey, W.L., Faghri, A.: Analysis of the fluid flow and heat transfer in a thin liquid film in the presence and absence of gravity, Int. J. Heat Mass Transfer, Vol. 34, pp. 103-114 (1991).

Rogers, G.F.C., Mayhew, Y.R.: Engineering Thermodynamics Work and Heat Transfer, Longman, London, 1967.

Schach, W.: Umlenkung eines Flussigkeitsstrahles an einer ebenen Platte, Ing.-Arch., Vol. 5, pp. 460-467 (1934).

Schlichting, H.: Boundary-Layer Theory, McGraw-Hill, New York, 7th edition, 1979 .

Seban, R.A., Shimazaki, T.T.: Heat Transfer to a Fluid Flowing Turbulently in a Smooth Pipe with Walls at Constant Temperature, Transactions of ASME, Vol. 73, p.803, 1951.

Shah, R.K., Bhatti, M.S.: Handbook of Single Phase Convective Heat Transfer, John Wiley , New York, 1987.

Shyy, W., Udaykumar, H.S., Rao, M.M., Smith, R.W.: Computational Fluid Dynamics with Moving Boundaries, Taylor and Francis, Washington, 1996.

Sibulkin, M.: Heat transfer near the forward stagnation point of a body of revolution, J. Aeron. Sci., Vol. 19, pp. 570-571 (1952).

Stevens, J., Webb, B.W.: The effect of inclination on local heat transfer under an axisymmetric, free liquid jet, Int. J. Heat Mass Transfer, Vol. 34, pp. 1227-1236 (1991).

Stevens, J.: Free surface flow profile and fluctuations of a circular hydraulic jump formed by an impinging jet, Journal of Fluids Engineering, Vol. 117 pp. 677-682 (1995).

Stevens, J., Webb, B.W.: Measurements of flow structure in the radial layer of impinging free-surface liquid jets. Int. J. Heat Mass Transfer, Vol. 36, pp. 3751-3758 (1993).

Stevens, J., Webb, B.W.: Measurements of the free surface flow structure under an impinging, free liquid jet, Journal of Heat Transfer, Vol. 114, pp. 79-84 (1992).

Stevens, J., Webb, B.W.: Local heat transfer coefficients under an axisymmetric, single-phase liquid jet, Journal of Heat Transfer, Vol. 113, pp. 71-78 (1991).

Thomas, S., Hankey, W., Faghri, A.: One-dimensional analysis of the hydrodynamic and thermal characteristics of thin film flows including the hydraulic jump and rotation, Transactions of the ASME, Vol. 112, pp. 728-735 (1990)

Townson, J.M.: Free-Surface Hydraulics, Unwin Hyman, London, 1991.

Vader, D.T., Incropera, F.P., Viskanta, R.: Local Convective Heat Transfer From a Heated Surface to an Impinging, Planar Jet of Water, Int. J. Heat Mass Transfer, Vol. 34, pp. 611-623 (1991).

Wang, Y.B., Chaussavoine, C., Teyssandier, F.: Two-dimensional modelling of a non-confined circular imipinging jet reactor - fluid dynamics and heat transfer, Int. J. Heat Mass Transfer, Vol. 36, pp. 857-873 (1993).

Wang, Y.B., Dagan, Z., Jiji, L.M.: Heat transfer between a circular free impinging jet and a solid surface with non-uniform wall temperature or wall heat flux-1. Solution for the stagnation region, Int. J. Heat Mass Transfer, Vol. 32, pp. 1351-1360 (1989).

Watson, E. J.: The radial spread of a liquid jet over a horizontal plane, Journal of Fluid Mech. Vol. 20, pp 481-495 (1964).

White, F. M.: Viscous Fluid Flow, McGraw-Hill, New York, 1991.

Wolf, D.H., Viskanta, R., Incropera, F.P.: Local convective heat transfer from a heated surface to a planar jet of water with a nonuniform velocity profile. Journal of Heat Transfer, Vol. 112, pp. 988-905 (1990).

Wolfstein, M.: The Velocity and Temperarure Distribution of One-Dimensional Flow with Turbulence Augmentation and Pressure Gradient, Int. J. Heat Mass Transfer, Vol. 12, pp. 301-318 (1969).

Zukauskas, A., Slanciauskas, A.: Heat Transfer in Turbulent Fluid Flows, Hemisphere Publishing Corporation, Washington, 1987.

Zumbrunnen, D.A.: Transient Convective Heat Transfer in Planar Stagnation Flows with Time-varying Surface Heat Flux and Temperature, Journal of Heat Transfer, Vol. 114, pp. 85-93 (1992).